# COMPUTATIONAL MODELLING AND SIMULATIONS OF MATERIALS FOR PHOTOCATALYTIC HYDROGEN PRODUCTION

**Doctoral Dissertation by**
**Håkon Eidsvåg**

Thesis submitted for
the degree of Philosophiae Doctor (PhD)
in
Computer Science:
Software Engineering, Sensor Networks and Engineering Computing

Department of Computer Science,
Electrical Engineering and Mathematical Sciences

Faculty of Engineering and Science

Western Norway University of Applied Sciences

20th of February 2023

Series of dissertation submitted to
the Faculty of Engineering and Science,
Western Norway University of Applied Sciences.

ISBN: 978-82-8461-010-8

Author: Håkon Eidsvåg
Title: Computational modelling and simulations of materials for photocatalytic hydrogen production

Printed production:
Molvik Grafisk / Western Norway University of Applied Sciences

Bergen, Norway, 2023

TO FRIENDS, FAMILY AND LOVED ONES,

*Without you, this Ph.D. would never have seen the light of day*

# PREFACE

The author of this thesis has been employed as a Ph.D. research fellow in the Advanced Nanomaterials for Clean Energy and Health Applications research group at the Department of Computer Science at Western Norway University of Applied Sciences, Norway.

The author has been enrolled into the PhD program Computer Science: Software Engineering, Sensor Networks and Engineering Computing, specialising in Engineering Computing.

The research presented in this thesis has been accomplished in cooperation with the Department of Chemistry at the University of Oslo, Norway, and the Department of Physics at the University of Jaffna, Sri Lanka.

This thesis is organised into two parts. Part I is an overview article providing an introduction to the research field of computational modelling and simulation. Part II consists of a collection of published and peer-reviewed research articles and submitted papers.

Paper A **H. Eidsvåg**, S. Bentouba, P. Vajeeston, S. Yohi, and D. Velauthapillai. $\mathrm{TiO_2}$ as a photocatalyst for water splitting – an experimental and theoretical review. In Molecules MDPI, volume 11, pages 3759-3769, 2021

Paper B **H. Eidsvåg**, M. Rasukkannu, P. Vajeeston, and D. Velauthapillai. Bandgap engineering in $\mathrm{CsSn_xPb_{1-x}I_3}$ and their influence on light absorption. In Materials Letters, volume 218, pages 253-256, 2018

Paper C C. P. Wanniarachchi, **H. Eidsvåg**, T. Arunasalam, P. Ravirajan, D. Velauthapillai, and P. Vajeeston. $\mathrm{Cs_2AgBiBr_6}$ as a mixed anion perovskites for photovoltaic applications: A first-principle study. In materialstoday: PROCEEDINGS, volume 64, Part 5, pages 1783-1788, 2022

Paper D **H. Eidsvåg**, M. Rasukkannu, D. Velauthapillai, and P. Vajeeston. In-depth first-principle study on novel $\mathrm{MoS_2}$. In RSC Advances, volume 11, pages 3759-3769, 2021

Paper E **H. Eidsvåg**, P. Vajeeston, and D. Velauthapillai. Doped $\mathrm{MoS_2}$ polymorph for improved hydrogen evolution reaction. Submitted to Journal of Computational Physics X, January 2023.

# Other scientific contributions

## *Publications*

1. C. P. Wanniarachchi, **H. Eidsvåg**, T. Arunasalam, P. Ravirajan, D. Velauthapilla, and P. Vajeeston. Deep insight into structural and optoelectronic properties of Mixed Anion Perovskites. Submitted to RSC Advances, February 2023.

## *Oral presentations*

1. **H. Eidsvåg**, M. Rasukkannu, D. Velauthapillai, and P. Vajeeston. (2017). Bandgap engineering in $\mathrm{CsSn_xPb_{1-x}I_3}$ and their influence on light absorption. *International Symposium on Nano materials for Clean Energy and Health Applications (ISNCHA) 2017*, Coimbatore, India.
2. **H. Eidsvåg**, D. Velauthapillai, and P. Vajeeston. (2019). A review of the current DFT simulations and experimental work done on solar powered water splitting. *The International Conference on Advanced Materials for Clean Energy and Health Applications (AMCEHA) 2019*, Jaffna, Sri Lanka.
3. **H. Eidsvåg**, M. Rasukkannu, D. Velauthapillai, and P. Vajeeston. (2020). In-depth first-principle study on novel MoS2 polymorphs. *Nasjonal konferanse for materialteknologi 2020*, Norway (online conference).
4. **H. Eidsvåg**, M. Rasukkannu, D. Velauthapillai, and P. Vajeeston. (2021). In-depth first-principle study on novel MoS2 polymorphs. *Technological Advances in Science, Medicine and Engineering (TASME) 2021*, virtual conference. Won best presentation award.

## *Popular science*

1. *H. Eidsvåg*. (2018). Hydrogen - What's the point?. High school visit at HVL.
2. Forskningsdagene 2019, Bergen, Norway.
3. Forskar grand prix 2021, Bergen, Norway.
4. FIN-samling 2021, Bergen, Norway.

# ACKNOWLEDGMENTS

---

This Ph.D. has been hard work and a long journey towards completion, which I could not have travelled without the help of my supervisors, colleagues, friends and family. First, I thank my supervisors, Professor Dhayalan Velauthapillai and Associate Professor Ponniah Vajeeston. Thank you for guiding me along the path, encouraging me, sharing your knowledge and giving me this opportunity. I would also like to thank Dr Murugesan Rasukannu for his mentoring and help in understanding our research group's computational tools and methods. All my co-authors and collaborators throughout the Ph.D. must also be thanked. You made my research possible.

Thank you, University of Jaffna, for having me during my research stay. Your staff and students were extremely welcoming and took great care of me. Thanks to the Sri Lankan (Asitha, Kajana, Pavithrakumar, Pirashantan, Sivagowri, Rajaramanan, Uthayaraj, Nathini, Meenilankco and others) and Indian (Selvakumar, Prabavathy and others) students that showed me around when I visited and stayed in your beautiful countries and cities. Those times were easily the highlights of my Ph.D. A special thanks to Nanthini and Meenilankco for their help finishing this thesis.

Many thanks go to my colleagues, fellow Ph.D. students and friends at HVL. Our discussions at lunch, after-work activities, and relaxed and fun atmosphere helped me through the rough patches and made it fun to go to work. I want to thank my friends for all the support, advice and ability to get me out of the Ph.D. bubble. An enormous thanks go to Victoria, Kristian, Marius and my friends for listening to me vent and raising my spirit. Kristian deserves a second mention for his efforts in proofreading this thesis and our discussions over the years.

I am incredibly grateful for my mom and dad's love and support; your belief in me kept me going through these years. I must also thank Saga, my dog, for her endless and unconditional love. Nothing beats coming home to your happy smile and demand for cuddles and playtime. Finally, I would like to thank Astrid. Without you by my side, this thesis and project would never have been finished. Thank you for always being there for me, no matter my mood or how late I would come home from work. Your love means the world to me.

# ABSTRACT

Photocatalytic hydrogen production has been of interest since Fujishima and Honda first demonstrated it in 1972 with the help of a titanium-oxide electrode. Thanks to the rapid development of nanotechnology, this method has received much attention in recent years due to the need for cost-effective green hydrogen production. At the same time, solar cell technology has seen swift improvement in efficiency and reduced production costs due to increased research and political goodwill. However, there are still some significant issues to be addressed regarding energy storage and availability during dark or cloudy periods.

A solution would be to store the solar energy in hydrogen through electrolysis or photocatalytic water splitting. Although electrolysis is the most developed technology, it is still quite expensive, requiring a connection of the electrolysers to the electrical grid or a direct electrical connection to a solar farm. This makes it primarily suitable for developed countries with an extensive electrical grid and high-standard infrastructure. Developing countries, on the other hand, which are often located in regions with a lot of sun, lack an electrical grid of high quality to transport electricity from solar farms to the electrolysers. In these cases, photocatalytic hydrogen production could be the solution, as it would make it possible to produce hydrogen directly from the sunlight and transport it using existing infrastructure. Photocatalytic hydrogen production effectively combines the solar absorption abilities of photovoltaics with electrolysers' ability to split water molecules into oxygen and hydrogen. Some challenges exist before the technology is viable for large-scale production facilities, such as low solar-to-hydrogen efficiency and technology maturity.

In this project, we have used computational models and simulations to investigate materials and their structural, optical, electronic, and photocatalytic properties to address these issues. This was done by approximating solutions to the Schrödinger equation with the help of the Vienna Ab Initio Simulation Package (VASP) and our own developed tools. These results were analysed using post-processing tools in combination with physics, material science and chemistry. The applied computational models and simulations are incredibly reliant on computing power, which necessitates high-performance computing, parallelisation, and the development of efficient numerical methods.

The scientific contribution of this project is threefold:

First, we thoroughly reviewed state-of-the-art experimental and theoretical research on $\mathtt{TiO_2}$ based photocatalysts. In this work, we identified four major challenges that must be overcome for the field to advance further:

1. No standardised measurement setting for hydrogen production rates.
2. The intrinsic properties of $\mathtt{TiO_2}$ are not good enough, other materials can easily outperform $\mathtt{TiO_2}$ based photocatalysts.

3. Lack of cooperation between theoretical and experimental work. Not playing on the strength of the two approaches to complement each other.
4. There does not exist scalable photocatalytic hydrogen production facilities.

We identified other materials that could outperform $\mathrm{TiO_2}$ based photocatalysts on cost, efficiency, and lifetime through computer simulation studies and our review article. The most interesting candidates were perovskites and transition metal dichalcogenides such as $\mathrm{MoS_2}$.

Secondly, we investigated the structural and electronic of perovskite materials, $\mathrm{CsPbI_3}$ and $\mathrm{CsSnI_3}$, to determine their suitability for photocatalytic applications. In order to tackle the challenges such as toxicity and long-term stability issues faced by well-known lead-based organic perovskites, we carried out an in-depth analysis of the properties of lead-free double perovskites, $\mathrm{Cs_2AgBiBr_6}$. To enhance the properties of $\mathrm{Cs_2AgBiBr_6}$, we also conducted another numerical study by substituting Br with other halide atoms in $\mathrm{Cs_2AgBiX_6}$ (X = Br, Cl, F, and I). These studies show that $\mathrm{Cs_2AgBiX_6}$ (X = Br, Cl, F, and I) can be prominent candidates for photocatalytic and photovoltaic applications through clever substitutions of the halide component.

Thirdly, we investigated $\mathrm{MoS_2}$ as a potential photocatalyst. Fourteen different polymorphs were proposed and analysed for the very first time using first-principle calculations based on density functional theory (DFT). Seven of the polymorphs ($\mathrm{1H, 2T, 2H, 2R_1, 3H_a, 3H_b}$, and 4T) were both mechanically and dynamically stable with indirect bandgaps ranging from 1.87 eV to 2.12 eV. This work was extended as we looked into how dopants would influence the photocatalytic properties of $\mathrm{MoS_2}$. We used the stable polymorphs from our earlier work, and all seven showed promising results regarding their *d*-band model and Gibbs free energy. We chose to substitutional dope $\mathrm{3H_b}$ with Al, Co, I, N and Ni. Replacing one Mo atom with either Al, Co, I, N and Ni lowered the Gibbs free energy by a factor of ten. However, only $\mathrm{3H_b}$ with one Mo atom replaced with Al or Ni were stable structures. This shows that $\mathrm{MoS_2}$ through doping is a photocatalyst that, with further optimisation, could be used in large-scale photocatalytic hydrogen production.

We expect that the results from the studies in this project will result in new and efficient low-cost materials that will help push the field of photocatalytic water splitting further.

# SAMANDRAG

Fotokatalytisk hydrogenproduksjon har vore ein spanande teknologi sidan Fujishima og Honda først demonstrerte den i 1972 hjelp av ein titandioksid elektrode. Takka være den raske utviklinga av nanoteknologi så har denne metoden fått mykje oppmerksemd dei siste åra på grunn av behovet for rimeleg og grøn hydrogenproduksjon. I løpet av den same perioden har også solcelleteknologien utvikla seg kraftig takka vera forsking og politisk velvilje. Dette har gjort solcellene rimelegare å produsera og meir effektive. Dessverre er det framleis utfordingar med lagring av overskottsenergi og produksjon når det er mørkt eller overskya. Ei løysing på dette vil vera å lagra solenergien i hydrogen produsert gjennom elektrolyse eller fotokatalytisk splitting av vatn. Av desse to teknologiane er elektrolyse mest moden, men den er framleis dyr og krevjar tilgang til det elektriske straumnettet eller ein direkte elektrisk kopling til ein solpark. Dette gjer at den først og fremst er aktuell i industriland med eit utbreidd straumnett og utvikla infrastruktur. Utviklingsland på den andre sida, som ofte er lokalisert i regionar med mykje sol, manglar eit skikkeleg straumnett som dekker heile landet. Noko som gjer det vanskeleg å frakta straumen frå solparkar til potensielle hydrogenproduksjonsanlegg. Ei løysing på desse problema kan vera fotokatalytisk hydrogen produksjon. Denne teknologien gjer det mogleg å produsera hydrogen direkte frå sollys og deretter kan ein transportera hydrogenet med hjelp av eksisterande veg infrastruktur. Fotokatalytisk hydrogen produksjon kombinerer sol absorpsjonen til solceller med vatn splitting eigenskapane til ein elektrolysør på ein effektiv måte. Naturlegvis, er det framleis nokon utfordringar som må bli løyst før teknologien er moden nok til å bli tatt i bruk. Dette går primært ut på lav sol-til-hydrogen effektivitet og teknologisk modnad.

I dette arbeidet, har me brukt datamodellering og simuleringar til å undersøka ulike materiale sine elektroniske, optiske, strukturelle og fotokatalytiske eigenskapar. Dette ble gjort med hjelp av Vienna Ab Initio Simulation Package (VASP), som approksimerer løysingar på Schrödinger likninga, og egne verktøy. Resultata frå desse berekningane vart så prosessert ved hjelp av ulike verktøy, fysikk, materialvitskap, og kjemi. Modellane som vart brukt krevjar mykje datakraft og gjorde det nødvendig å bruka superdatamaskinar, parallellprosessering, og utvikling av effektive numeriske metodar.

Det vitskaplege bidraget til prosjektet kan delast i tre deler:

Først gjennomførte me ei nøye studie av toppmoderne eksperimentell og teoretisk forsking basert på $TiO_2$ fotokatalysatorar. I dette arbeidet, identifiserte me fire store utfordringar som feltet står ovanfor:

1. Det eksisterer ikkje nokon standard måte å måla og rapportera hydrogen produksjons ratar på.
2. Dei ibuande eigenskapane til TiO2 er ikkje gode nok, og andre materiale kan

enkelt overgå resultata til TiO2 baserte fotokatalysatorar.

3. Manglande samarbeid mellom eksperimentelt og teoretisk arbeid gjer at ein ikkje spelar på styrkane til kvarandre.
4. Det eksisterer ikkje nokon planer for medium eller store fotokatalytiske hydrogen produksjons anlegg.

Gjennom datasimuleringar studiar og oversiktsartikkelen vår, identifiserte me andre materiale som kan utkonkurere $TiO_2$ fotokatalysatorar på kostnad, levetid og effektivitet. Dei to mest interessante kandidatane var perovskittar og $MoS_2$.

Det andre me gjorde var å undersøka dei strukturelle og elektroniske eigenskapane til perovskittar ,$CsPbI_3$ og $CsSnI_3$, for å sjå om dei er aktuelle for fotokatalytisk hydrogenproduksjon. For å gjera noko med dei kjente giftigheit og stabilitets problema til perovskittar med bly i seg, undersøkte me eigenskapane til den blyfri doble perovskitten, $Cs_2AgBiBr_6$,. I tillegg gjennomførte me ei ny numerisk studie kor Br blei substituert med andre halogenidar i $Cs_2AgBiX_6$, (X = Br, Cl, F og I). Desse studiane visar at $Cs_2AgBiX_6$, (X = Br, Cl, F og I), har eit stort potensiale innanfor fotokatalytiske og solcelle applikasjonar gjennom halogenid doping.

Til sist, undersøkte me $MoS_2$ som ein potensiell fotokatalysator. Fjorten ulike $MoS_2$ polyformer vart, for første gang nokosinne, foreslått og analysert ved hjelp av førsteprinsipp berekningar basert på tettheit-funksjonell teori (DFT). Sju av desse polymorfane ($1H$, $2T$, $2H$, $2R_1$, $3H_a$, $3H_b$ og $4T$) var både mekanisk og dynamisk stabile med indirekte båndgap frå 1.87 eV til 2.12 eV. Arbeidet vart utvida med ei studie der me undersøkte korleis doping ville påverka dei fotokatalytiske eigenskapane til $MoS_2$. Me brukte dei stabile polymorfane frå vårt tidlegare arbeid og alle viste potensiale basert på *d*-band senter og Gibbs fri energi. Me valte ut $3H_b$ for videre berekningar og substituerande dopa den med Al, Cl, I, N eller Ni for eit Mo eller eit S atom. Når me erstatta eit Mo atom med enten Al, Cl, I, N eller Ni vart Gibb fri energien senka med ein faktor på ti. Av desse fem strukturane var det berre når Al eller Ni erstatta Mo at strukturen var mekanisk og dynamisk stabil. Dette visar at $MoS_2$ kan gjerast til effektive fotokatalysatorar gjennom doping og med videre optimalisering er det mogleg å realisera stor-skala produksjonsanlegg.

Me forventar at resultata frå studiane våre vil resultera i nye og effektive fotokatalysatorar som vil vera med å driva feltet videre framover.

# Contents

# Part I

# OVERVIEW

# CHAPTER 1

# INTRODUCTION

In April 2022, the UN released a new report on climate change, concluding that it is now or never if we are to achieve the 1.5-degree goal of the Paris Agreement. The world is currently on the "fast track" to disaster, and change is needed [1]. The Sustainable Development Goals (SDGs), released by the United Nations (UN) in 2015, are a collection of 17 interlinked global goals that intend to provide a blueprint for achieving a better and more sustainable future for all [2]. Renewable and clean energy is a critical part of the solution if we want to reach these goals, which are also stated in Goal 7, affordable and clean energy, and Goal 13, climate action [3]. Through Goal 7, the UN wants to ensure access to affordable, reliable, sustainable, and modern energy for everyone. This means that not only must first-world countries move away from non-renewable energy sources, but we must also help ensure access to electricity for the millions living in developing countries currently without reliable energy sources [3]. Goal 13 urges action to combat climate change and its impact on the world and society. To meet the 1.5 °C maximum target for temperature rise by 2050, greenhouse gas emissions must decrease by 7.6% per year starting in 2020 [2]. This means we can not solve Goal 7 by increasing the production and consumption of non-renewable energy sources such as coal, oil and natural gas.

Instead, we must turn towards renewable energy sources such as wind, solar, hydro, or geothermal. However, most of them come with drawbacks that make the transition difficult. Hydropower requires access to waterfalls and the production of high-cost dams that will cause drastic changes in the surrounding ecosystems. Electricity from wind turbines lacks good storage options, and the technology struggles with intermittency problems caused by varying wind speeds. Nevertheless, offshore wind farms storing excess energy as hydrogen is a promising venture [4]. Geothermal energy only works in specific areas and has a limited lifetime, which makes it more suited as an additional energy resource in suitable regions [5]. On the other hand, the Earth gets enough power from the sun in one hour to satisfy the global energy consumption for a year [6]. This makes solar power the most viable clean energy resource currently available. Thus, the solution to the energy crisis could be directly harvesting solar light and converting it into electrical energy with photovoltaic cells or chemical energy through photoelectrochemical reactions. Conventionally, both technologies rely on collecting light in semiconductor materials with appropriate band gaps, matching the solar spectrum and thus providing a high-energy conversion efficiency. Unfortunately, the technology has drawbacks which prevent it from overtaking non-renewable energy as the primary energy source.

Two significant issues are the uneven power distribution caused by varying solar irradiance and a lack of proper storage alternatives. This has increased research on storage options for the produced electricity, which we can divide into mechanical and electrochemical storage systems. For example, in Oceania, pumped hydroelectricity (mechanical) is the most common storage system for excess electricity [7]. While the electrochemical storage options are different batteries (Lithium-ion, sodium-sulphur, vanadium, and similar materials), hydrogen, and supercapacitors [7], there are several reasons for choosing hydrogen as a way to store solar energy. Some examples are the high abundance of hydrogen from renewable sources, it is eco-friendly when used, hydrogen has a high-energy yield, and it is easy to store as either a gas or a liquid [8][9][10]. The high energy yield and ease of storage make green hydrogen viable as fuel for the long transport sector; aeroplanes, cruise ships, trailers, and cargo ships [11][12]. Realising a green energy shipping fleet could cut 2.5% of global greenhouse emissions (GHG) yearly [13]. However, to succeed in this strategy, we must produce hydrogen clean and renewable.

The majority of commercial production of hydrogen stems from four sources: natural gas, coal, oil and electrolysis. Of these, steam reforming alone represents 48% of the world's hydrogen production, while coal contributes 18%, oil 30% and electrolysis the last 4% [14]. Steam methane reforming is a high-temperature and high–pressure method, with temperatures varying from 700 to 900 °C [15]. It is a very energy-intensive process with $CO_2$ as a by-product of the reaction. Of the non-renewable energy sources, coal is the cheapest one. In addition, coal gasification can be used to improve $CO_2$ mitigation at power plants [16]. Oil refineries/platforms produce and consume hydrogen onsite as a part of their process, which could be expanded. However, these three processes all have greenhouse gases and other pollutants as by-products, which makes them unsuitable if we are to achieve SDG 7. Some of this could be compensated by improved technology and the addition of $CO_2$ capture, but there will always be some emissions. However, a better solution would be to produce green hydrogen, i.e. hydrogen produced using renewable energy sources without any climate gas emissions. That is why more than 25 countries have committed to a hydrogen policy and to use hydrogen as a clean energy vector in their energy system. Norway established two renewable research centres on hydrogen in 2022, HyValue and HYDROGENi. These two centres aim to solve many problems the hydrogen economy faces before it can be realised, such as production cost, storage, transport, public acceptance and technology maturity. The most common way to produce green hydrogen today is electrolysis powered by a renewable energy source. As mentioned above, this makes it possible to store renewable energy from sources with intermittency problems, wind and solar. Projects such as Deep Purple [17], explore the possibility of combining offshore wind farms with electrolysers on the ocean floor to produce and store hydrogen. Regarding solar energy, there are pilot projects, e.g. in Portugal [18], Spain [19], and UAE [20], combining solar plants with electrolysers. However, these technologies are expensive and usually require a well-developed grid, especially if the wind or solar farm is not located close to the hydrogen production facilities. This makes it unsuited in developing countries due to the costs involved and poorer standards on the electrical grid.

An alternative technology for these areas, which most often are regions with high solar irradiation, is photocatalytic hydrogen production. This technology combines solar cells' solar absorption with the water-splitting capabilities of electrolysers into one material. That way, there is no need for electricity transport and facilities can built it in areas where high temperatures makes solar farms unviable. In photocatalytic hydrogen production, the photocatalytic material is submerged in continuously circulating water to ensure an abundance of water molecules for the reaction. In addition, the circulation will help cool down the system. Since electrolysis and solar cells are combined, it is less area intensive and can use existing infrastructure to transport the hydrogen. Several methods combine solar energy and water splitting; thermochemical, photo-biological, and photocatalytic water splitting [21]. Thermochemical water splitting is is conceptually simple, but requires extensive and expensive solar collectors to achieve the needed temperature (2500K) [22]. There are two different Photo-biological processes, which depends on the microorganisms used [23]. Despite being a green and renewable technology, it struggles with low hydrogen yield and difficulties designing and upscaling the bioreactor [22][23]. This leaves photocatalytic water splitting as the best option, and there are several reasons for that: (1) good solar-to-hydrogen efficiencies; (2) low production cost; (3) the possibility of separating oxygen and hydrogen streams; and (4) it could be used on small scales as well [8][22][24].

## 1.1 History of water splitting

Electrolysis of water was first discovered and understood in 1789 by Adriaan Paets van Troostwijk, and Johan Rudolph Deiman [25]. The technology has since then been improved on and developed several times. See figure 1.1 for some of the most important historical events. In 1888, Dmitry Lachinov developed the first industrial process for producing hydrogen through water splitting [26]. This sped up the development process, and by 1902 more than 400 industrial water electrolysers were in use globally. The period between the 1920s and 1970s was the golden age for improving electrolysis and water-splitting technologies. Most of the traditional designs seen and used today stem from this period [27]. The fast development was driven by the need for large quantities of hydrogen to produce ammonia fertilisers.

However, it was not until the 1970s that photoelectrochemical and photocatalytic water splitting (PWS) were achieved for the first time. In 1972 Fujishima and Honda used a $\mathrm{TiO_2}$ photoelectrode for light absorption and split water into oxygen and hydrogen [28]. Since then, many different materials and compounds have been tried as semiconductors for photocatalytic water splitting. Unfortunately, most of them do not absorb enough visible light for viable scale-up from lab experiments to proof of concept facilities [29].

Although $\mathrm{TiO_2}$ was used to achieve PWS for the first time, it cannot split water or perform the hydrogen evolution reaction (HER) photocatalytically on its own. For example, it needs to be modified with noble metal decoration, doping or through

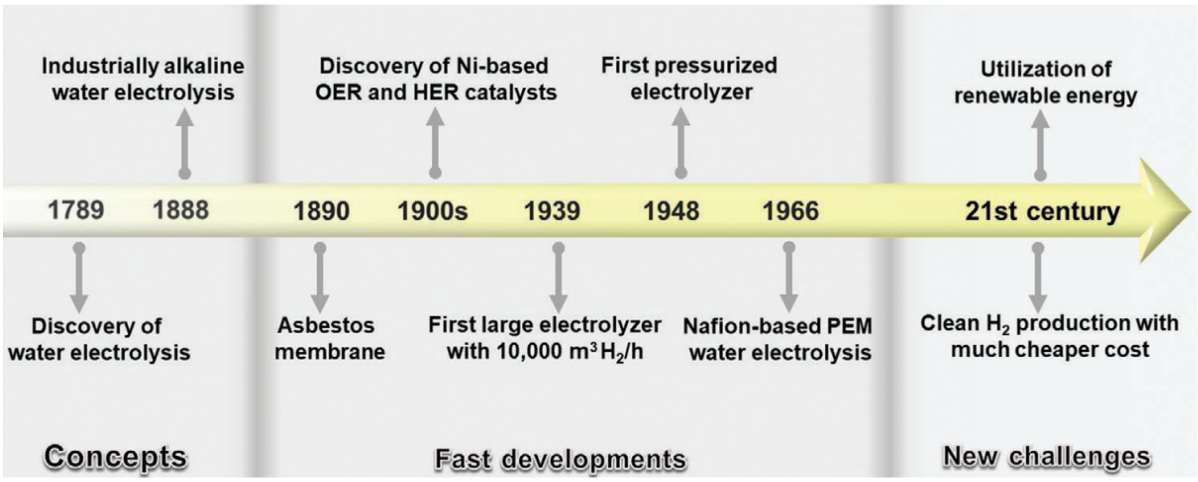

**Figure 1.1:** The history of water splitting and its development. Taken from [27]

.

the formation of a heterojunction. In the early 2000s it was common to use nonmetal dopants like nitrogen and sulfur anions to improve $TiO_2$ performance. Nowadays, researchers try to utilise nanostructures, quantum dots and dopants to create complex $TiO_2$ structures in an attempt to improve the photocatalytic water splitting capabilities of the material [30]. However, these structures are often too complex or have expensive materials making large-scale production unrealistic.

This has led to a renaissance of many new metal oxide photocatalysts first discovered and investigated in the 1980s and 1990s. These materials could generally be classified as either $d^0(Ti^{4+}, Zr^{4+}, Ta^{5+}, Nb^{5+}, W^{6+})$ or $d^{10}(Ga^{3+}, In^{3+}, Ge^{4+}, Sb^{5+})$ electron configurations [31]. In 1980 Domen et al. demonstrated that $SrTiO_3$, when decorated with NiO, could perform photocatalytic water splitting [32]. Konta et al. improved the photocatalyst by using metal cations (Ru, Mn, Rh, and Ir) as dopants, making it possible for $SrTiO_3$ to absorb visible light [33]. This turned $SrTiO_3$ into one of the most used photocatalysts for photocatalytic water splitting [31]. Aluminium, Lanthanum and Gallium have also proven to be efficient dopants for $SrTiO_3$. Takata et al. found that using such lower valence cations as dopants introduces oxygen vacancies and decreases the compound's amount of $Ti^{3+}$, enhancing the photocatalytic activity [34]. In 2016 Wang et al. created a powder-based photocatalyst combining La/Rh-doped $SrTiO_3$ with Mo-doped $BiVO_4$, achieving a solar-to-hydrogen efficiency of 1.1% [35]. Several other studies have been done, and in 2020 an external quantum efficiency of 95.6% at 360 nm was reported by Takata et al. [36]. They used aluminium as the dopant before they decorated it with $Rh/Cr_2O_3$ and added CoOOH as a co-catalysts.

In 1998 Kato and Kudo showed for the first time that $NaTaO_3$ is suitable for photocatalytic water splitting [37]. By doping it with Lanthanum and decorating it with NiO, Kato et al. achieved a record high quantum efficiency of 56% at 270 nm in 2003 [38]. This has been further improved by introducing other dopants, such as strontium [31].

Over the last forty years, several other materials have been investigated, for example, $Ga_2O_3$, layered carbon nitride (e.g. $g - C_3N_4$), $WO_3$, $Fe_2O3$, CdS and GaAs. In recent years people have also started experimenting with perovskites as a photocatalyst for solar-driven water splitting [39]. Perovskites are structural simple systems, where an ideal system is cubic with the formula $ABX_3$. A is often alkali, alkaline-earth or rare-earth metals, B is often transition metals, and X is usually nonmetal elements. This spread of valid elements for a perovskite ensures excellent structural flexibility, making it possible to design and develop a highly efficient perovskite by altering its composition and morphology. Especially in theoretical work, it is simple to vary A, B and X to create a perovskite ideal for photocatalytic water splitting. Nonetheless, they all struggle with different limiting factors regarding their solar-to-hydrogen efficiency. Repeating problems include no suitable band positions, proneness to photocorrosion, hydrogen and oxygen not being produced simultaneously, short recombination time, stability, and lifetime. These must be solved if we are to reach a solar-to-hydrogen efficiency of 10 % that is needed for large-scale applications [40]. This project will use numerical models and computational calculations to investigate materials that could be used for photocatalytic water splitting and try to solve some of the problems mentioned earlier. We seek to make a modest contribution to realising photocatalytic water splitting as a large-scale hydrogen production method.

## 1.2 Summary

This work has resulted in four first-author papers, two second-author papers, several presentations at academic conferences and contributions to popular science. To analyse new materials for hydrogen production using photocatalytic water splitting, we started working on an in-depth review article on the current leading photocatalyst, $TiO_2$. The goal was to get an overview of what has been done, experimentally and theoretically, regarding $TiO_2$ based photocatalysts over the last years. It became clear that although $TiO_2$ has been relatively successful so far, other materials could easily overcome it. Our analyses in this review article showed that perovskites have promising attributes for photocatalytic water splitting applications [41]. Two main reasons are their high phonon absorption in the visible spectra, and their long charge-carrier diffusion lengths compared to the incident light absorption depths [41]. This led us to the second article, band gap engineering in $CsSn_xPb_{1-x}I_3$ and its influence on light absorption. The goal was to combine two well-known perovskites with different absorption ranges to create a material with a more extensive absorption range. This would increase the number of absorbed photons and the solar-to-hydrogen efficiency. Later in the Ph.D., an article was co-authored with Chapa Wanniarachchi where we looked further into the electronic and optical properties of perovskites [42]. Here, we used a lead-free perovskite, as lead toxicity and long-term stability are issues for lead-based perovskites. This was expanded in a second article with Chapa, where we investigated how the properties would change if Br were substituted with Cl, F or I. Another finding in the review article was the potential of transition metals, especially $MoS_2$, due to their remarkable electronic, optical and structural properties. Experimental results from our group [43] support this, and we decided to investigate it further. $MoS_2$ has already been used as a lubricant, diode, photovoltaic cell, gas-sensor, biosensor, and recently in dye degradation. This versatility made it a very interesting candidate for photocatalytic water splitting. We investigated 14 novel $MoS_2$ polymorphs to find the most suitable one for photocatalytic and photovoltaic applications. This study was further expanded in paper four, where the seven most stable polymorphs were investigated using hydrogen evolution reaction indicators. Here dopants were introduced as an element to improve the structures' properties.

## 1.3 Objectives

This project aims to improve on and find new materials for photocatalytic water splitting that would increase solar-to-hydrogen efficiency through computer modelling and simulations. This is done by employing a quantum approach based on first-transfer principles utilising simulations to investigate the electronic structure, optical properties, structural and mechanical stability, and water-splitting properties of relevant materials. Various established and new materials for photocatalytic hydrogen production are the main focus. In addition, studies on how to alter the optoelectronic properties of these materials using dopants are another focused area. The project's goal can be divided into four objectives, described below.

*Objective I (Paper A)*

- To achieve deep insight into theoretical and experimental research on the most prominent photocatalytic material $\mathrm{TiO_2}$ and to establish an understanding of the challenges and opportunities with this material, which will greatly benefit the research community.

*Objective II (Paper D and E)*

- Based on modelling and simulations, investigate a variety of structural $\mathrm{MoS_2}$ polymorphs, another prominent photocatalytic material, and investigate how these different polymorphs would perform as materials for optoelectronic and photocatalytic applications.

*Objective III (Paper E)*

- Investigate how the performance of the $\mathrm{MoS_2}$ could be optimised and enhanced through doping.

*Objective IV (Paper B and C)*

- Carry out an in-depth computational study of new cheap and flexible perovskite materials for photocatalytic applications and engineer their structures through substitutional doping to achieve optimal characteristics.

## 1.4 Thesis organisation

This thesis consists of the theoretical background, the computational techniques we have used and the articles we have produced. We have divided it into two sections; Overview and Articles. The overview comprises six chapters and starts with an introduction (Chapter 1) that establishes the context and motivation for the thesis. Chapter 2 presents the theoretical background needed to understand our work. Within chapter 3, the working principle of a photocatalytic device is explained along with the theory behind the most important indicators for suitable photocatalytic hydrogen production materials. The computational method, software and developed tools used in this thesis are presented and explained in chapter 4. In chapter 5, we have presented a summary of the research articles based on this study. Finally, in chapter 6, the thesis is concluded with a summary and suggestions for future work to be done in this exciting field of hydrogen production. The papers are displayed in Part II.

# THEORY

In this project, we have been focusing on nanomaterials, materials with at least one dimension on the nanoscale ($10^{-9}$) that will be used for photocatalytic water splitting. Due to the scale we are operating on, the project should be based on quantum mechanics, which deals with the behaviour of matter and light on the atomic and subatomic scale. The fundamental equation for these types of studies is the Schrödinger equation that describes the wave functions that govern the motion of small particles and how they are influenced by external forces. Through the Schrödinger equation it is possible to predict the future behaviour of a dynamic system. A parallel between Newton's laws and energy conservation in classical mechanics can be drawn.

The Schrödinger equation was first postulated in 1925 by Erwin Schrödinger before he published it in 1926 [44]. It is a linear partial differential equation that controls the wave function of a quantum-mechanical system, and the time-independent form is [45]

$$H\Psi(\mathbf{r}) = \left[-\frac{\hbar^2\nabla^2}{2m} + v(\mathbf{r})\right]\Psi(\mathbf{r}) = E\Psi(\mathbf{r}). \tag{2.1}$$

Where H is the Hamiltonian operator, E is the energy, $v$ is the particle's potential, and $\Psi$ is the wave function. This wave function contains all the information we can think of for a given system. Therefore, if we could solve the Schrödinger equation for a specific system, we could predict all the observable properties from the wave function for the particular system. We must use the many-electron wave function for larger systems (solids or larger atoms). For such a many-body problem, the Hamiltonian looks like this

$$H_{tot}\Psi = [T_n + T_e + V_{nn} + V_{ne} + V_{ee}]\,\Psi = E\Psi \tag{2.2}$$

with

$$\begin{aligned} H_{tot} = &-\sum_I \frac{\hbar^2}{2M_I}\nabla^2_{\mathbf{R}_I} - \sum_i \frac{\hbar^2}{2m_e}\nabla^2_{\mathbf{r}_i} + \frac{1}{2}\sum_{I,J I\neq J}\frac{Z_I Z_J e^2}{|\mathbf{R}_I - \mathbf{R}_J|} \\ &+ \frac{1}{2}\sum_{i,j i\neq j}\frac{e^2}{|\mathbf{r}_i - \mathbf{r}_j|} - \sum_{I,i}\frac{Z_I e^2}{|\mathbf{R}_I - \mathbf{r}_i|}. \end{aligned} \tag{2.3}$$

Where the indices I and J are for nuclei, i and j are electrons, $\mathbf{R}_{I,J}$ are the positions of the nuclei, $M_{I,J}$ are the masses of the nuclei, $\mathbf{r}_{i,j}$ are the positions of the electrons, $m_e$ are the masses of the electrons, $Z_I$ is the atomic number of nucleus I, and $Z_J$ the atomic number of nucleus J. The first two terms on the right-hand side of equation (2.1) ($T_n$ and $T_e$) represent the kinetic energy of the nuclei and electrons, respectively; the last three terms ($V_{nn}$, $V_{ne}$ and $V_{ee}$) represent the Coloumbic interaction between nuclei, electrons, nuclei and electrons. Unfortunately, the Schrödinger equation is only solvable in a few simple cases, such as the hydrogen atom. In solid matter, the number of particles is in the order of $10^{23}$, making it impossible to get accurate solutions with current computing technology.

A standard approximation used to simplify equation (2.3) is the Born-Oppenheimer approximation. It states that since the nuclei are much heavier than the electrons, the nuclei will move much slower than the electrons. We can therefore separate the movement of nuclei and electrons;

$$\Psi(r, R) = \Psi_n(R)\Psi_e(r, R). \tag{2.4}$$

Here $\Psi_n(R)$ is the wavefunction describing nuclei, and it only relates to the nuclei position, while $\Psi_e(r, R)$ is the electron's wavefunction pertaining both to the nuclei and electron position. This means that we can write the Schrödinger equation as

$$\begin{aligned} H_e(r, R)\Psi_e(r, R) &= E_e\Psi_e(r, R), \\ H_n(R)\Psi_n(R) &= E_n\Psi_n(R). \end{aligned} \tag{2.5}$$

$E_e$ and $E_n$ are the electron and nuclei energy, respectively.

## 2.1 Hartree-Fock approximation

Although the Born-Oppenheimer approximation separated the nucleus and electron wave functions, solving the Schrödinger equation for a many-body system is still challenging. To solve this problem, Douglas Hartree proposed the Hartree method in 1928. It is a self-consistent field method, which simplifies the wave functions description and energy calculation of the atoms and ions [46]. Hartree proposed that one could calculate the solutions to Schrödinger's equation for individual electrons 1, 2, 3, ..., n, in the states a, b, c, ..., z, which would result in unique solutions for each electron. As each $\Psi$ is a solution to the Schrödinger equation, the product should approximate a solution to the entire system

$$\Psi_H = \Psi_a(\mathbf{r_1})\Psi_b(\mathbf{r_2})\Psi_c(\mathbf{r_3})...\Psi_z(\mathbf{r_n}). \tag{2.6}$$

This method makes the system separable and reduces its complexity. However, it does not follow the Pauli principle; two electrons cannot be simultaneously in the same quantum state, as equation (2.6) is not anti-symmetric.

Slater [47] and Fock [48] proposed a solution to this in 1930 by introducing a Slater determinant to represent the wavefunction of the many-body system instead of equation (2.6):

$$\Psi_{HF} = \frac{1}{\sqrt{N!}} \begin{bmatrix} \Psi_a(r_1) & \Psi_b(r_1) & \cdots & \Psi_z(r_1) \\ \Psi_a(r_2) & \Psi_b(r_2) & \cdots & \Psi_z(r_2) \\ \vdots & \vdots & \ddots & \vdots \\ \Psi_a(r_n) & \Psi_b(r_n) & \cdots & \Psi_z(r_n) \end{bmatrix}. \tag{2.7}$$

The columns represent single wave functions, while the rows are electron coordinates. We see that if any rows or columns are interchanged, the sign of equation (2.7) will change, ensuring that the anti-symmetry principle is followed. The determinant also guarantees that two different electrons cannot occupy the same quantum state simultaneously because two equal rows or columns give zero value in the determinant.

In summary, the Hartree-Fock method is based on five approximations:

1. The Born-Oppenheimer approximation.
2. All relativistic effects are ignored. All the operators are non-relativistic.
3. The solution is assumed to be a linear combination of basis functions, which are often chosen to be orthogonal.
4. A single Slater determinant is used to obtain the energy eigenfunctions.
5. Since the Hartree-Fock method uses a mean-field environment, the electron correlation effects (how one electron's position influences another electron) are ignored.

The fifth approximation leads to significant deviations between experimental and computational results, as the electron correlation contributes to the total energy. We can define the correlation effect as

$$E_{correlation} = E_{exact} - E_{HF}. \tag{2.8}$$

The Hartree-Fock method generally overestimates the ground state energy, $E_0$, since a single Slater determinant is used to approximate the wave function. It is important to add the correlation effect and calculate it properly for more accurate results. A more robust computational method is density functional theory (DFT), developed to deal with exchange and correlation energies. An advantage of using DFT over Hartree-Fock is that we can include the effect of long-range, non-classical electron correlations.

## 2.2 Density functional theory

Density functional theory was developed in the 1960s by Kohn and Hohenberg [49], and it was later improved on by Kohn and Sham [50]. It uses electron density as the basic variable instead of the wave function to describe the properties of a system. Thomas [51] and Fermi [52], in 1927, first implemented the electron density as the basic variable, and they assumed uncorrelated motion between the electrons. In other words, they ignored the exchange and correlation terms we discussed earlier. In 1930, Dirac improved the model by adding a local exchange term [53]. However, the model fails to describe the bonds between atoms due to the crude approximations used. The foundation for DFT is based on two theorems postulated by Hohenberg and Kohn in 1964 [49][54]

- **Theorem I**: For any system of interacting particles in an external potential $V_{ext}(\mathbf{r})$, the potential $V_{ext}(\mathbf{r})$ is determined uniquely, except for a constant, by the ground state particle density $n_0(\mathbf{r})$.
- **Corollary I**: Since the Hamiltonian is thus fully determined, except for a constant energy shift, it follows that the many-body wave functions for all states (ground and excited) are determined. Therefore all properties of the system are entirely determined given only the ground state $n_0(\mathbf{r})$.
- **Theorem II**: A universal functional for the energy $E[n]$, $E[n] := \int n(\mathbf{r})V_{ext}(\mathbf{r})d\mathbf{r} + F[n(\mathbf{r})]$ in terms of the density $n(\mathbf{r})$, can be defined, which is valid for any external potential $V_{ext}(\mathbf{r})$. For any particular $V_{ext}(\mathbf{r})$, the exact ground state energy of the system is the global minimum value of this functional, and the density $n(\mathbf{r})$ that minimizes the functional is the exact ground state density $n_0(\mathbf{r})$.
- **Corollary II**: The functional $E[n]$ alone is sufficient to determine the exact ground state energy and density. In general, the excited states of the electrons must be determined by other means.

This means that if we want to get the system's total energy, we first have to find the ground state density of the system. In 1965 Kohn and Sham [50] proposed an ansatz (the Kohn-Sham ansatz), which made it feasible to use the Hohenberg-Kohn theorems to solve a many-body system. This ansatz drastically reduced the computing power needed for the calculations, and today, minor calculations can be performed on a personal computer. In 1998 Kohn received the Noble Prize in chemistry for his work on DFT. The ansatz proposed to replace the original many-body system with an auxiliary independent particle problem [50]. In other words, the new ansatz assumes that the ground state density of a chosen non-interacting system is equal to that of our starting interacting system. Following this, they introduced one of the Kohn-Sham equations:

$$(-\frac{\hbar^2}{2m}\nabla^2 + \nu_{KS}(r))\phi_i(r) = \epsilon_i\phi_i(r), \tag{2.9}$$

where $\nu_{KS}$ is the Kohn-Sham potential representing the effective external potential where the non-interacting particles move. $\phi_i$ is the Kohn-Sham orbital function, and $\epsilon_i$ is the corresponding eigenvalue. Now it is possible to find the electron density using:

$$n(r) = \sum_i^N |\phi_i(r)|^2 \tag{2.10}$$

and

$$\int n(\mathbf{r})d\mathbf{r} = N, \tag{2.11}$$

where N is the number of electrons in the system. We can also write the Kohn-Sham potential, $\nu_{KS}$ as

$$\nu_{KS}(r) = V_{ext}(r) + e^2 \int \frac{n(r')}{|r - r'|} dr' + V_{XC}(r), \tag{2.12}$$

where $E_{XC}$ is the exchange-correlation potential:

$$V_{XC} = \frac{\delta E_{XC}(n)}{\delta n(r)}, \tag{2.13}$$

with $E_{XC}$ as the exchange-correlation energy, and it and the related potential are the only unknown terms in the Kohn-Sham approach to DFT.
Rewriting the universal functional to include the exchange-correlation energy, we get

$$E[n] = T_s[n] + \int d\mathbf{r} \nu_{ext}(\mathbf{r}) n(\mathbf{r}) + E_H[n] + E_{XC}[n]. \tag{2.14}$$

$T_S$ is the Kohn-Sham kinetic energy, $\nu_{ext}$ is as before the external potential acting on the interacting system, and $E_H$ is the Hartree (or, if suitable, the Coulomb energy). We will get the ground state density and the Kohn-Sham equations by minimising equation (2.14) using Lagrange multipliers. Of the terms in equation (2.14), only the exchange-correlation energy is unknown, and unfortunately, it is impossible to get an exact value for it. Therefore, DFT does not provide an exact solution to the Schrödinger's equation, and we need a good approximation of $E_{XC}$ to get accurate results from our calculations.

### 2.2.1 Exchange-correlation functionals

Two of the most common and popular approximations for $E_{XC}$ are the local (spin) density approximation (L(S)DA) and the generalised gradient approximation (GGA). The local density approximation is a simple but effective way to address the exchange-correlation term in equation (2.14). It assumes that the exchange-correlation energy per electron at a given point is the same as the energy of homogenous gas with the same electron density at the same point [55]. For a non-spin polarised system, the exchange-correlation energy is:

$$E_{XC}^{LDA}[n(\mathbf{r})] = \int n(\mathbf{r}) \epsilon_{XC}[n(\mathbf{r})] d\mathbf{r}. \tag{2.15}$$

Where $n$ is still the density and $\epsilon_{XC}$ is the exchange-correlation energy per particle. Extending equation (2.15) for a spin-polarised system with regard to the exchange energy is straightforward. It is unfeasible to compute exact exchange-correlation energies, and we must use simulations (e.g. Monte Carlo) to find approximate values. The intermediate electron density can be obtained with accurate correlation energies through interpolation. Accounting for the spin, we get local spin density approximation (LSDA):

$$E_{XC}^{LDA}[n_\uparrow(\mathbf{r}), n_\downarrow(\mathbf{r})] = \int n(\mathbf{r})\epsilon_{XC}[n_\uparrow\mathbf{r}, n_\downarrow\mathbf{r}]d\mathbf{r}. \tag{2.16}$$

L(S)DA achieves high accuracy regarding molecular geometries and vibrational frequencies. However, it performs poorly when calculating bonding energies due to underestimating exchange energies and overestimating correlation energies [56]. A popular and better approximation is the generalised gradient approximation (GGA), which includes density gradient corrections and higher spatial derivatives of the electron density. This makes it possible to consider the inhomogeneities of the real electron density. Several variations and forms of GGA exist, and the three most used are proposed by Becke [57] (B88), Perdew et al. [58], and Perdew, Burke and Enzerhof [59] (PBE). The exchange-correlation energy in GGA is a generalised form of the LSDA equation (2.16), to include correction from a density gradient $\nabla n(\mathbf{r})$

$$E_{XC}^{GGA}[n_\uparrow(\mathbf{r}), n_\downarrow(\mathbf{r})] = \int n(\mathbf{r})\epsilon_{XC}^{GGA}(n_\uparrow(\mathbf{r}), n_\downarrow(\mathbf{r}), |\nabla n_\uparrow(\mathbf{r})|, |\nabla n_\downarrow(\mathbf{r})|, \dots)d\mathbf{r} \tag{2.17}$$

$$= \int n(\mathbf{r})\epsilon_{XC}^{GGA}(n(\mathbf{r}))F_{XC}(n_\uparrow(\mathbf{r}), n_\downarrow(\mathbf{r}), |\nabla n_\uparrow(\mathbf{r})|, |\nabla n_\downarrow(\mathbf{r})|, \dots)d\mathbf{r}. \tag{2.18}$$

Where $E_{XC}$ is dimensionless and $\epsilon_X^{GGA}$ is the exchange density of the unpolarised homogenous electron gas. The difference between the various GGA forms lies in how they treat $E_{XC}$, as it can be decomposed linearly into an exchange term and a correlation term: $E_{XC} = E_X + E_C$.

GGA outperforms L(S)DA when it comes to predicting bond length, binding energies of molecules, crystal lattice constants, and other lattice or energy parameters. However, it overestimates the lattice constant of the heaviest elements and generally underestimates the band gap. This has led to newer and more complex approximations with increased accuracy at the cost of computing time.

### 2.2.2 *Hybrid exchange correlation functional*

LDA and GGA severely underestimate band gap values for bulk or surface systems; thus, another approach is needed to investigate these values. A better solution is to use hybrid exchange-correlation functionals, which incorporate an amount of the exact exchange from the Hartree-Fock theory with the rest of the exchange-correlation energy coming from other sources. In other words, it is a mix of exact and approximated functionals. The ratio between exact and approximated functionals is determined by fitting the prediction of the functional to experimental atomisation energies. To obtain more accurate results, we have used the Heyd-Scuseria-Ernzerhof (HSE06) exchange-correlation [60] [61] [62]

$$E_{XC}^{HSE} = \alpha E_X^{HF,SR}(\omega) + (1-a)E_X^{PBE,SR}(\omega) + E^{PBE,LR}(\omega) + E_C^{PBE}, \tag{2.19}$$

where $\alpha$ is the mixing parameter, and $\omega$ is an adjustable parameter controlling the short-rangeness of the interaction. In HSE06, typical values for $\alpha$ and $\omega$ are 0.25 and 0.2, respectively. $E_X^{HF,SR}(\omega)$ is the short-range Hartree-fock exact exchange functional, $E_X^{PBE,SR}(\omega)$ and $E_X^{PBE,LR}(\omega)$ are the short- and long-range components of the PBE exchange functional, and $E_C^{PBE}(\omega)$ is the PBE correlation functional. Figure 2.1 shows an example where GGA, HSE06 and experimental values are compared. In addition, it compares the different methods of calculating the static dielectric constant values.

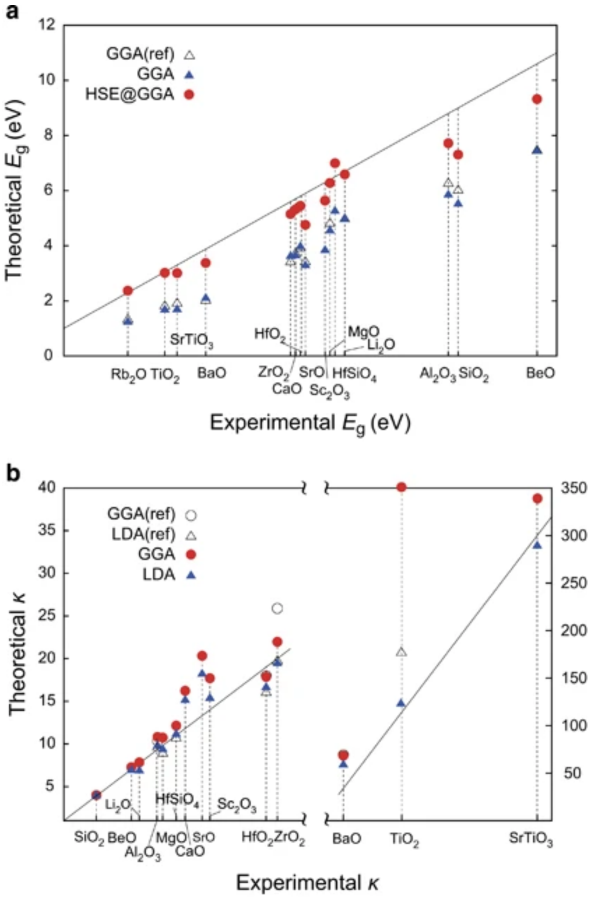

**Figure 2.1:** Comparison of theoretical and experimental data for the (a) band gap ($E_g$) and (b) static dielectric constant (κ); some reference data from other ab initio studies (LDA and GGA) are also shown as open symbols. The solid line indicates perfect agreement with the experiment. HSE@GGA level indicates the band gap obtained using the hybrid-functional calculations on the band-edge points identified by GGA. Taken from Yi et al. [63].

These research reports comparing LDA, GGA and HSE06 for various materials have shown that HSE06 calculated band gap values are in better agreement with the experimental values than its counterparts [63]. However, for the static dielectric constant, GGA and LDA are shown to be in good agreement with the experimental values. Thus, it comes down to the study performed and the accuracy needed for the results, as HSE06 calculations will take up to 100 times longer than GGA calculations. This means that GGA is often used to screen materials and quickly get an idea about materials' electronic structure. In contrast, HSE06 calculations are used when a few specific materials are investigated thoroughly.

CHAPTER 3

# PHOTOCATALYTIC WATER SPLITTING

There are several ways to produce green hydrogen, however, the majority of them require the development of both photovoltaic cells and electrolysers. In photocatalytic water splitting, these are combined into one material to save on cost and ecological footprint. The aim of this chapter is to explain the general working principle of photocatalytic hydrogen production and the most important material properties of an efficient photocatalyst.

## 3.1 The principles of photocatalytic water splitting

The photocatalytic process divides water $(H_2O)$ into hydrogen $(H_2)$ and oxygen $(O_2)$ with the help of a catalyst and natural light. This is similar to photosynthesis; the photocatalytic process converts solar/radiation energy to chemical energy. Hence, the working principle is quite simple: photons from the sun with energy higher than the band gap of the catalyst are absorbed, and an electron gets excited from the valence band to the conduction band. This creates an electron $(e^-)$ – hole $(h^+)$ pair that may either travel to the catalyst surface and take part in a reaction, or they could recombine they reach the surface, resulting in no reaction. On the surface $h^+$ oxidises water molecules, splitting them into protons $(H^+)$ and oxygen atoms, while the electrons reduce the protons into molecular hydrogen. The oxygen atoms combine into molecular oxygen. In figure 3.1, the overall process is shown, and the chemical reactions on the surface of the photocatalyst are described by the following equations [64]:

$$\begin{gathered}
\text{Oxidation: } H_2O + 2h^+ => 2H^+ + \tfrac{1}{2}O_2, \\
\text{Reduction: } 2H^+ + 2e^- => H_2 \\
\text{Overall reaction: } H_2O + 1.23eV => H_2 + \tfrac{1}{2}O_2.
\end{gathered}$$

The reaction requires Gibbs free energy of 1.23 eV per electron. Unlike photovoltaic solar cells that are limited by the detailed balance limit concerning maximum theoretical efficiency, photocatalytic catalysts do not have a well-defined upper limit. This does not mean that there are no limiting factors. There are several important ones that are just not as easily summarized in one rule. The six main limiting factors are

1. Photon absorption

2. Exciton separation
3. Carrier diffusion
4. Carrier transport
5. Catalytic efficiency
6. Mass transfer of reactants and products

These six main factors can be further divided into several other sub-factors influencing them; see figure 3.2 for an overview. For photon absorption, the band gap and its position are crucial factors. As mentioned, the reaction requires Gibbs free energy of 1.23 eV per electron. Thus, the band gap must be at least 1.23 eV, or the excited electrons will not have enough energy to start the reaction. However, experiments have shown that an energy of 1.6 eV to 1.8 eV is needed for the reaction. Factors like activation energy, charge transfer resistance and mass concentration make the system less ideal and increase the required overpotential[64]. The overpotential is the potential difference between the theoretically determined reduction potential and the potential the reduction reaction is experimentally observed to occur at. If the band gap is set high (> 3.0 eV), you ensure that the excited electrons will have enough energy, but you will also lose out on roughly 85 % of the photons in the visible spectrum. In addition, the excess energy the electrons contain will be wasted as heat since the reaction only needs 1.6 eV to 1.8 eV. Experimental findings have found that an upper limit for the band gap should be 2.4 eV [65]. This means that it is essential to find suitable catalysts with a band gap between 1.6 – 2.4 eV to ensure maximum absorption of the incoming light, which is our goal in this project.

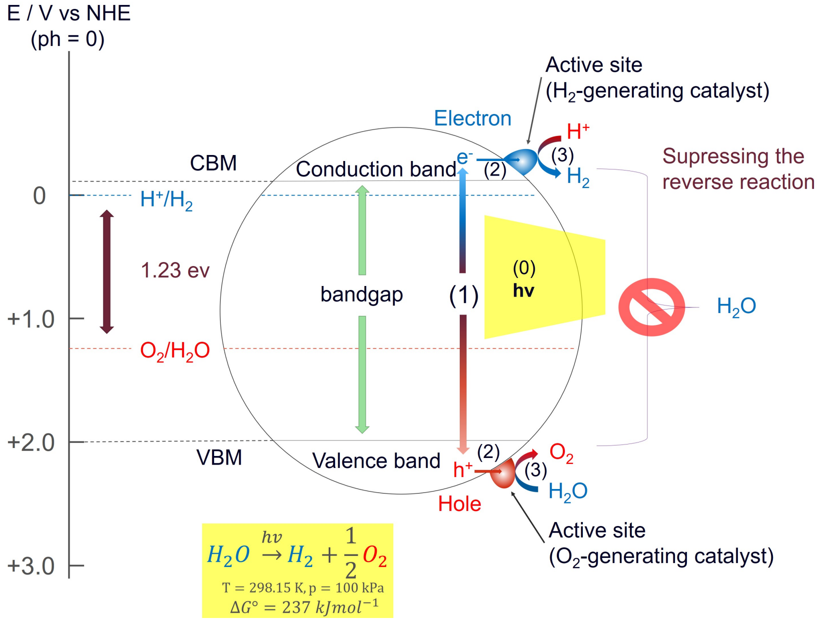

**Figure 3.1:** Schematic energy diagram of photocatalytic water splitting. 1) photons with the appropriate band gap are absorbed and excite electrons to the conduction band. 2) The electrons and holes will travel to the material's surface, usually to a catalyst. 3) The holes oxidize water molecules into oxygen and protons, while the electrons reduce protons into hydrogen gas.

The exciton binding energy is the energy required to ionize an exciton from its lowest energy state [66], where an exciton is the bound state of an electron and a hole. Two key factors influencing the exciton binding energy are the effective masses (explained in section 3.3.2) and the material's dielectric constant, two values that DFT can accurately calculate. The goal is to minimize the exciton binding energy within a material. Carrier diffusion and transport are the third and fourth properties that must be maximized. It is vital that the excited electrons and holes make it to the material's surface and do not get stuck on defects or recombine on their way.

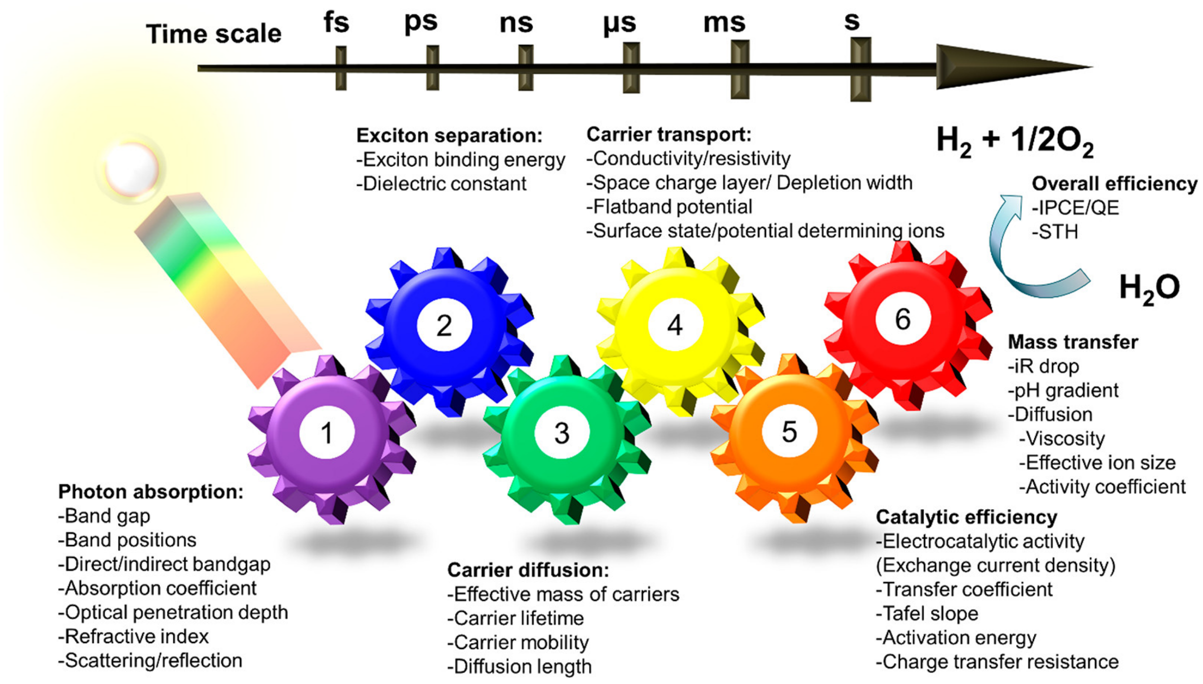

**Figure 3.2:** The six main factors limiting photocatalytic water splitting and the timescale they work on. Taken from [67].

Electrocatalytic activity is what separates photocatalysts from other semiconductors and solar cells. It is the material's ability to use the absorbed solar light to perform chemical reactions on its surface. In the water-splitting reaction, the photogenerated charge carriers are consumed to split water molecules into hydrogen in a redox reaction. The catalytic efficiency looks at what makes this process as efficient as possible, assuming that charge carriers have made their way to the catalysts. So far, the primary focus has been on handling photons in bulk materials and on the material surface. However, the mass transfer of reactants and ions cannot be ignored if photocatalytic hydrogen production is to be commercially viable. If, for example, the ion transportation rate is too high, it can easily lead to the depletion of reactants, heavily decreasing efficiency. This shows that creating and improving photocatalysts for photocatalytic water splitting is a complex and challenging task. Several catalyst properties need to be optimized, and you will often find that improving one affects another. Computer simulations can be used as a cost-effective tool to investigate specific properties of a material or several thousands of materials. In this work, we have used several different indicators (table 3.1), for each limiting factor discussed in this chapter to help determine if a material is suitable for photocatalytic water splitting.

| **Limiting factors** | **Indicators in this work** |
|---|---|
| Photon absorption | band gap, Band position, Absorption coefficient, and Refractive index |
| Exciton separation | Effective mass and Dielectric constant |
| Carrier diffusion | Effective mass |
| Carrier transport | Effective mass |
| Catalytic efficiency | d-band and Gibbs free energy |
| Mass transport | Not looked at in this work |

**Table 3.1:** The table shows how we have investigated the factors that would limit the efficiency of a photocatalyst.

## 3.2 Stability

In addition to these factors, we have also investigated the mechanical and dynamical stability of the materials to ensure that the materials could be synthesised and used in lab/small/large scale test facilities. The mechanical properties are calculated using a generalised Hooke's law, which in Voigt notation simplifies to

$$\sigma_i = \sum_{j=1}^{6} c_{ij}\epsilon_j, \tag{3.1}$$

where $\sigma$ is the stress response for a solid when an external load $\epsilon$ is applied. This means that the strain or stress is represented by a 6x6 symmetric matrix, where only six components are dependent. This is called the stiffness matrix, $C_{ij}$, and can be calculated using first-order derivatives of stress-strain curves. Through these derivatives, we can determine if a material is mechanically stable, i.e. the material's ability to withstand shear and strain forces. Using phonon calculations, we investigated the dynamical stability, i.e. that the atoms are at local minima and will stay there after synthesis. This is important as a dynamically unstable material will not last long after synthesis, if it even can be created.

## 3.3 Electronic properties

The electronic structure and properties are vital when looking into the photocatalytic capability of a material. They describe the state and behaviour of the electrons in a material.

### 3.3.1 *Band structure*

In an atom, the electrons move in orbitals around the atomic nucleus, where each orbital represents a discrete energy level. The electrons cannot have an energy level corresponding to anything other than these orbital. These orbital will be affected by nearby atoms, both bonded and unbonded atoms, and the energy levels will be shifted as a consequence. New orbitals with slightly different energy will be formed. Figure 3.3 illustrates how the number of neighbouring atoms, n, affects the electron energy level structure. Starting off with clearly discrete energy levels for a single atom that evolves into continuous bands as the number of neighbouring atoms,n, increases, and we end up with a solid.

In general, the electrons are in the ground state. That is the energetically lowest possible band, and they will always fill up a band completely before entering a new one. The outermost energy band with electrons is called the valence band, and the innermost empty energy band is called the conduction band. An electron can move across this gap, called the band gap and measured in eV, if it absorbs energy equal to the band gap height. Photovoltaic solar cells and photocatalytic water splitting utilise this property of a semiconductor to absorb solar light and convert it into electricity. We can also use the separation of the valence and conduction band to differentiate between conductors, semiconductors and insulators. See figure 3.4 for a schematic illustration.

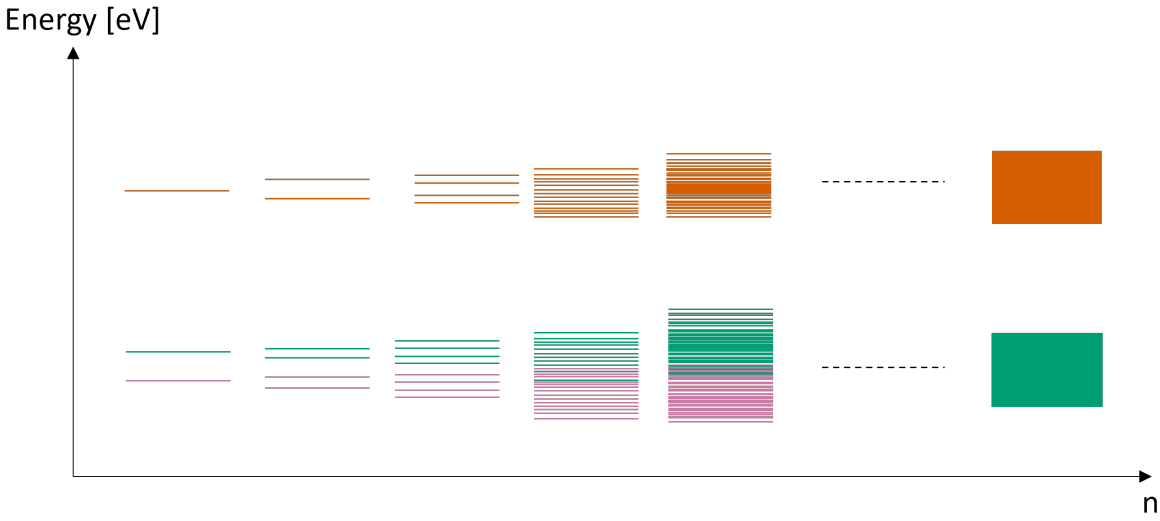

**Figure 3.3:** The energy of electrons around an atom is split into discrete energy levels. The energy difference between the levels decreases as several atoms are brought together to form a crystal lattice. In the end, a continuous band is formed, in contrast to the discrete levels atoms would have. However, a gap between energy levels that are far enough away from each other can still exist.

A conductor has overlapping valence and conduction bands. In other words, the electrons can move freely in the crystal structure. Due to this, conductors have high conductivity, and most metals are in this category. When a band gap separates the valence and conduction bands, the electrons need extra energy to move around in the crystal structure. The larger the gap, the fewer electrons can move into the conduction band. Materials with a small band gap (< 3.5 eV) are called semiconductors, while materials with a large band gap are called insulators (e.g. glass and rubber). As mentioned in chapter 3.1, we are looking for semiconducting materials with a band gap in the range of 1.6 eV to 2.4 eV. We employ GGA and HSE06 exchange-correlation functions for these calculations, which are explained in chapter 2.2.1 and 2.2.2, respectively.

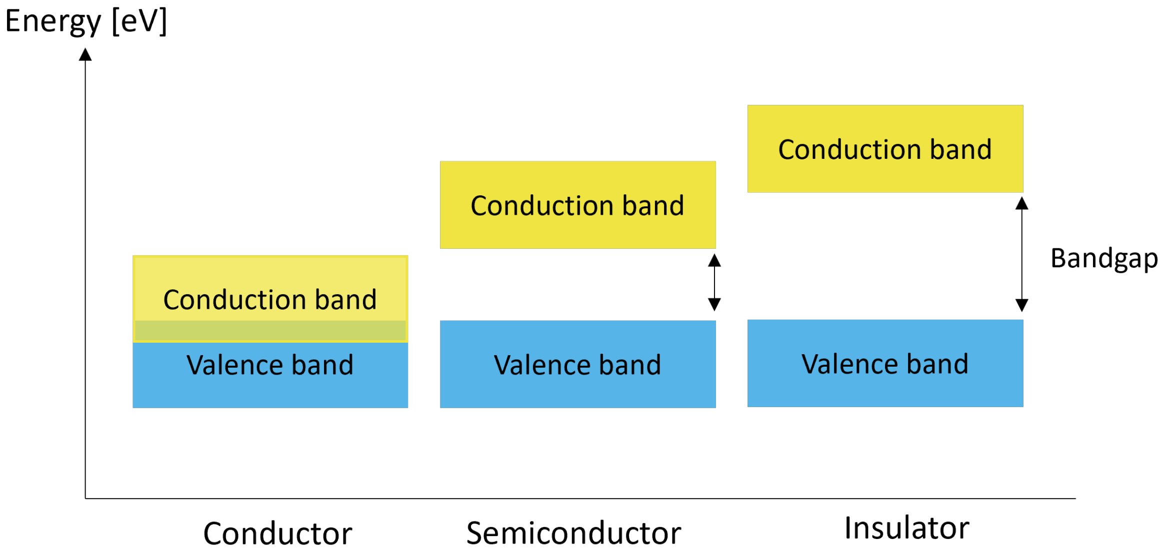

**Figure 3.4:** Schematic showing the difference between insulators, semiconductors and conductors

### 3.3.2 *Effective mass*

One can use the effective masses of electrons and holes to describe the charge mobility, electrical resistivity, and free-carrier optical response. These are essential factors when determining if a material is suitable for photocatalytic applications. In the Drude model, electron and hole mobility is given as

$$\mu = \frac{q\tau}{m^*}, \tag{3.2}$$

where q is the charge, $\tau$ is the scattering time of a charge carrier, and $m^*$ is the effective mass. From equation (3.2), we see that low effective mass corresponds to a high charge carrier mobility, which corresponds to a high conductivity for the material. Therefore, we want a low effective mass for our materials.

## 3.4 Optical properties

How a material interacts with light is defined by its optical properties, and the complex optical dielectric function $\epsilon(\omega) = \epsilon_1(\omega) + i\epsilon_2(\omega)$ shows how the optical properties are dependent on the incident wavelength of light. $\epsilon_1$ and $\epsilon_2$ are the real and imaginary dielectric functions, respectively. It is defined as the system's linear response to electromagnetic radiation and describes radiation propagation in a medium. In this work, we have focused on the absorption coefficient, as it determines how far into the material light of a specific wavelength will travel before it is absorbed. A material with a low absorption coefficient will absorb light poorly and will not be a good candidate for photocatalytic water splitting. The goal is to find a material with a high absorption coefficient in the visible light region to ensure maximum absorption of the incoming solar radiation.

## 3.5 Water splitting properties

### 3.5.1 d-band model

Understanding the interaction between the adsorbate and the *d*-electrons of the transition metal surface is essential. One of the most used models to describe this interaction is the *d*-band model developed by Hammer and Nørskov [68][69][70]. The model approximates the bond formation at the surface of a transition metal and describes the interaction between the valence states of the adsorbate and the *s* and *d* states of the surface. Hammer and Nørskov [68] claim that the variation in adsorption energy for various transition metal surfaces stems from an upward shift of the *d*-band centre concerning the Fermi energy. The stronger the upward shift, the stronger the binding energy, as the upward shift makes it possible for a larger number of empty anti-bonding states to form. Hence, a downward shift of the *d*-band centre regarding the Fermi energy could indicate good catalytic properties. The model has limitations for systems with high spin polarisation or complex structures and needs to be expanded upon in those cases [71].

### 3.5.2 Gibbs free energy

Photocatalytic water splitting can be divided into two half-reactions: hydrogen evolution reaction (HER) and oxygen evolution reaction (OER). The overall HER can follow two different trajectories: Volmer-Tafel and Volmer-Heyrovsky. The first step, the Volmer step, is similar for both paths, and here the protons are reduced to produce adsorbed hydrogen on the material surface. Following this step, the reaction can either follow the Tafel or the Heyrovsky route. In the Tafel reaction, two adsorbed hydrogen atoms on the material's surface will combine into a hydrogen molecule. The Heyrovsky reaction, on the other hand, produces a hydrogen molecule using a proton from the surrounding water and an adsorbed hydrogen atom from the surface. The adsorption energy of the hydrogen on the surface plays a vital role in determining the catalytic activity of a material. The adsorption energy of a material is linked to the Gibbs free energy ($\Delta G_H$) [72] [73]

$$\Delta G_H = E_{ads} - \Delta E_{ZPE} - T\Delta S_H, \tag{3.3}$$

where $E_{ads}$ is the adsorption energy, $\Delta E_{ZPE}$ is the zero-point energy difference between $H_2$ in the adsorbed state and the gas phase state with its values ranging from 0.01 to 0.04 eV, and $T\Delta S_H$ is the entropy changes for finite variations at constant temperature T. We can approximate the value for the last two terms so that we can rewrite equation (3.3) to [74]

$$\Delta G_H = E_{ads} + 0.24 eV. \tag{3.4}$$

This means we can evaluate the Gibbs free energy only needing to calculate the adsorption energy. This can be done as follows:

$$E_H^{ads} = E_T[system + H] - E_T[system] - \frac{1}{2}E_{H_2}. \tag{3.5}$$

Where $E_T[system + H]$ represents the total energy of the material in addition to the energy of an adsorbed H atom, $E_T[system]$ is the energy of the material without any adsorbed hydrogen, and $E_{H_2}$ is the energy of a hydrogen molecule in the gas state.

# CHAPTER 4

# COMPUTATIONAL METHODS

In this study, we apply atomic models, employ mathematical tools and develop/use scripts/software to solve complex cross-disciplinary problems associated with materials at the nanoscale. The entire project exists in the cross-section of computer science, physics, mathematics, material science and chemistry. Modelling and simulations investigating these materials' optoelectronic and photocatalytic properties require a high amount of computer memory, efficient algorithms and mathematical approximations to reduce the computing time. To solve the many-body Schrödinger equation, we developed our own scripts, and we use them along with the Vienna ab-initio simulation package (VASP) [75] [76] [77]. VASP is a tool that models materials on an atomic scale from first principles and can e.g. be used for electronic structure, optical properties, and structural stability calculations. We have employed DFT and the Kohn-Sham equations or hybrid functionals depending on our system and needed accuracy. VASP uses plane-wave basis sets to express quantities like the one-electron orbitals, the electronic charge density and the local potentials. To study the interaction between the electrons and ions, we used the PAW method [78]. VASP only provides raw data that must be processed and analysed. In this comprehensive study, various computational tools for pre- and post-processing the data achieved from VASP are used and developed. The fundamental physics behind the concepts explained here is covered in chapter 3.

## 4.1 Computational tool - VASP

To solve the Kohn-Sham equation (2.14) as seen in chapter 2, we employ several minimization algorithms. These algorithms are based on the conjugate gradient scheme [79][80], block Davidson scheme [81][82], or a residual minimization scheme that is a direct inversion of the iterative subspace (RMM-DIIS) [83][84]. Algorithms are implemented using an iterative matrix-diagonalisation scheme, while the charge density is a mix of Broyden/Pulay mixing schemes [84][85][86].

In general, VASP uses the self-consistent field method to calculate a system's electronic ground state energy. Figure 4.1 shows an example of such a flow. The input charge density ($\rho_{in}$) and wavefunction ($\phi_{in}$) are quantities chosen before the calculation is started and are independent values. These values are then used to set up the potentials, Hamiltonian, and wave functions. Then the wave functions are optimised iteratively in an attempt to get them as close as possible to the exact wave functions of this Hamiltonian. After the wave functions have been optimised, they are used to calculate a new charge density mixing it with the input charge density. This loop continues until the input charge density, and new charge density converge to a preset criterion. When convergence is reached, the ground state energy can be used to calculate properties such as band energies, forces, optical properties and more.

Due to the way the conjugate gradient and the residual minimization scheme calculate the Kohn-Sham eigenfunction, they do not recalculate the exact values but rather a random linear combination of the eigenfunctions to the lowest Kohn-Sham or Quasiparticle orbitals, an additional subspace diagonalisation is required. Here the Hamiltonian is diagonalised in the subspace spanned by the trial wave functions, and the wave functions are transformed accordingly:

$$\langle \phi_j | \mathbf{H} | \phi_i \rangle = H_{ij}, H_{ij} Ujk = \epsilon_k U_{ik}, \phi_j \leftarrow U_{jk} \phi_k. \tag{4.1}$$

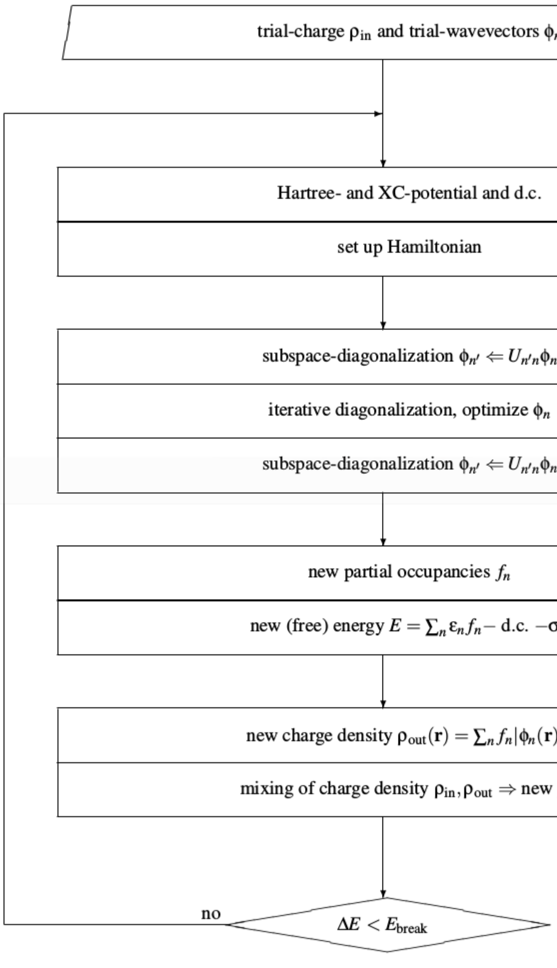

**Figure 4.1:** Flowchart showing the self-consistent cycle VASP follows in their calculations of the electronic ground state.

## 4.2 Crystal symmetry

The number of electrons in a material is too high to model with the Schrödinger equation, even when using DFT and the "Kohn-Sham equations as described in chapter 2 to model the Schrödinger equation. However, infinite crystals have periodic potentials. In other words, it is invariant under a lattice translation **T**, and through the translational symmetry of the crystal, the solution of the Kohn-Sham equations in one part of the system can give the solution for the entire system:

$$V(\mathbf{r}+\mathbf{T}) = V(\mathbf{r}), \tag{4.2}$$

$$\mathbf{T} = m_1\mathbf{a}_1 + m_2\mathbf{a}_2 + m_3\mathbf{a}_3. \tag{4.3}$$

Where the $\mathbf{a}_i$ are the real-space Bravais lattice vectors that span the entire crystal, and $m_i$ are integers. Bloch proved that the eigenstates could take the form of a plane wave multiplied by the periodicity of the Bravais Lattice:

$$\Psi_{\mathbf{k}}(\mathbf{r}+\mathbf{T}) = e^{i\mathbf{k},\mathbf{T}}\Psi_k(\mathbf{r}). \tag{4.4}$$

**k** is the Bloch wave vector. This makes it possible to rewrite the one-electron function and characterise it and the corresponding eigenvalues $\epsilon_n$ with **k** as:

$$H(\mathbf{r})\Psi_n(\mathbf{k};\mathbf{r}) = \epsilon_n(\mathbf{k})\Psi_n(\mathbf{k};\mathbf{r}), \tag{4.5}$$

where n is now the quantum number. If the wave vector corresponds to the reciprocal lattice vector

$$\mathbf{g} = 2\pi(n_1\mathbf{b}_1 + n_2\mathbf{b}_2 + n_3\mathbf{b}_3) \tag{4.6}$$

where $n_i$ are integers and $\mathbf{b}_i$ are the reciprocal lattice's basis vectors, the phase factor will be 1. This means that for **k** = g we get

$$e^{i\mathbf{k}.\mathbf{T}} = e^{ig,T} = e^{2\pi i m_i n_i} = 1. \tag{4.7}$$

Hence, if the real space is periodic, then the reciprocal space (**k**) will also be periodic and an electron state with the wave vector

$$\mathbf{k}' = \mathbf{k} + g \tag{4.8}$$

will satisfy the Bloch theorem; a solution to the Schrödinger equation in a periodic potential will take the form of a plane wave modulated by a periodic function. Therefore, we do not have to consider the vectors when describing the electronic structure of materials. It is enough to use the wave vectors inside the Brillouin Zone. That is, wave vectors in a uniquely defined primitive cell in the reciprocal space. There are also rotational symmetries in addition to the translation symmetries, reducing our problem. The smallest symmetry-independent section of the Brillouin zone is called the irreducible Brillouin zone, and we only have to find solutions to our equations within the irreducible Brillouin zone for electronic structures.

## 4.3 Electronic properties

### 4.3.1 *Band structure*

The band structure of a material describes the eigenvalues of the orbitals, in our case, KS or QP orbitals, throughout the Brillouin zone. For a thorough explanation of the band structure, see chapter 3.3.1. Generally, the Kohn-Sham orbitals and eigenenergies are computed along a reciprocal space path connecting with high-symmetry points in the irreducible Brillouin zone. In other words, it is a regular calculation solving the Kohn-Sham equation, see chapter 2.2.1 and 2.2.2 for the details, following a specific path to ensure that we encapsulate the band minima, maxima etc. In addition, the band structure is closely related to the crystal structure.

### 4.3.2 *Density of states*

The density of states (DOS) is the number of different states at a specific energy level that electrons can occupy. Based on the Pauli principle and the fact that the total energy of a material is always minimized, the eigenstates with their respective values $\epsilon_i(\mathbf{k})$ are filled from the bottom and up. That is, the eigenvalue with the lowest energy is filled first. The energy corresponding to the highest filled eigenstate is the Fermi energy ($E_F$) and is given as

$$N = \int_{-\infty}^{\epsilon_F} D(\epsilon) d\epsilon. \tag{4.9}$$

N is the number of valence electrons, and $D(\epsilon)$ is the density of states. We calculate the DOS as

$$D(\epsilon) = \frac{2}{8\pi^3} \int_{S(\epsilon)} \frac{dS}{|\nabla \epsilon(\mathbf{K})|} \tag{4.10}$$

and the integral is taken over a surface of constant energy, $S(\epsilon)$, in the irreducible Brillouin zone.

### 4.3.3 *Effective mass calculations*

To calculate the effective mass for the electrons and holes in our structure, we have used the effective mass calculator created by Fonari and Sutton [87]. See chapter 3.3.2 for the physical explanation of effective mass.

The effective mass is defined as [45]:

$$\left(\frac{1}{m^*}\right)_{ij} = \frac{1}{\hbar^2}\frac{\delta^2 E_n(\mathbf{k})}{\delta k_i k_j}, i, j = x, y, z. \tag{4.11}$$

Where x, y, and z are the directions in the reciprocal Cartesian space, and $E_n(k)$ is the dispersion relation for the n-th electronic band. For covalently bonded group III-IV semiconductors $E_n(k)$ at the band maximum, or minimum, can be approximated by a parabola [87]:

$$E_n(k) = \alpha_1 k_x^2 + \alpha_2 k_y^2 + \alpha_3 k_z^2, \tag{4.12}$$

which means that the effective mass for these semiconductors can be calculated as:

$$m_{xx}^* = \frac{\hbar}{2\alpha_1}, m_{yy}^* = \frac{\hbar}{2\alpha_2}, m_{zz}^* = \frac{\hbar}{2\alpha_3}. \tag{4.13}$$

Unfortunately, for organic semiconductors, it is not always possible to fit the band to a quadratic polynomial. To find the effective mass for these materials, the derivatives in equation (4.11), we must evaluate them numerically. Using the finite difference method, the right-side symmetric tensor in equation (4.11) is [87]:

$$\frac{d^2E}{dk^2} = \begin{bmatrix} \frac{d^2E}{dk_x^2} & \frac{d^2E}{dk_x dk_y} & \frac{d^2E}{dk_x dk_z} \\ \frac{d^2E}{dk_x dk_y} & \frac{d^2E}{dk_y^2} & \frac{d^2E}{dk_y dk_z} \\ \frac{d^2E}{dk_x dk_z} & \frac{d^2E}{dk_y dk_z} & \frac{d^2E}{dk_z^2} \end{bmatrix}. \tag{4.14}$$

The second and mixed derivatives are calculated using a five-point stencil with an error on the order of $O(h^4)$ [88]. From this, it follows that the effective mass of organic semiconductors can be calculated as the inverse of the eigenvalues of equation (4.14), while the eigenvectors are the direction of the effective mass component. We can perform the needed calculations by extracting the eigenvalues from an appropriate VASP calculation [4.11].

## 4.4 Optical properties

The importance of optical properties with regard to photocatalytic water splitting is discussed in chapter 3.4. Evaluation of the optical properties of a material is based on the complex dielectric function

$$\epsilon(\omega) = \epsilon_1(\omega) + i\epsilon_2(\omega), \tag{4.15}$$

where $\epsilon_1$ and $\epsilon_2$ are the material's real and imaginary dielectric functions, and $\omega$ is the photon frequency. For a simplified system, the local field effects for the dielectric function are ignored, and the imaginary part of the dielectric function can be written as [89]:

$$\epsilon_2(\omega) = \frac{4\pi^2 e^2}{\Omega} \lim_{q\to 0} \frac{1}{q^2} \times \sum_{c,v,\mathbf{k}} w\omega_{\mathbf{k}} \delta(E_c - E_v - \omega) \left|\langle c\,|\mathbf{e}\cdot\mathbf{q}|\,v\rangle\right|^2 . \tag{4.16}$$

Here $|\langle c\,|\mathbf{e}\cdot\mathbf{q}|\,v\rangle|^2$ is the integrated optical transitions from the valence states $(v)$ to the conduction states $(c)$, $\mathbf{e}$ is the polarization direction of the photon, $\mathbf{q}$ is the electron momentum operator, and $E_v$ and $E_c$ are the valence band and conduction band energies respectively. The integration over $\mathbf{k}$ is performed by summation over special $k$-points with a corresponding weighting factor $\omega_k$ [90]. By using the Kramers-Kronig relation, the real part of the dielectric function is given by

$$\epsilon_1(\omega) = 1 + \frac{2}{\pi} P \int_0^\infty \frac{\epsilon_2(\omega')\omega'}{\omega'^2, -\omega^2 + i\eta} d\omega', \tag{4.17}$$

where $P$ is the principle value and $\eta$ is the complex shift parameter [90]. After a simulation, we can extract the values for $E_v$ and $E_c$ and thus compute the dielectric functions. Now that the equations for the dielectric functions are established, it is possible to calculate the frequency-dependent linear optical spectra, which is the absorption coefficient $(\alpha(\omega)$, refractive index $n(\omega)$, extinction coefficient $k(\omega)$, energy-loss function $L/\omega)$, and reflectivity $R(\omega)$ [91]:

$$\alpha(\omega) = \frac{\sqrt{2\omega}}{c} \left[ \sqrt{\epsilon_1^2(\omega) + \epsilon_2^2(\omega)} - \epsilon_1(\omega) \right], \tag{4.18}$$

$$n(\omega) = \sqrt{\frac{\sqrt{\epsilon_1^2 + \epsilon_2^2} + \epsilon_1}{2}}, \tag{4.19}$$

$$k(\omega) = \sqrt{\frac{\sqrt{\epsilon_1^2 + \epsilon_2^2} - \epsilon_1}{2}}, \tag{4.20}$$

$$L(\omega) = \mathrm{Im}\left(\frac{-1}{\epsilon(\omega)}\right) = \frac{\epsilon_2}{\epsilon_1^2 + \epsilon_2^2}, \tag{4.21}$$

$$R(\omega) = \frac{(n-1)^2 + k^2}{(n+1)^2 + k^2}. \tag{4.22}$$

Where $c$ is the speed of light in a vacuum. We utilised VASPKIT [90] for these calculations, which is a tool that can perform high-throughput analysis of a variety of material properties from the raw data produced by VASP.

## 4.5 *d*-Band model

We use the *d*-band model as an indicator for an efficient photocatalyst and explain in detail how it works in chapter 3.5.1. To calculate the *d*-Band, $\epsilon_d$, center we use the following equation [90]:

$$\epsilon_d = \frac{\int_{-\infty}^{\infty} n_d(\epsilon)\epsilon d\epsilon}{\int_{-\infty}^{\infty} n_d(\epsilon) d\epsilon} \tag{4.23}$$

where $n_d(\epsilon)$ is the *d*-band density, $\epsilon_d$ is the *d*-band energy and $n_d(\epsilon)d\epsilon$ is the number of transition metal d-states. These values are easily extracted from the output files after a density of state (DOS) calculation using VASP, and equation (4.23) is then solved using tools such as excel, python and originlab.

## 4.6 Phonon calculations

As described in chapter 3.2 we use Phonons to evaluate the dynamical stability of a material. These calculations are performed by doing a Taylor expansion of the total energy E in terms of the ionic displacement,

$$u_{I\alpha} = r_{I\alpha} - r^0_{I\alpha}, \tag{4.24}$$

around the equilibrium positions of the nuclei $r^0_{I\alpha}$. This looks like

$$E(\mathbf{r}) = E(\mathbf{r}^0) + \sum_{I\alpha} -F_{I\alpha}(\mathbf{r}^0)u_{I\alpha} + \sum_{I\alpha J\beta} \phi_{I\alpha J\beta}(\mathbf{r}^0)u_{I\alpha}u_{J\beta} + O(\mathbf{r}^3) \tag{4.25}$$

with $F_{I\alpha}$ being the atomic forces and $\phi_{I\alpha J\beta}$ the second-order force constants. If the forces are zero and the structure is in equilibrium, then we find the normal modes of the vibration of the system from the eigenvalue problem:

$$\sum_{J\beta} \frac{1}{\sqrt{M_I M_J}} \phi_{I\alpha J\beta} e^{i\mathbf{q}\cdot(\mathbf{r}_J - \mathbf{r}_I)}(\mathbf{q})\epsilon_{J\beta,\nu}(\mathbf{q}) = \omega(\mathbf{q})^2 \epsilon_{J\alpha,\nu}(\mathbf{q}) \tag{4.26}$$

where $\epsilon_{J\alpha,\nu}(\mathbf{q})$, the normal modes with corresponding frequencies $\omega(\mathbf{q})^2$, are the phonons in the adiabatic harmonic approximation. The second-order force constants we calculated using the supercell approach with either finite-differences or density functional perturbation theory.

## 4.7 Development of efficient numerical methods

Performing quantum mechanical calculations of nanomaterials based on DFT is a computer-time demanding exercise. Developing efficient numerical methods for reducing computing time is one of the prime concerns of this study. By generalising the pseudopotentials and linear augmented plane waves, it is possible to save on computer power without reducing the accuracy of the calculations.

According to Bloch's theorem, solutions to the Schrödinger equation with a periodic potential will take the form of periodic plane waves [45]. Therefore, we can use plane waves to describe the tight bonding between the core orbitals and the rapid oscillations of the wave function in the core region. The large amount (>10 000) of plane waves needed for accurate results makes it computationally expensive to perform electronic structure calculations. A successful way of reducing the number of plane waves is to ignore the core electrons; they will be frozen during the calculations, as the valence electrons are important for most electronic, optical and physical properties. This is called the pseudopotential approximation, where the pseudopotential with only active valence electrons (core electrons are frozen) replaces the original potential [92][93][94][95]. The difference between the all-electron and pseudoelectron potential is shown in figure 4.2. The wavefunction oscillates rapidly in the core region due to the strong ionic potential, which differs from the pseudopotential. However, as the radius increases, we see that the two potentials overlap.

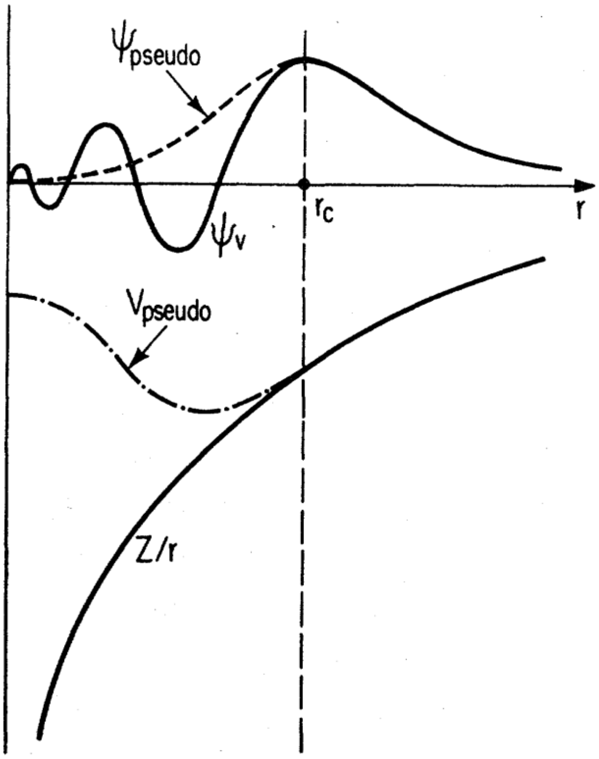

**Figure 4.2:** Schematic illustration of all-electron (solid lines) and pseudoelectron (dashed lines) potentials and their corresponding wave functions. Taken from [96]

Blöchl further improved the pseudopotential approximation by combining it with the linear augmented-plane-wave (LPAW) method [97]. The projected augmented wave method describes the wave function using atomic and pseudo-atomic orbitals at each atom, in addition, to the plane waves. It uses plane waves to describe the wave function's bonding and tail region. At the same time, the expansion of the atomic orbitals allows for an accurate description of the wave function near the nucleus. The

PAW method does not determine the coefficient of the atomic orbitals variationally. Instead, they are unique functions of the plane wave coefficients. By doing this, one no longer needs to perform two electronic structure calculations, one for the plane waves and one for the orbitals. If it was possible to get a complete and exact expansion of the atomic orbitals and plane waves, then PAW could find the exact DFT energy. PAW was developed to increase computational efficiency while keeping the accuracy of the calculations. This means we can use it on solids, surfaces and molecules as the limitations of the plane wave basis sets regarding periodic systems (crystals) can be overcome by making large enough unit cells and decoupling long-range interactions.

## 4.8 Pre- and post-processing

VASP is an extremely powerful tool, but to employ it efficiently, a wide range of scripts must be developed both for pre- and post-processing of data, as VASP provides only the raw data. . The output data must be analysed and used in further calculations before it is presentable. In addition, suitable input files must be created to ensure accurate and correct calculations. We have used a wide range of tools and in-house produced scripts, which are discussed and explained in this chapter. These tools have been chosen to speed up pre-and post-processing, as there is no reason to reinvent the wheel daily. After the data has been processed using these tools, it is analysed using a mix of chemistry and physics to understand the results. For example, what does a band gap of 1.8 eV signify, how does it affect our material's solar absorption, or what do the IR spectra tell us? Chapter 3 explains some of the essential factors and properties we have looked into and explains the mathematics, physic and chemistry behind them.

### *4.8.1 Scripts*

Based on our research group's expansive database of cross-disciplinary knowledge, we have created scripts and computing tools that simplify and improve the pre- and post-processing related to our calculations. Most scripts are written in Python, taking advantage of the vast amount of available packages. The complexity of the scripts vary from the simpler ones to create supercells needed for calculations of larger structures to more complex ones used for K-point generation and bandstructure plots.

## 4.9 High-performance computing

To simulate larger systems (more than 2-3 atoms) with VASP, we need to use supercomputers organised in clusters. A supercomputer is a computer made up of several central processing units (CPUs) that use parallel processing instead of serial processing as a regular computer does and helps to perform high-performance computing. The CPUs are then grouped into groups of nodes and memory. These nodes use parallel processing to communicate with each other when solving problems. In general, a supercomputer is much more powerful than a regular computer, and the processing speed is measured in floating point operations per second (FLOPS).

### 4.9.1 *Parallelization*

For the supercomputer to do several calculations at once, the calculation process has to be split into several small processes that can be done simultaneously. In VASP, this is done by distributing the number of bands over the available message-passing interface (MPI) ranks, where a rank corresponds to a process participating in the overall parallel communication. The number of bands is controlled by the tag NBANDS, specifying the total number of Kohn-Sham (KS) or Quasi-Particle (QP) orbitals in the calculation. In addition, it is possible to add parallelization of the Fast Fourier Transformations (FFTs), parallelization over **k** points, and parallelization over separate calculations depending on your need. For efficient parallelization, it is important to keep processes that need to communicate on the same node, where a node is a physical entity made up of several CPUs and potentially graphical processing units (GPUs). This is because communication between nodes is slower than communication within one.

For example, when a calculation with 20 ranks on two nodes is run, VASP expects rank 1-10 on node 1 and rank 11-20 on node 2. However, with the wrong tags in the input files, it is possible to place, for example, all odd ranks on node 1 and all even ranks on node 2. This results in cross-node communication for every parallel FFT performed by VASP and severely reduces the calculation's performance.

### 4.9.2 *High-performance computing facilities*

In Norway, the high-performance computing facilities are managed by the Norwegian research infrastructure services (NRIS), providing access to the national supercomputer clusters. In this project, we used the supercomputer cluster Stallo at UiT and Saga at NTNU. The clusters are managed by Sigma2, which has the strategic responsibility for and manages the national e-infrastructure for large-scale data- and computational science in Norway. Table 4.1 show some key information about the two supercomputer clusters.

| Details | Saga | Stallo |
|---|---|---|
| Number of Cores | 16064 | 11424 |
| Number of nodes | 364 | 632 |
| Total max FLOPS | 645 Teraflop/s (CPUs) + 160 Teraflop/s (GPUs) | 312 Teraflop/s |
| Total memory | 97.5 TiB | 26.2 TiB |
| CPU hours used | 569921 | NA |

**Table 4.1:** The table shows some key information about the supercomputer clusters Saga and Stallo

From the data in table 4.1, we see that Saga was a clear upgrade from Stallo with respect to computing speed, cores and memory. Thus increasing the speed of our calculations and making it possible to investigate larger systems.

# CHAPTER 5

# SUMMARY OF STUDIES

This chapter contains a summary of the five papers included in this thesis. This is a highly complex field, so it is essential to look at theoretical and experimental work to understand the field entirely. With this in mind, we started working on the review article as an independent and comprehensive article, and not an introduction to this thesis. The resulting article is clearly important to the field, with more than 5000 views and 75+ citations. Our findings in this article laid the foundation for our future work as it ties together the various difficulties $TiO_2$ photocatalysts face and potential solutions. One material, which shows great promise as a photocatalyst is perovskites, and for that reason, our next two articles focused on them. Although our studies confirm their potential, we also identify some remaining issues that need to be solved. Another promising candidate for photocatalytic water splitting emerging from the review is $MoS_2$, which is well established as a lubricant, diode, catalyst and in photocatalytic dye degrading in industry. Hence, we decided to look further into its optical, electronic, structural and photocatalytic properties in our fourth and fifth article.

## 5.1 Paper A: $TiO_2$ as a photocatalyst for water splitting – an experimental and theoretical review

In this study, we reviewed state-of-the-art experimental and theoretical research on $TiO_2$ based photocatalysts in this study. The goal was to identify challenges and problems that must be dealt with for the field to advance. Since the 1970s, $TiO_2$ has been one of the most used photocatalysts due to several attractive properties, low cost, chemical stability, availability, and non-toxicity. However, it also sports a wide band gap of 3.0 - 3.2 eV which reduces the amount of visible light absorbed by the catalyst. In general, $TiO_2$ exists in several stable polymorphs, where the most common are rutile, brookite, anatase and amorphous. Rutile and anatase are most commonly used for photocatalytic water splitting. Several attempts have been made to alter the electronic and optical structure of $TiO_2$ using dopants, nanostructures, particles, or thin films. Based on the collected data from experimental work, we observe a clear trend toward complex structures that consists of several different layers, materials and nanostructures, e.g. $CuO@TiO_2$ nanowires, Ni-doped $TiO_2$ nanotubes, or graphene QDs decorated rutile $TiO_2$ nanoflowers. This has proven very effective, resulting in a band gap of 2.15

eV using a $S - TiO_2/S$-reduced graphene oxide catalyst. Unfortunately, the complex structures increase the cost and difficulties of achieving large-scale production. In addition, there is uncertainty during the synthesis of the photocatalysts concerning the exact composition and structure of the compound. The properties of the compound will also be affected by the deposition technique used. This makes it difficult to verify and compare the different structures.

Theoretical studies, on the other hand, have focused more on using dopants and more straightforward nanostructures on anatase $TiO_2$. For example, a band gap of 2.15 eV was achieved by co-doping $TiO_2$ with sulphur and niobium. Theoretical work is limited by the available computing power, which reduces the size and complexity of structures investigated structures. However, creating the exact structure one wants to investigate is possible. Therefore, we can investigate specific structures, reactions, and how changes to the structures influence relevant properties. We identified four significant obstacles $TiO_2$ based photocatalytic water splitting has to overcome before it can be a low-cost and efficient way of producing hydrogen. The first challenge is a lack of standardised measurement settings for hydrogen production rates. Researchers will, for example, use different light sources, water solutions, potentials, and co-catalyst when measuring production rates. This makes it difficult to compare results and determine the better compound. For theoretical work, there is no exact calculation for hydrogen- and oxygen production rates. However, several alternatives are good indicators of HER and OER. The second challenge is $TiO_2$ itself and its wide band gap. As seen above, solutions to narrow it exist but are complex and challenging to synthesise. This makes large-scale production facilities unfeasible. The third challenge is the lack of cooperation between theoretical and experimental work. Both approaches have weaknesses and strengths, and combining them can achieve higher solar-to-hydrogen efficiency. Theoretical simulations can be used to screen thousands of materials quickly and investigate the fundamental processes of photocatalytic water splitting. Experimental work can use this knowledge to verify and develop new catalytic structures. The last challenge is the lack of scalable hydrogen production facilities. So far, most experiments are done at a lab scale and the larger ones that exist only have a solar-to-hydrogen efficiency of 1.8%. Several issues, such as gas separation, catalyst lifetime and efficiency, must be solved before we can produce a prototype facility.

Based on our findings here we decided to investigate perovskites, papers B and C, and $MoS_2$, papers D and E, further as they have intriguing optical and electronic properties.

## 5.2 Paper B: band gap engineering in $CsSn_xPb_{1-x}I_3$ and their influence on light absorption

The main purpose of study B [98] was to increase the efficiency of perovskite photovoltaics through band gap engineering of $CsSn_xPb_{(1-x)}I_3$, where x = 0.5 and x = 1. We used density functional theory with hybrid functionals to investigate the electronic, optical and structural properties of $CsPbI_3$, $CsSnI_3$ and $CsSn_{0.5}Pb_{0.5}I_3$. First, we looked into the different polymorphs' structural composition and relative stability. This ensures that our structures match experimental work and that we use the most stable structure for further calculations. $CsSnI_3$ exists in four different polymorphs; depending on temperature and pressure, it can change between them. Since the energy difference between the four polymorphs is quite small, we included all of them in our study. It has been proven experimentally that it is possible to synthesise all of them. For $CsPbI_3$ we found two structures, one of them is an orthorhombic structure at room temperature, and the other is a cubic structure when at higher temperatures. $CsSn_{0.5}Pb_{0.5}I_3$ is a new and unknown crystal structure. However, our model predicts it to be an orthorhombic $Sn_2S_3$-derived structure at ambient conditions. We investigated the band structures for the low-energy polymorphs using HSE06 to find their band gap values and if they are direct or indirect band gaps. Direct band gaps are ideal for photovoltaic applications as they ensure efficient electron-hole transport. Three of the $CsSnI_3$ structures have direct band gaps, while the last has an indirect gap. $CsPbI_3$ has a direct band gap for both structures, although the band gap value is more than double that of $CsSnI_3$. $CsSn_{0.5}Pb_{0.5}I_3$ was very interesting as we observed an indirect band gap between Y-H and Z-D, see figure 5.1. However, the minimum electron/hole jump distance is at Z-D. In other words, this material can function as a direct band gap material.

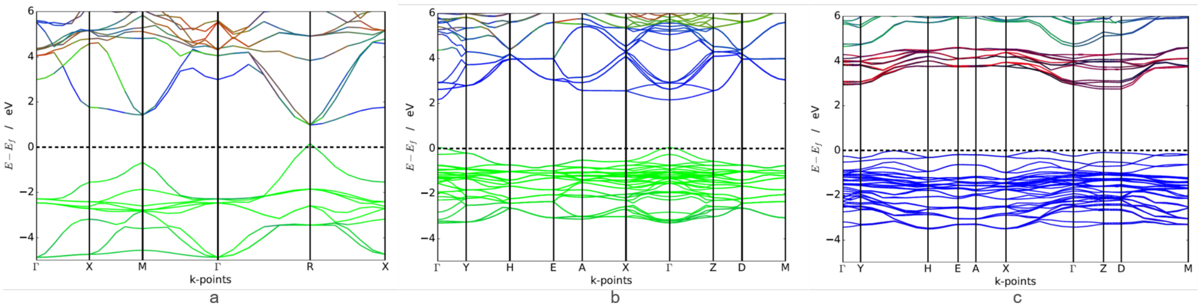

**Figure 5.1:** Calculated band structures for the stable orthorhombic structures of a) $CsSnI_3$, b9 $CsPbI_3$ and c) $CsSn_{0.5}Pb_{0.5}I_3$

From the absorption spectra, we found that $CsSnI_3$ primarily absorbs light in the blue and ultraviolet region, while $CsPbI_3$ absorbs in the ultraviolet region. $CsSn_{0.5}Pb_{0.5}I_3$ we expected to behave similar to its components, but were surprised to find the absorption peak blue-shifted compared to $CsSnI_3$ and $CsPbI_3$.

In short, we demonstrated that combining perovskites leads to completely new electronic and optical structures. This could make combining various compounds in the hunt for improved photovoltaic efficiencies viable.

The work on perovskites was expanded upon in two more papers as we wanted to look at lead-free perovskites and see how we could alter their properties by changing one compound.

## 5.3 Paper C: $Cs_2AgBiBr_6$ as a mixed anion perovskites for photovoltaic applications: A first-principle study

As a continuation of our work on perovskites in study B, we decided to look at a lead-free perovskite, $Cs_2ABiBr_6$, to avoid the toxicity and long-term stability issues of lead-based perovskites. $Cs_2ABiBr_6$ has, in other studies, proven to have good thermal and ambient stability, high hole mobility, and it is a semiconductor. At room temperature, $Cs_2ABiBr_6$ exists in a cubic structure (Fm-3m), while at 122 K a phase transition to a tetragonal structure (I4/m) occurs. This phase transition could also be induced by increasing the pressure to 4.5 GPa. Thus, we investigated both structures to see how the phase transition would influence their optical and electronic properties. Both structures were mechanically stable, while only the tetragonal phase was dynamically stable. This means that the cubic phase could be a metastable phase, while the tetragonal phase is a stable structure. This was backed up by comparing the total energy of both structures, where the tetragonal structure had a lower total energy than the cubic one. In addition, both of the structures were found to be ductile. Our band gap calculations confirm that both structures are semiconductors with an indirect band gap. Based on HSE06 calculations the band gaps are 1.97 eV for cubic $Cs_2ABiBr_6$ and 2.4 eV for tetragonal $Cs_2ABiBr_6$, which is in good agreement with previous studies. We also calculated the effective mass to investigate the structures' charge mobility, and found that both structures have higher electron mobility than hole mobility. This is expected as holes have a higher mass than electrons. Finally, we calculated the chemical bonding of the structures to get a better idea of the charge distribution. It was clear that the charge resided in the vicinity of the nuclei and that this was similar for both the cubic and tetragonal structures. Both ionic and covalent bonding was seen, indicating that $Cs_2ABiBr_6$ is a mixed bonding material. Using first-principle calculations, we found that the cubic and tetragonal structure of $Cs_2ABiBr_6$ could have potential in optoelectronic applications. Further work is needed to investigate the structures' optical and photocatalytic properties. As an extension to this work, we studied $Cs_2ABiX_6$ with X = Br, Cl, F and I to see how the different halide substitutions would affect optical and electronic properties, in addition to the structural stability. Here we found that the perovskite kept its indirect band gap, but it varied from 1.78 eV to 4.53 eV. Once again, it shows the flexibility of perovskite catalysts and how it is possible to design an ideal photocatalyst for photocatalytic water splitting through compound engineering.

These articles concluded our research on perovskites, as we previously in paper A had identified $MoS_2$ as another potential photocatalyst for photocatalytic water splitting that we wanted to investigate further.

## 5.4 Paper D: In-depth first-principle study on novel $MoS_2$

This article [99] was inspired by the findings in paper A, where we concluded that for photocatalytic water splitting to be realised, we must use different materials than $TiO_2$. Molybdenum disulphide ($MoS_2$) is a transition metal already used in photovoltaics, diodes, electronic circuits, lubricants and transistors. This is due to its unique optical, electronic and structural properties that depend on transition metals' layered structure. We investigated 14 different $MoS_2$ polymorphs to find structures suitable for photocatalytic water splitting. $MoS_2$ consists of S-Mo-S layers or sandwiches bonded to each other by weak van der Waals-type forces. Changing the stacking sequence and registry of successive S-Mo-S sandwiches along the c-axis makes it possible to create many different polymorphs in three dimensions. These phases are known as 1T, 2H, 3R, $4H_a$, $4H_b$ and 6R. T, H, and R stand for trigonal, hexagonal and rhombohedral, respectively. The integer indicates the number of S-Mo-S sandwiches along the c-axis. Figure 5.2 illustrates the difference in crystal structure for 2H and 1T $MoS_2$ structures.

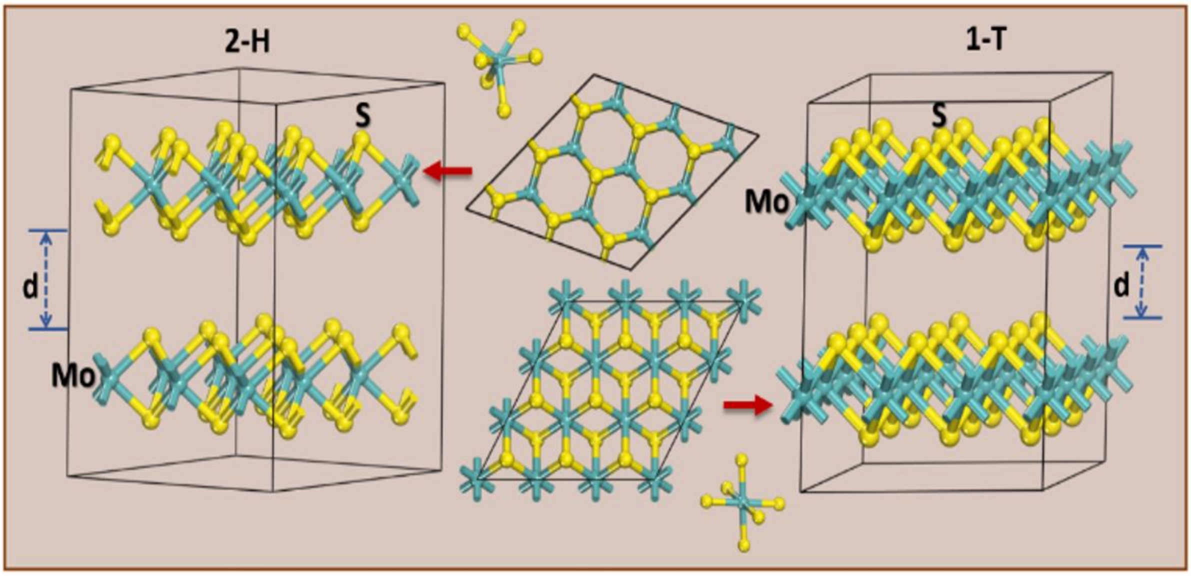

**Figure 5.2:** A comparison of 2H (a) and 1T (c) $MoS_2$ structures. b) shows a top-down look at the hexagonal polymorph of 2H (top) and 1T (bottom).

We started with 14 structures but immediately discarded three as they were less stable than the other 11. The remaining 11 structures could be divided into group A ($2R_1$, 2H, $3H_b$, $3H_a$, 4T, 2T and 1H) and group B ($1T_1$, $1T_2$, 3T and $2R_2$) based on their energy vs volume curves. The seven structures in group A have similar minimum energies and are therefore expected to be equally stable. We found group B to have slightly higher minimum energies. Throughout the study, we found that the group A polymorphs are all semiconductors with an indirect band gap that ranges from 1.87 eV to 2.12 eV. Based on our phonon calculations, they should all be dynamically and mechanically stable. In other words, they are ready to be synthesised. Group B, on the other hand, were only mechanically stable and turned out to be metallic. This makes them unsuited for any photocatalytic/voltaic application. $1T_2 - MoS_2$ was neither dynamically nor mechanically stable. In conclusion, several $MoS_2$ polymorphs could be viable for photocatalytic water splitting, but experimental verification and further studies on hydrogen activity are needed.

We continued the work on the seven stable polymorphs in paper E as they showed great promise as photocatalysts.

## 5.5 Paper E: Doped $MoS_2$ polymorph for improved hydrogen evolution reaction

Based on our findings in paper D, we decided to further investigate the seven stable $MoS_2$ polymorphs with regard to their inherent photocatalytic properties and how dopants could affect these properties. Well-known catalytic indicators such as d-band centre, Gibbs free energy and absorption coefficient were used. In addition, we wanted to investigate if temperature changes caused any phase transitions. The seven included polymorphs were $2R_1, 2H, 3H_b, 3H_a, 4T, 2T$ and $1H$, and based on our previous results in Paper D, $3H_b$ was chosen to be doped with Al, Co, I, N and Ni. First, we found that no phase transition will occur with increasing temperature, meaning each polymorph can be used at any temperature without the fear of changing its structure. The *d*-band centre values were compared to that of platinum, which is seen to have an optimal *d*-band centre for photocatalytic water splitting. None of the seven polymorphs has as good *d*-band centre as platinum, but $2R_1$ and $3H_a$ were close (within 20 %) and should have low enough binding strength with hydrogen to be efficient catalysts. All seven polymorphs had downshifted *d*-band centres with regards to the Fermi level, which is an indicator for potential effective photocatalysts. The absorption coefficient of all the polymorphs was within the visible spectra, with peaks in both ends of the spectra. In general, the Gibbs free energy should be close to zero for an efficient photocatalyst, while our obtained values range from 1.746 eV to 1.852 eV, indicating that the adsorbed hydrogen is bound strongly to the surface. The ideal catalyst should both have *d*-band centres that are downshifted from the Fermi level and Gibbs energy levels close to zero. Thus we decided to dope $3H_b - MoS_2$ with Al, Co, I, N and Ni to see how that would affect the Gibbs free energy, structural stability and electronic properties. Ten new polymorphs were created, where either one Mo or one S was replaced with one Al, Co, I, N or Ni. For $3H_b$ with one Mo replaced, the Gibbs free energy was decreased by a factor of ten, on the paper, creating an effective photocatalyst. As it is clear that the dopants affect the polymorph properties, we looked into the electronic structure and band gap. The structures must be semiconductors, or they will not work as catalysts. We found that different dopants result in varying band gaps. Only four of the ten doped structures were semiconductors: Mo substituted with Al and I, and S substituted with Co and Ni. The next question was then whether the structures were stable and would survive the synthesis process. Our calculations show that only Co, I and N for Mo-doped $3Hb - MoS_2$ are dynamically unstable, while the other seven are both mechanically and dynamically stable. Based on this, we propose $3Hb - MoS_2$ substitutional doped with Al for Mo atoms as a potential candidate for photocatalytic water splitting. Future work should have to conclude on the optimal dopant and doping percentage.

# CHAPTER 6

# CONCLUSIONS AND FUTURE WORK

This chapter will summarise the key findings of this project with regard to our research questions and their contribution to the relevant research fields. In addition, it will also look at the limitations of the thesis and propose future work. The common goal of the work done in this project was to explore existing and new materials that could function as a catalyst for photocatalytic hydrogen production.

$TiO_2$ has been the go-to photocatalyst for photocatalytic water splitting over the past years. However, the material's intrinsic properties have been detrimental to the realisation of large-scale photocatalytic hydrogen production based on $TiO_2$ catalysts. Other materials with better-suited properties are commonly used in different fields and industries today. With their intriguing properties, perovskites could be optimised through band gap engineering and doping into highly efficient photocatalysts. Our work showed that computational calculations could accurately predict structure changes and polymorphs, as seen in experimental studies. We found that by altering the composition of the perovskites, it was possible to change and improve the band gap of the involved structures. Further work on a lead-free perovskite, $Cs_2AgBiBr_6$, showed that it is dynamically and mechanically stable in its tetragonal form with an indirect band gap of 2.4 eV and a high charge mobility. Changing the halide ion in $Cs_2AgBiX_6$, where X = Br, Cl, F and I, demonstrated that the perovskite kept its indirect band gap. However, the band gap value varied from 1.75 eV to 4.53 eV. This showcases how perovskites are flexible structures that can be optimised through substitution and doping.

Another interesting group of materials for PWS is transition metal dichalcogenides, where especially $MoS_2$ have showcased exciting properties when used as a lubricant, catalyst, gas-sensor, biosensor, and recently in dye degradation. Out of 14 $MoS_2$ polymorphs, we found that seven of them (1H, 2H, $2R_1$, 2T, $3H_a$, $3H_b$ and 4T) are mechanically and dynamically stable, which means it is possible to synthesise them. Those seven are also semiconductors with an indirect band gap ranging from 1.87 eV to 2.12 eV, making them suitable for photovoltaic and photocatalytic applications. One specific polymorph, $3H_b - MoS_2$, had an effective electron mass of $0.22m_e$ ($TiO_2$ has an effective electron mass of $1.4m_e$) and thus a high carrier mobility. This is very important for an efficient photocatalyst. There are no phase transitions caused by increasing temperature for the seven polymorphs, and they all have absorption peaks in the visible light region. However, based on the Gibbs free energy, they are not ideal catalysts for photocatalytic water splitting. Substitutional doping of $3H_b - MoS_2$ with Al, Co, I, N or Ni replacing one Mo atom reduced the Gibbs free energy by a factor of ten, to the level of $MoS_2$ edge sites. Furthermore, it was found that Mo substituted with Al or I and S substituted with Co or Ni are semiconductors. In contrast, S substituted with I is an insulator, and the other five doped structures are metallic. We also investigated the structural and dynamical stability of the doped structures. Seven of them (Mo substituted with Al or Ni and S substituted with Al, Co, I, N or Ni) are stable, ensuring that it is possible to synthesise the structures. This shows that $MoS_2$ substitutional doped with Al could be a very effective photocatalyst. However, the optimal doping percentage must be decided.

Finding an efficient photocatalyst is vital for this field. However, we identified other challenges that will hinder this development if not solved. A significant problem is the lack of standardised measurement setups for photocatalysts, which makes it difficult to compare and discuss results. This is mainly a problem in the experimental field. The second issue is the lack of collaboration between theoretical and experimental work, which prevents them from playing on each other's strengths. The final problem is that no proven plans exist for medium/large-scale photocatalytic hydrogen production facilities.

To summarise, we found that both perovskites and $MoS_2$ based catalysts can quickly overcome $TiO_2$ catalysts for PWS, especially doped $MoS_2$ shows excellent promise. We also see that computational calculations can play a vital role in developing photocatalysts due to their screening capabilities and the possibility of making new compounds at a low cost. This means that a large amount ($> 1000$) of materials can be evaluated simultaneously to find promising candidates. Then using those results, it is possible to create new compounds and investigate their properties before proposing stable and promising candidates for experimental verification. This would significantly reduce the cost and time of each photocatalyst produced in a laboratory.

To further progress this field, future work should develop a standardised method for measuring solar-to-hydrogen efficiency for experimental work and a standard way to present theoretically obtained results. This would increase the comparability of research and make it easier to decide which catalysts are the most promising. Regarding $MoS_2$, further work is needed to find the ideal dopant and optimal doping percentage. This should be done as a collaboration between experimental work and theoretical work to gain benefits from both methods.

# BIBLIOGRAPHY

[1] Intergovermental Panel on Climate Change. Climate Change 2022: Mitigation of Climate Change. Report, UN, 2022. 1

[2] Emmanuel Tsekleves, Rachel Cooper, and Jak (EdS.) Spencer. *Design for Global Challenges and Goals (1st ed.)*. Routhledge, 2021. 1

[3] UN. United Nations Sustainable Development Goals. 1

[4] K. Agbossou, M. Kolhe, J. Hamelin, and T. K. Bose. Performance of a stand-alone renewable energy system based on energy storage as hydrogen. *IEEE Transactions on Energy Conversion*, 19(3):633–640, 2004. Type: Journal Article. 1

[5] U. Bach, D. Lupo, P. Comte, J. E. Moser, F. Weissörtel, J. Salbeck, H. Spreitzer, and M. Grätzel. Solid-state dye-sensitized mesoporous TiO2 solar cells with high photon-to-electron conversion efficiencies. *Nature*, 395(6702):583–585, October 1998. 1

[6] İbrahim Dinçer and Calin Zamfirescu. *Sustainable Energy Systems and Applications*. Springer US, 1 edition, 2012. Type: Book. 1

[7] Yueyu Tong, Ji Liang, Hua Kun Liu, and Shi Xue Dou. Energy storage in Oceania. *Energy Storage Mater.*, 2019. Type: Journal Article. 1

[8] T. Jafari, E. Moharreri, A. S. Amin, R. Miao, W. Song, and S. L. Suib. Photocatalytic Water Splitting-The Untamed Dream: A Review of Recent Advances. *Molecules*, 21(7), 2016. Type: Journal Article. 1

[9] Poonam Sharma and Mohan L. Kolhe. Review of sustainable solar hydrogen production using photon fuel on artificial leaf. *Int. J. Hydrogen Energ.*, 42(36):22704–22712, 2017. Type: Journal Article. 1

[10] J.A. Ortega Méndez, Cristina R. López, E. Pulido Melián, O. González Díaz, J.M. Doña Rodríguez, D. Fernández Hevia, and M. Macías. Production of hydrogen by water photo-splitting over commercial and synthesised Au/TiO2 catalysts. *Applied Catalysis B: Environmental*, 147:439–452, April 2014. 1

[11] Yusuf Bicer, Ibrahim Dincer, Calin Zamfirescu, Greg Vezina, and Frank Raso. Comparative life cycle assessment of various ammonia production methods. *Journal of Cleaner Production*, 135:1379–1395, November 2016. 1

[12] L. van Biert, M. Godjevac, K. Visser, and P. V. Aravind. A review of fuel cell systems for maritime applications. *J. Power Sources*, 327:345–364, 2016. Type: Journal Article. 1

[13] IMO. Third IMO GHG Study 2014. Technical Report 3rd, IMO, 2014. 1

[14] Klaus-Michael Mangold. Introduction to Hydrogen Technology.By Roman J. Press, K. S. V. Santhanam, Massoud J. Miri, Alla V. Bailey, and Gerald A. Takacs. *ChemSusChem*, 2(8):781–781, 2009. Type: Journal Article. 1

[15] D. L. Hoang, S. H. Chan, and O. L. Ding. Kinetic and modelling study of methane steam reforming over sulfide nickel catalyst on a gamma alumina support. *Chem. Eng. J.*, 112(1-3):1–11, 2005. Type: Journal Article. 1

[16] Hasan Ozcan and Ibrahim Dincer. Thermodynamic analysis of a combined chemical looping-based trigeneration system. *Energ. Convers. Manage.*, 85:477–487, 2014. Type: Journal Article. 1

[17] Deep Purple™ Pilot - TechnipFMC plc. 1

[18] Fusion Fuel and Ballard Power Commission H2Évora Green Hydrogen Plant - Fusion Fuel. 1

[19] IBERDROLA CORPORATIVA. Iberdrola builds the largest green hydrogen plant for industrial use in Europe. 1

[20] Green Hydrogen Project: clean fuel from solar power in Dubai. 1

[21] Chi-Hung Liao, Chao-Wei Huang, and Jeffrey C. S. Wu. Hydrogen Production from Semiconductor-based Photocatalysis via Water Splitting. *Catalysts*, 2(4):490, 2012. Type: Journal Article. 1

[22] A. Steinfeld. Solar hydrogen production via a two-step water-splitting thermochemical cycle based on Zn/ZnO redox reactions. *International Journal of Hydrogen Energy*, 27(6):611–619, June 2002. 1

[23] Ida Akkerman, Marcel Janssen, Jorge Rocha, and René H. Wijffels. Photobiological hydrogen production: photochemical efficiency and bioreactor design. *BIOHYDROGEN 2002*, 27(11):1195–1208, November 2002. 1

[24] Akihiko Kudo. Photocatalysis and solar hydrogen production. *Pure and Applied Chemistry*, 79(11):1917–1927, 2007. 1

[25] Robert De Levie. The electrolysis of water. *Journal of Electroanalytical Chemistry*, 476(1):92–93, October 1991. 1.1

[26] Diogo M. F Santos, Cèsar A. C. Sequeira, and Josè L. Figueiredo. Hydrogen production by alkaline water electrolysis. *Quìmica Nova*, 36(8), 2013. 1.1

[27] Zi-You Yu, Yu Duan, Xing-Yu Feng, Xingxing Yu, Min-Rui Gao, and Shu-Hong Yu. Clean and Affordable Hydrogen Fuel from Alkaline Water Splitting: Past, Recent Progress, and Future Prospects. *Advanced Materials*, 33(31):2007100, 2021. 1.1, 1.1

[28] Akira Fujishima and Kenichi Honda. Electrochemical Photolysis of Water at a Semiconductor Electrode. *Nature*, 238:37, 1972. Type: Journal Article. 1.1

[29] Sohail Ahmad and Sugata Mukherjee. A Comparative Study of Electronic Properties of Bulk MoS2 and Its Monolayer Using DFT Technique: Application of

Mechanical Strain on MoS2 Monolayer. *Graphene*, 03:52–59, 2014. Type: Journal Article. 1.1

[30] Håkon Eidsvåg, Said Bentouba, Ponniah Vajeeston, Shivatharsiny Yohi, and Dhayalan Velauthapillai. TiO2 as a Photocatalyst for Water Splitting—An Experimental and Theoretical Review. *Molecules*, 26(6), 2021. 1.1

[31] Roland Marschall. 50 Years of Materials Research for Photocatalytic Water Splitting. *European Journal of Inorganic Chemistry*, 2021(25):2435–2441, 2021. Type: https://doi.org/10.1002/ejic.202100264. 1.1

[32] Kazunari Domen, Shuichi Naito, Mitsuyuki Soma, Takaharu Onishi, and Kenzi Tamaru. Photocatalytic decomposition of water vapour on an NiO–SrTiO3 catalyst. *Journal of the Chemical Society, Chemical Communications*, 8(12):543–544, 1980. Publisher: The Royal Society of Chemistry. 1.1

[33] Ryoko Konta, Tatsuya Ishii, Hideki Kato, and Akihiko Kudo. Photocatalytic Activities of Noble Metal Ion Doped SrTiO3 under Visible Light Irradiation. *The Journal of Physical Chemistry B*, 108(26):8992–8995, July 2004. Publisher: American Chemical Society. 1.1

[34] Tsuyoshi Takata and Kazunari Domen. Defect Engineering of Photocatalysts by Doping of Aliovalent Metal Cations for Efficient Water Splitting. *The Journal of Physical Chemistry C*, 113(45):19386–19388, November 2009. Publisher: American Chemical Society. 1.1

[35] Qian Wang, Takashi Hisatomi, Qingxin Jia, Hiromasa Tokudome, Miao Zhong, Chizhong Wang, Zhenhua Pan, Tsuyoshi Takata, Mamiko Nakabayashi, Naoya Shibata, Yanbo Li, Ian D. Sharp, Akihiko Kudo, Taro Yamada, and Kazunari Domen. Scalable water splitting on particulate photocatalyst sheets with a solar-to-hydrogen energy conversion efficiency exceeding 1. *Nature materials*, 15(6):611–615, June 2016. Place: England. 1.1

[36] Tsuyoshi Takata, Junzhe Jiang, Yoshihisa Sakata, Mamiko Nakabayashi, Naoya Shibata, Vikas Nandal, Kazuhiko Seki, Takashi Hisatomi, and Kazunari Domen. Photocatalytic water splitting with a quantum efficiency of almost unity. *Nature*, 581(7809):411–414, May 2020. 1.1

[37] Hideki Kato and Akihiko Kudo. New tantalate photocatalysts for water decomposition into H2 and O2. *Chemical Physics Letters*, 295(5):487–492, October 1998. 1.1

[38] Hideki Kato, Kiyotaka Asakura, and Akihiko Kudo. Highly Efficient Water Splitting into H2 and O2 over Lanthanum-Doped NaTaO3 Photocatalysts with High Crystallinity and Surface Nanostructure. *Journal of the American Chemical Society*, 125(10):3082–3089, March 2003. Publisher: American Chemical Society. 1.1

[39] Elif Can and Ramazan Yildirim. Data mining in photocatalytic water splitting over perovskites literature for higher hydrogen production. *Applied Catalysis B: Environmental*, 242:267–283, March 2019. 1.1

[40] Blaise A. Pinaud, Jesse D. Benck, Linsey C. Seitz, Arnold J. Forman, Zhebo Chen, Todd G. Deutsch, Brian D. James, Kevin N. Baum, George N. Baum, Shane Ardo, Heli Wang, Eric Miller, and Thomas F. Jaramillo. Technical and economic feasibility of centralized facilities for solar hydrogen production via photocatalysis and photoelectrochemistry. *Energ. Environ. Sci.*, 6(7):1983–2002, 2013. Type: Journal Article. 1.1

[41] Md Moniruddin, Baurzhan Ilyassov, Xiao Zhao, Eric Smith, Timur Serikov, Niyazbek Ibrayev, Ramazan Asmatulu, and Nurxat Nuraje. Recent progress on perovskite materials in photovoltaic and water splitting applications. *Materials Today Energy*, 7:246–259, March 2018. 1.2

[42] W. A. Chapa Pamodani Wanniarachchi, Håkon Eidsvåg, Thevakaran Arunasalam, Punniamoorthy Ravirajan, Dhayalan Velauthapillai, and Ponniah Vajeeston. Cs2AgBiBr6 as a mixed anion perovskites for photovoltaic applications: A first-principle study. *Materials Today: Proceedings*, July 2022. 1.2

[43] Sivagowri Shanmugaratnam, Elilan Yogenthiran, Ranjit Koodali, Punniamoorthy Ravirajan, Dhayalan Velauthapillai, and Yohi Shivatharsiny. Recent Progress and Approaches on Transition Metal Chalcogenides for Hydrogen Production. *Energies*, 14(24):8265, January 2021. Number: 24 Publisher: Multidisciplinary Digital Publishing Institute. 1.2

[44] E. Schrödinger. An Undulatory Theory of the Mechanics of Atoms and Molecules. *Physical Review*, 28(6):1049–1070, December 1926. Publisher: American Physical Society. 2

[45] Philip Hofmann. *Solid State Physics: An Introduction, 2nd Edition*. Wiley, 2015. 2, 4.3.3, 4.7

[46] D. R. Hartree. The wave mechanics of an atom with a non-coulomb central field. Part I. Theory and methods. *Mathematical Proceedings of the Cambridge Philosophical Society*, 24(1):89–110, 1928. Publisher: Cambridge University Press. 2.1

[47] J. C. Slater. Note on hartree's method. *Physical Review*, 35(2):210–211, January 1930. Number of pages: 0 Publisher: American Physical Society. 2.1

[48] V. Fock. Näherungsmethode zur lösung des quantenmechanischen mehrkörperproblems. *Zeitschrift fur Physik*, 61(1-2):126–148, January 1930. tex.adsnote: Provided by the SAO/NASA Astrophysics Data System tex.adsurl: https://ui.adsabs.harvard.edu/abs/1930ZPhy...61..126F. 2.1

[49] P. Hohenberg and W. Kohn. Inhomogeneous Electron Gas. *Physical Review*, 136(3B):B864–B871, 1964. Type: Journal Article. 2.2

[50] W. Kohn and L. J. Sham. Self-Consistent Equations Including Exchange and Correlation Effects. *Physical Review*, 140(4A):A1133–A1138, 1965. Type: Journal Article. 2.2

[51] L. H. Thomas. The calculation of atomic fields. *Mathematical Proceedings of*

*the Cambridge Philosophical Society*, 23(5):542–548, 1927. Publisher: Cambridge University Press. 2.2

[52] Enrico Fermi. Un Metodo Statistico per la Determinazione di alcune Priopriet dell'Atomo. *Accademia Nazionale dei Lincei*, 6(602-607). 2.2

[53] P. A. M. Dirac. Note on exchange phenomena in the thomas atom. *Mathematical Proceedings of the Cambridge Philosophical Society*, 26(3):376–385, 1930. Publisher: Cambridge University Press. 2.2

[54] Richard M. Martin. *Electronic Structure*. Cambridge University Press, 2004. Type: Book. 2.2

[55] Robert G. Parr and Yang Weitao. *Density-Functional Theory of Atoms and Molecules*. International Series of Monographs on Chemistry. Oxford University Press, New York, 1995. 2.2.1

[56] Axel D. Becke. Perspective: Fifty years of density-functional theory in chemical physics. *The Journal of Chemical Physics*, 140(18):18A301, May 2014. Publisher: American Institute of Physics. 2.2.1

[57] A. D. Becke. Density-functional exchange-energy approximation with correct asymptotic behavior. *Physical Review A: Atomic, Molecular, and Optical Physics*, 38(6):3098–3100, September 1988. Number of pages: 0 Publisher: American Physical Society. 2.2.1

[58] John P. Perdew, J. A. Chevary, S. H. Vosko, Koblar A. Jackson, Mark R. Pederson, D. J. Singh, and Carlos Fiolhais. Atoms, molecules, solids, and surfaces: Applications of the generalized gradient approximation for exchange and correlation. *Physical Review B*, 46(11):6671–6687, September 1992. Publisher: American Physical Society. 2.2.1

[59] John P. Perdew, Kieron Burke, and Matthias Ernzerhof. Generalized Gradient Approximation Made Simple. *Phys. Rev. Lett.*, 77(18):3865–3868, 1996. Type: Journal Article. 2.2.1

[60] Jochen Heyd, Gustavo E. Scuseria, and Matthias Ernzerhof. Hybrid functionals based on a screened Coulomb potential. *J. Chem. Phys.*, 118(18):8207–8215, 2003. Type: Journal Article. 2.2.2

[61] Jochen Heyd, Juan E. Peralta, Gustavo E. Scuseria, and Richard L. Martin. Energy band gaps and lattice parameters evaluated with the Heyd-Scuseria-Ernzerhof screened hybrid functional. *J. Chem. Phys.*, 123(17):174101, 2005. Type: Journal Article. 2.2.2

[62] J. Heyd and G. E. Scuseria. Efficient hybrid density functional calculations in solids: assessment of the Heyd-Scuseria-Ernzerhof screened Coulomb hybrid functional. *J. Chem. Phys.*, 121(3):1187–1192, 2004. Type: Journal Article. 2.2.2

[63] Kanghoon Yim, Youn Yong, Joohee Lee, Kyuhyun Lee, Ho-Hyun Nahm, Jiho Yoo, Chanhee Lee, Cheol Seong Hwang, and Seungwu Han. Novel high-k dielectrics for next-generation electronic devices screened by automated ab initio calculations.

*NPG Asia Materials*, 7(6):e190–e190, June 2015. Number: 6 Publisher: Nature Publishing Group. 2.1, 2.2.2

[64] Jum Suk Jang, Hyun Gyu Kim, and Jae Sung Lee. Heterojunction semiconductors: A strategy to develop efficient photocatalytic materials for visible light water splitting. *Catal. Today*, 185(1):270–277, 2012. Type: Journal Article. 3.1, 3.1

[65] Michael G. Walter, Emily L. Warren, James R. McKone, Shannon W. Boettcher, Qixi Mi, Elizabeth A. Santori, and Nathan S. Lewis. Solar Water Splitting Cells. *Chemical Reviews*, 110(11):6446–6473, November 2010. Publisher: American Chemical Society. 3.1

[66] G. Bastard, E. E. Mendez, L. L. Chang, and L. Esaki. Exciton binding energy in quantum wells. *Physical Review B*, 26(4):1974–1979, August 1982. Publisher: American Physical Society. 3.1

[67] Kazuhiro Takanabe. Photocatalytic Water Splitting: Quantitative Approaches toward Photocatalyst by Design. *ACS Catalysis*, 7(11):8006–8022, November 2017. Publisher: American Chemical Society. 3.2

[68] B. Hammer and J. K. Nørskov. Electronic factors determining the reactivity of metal surfaces. *Surface Science*, 343(3):211–220, 1995. Type: Journal Article. 3.5.1

[69] B. Hammer and J. K. Norskov. Why gold is the noblest of all the metals. *Nature*, 376(6537):238–240, 1995. Type: Journal Article. 3.5.1

[70] K. Nørskov Jens, Frank Abild-Pedersen, Felix Studt, and Thomas Bligaard. Density functional theory in surface chemistry and catalysis. *Proceedings of the National Academy of Sciences*, 108(3):937–943, 2011. Type: Journal Article. 3.5.1

[71] Satadeep Bhattacharjee, Umesh V. Waghmare, and Seung-Cheol Lee. An improved d-band model of the catalytic activity of magnetic transition metal surfaces. *Scientific Reports*, 6(1):35916, November 2016. Number: 1 Publisher: Nature Publishing Group. 3.5.1

[72] Qing Tang and De-en Jiang. Mechanism of Hydrogen Evolution Reaction on 1T-MoS2 from First Principles. *ACS Catalysis*, 6(8):4953–4961, 2016. Type: Journal Article. 3.5.2

[73] Xiaoxin Zou and Yu Zhang. Noble metal-free hydrogen evolution catalysts for water splitting. *Chemical Society Reviews*, 44(15):5148–5180, 2015. Type: Journal Article. 3.5.2

[74] Showkat H. Mir, Sudip Chakraborty, Prakash C. Jha, John Wärnå, Himadri Soni, Prafulla K. Jha, and Rajeev Ahuja. Two-dimensional boron: Lightest catalyst for hydrogen and oxygen evolution reaction. *Applied Physics Letters*, 109(5):053903, 2016. Type: Journal Article. 3.5.2

[75] G. Kresse and J. Hafner. Ab initio molecular dynamics for liquid metals. *Physical Review B*, 47(1):558–561, January 1993. Publisher: American Physical Society. 4

[76] G. Kresse and J. Furthmüller. Efficiency of ab-initio total energy calculations for

metals and semiconductors using a plane-wave basis set. *Computational Materials Science*, 6(1):15–50, July 1996. 4

[77] G. Kresse and J. Furthmüller. Efficient iterative schemes for ab initio total-energy calculations using a plane-wave basis set. *Physical Review B*, 54(16):11169–11186, 1996. Type: Journal Article. 4

[78] G. Kresse and D. Joubert. From ultrasoft pseudopotentials to the projector augmented-wave method. *Physical Review B*, 59(3):1758–1775, 1999. Type: Journal Article. 4

[79] Michael P. Teter, Michael C. Payne, and Douglas C. Allan. Solution of Schrödinger's equation for large systems. *Physical Review B*, 40(18):12255–12263, December 1989. 4.1

[80] D. M. Bylander, Leonard Kleinman, and Seongbok Lee. Self-consistent calculations of the energy bands and bonding properties of B 12 C 3. *Physical Review B*, 42(2):1394–1403, July 1990. 4.1

[81] G. H. F. Diercksen and S. Wilson, editors. *Methods in Computational Molecular Physics*. Springer Netherlands, Dordrecht, 1983. 4.1

[82] Various Authors. NUMERICAL ALGORITHMS IN CHEMISTRY: ALGEBRAIC METHODS. REPORT ON THE WORKSHOP. August 1978. 4.1

[83] D M Wood and A Zunger. A new method for diagonalising large matrices. *Journal of Physics A: Mathematical and General*, 18(9):1343–1359, June 1985. 4.1

[84] Péter Pulay. Convergence acceleration of iterative sequences. the case of scf iteration. *Chemical Physics Letters*, 73(2):393–398, July 1980. 4.1

[85] Stefan Blügel. First principles calculations of the electronic structure of magnetic overlayers on transition metal surfaces. Technical Report FZJ-2018-02859, Kernforschungsanlage Jülich, Verlag, 1988. 4.1

[86] D. D. Johnson. Modified Broyden's method for accelerating convergence in self-consistent calculations. *Physical Review B*, 38(18):12807–12813, December 1988. 4.1

[87] Alexandr Fonari and Christopher Sutton. Effective Mass Calculator, 2012. Type: Computer Program. 4.3.3, 4.3.3, 4.3.3

[88] Milton Abramowitz and Irene A. Stegun, editors. *Handbook of Mathematical Functions: with Formulas, Graphs, and Mathematical Tables*. Dover Publications, New York, NY, 0009-revised edition edition, June 1965. 4.3.3

[89] M. Gajdoš, K. Hummer, G. Kresse, J. Furthmüller, and F. Bechstedt. Linear optical properties in the projector-augmented wave methodology. *Physical Review B*, 73(4):045112, January 2006. Publisher: American Physical Society. 4.4

[90] Vei Wang, Nan Xu, Jin Cheng Liu, Gang Tang, and Wen-Tong Geng. VASPKIT: A User-friendly Interface Facilitating High-throughput Computing and Analysis

Using VASP Code. *arXiv e-prints*, page arXiv:1908.08269, August 2019. _eprint: 1908.08269. 4.4, 4.4, 4.4, 4.5

[91] Mark Fox. Optical Properties of Solids. *American Journal of Physics*, 70(12):1269–1270, December 2002. Publisher: American Association of Physics Teachers. 4.4

[92] James C. Phillips. Energy-Band Interpolation Scheme Based on a Pseudopotential. *Physical Review*, 112(3):685–695, November 1958. Publisher: American Physical Society. 4.7

[93] M. T. Yin and Marvin L. Cohen. Theory of ab initio pseudopotential calculations. *Physical Review B*, 25(12):7403–7412, June 1982. Publisher: American Physical Society. 4.7

[94] Leonard Kleinman and D. M. Bylander. Efficacious Form for Model Pseudopotentials. *Physical Review Letters*, 48(20):1425–1428, May 1982. Publisher: American Physical Society. 4.7

[95] David Vanderbilt. Soft self-consistent pseudopotentials in a generalized eigenvalue formalism. *Physical Review B*, 41(11):7892–7895, April 1990. Publisher: American Physical Society. 4.7

[96] M. C. Payne, M. P. Teter, D. C. Allan, T. A. Arias, and J. D. Joannopoulos. Iterative minimization techniques for ab initio total-energy calculations: molecular dynamics and conjugate gradients. *Reviews of Modern Physics*, 64(4):1045–1097, October 1992. Publisher: American Physical Society. 4.2

[97] P. E. Blöchl. Projector augmented-wave method. *Physical Review B*, 50(24):17953–17979, 1994. Type: Journal Article. 4.7

[98] H. Eidsvåg, M. Rasukkannu, P. Vajeeston, and D. Velauthapillai. Bandgap engineering in CsSnxPb((1-x))I-3 and their influence on light absorption. *Materials Letters*, 218:253–256, 2018. Type: Journal Article. 5.2

[99] Håkon Eidsvåg, Murugesan Rasukkannu, Dhayalan Velauthapillai, and Ponniah Vajeeston. In-depth first-principle study on novel MoS2 polymorphs. *RSC Advances*, 11(6):3759–3769, 2021. Type: Journal Article. 5.4

# Part II

# ARTICLES

# $TiO_2$ AS A PHOTOCATALYST FOR WATER SPLITTING – AN EXPERIMENTAL AND THEORETICAL REVIEW

---

H. Eidsvåg, S. Bentouba, P. Vajeeston, S. Yohi, and D. Velauthapillai

*In Molecules MDPI*, volume 11, pages 3759-3769, 2021

molecules

MDPI

*Review*

# $TiO_2$ as a Photocatalyst for Water Splitting—An Experimental and Theoretical Review

**Håkon Eidsvåg [1,*], Said Bentouba [1], Ponniah Vajeeston [2], Shivatharsiny Yohi [3] and Dhayalan Velauthapillai [1,*]**

[1] Department of Computing, Mathematics and Physics, Western Norway University of Applied Sciences, Inndalsveien 28, Box 5063, N-5009 Bergen, Norway; Said.Bentouba@hvl.no
[2] Center for Materials Science and Nanotechnology, Department of Chemistry, University of Oslo, Box 1033 Blindern, N-0315 Oslo, Norway; ponniah.vajeeston@smn.uio.no
[3] Department of Chemistry, Faculty of Science, University of Jaffna, Sir. Pon, Ramanathan Rd, Jaffna 40000, Sri Lanka; srtharsha12@gmail.com
* Correspondence: heid@hvl.no (H.E.); dhayalan.velauthapillai@hvl.no (D.V.); Tel.: +47-980-61-444 (H.E.); +47-55-58-77-11 (D.V.)

**Abstract:** Hydrogen produced from water using photocatalysts driven by sunlight is a sustainable way to overcome the intermittency issues of solar power and provide a green alternative to fossil fuels. $TiO_2$ has been used as a photocatalyst since the 1970s due to its low cost, earth abundance, and stability. There has been a wide range of research activities in order to enhance the use of $TiO_2$ as a photocatalyst using dopants, modifying the surface, or depositing noble metals. However, the issues such as wide bandgap, high electron-hole recombination time, and a large overpotential for the hydrogen evolution reaction (HER) persist as a challenge. Here, we review state-of-the-art experimental and theoretical research on $TiO_2$ based photocatalysts and identify challenges that have to be focused on to drive the field further. We conclude with a discussion of four challenges for $TiO_2$ photocatalysts—non-standardized presentation of results, bandgap in the ultraviolet (UV) region, lack of collaboration between experimental and theoretical work, and lack of large/small scale production facilities. We also highlight the importance of combining computational modeling with experimental work to make further advances in this exciting field.

**Keywords:** $TiO_2$; water-splitting; theoretical; experimental; DFT

check for updates

**Citation:** Eidsvåg, H.; Bentouba, S.; Vajeeston, P.; Yohi, S.; Velauthapillai, D. $TiO_2$ as a Photocatalyst for Water Splitting—An Experimental and Theoretical Review. *Molecules* **2021**, *26*, 1687. https://doi.org/10.3390/molecules26061687

Academic Editor: Smagul Karazhanov

Received: 2 February 2021
Accepted: 10 March 2021
Published: 17 March 2021

## 1. Introduction

Over the last years, there has been a steadily increasing focus on clean, renewable energy sources as a priority to hinder the irreversible climate change the world is facing and to meet the continuously growing energy demand [1]. One hour of solar energy can satisfy the energy consumption of the whole world for a year [2]. Hence, direct harvesting of solar light and its conversion into electrical energy with photovoltaic cells or chemical energy by photoelectrochemical reactions are the most relevant technologies to overcome this challenge. Conventionally, both technologies rely on the collection of light in semiconductor materials with appropriate bandgaps matching the solar spectrum, and thus providing a high-energy conversion efficiency.

Unfortunately, the technology has drawbacks, which prevent it from overtaking non-renewable energy as the main energy source. A major issue is the uneven power distribution caused by varying solar radiation and a lack of proper storage alternatives. As a solution to this problem, the focus is moving toward research on storage options for the produced electricity, which we can divide into mechanical and electrochemical storage systems. For example, in Oceania, pumped hydroelectricity (mechanical) is the most common storage system for excess electricity [3]. Different batteries (lithium–ion, sodium–sulfur (S), vanadium, etc.), hydrogen fuel cells, and supercapacitors are the current focus areas for electrochemical storage [3]. There are several reasons for choosing hydrogen as a way to store solar energy, namely, (1) there is a high abundance of hydrogen from renewable sources; (2) it is eco-friendly when used; (3) hydrogen has a high-energy yield, and (4) it is easy to store as either a gas or a liquid [4–6].

The high energy yield and ease of storage make hydrogen viable as fuel for the long transport sector; airplanes, cruise ships, trailers, and cargo ships [7,8]. The realization of a green energy shipping fleet could alone yearly cut 2.5% of global greenhouse emissions (GHG) [9]. However, to succeed in this strategy, hydrogen must be produced in a clean and renewable way.

As water splitting got the attention of the researchers in the 1970s, titanium dioxide became the most prominent photocatalyst used [10]. There are several good reasons for this: low cost, chemical stability, earth abundance, and nontoxicity [11]. However, $TiO_2$ also sports a wide bandgap (3.0–3.2 eV), which reduces the potential for absorption of visible light [11]. Due to $TiO_2$s structural and chemical properties, it is possible to engineer the bandgap, light absorption properties, recombination time, etc. by increasing the active sites and improving the electrical conductivity [12]. $TiO_2$ exists in several different polymorphs that all behave differently. The most common ones are rutile, brookite, and anatase as shown in Figure 1. Rutile and anatase $TiO_2$ are the most used polymorphs for photocatalytic water splitting; nevertheless, some attempts with amorphous $TiO_2$ ($aTiO_2$) have been made as shown in Figure 2.

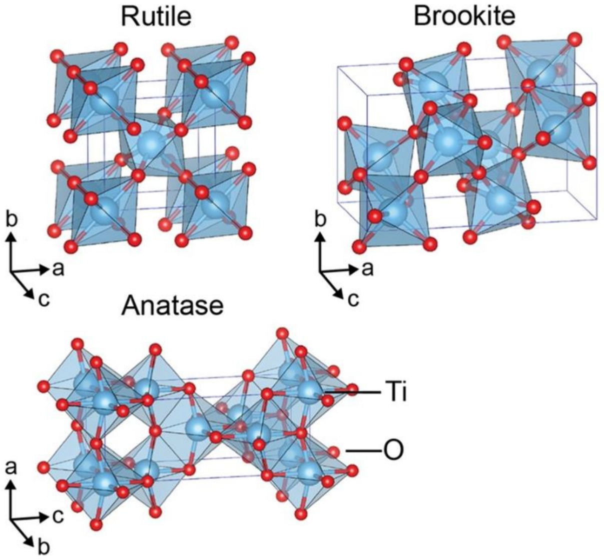

**Figure 1.** Crystal structures of $TiO_2$ rutile (tetragonal, P42/mmm), brookite (orthorhombic, Pbca), and anatase (tetragonal, I41/amd) polymorphs. Reused with permission from [13].

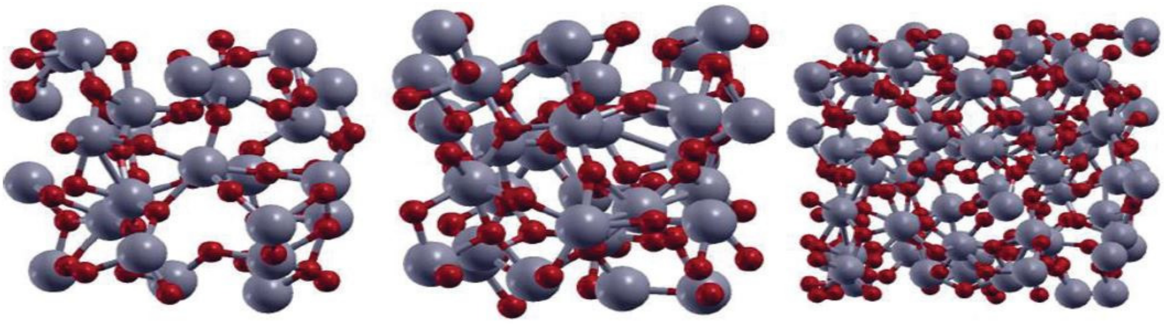

**Figure 2.** The structure of 72-atom (**left**), 96-atom (**middle**), and 216-atoms (**right**) models of amorphous $TiO_2$. The red and grey spheres represent O and Ti atoms respectively. Reused with permission from [14]. Copyright 2012, with permission from Elsevier.

Several attempts have been made to introduce dopants to improve the optical absorption of $TiO_2$. For example, Zhang et al. found that 12.5% copper (Cu)-doped anatase $TiO_2$ showed a broader absorption peak than pure anatase titanium dioxide [15]. Through a theoretical study, they found that Cu introduces an unoccupied impurity continuum band at the top of the valence band, which explains the improved optical absorption. Another theoretical study, conducted by Morgade and Cabeza in 2017, shows that co-doping of $TiO_2$ with (Pt, V) and (C, N) narrows the bandgap and favorably modifies the position of the valence and conduction band edges [16]. Our study will provide an insight into current theoretical and computational studies carried out on water splitting using either pure or doped $TiO_2$ semiconductors. In addition, we will compare it with the state of art experimental studies conducted within the field. Our aim is to help bridge the gap between theoretical simulations and experimental research. The two approaches complement each other and when combined could support the field moving forward toward the realization of the hydrogen economy. The theoretical study allows testing of the properties of thousands of different materials with different parameters to gain an understanding of how and why certain dopants and material combinations work. However, the computational models are worked out using perturbation theory, which lowers the overall accuracy of the results. At the same time, an experimental study is important to verify the theoretical results and find the best methods to synthesize the materials in practice.

## 2. Solar-Driven Hydrogen Production

Most of the commercial production of hydrogen stems from four sources: natural gas, coal, oil, and electrolysis. Of these, steam reforming alone stands for 48% of the world's hydrogen production, while coal contributes 18%, oil 30%, and electrolysis 4% [17]. The first three hydrogen production processes are energy-consuming and use non-renewable energy sources, which is unattractive for environment protection and climate change [18,19]. However, the production of hydrogen by electrolysis requires only water and electrical current. To have green hydrogen, produced friendly to the environment, we propose to use renewable energy sources—wind, hydro, and solar power—to produce the electric current needed for the electrolysis of water. Solar power is ideal due to the high amount of incoming energy. There are several functional methods used in driving the electrolysis process, i.e., thermochemical water splitting [20], photo-biological water splitting [21], and photocatalytic water splitting [22]. Furthermore, photocatalytic water splitting (PWS) is considered the best option, due to the following reasons: (1) PWS has a good solar-hydrogen conversion efficiency, (2) it has a low production cost, (3) oxygen and hydrogen can easily be separated during the PWS process, and (4) hydrogen electrolysis could be used on both small- and large-scale facilities [4,22,23].

### *2.1. Photocatalytic Water Splitting (PWS)*

The photocatalytic process splits water ($H_2O$) into hydrogen ($H_2$) and oxygen ($O_2$) in the presence of a catalyst and natural light; it is an artificial photosynthesis method. Figure 3 shows a schematic illustration of the major steps involved in the process of photocatalytic water splitting. In the first step (1), electron–hole pairs are generated in the presence of irradiation. This is carried out by utilizing the semiconducting nature of the photocatalyst to excite electrons from the valence band (VB) to the conduction band (CB). Photons with energies larger than the bandgap can excite electrons from the VB to the CB. The second step (2) consists of charge separation and migration of the photogenerated electron-hole pairs. Ideally, all electrons and holes reach the surface without recombination to maximize the efficiency of the photocatalyst. In the final step (3), the electrons, which move from the CB to the surface of the catalyst participate in a reduction reaction and generate hydrogen, and the holes diffuse from the VB to the surface of the photocatalyst involved in an oxidation reaction to form oxygen. In general, the efficiency of the catalyst can be enhanced by including dopants or co-catalysts that include metals or metal oxides, such as Pt, NiO, and $RuO_2$, which can act as the active sites via enhancing electron mobility.

The redox and oxidations reactions on the surface of the photocatalyst are described by the following equations [24]:

$$\text{Oxidation}: \ H_2O + 2h^+ \rightarrow 2H^+ + \tfrac{1}{2}O_2. \quad (1)$$

$$\text{Reduction}: \ 2H^+ + 2e^- \rightarrow H_2. \quad (2)$$

$$\text{Overall reaction}: \ H_2O + 1.23\ \text{eV} \rightarrow H_2 + \tfrac{1}{2}O_2. \quad (3)$$

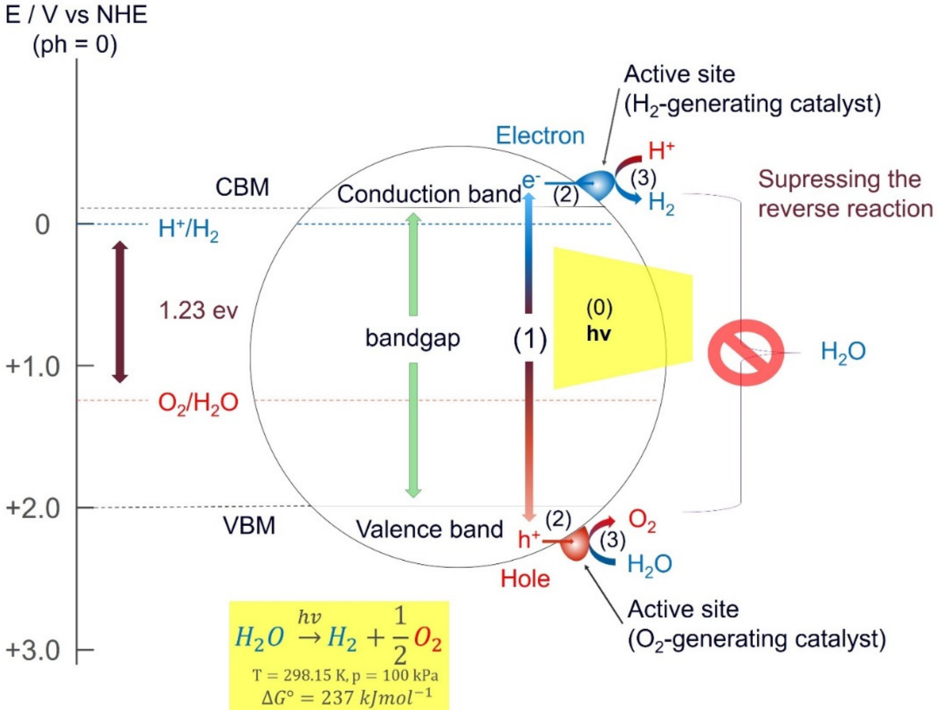

**Figure 3.** Schematic illustration of the main photocatalytic steps for a semiconductor photocatalyst: (1) light is absorbed to generate electron–hole pairs; (2) migration of excited carriers (electrons and holes) to the surface; (3) surface reaction to produce hydrogen with electrons and oxygen with holes. Reproduced with permission from [25], Copyright 2013, with permission from Elsevier.

The process of water splitting is highly endothermic and requires a Gibbs free energy of 1.23 eV per electron, which corresponds to light with a wavelength of 1008 nm. This means that the photocatalyst must have a bandgap > 1.23 eV, or else the electrons will not have enough energy to start the reaction. In practice, this limit should be 1.6 eV to 1.8 eV due to some overpotentials [24]. Naturally, it should not be too high either, as that would reduce the amount of visible light the photocatalyst can absorb. This means that it is important to find suitable catalysts with a bandgap between 1.6–2.2 eV to ensure maximum absorption of the incoming light. Another important factor regarding the efficiency of a photocatalyst is the recombination time, i.e., the time it takes for an electron to recombine with a hole. If recombination occurs before the electrons can reach the surface and interact with the water molecules, the energy gets wasted and no redox reaction takes place. Unfortunately, there are only a few materials with sufficient recombination time and a satisfactory bandgap that have been identified. However, a recent study by Takata et. al. demonstrates that it is possible to achieve water splitting without any charge recombination losses [26]. With $SrTiO_3$ as the photocatalyst loaded with Rh, Cr, and Co as cocatalysts, they achieved an external quantum efficiency up to 96% at wavelengths between 350 nm and 360 nm [26]. This is equivalent to having an internal quantum efficiency of almost unity. The requirements for having an efficient photocatalyst can be summarized in the solar–hydrogen conversion efficiency (STH) equation [27] as follows:

$$\eta_{STH} = \eta_A \times \eta_{CS} \times \eta_{CT} \times \eta_{CR}. \tag{4}$$

The STH conversion efficiency depends on (1) the efficiencies of light absorption ($\eta_A$), (2) charge separation ($\eta_{CS}$), (3) charge transport ($\eta_{CT}$), and (4) charge collection/reaction efficiency ($\eta_{CR}$). The efficiency of the photocatalyst depends on several factors and they are elaborated in the following section.

### 2.2. Important Aspects of Photocatalytic Efficiency for Nanomaterials

There are several ways to improve and modify the fundamental properties of a photocatalyst by focusing on its shape, size, order, uniformity, and morphology.

#### 2.2.1. Crystallinity

Research has shown that the crystallinity of the material affects its optoelectronic properties [28,29]. Structures with a high crystallinity perform better than amorphous variations of the same material. The increase in crystallinity reduces the number of defects in the structures and thus decreases the electron-hole recombination sites, which leads to a better catalytic activity [30–33]. Liu et al. studied the effect of crystalline $TiO_2$ nanotubes against that of amorphous $TiO_2$ nanotubes and found that better photocurrent properties were attained with the crystalline structures due to the lower amount of electron-hole recombination [34]. In another study, enhanced hydrogen production was obtained using extremely ordered nanotubular $TiO_2$ arrays [35].

#### 2.2.2. Dimensionality

Nanomaterials can be classified into four different categories depending on their dimensionality—zero-dimensional (0D), one-dimensional (1D), two-dimensional (2D), and three-dimensional (3D) [36,37]. Zero-dimensional (0D) nanostructures used in PWS are primarily quantum dots (QDs) and hollow shells. In general, QDs are used to decorate the photocatalyst because they increase the visible light absorption and reduce the electron-hole recombination [38–40]. One-dimensional (1D) structures include nanorods, nanotubes, and nanowires, which are all attractive for photocatalysts. It is found that nanorod and nanowire arrays result in a more efficient photogenerated electron transport and collection [41–43]. On the other hand, nanotubes have a higher surface area for redox reactions compared to nanorods or nanowires although they have less material for light absorption [44,45]. Two-dimensional (2D) nanostructures have a high surface area and a small thickness that reduces the travel distance for generated holes. This results in efficient light harvesting. Lastly, 3D nanostructures are promising candidates for PWS because they can be designed into high-performance photoanodes [27]. In general, it is possible to design and create nanostructures that cater to specific tasks.

#### 2.2.3. Temperature and Pressure

Temperature and pressure during the production phase will affect the resulting properties of a photocatalyst. Research shows that by varying the pressure, the STH performance of the catalyst will change [46]. Another research group found that by using a low-temperature thermal treatment process the charge transfer resistance could be reduced [47].

#### 2.2.4. Size

As mentioned $TiO_2$ exist in three phases, anatase (tetragonal; a = 3.7845 Å; c = 9.5143 Å), rutile (tetragonal; a = 4.5937 Å; c = 2.9587 Å), and brookite (orthorhombic; a = 5.4558 Å; b = 9.1819 Å; c = 5.1429 Å). Among the three different crystalline phases of $TiO_2$, anatase exhibits the highest stability for particle size less than 11 nm, whereas rutile shows thermodynamic stability for particle size greater than 35 nm, and brookite is stable in the size range of 11–35 nm. The size of the nanomaterials and cocatalyst can alter the overall performance of the system. Smaller particles are dominated by electrokinetics and are thus more suited for photocatalysis. Alternatively, larger particles are better suited for photoelectrochemical (PEC) water splitting because they have a lower electron–hole recombination rate [48]. The size of the particles also influences the electron-hole recombination time. In larger particles the travel distance to the active sites on the surface becomes longer, thus increasing the probability for electron-hole recombination. This probability is decreased in smaller particles due to the shorter migration distance [49,50].

#### 2.2.5. Bandgap

The bandgap is one of the most important properties of the photocatalyst. It is defined as the energy needed for an electron to move from the valence band maximum (VBM) to the conduction band minimum (CBM) in a semiconductor. In addition to a fitting bandgap, the CBM must be more negative than the redox potential of $H^+/H_2$ (0 V vs. normal hydrogen electrode (NHE)), while the VBM must be more positive than the redox potential of $O_2/H_2O$ (1.23 V). Therefore, the theoretical minimum bandgap for water splitting is 1.23 eV. Nanomaterials are used to tune the band positions and the bandgap toward the appropriate range of 1.6 eV to 2.2 eV [51–53].

#### 2.2.6. pH Dependency

The pH value of the solution in which the photocatalyst is placed affects the end STH efficiency [54]. It will similarly affect the stability and lifetime of the catalyst. Photoelectrochemical water splitting is very dependent on the pH of the electrolyte solution, which determines the net total charge adsorbed at the surface of the catalyst. The migration of ions during the reactions may weaken the surface of the electrode. The electrode incorporated with nanomaterials exhibits better stability in different pH conditions, however, it was evident that the stability was further improved when the solution is buffered [55–57].

#### 2.2.7. Light

It is important that the light source be specified, as semiconductors doped with nanomaterials can absorb both infrared and UV light in addition to visible light [58].

### *2.3. Theoretical Methods*

Numerical studies of electronic, optical and mechanical characterization of $TiO_2$ polymorphs are performed as ab initio calculations within the framework of density functional theory (DFT). However, the calculation model and details vary between the researchers depending on the calculation tool/code chosen; for example, Vienna ab initio simulation package (VASP) [59–64], CASTEP [65], CRYSTAL [66,67], and GPAW [68]. In general, the interaction between the core and the valence electrons is described by the projector augmented-wave method [69,70]. The electron properties are calculated by $G_0W_0$ [71,72], HSE06 [73,74], or by the generalized gradient approximation (GGA, which is less accurate but faster) [75]. It is possible to calculate the stress tensor by applying a set of strains to the crystal, which leads to the elastic constants (e.g., VASPKIT [76]). Moreover, it is possible to calculate the real space force constants of the supercell, and then to evaluate this with appropriate software (e.g., Phonopy [77]) in order to find the phonon frequencies for dynamical stability, heat capacity, free energy, and entropy analysis.

### *2.4. Experimental Methods*

Several synthesis methods are used for the synthesis of $TiO_2$ materials depending on the end application and experiment performed. The methods can roughly be divided into thermal reactions, deposition methods, sol–gel, Micelle, and electromagnetic methods. In general, the thermal methods are heterogeneous reactions in the presence of aqueous solvents or mineralizers under high pressure and temperature [78–80]. Deposition methods (e.g., chemical vapor deposition and electrodeposition) are primarily used to create thin-film materials or coatings on a substrate [81–83]. Sol–gel methods utilize the conversion of a liquid solution (sol) into a solid gel phase, in which the nanoparticles are formed by hydrolysis and condensation [78,84]. Micelles are the long-chain molecules made by surfactants, which contain a hydrophilic head and a hydrophobic chain. Self-assembling of these amphiphilic molecules forms an organized structure in solution [85]. The ultrasound technique can be used for preparations of a wide range of nanomaterials, especially high-surface-area transition metals, carbides, oxides, alloys, and colloids [84,86]. However, if the goal is to create a dielectric material, then the microwave method can be used [78,87].

## 3. Theoretical Research

The amount of theoretical and computational research has increased over the last years due to improved accuracy of the models and increased computing power. As with experimental work, most of the focus is on various dopants for $TiO_2$. The majority of research is conducted on anatase because that phase seems most promising for water splitting. However, rutile $TiO_2$ does have some interesting properties.

### *3.1. Metal Dopants*

A large part of the conducted research is devoted to metal dopants and their contribution to a broadened bandgap of photocatalyst $TiO_2$. In a comprehensive study, Pan et al. investigated how noble metals could enhance the catalytic activity of anatase $TiO_2$ for hydrogen evolution reaction [88]. They proposed three different structural models for hydrogenated anatase $TiO_2$, as seen in Figure 4, and proposed the preferred location (H1 in Figure 4a) of the hydrogen atom when $TiO_2$ was noble metal doped. This is because of the strongly localized hybridization between hydrogen and $TiO_2$ [88]. Based on these findings, they showed that anatase $TiO_2$ was easy to hydrogenate, and the introduced hydrogen could improve the electronic transport between the conduction band and valence band near the Fermi level [88]. In general, silver (Ag)- and gold (Au)-doping are more thermodynamically stable than that of platinum (Pt)-, palladium (Pd)- and ruthenium (Ru)-doping. The band structures for noble metal-doped $TiO_2$ are shown in Figure 5, and it is clearly seen that the introduction of dopants reduces the bandgap of $TiO_2$. However, Ag-doping seems to be the best option for noble metal doping of $TiO_2$ as the other dopants reduce the bandgap below 1.23 eV [88].

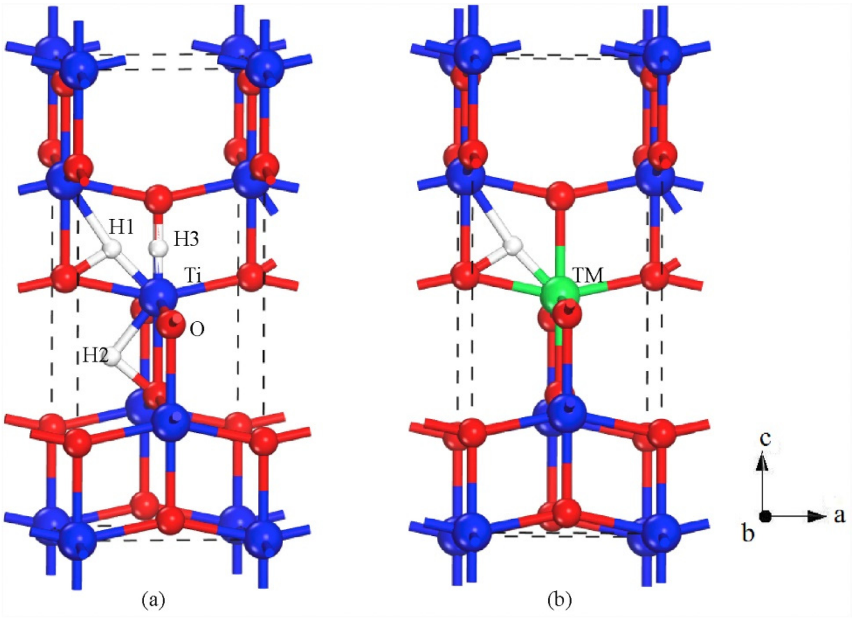

**Figure 4.** Structural model for (**a**) possible locations of H dopants and (**b**) hydrogenated noble-metal doped $TiO_2$. Reprinted with permission from [88]. Copyright 2018, with permission from Elsevier.

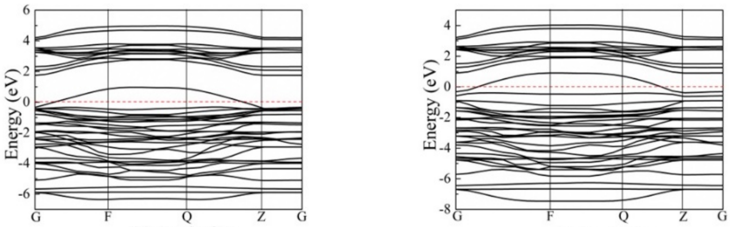

(a) Ag-doping (b) Au-doping

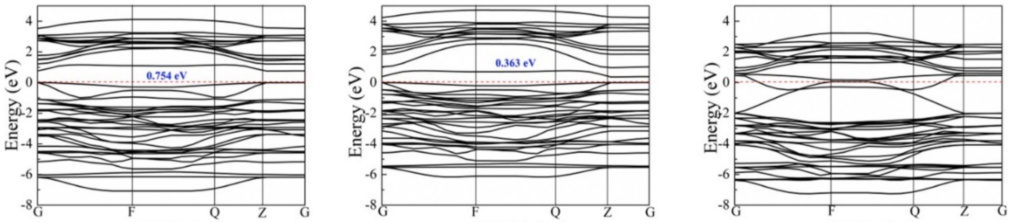

(c) Pt-doping (d) Pd-doping (e) Ru-doping

**Figure 5.** Calculated band structure, using generalized gradient approximation (GGA) with Perdew-Burke-Ernzerhof (PBE) exchange-energy, in the Brillouin zone for, (**a**) Ag-doping, (**b**) Au-doping, (**c**) Pt-doping, (**d**) Pd-doping, and (**e**) Ru-doping. Reprinted with permission from [88]. Copyright 2018, with permission from Elsevier.

Y. Zhang et al. doped (001) anatase $TiO_2$ with Pt, cobalt (Co), and Ru [89], which led to surface-localized states that enhanced the electron transfer at the surface. However, another study by S.T Zhang et al. showed that to achieve a stable interface between supported $Ru_n$ ($n$ = 1–10, 20, 22) clusters and $TiO_2$, $n > 6$ was needed [90]. Interestingly enough, this is among the preferred geometries for $TiO_2$ [90].

Metal dopants decrease the bandgap, and as shown by Jin et al., Pt, Pd, rodhium (Rh), and Ru single atom doping significantly reduces the work function of the compound [91].

Another option to increase the optical absorption is to use iron (Fe) or nickel (Ni) as dopants because they will induce impurity states in the forbidden region [92]. Electrons with energy less than the bandgap can use these impurity states as steps when moving from the valence band to the conduction band. Especially co-doping of $TiO_2$ with Fe and Ni results in higher absorption and reduced electron–hole recombination according to Lin et al. [92]. Ghuman et al. also showed that $Fe^{2+}$ doped a$TiO_2$ adsorbs water better than pristine a$TiO_2$ and that it also has a better photocatalytic effect [93].

Introducing Cu and/or N dopants will also create isolated states in the bandgap, and therefore, $TiO_2$ doped with these dopants function better than pure anatase $TiO_2$ [94]. Assadi et al. showed that the improved photocatalytic activity in Cu/$TiO_2$ was because of effective bandgap narrowing and increased charge transfer (electronic interactions) and not surface chemistry [95]. Wei Zhang et al. found that the stability of Cu doped $TiO_2$ depends on which oxygen atoms that is replaced with Cu atoms. [15] They observed a blueshift in absorption for anatase $TiO_2$ (101) compared to bulk $TiO_2$, while in Cu-doped bulk anatase $TiO_2$ they observed a redshift in optical absorption [15]. Co-doped $SrTiO_3$ has a narrower bandgap compared to that of pure $TiO_2$ according to Sikam et al. and this is due to states being formed in the gap [96]. In addition, they also found that co-doping resulted in magnetism due to inequality of spin down and spin up states [96]. Ghuman et al. looked into the difference between monodoping and co-doping using nitrogen (N) and niobium (Nb) on amorphous $TiO_2$ [97]. They found that monodoping reduces the bandgap but it also increases the number of recombination centers [97]. Charge compensated co-doping, on the other hand, reduces the bandgap with 0.4 eV and suppresses the recombination effect by eliminating band gap states [97]. S and Nb co-doping of anatase $TiO_2$ resulted in a bandgap of 2.15 eV as shown by Ren et al. [98].

However, not all states in the bandgap are appreciated; Gao et al. looked into how Mg doping could reduce the shallow defect states under the CBM in $TiO_2$, increasing the photocatalytic effect [99].

Although several different dopants have been proposed and tested, not all of them are viable to be incorporated into $TiO_2$. Chen et al. used cerium (Ce), praseodymium (Pr), europium (Eu), and gadolinium (Gd) dopants to see how they would incorporate with $TiO_2$ [100]. They found that Ce was the easiest among these, while Pr and Gd had low substitutional energy and should be able to be incorporated into $TiO_2$ [100]. Eu on the other hand was difficult to incorporate with $TiO_2$ [100]. Ce, Pr, and Eu monodoping should move the light absorption more toward/into the visible light region [100]. Another approach when using lanthanides could be ion triple doping as showcased by Li et al. [101]. Through co- and triple-doping they improved the oxidizing ability, light absorption, and charge carrier separation of their photocatalyst ($Bi_2MoO_6$) [101].

### *3.2. Non-Metal Dopants*

In an attempt to find non-metal dopant alternatives Shi et al. co-doped anatase $TiO_2$ with C and neodymium (Nd) and found tuned band gaps, which were lower than that of pure $TiO_2$: C@O and Nd@Ti, 2.372 Ev, and carbon (C) and Nd @ $TiO_2$, 2.850 eV [102]. The main function of the C and Nd dopants is to enhance the intensity of light absorption and to extend the optical absorption range into the visible light region respectively. This is clearly seen from Figure 6, in which the optical absorption spectra of $TiO_2$ do not extend into the visible light region, while both C doping and C and Nd doping extend the absorption range into the visible light region and effectively enhancing the efficiency of the photocatalysts. Experimental studies shown in Figure 6c confirmed these findings. By using graphite carbon spheres on $TiO_2$ Jiang et al. introduced isolated energy levels between the VBM and the CBM [103]. These intermediate bandgaps increase the number of electrons that could be excited from the VB to the CB.

Gurkan et al. found that selenium (Se) doping introduces localized mid-gap levels that increase the visible light photocatalytic effect [104]. However, no significant change in the position of the band edges was observed. A study by Zhao et al. showed that N, Co, Co–N, Co–2N, and Co–3N dopants all increased the optical absorption rate compared to that of undoped $TiO_2$ [105]. Unfortunately, Co–N and Co–3N shift the CBM below the $H^+/H_2$ reduction potential, which means that it is not useful for water splitting [105]. Pengfei Wang et al. revealed that carbonate could be incorporated into mesoporous $TiO_2$ and significantly improve the visible light hydrogen evolution [106]. In addition, the intimate homo-junctions between anatase and rutile phases and graphite carbon on the surface of $TiO_2$ can significantly help promote the separation of charge carriers [106].

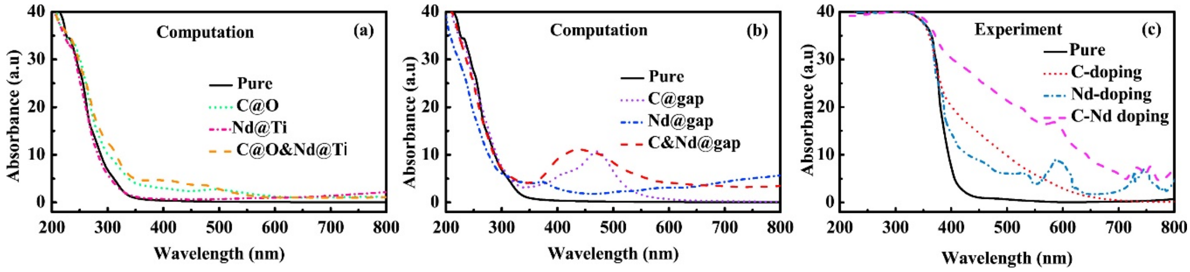

**Figure 6.** Theoretical and experimental optical absorption spectra for pure and doped $TiO_2$ structures. (**a**) Computational obtained spectra for substitutional doping, (**b**) computational obtained spectra for $TiO_2$ doped with the dopants at different interstitial sites, and (**c**) experimental obtained optical absorption spectra for C, Nd, and C+Nd doped $TiO_2$ from [107]. Reprinted with permission from [102]. Copyright 2017, with permission from Elsevier.

In an attempt to decrease the bandgap of $TiO_2$, Zongyan et al. used boron (B), C, N, fluorine (F), phosphorus (P), S, and chlorine (Cl) as dopants on anatase $TiO_2$ [108]. The tuned bandgaps for $TiO_2$ with the dopants (B, C, N, P and S) were 2.72 eV, 2.44 eV, 2.74 eV, 2.38 eV, and 2.59 eV, respectively [108]. The improvements are due to new impurity energy levels, which red-shift their fundamental absorption edges to the visible light region [108].

In addition, they found that higher dipole moments could lead to easier separation of the photoexcited electron-hole pairs, which would increase the photocatalytic effect [108].

There has been some research on $TiO_2/g–C_3N_4$ heterostructure photocatalysts. For example, Yali Zhao et al. co-doped $TiO_2/g–C_3N_4$ with Cu and N [109]. This resulted in an obvious narrowing of the bandgap compared with pure $TiO_2$, co-doping induces impurity states of N 2p and hybridized states of Cu 3d and N 2p in the bandgap of $TiO_2/g–C_3N_4$ [109]. Yanming Lin et al. used $TiO_2/g–C_3N_4$ heterostructure through interfacial coupling for $H_2$ production. The calculated band gap was significantly reduced compared to pure $TiO_2$ [110]. $TiO_2/g–C_3N_4$ heterostructure also has a higher CBM energy, which provides the photoexcited electrons with stronger reducing power to produce more hydrogen per unit time compared with $TiO_2$ [110].

### 3.3. Rutile

Although most researchers focus on anatase $TiO_2$, there has been some development on rutile $TiO_2$ as well. Atanelov et al. doped rutile $TiO_2$ with C and it seems to have worse photocatalytic performances than pure $TiO_2$, this is due to C–O dimes creating mid-band states [111]. However, N doped rutile $TiO_2$ introduced no mid-bandgap states [111]. Ghuman et al. used Rh to dope rutile $TiO_2$ and found that it had a lower bandgap but with more recombination centers [112]. By using Rh–Nb (charge compensated doping) as co-dopants on rutile $TiO_2$, they obtained no isolated bandgap states that might act as a recombination center [112]. Moreover, the bandgap was decreased by 0.5 eV, which makes it a better photocatalyst [112].

### 3.4. Nanotubes

Research on different $TiO_2$ nanostructures has led to some interesting results. Lisovski et al. doped $TiO_2$ nanotubes with sulfur and achieved a narrower bandgap compared to that of pure $TiO_2$ [113]. The band edges were also close to the limits for efficient water splitting [113]. In another article, Lisovski et al. present nitrogen (N), S, and S-and-N doping of six-layer (101) anatase $TiO_2$ nanotubes [114]. They found that monodoping with N or S reduces the photocatalytic effect of the nanotubes [114]. However, co-doping with N and S could improve the photocatalytic activity, although it depends on the defect concentration [114]. Dmitry Bocharov et al. used $TiO_2$ (4,4) nanotubes doped with scandium (Sc), depicted in Figure 7, and found that they were a good candidate with a bandgap of 1.8–1.9 eV [115]. Working on the same variation of nanotubes, E.P. D'yachkov et al. found that doping with Nb, molybdenum (Mo), technetium (Tc), and Pd leads to bandgaps around 2 eV [116]. This is a significant decrease from around 4 eV for undoped (4,4) $TiO_2$ nanotubes [116]. Lisovski et al. also investigated if the arrangement of bandgap edges would change when going from bulk to nanotubes. They found that this only happened if the diameter of the nanotubes was small, i.e., the internal strain was extremely large [117].

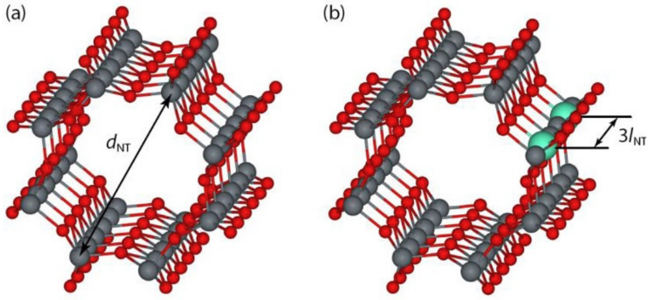

**Figure 7.** Structural models of non-optimized (**a**) pristine and (**b**) doped armchair type (4,4) fluorite-structured $TiO_2$ nanotubes. The red balls represent O, grey balls are $TiO_2$, and the turquoise balls represent the 3d-metal dopants substituted for Ti atoms. The nanotube diameter ($d_{nt}$) is 0.84 nm and the dopant concentration is considered to be 4.17%. Reprinted with permission from [115]. Copyright 2017, with permission from Elsevier.

### 3.5. Pure $TiO_2$

Naturally, some focus had been on pure $TiO_2$ and its different states, looking into which one was most suited for photocatalytic activity.

Ma et al. found that the (101) facet had higher activity compared to other facets of $TiO_2$ [118], which was an important breakthrough. If we have pristine conditions and water molecules, water splitting can be expected both with rutile and anatase $TiO_2$ according to Deak et al. [119]. This is generally not the case because the surface will contain bridging $OH^+$ and the terminal $OH^-$ (dissociated water). In these conditions, anatase $TiO_2$ is the best for water splitting [119]. However, by increasing the $OH^+/OH^-$ ratio, one can increase the driving force for water splitting [119]. Hanaor et al. [120] looked into the phase stability of anatase and rutile $TiO_2$, with and without doping. Pure $TiO_2$ has a more stable rutile phase than anatase and the transformation from anatase $TiO_2$ to rutile $TiO_2$ is irreversible [120]. F, Si, Fe, and Al as dopants work as inhibitors for the transformation process, and they slow down the process from anatase to rutile [120]. Alghamdi et al. report no sign of overlapping HOMO levels between $H_2O_2$ and $TiO_2$ rutile (110) surface; this in addition to the high adsorption energy could explain why water splitting is slow [121].

### 3.6. Collected Data

In Table 1 we have tabulated the bandgap, photocurrent density, hydrogen, and oxygen production rate from the articles discussed in this section.

**Table 1.** This table displays the theoretical bandgap values for different doped $TiO_2$ materials and for a few of these the $H_2$ production rate is presented if published.

| Nanomaterial | Bandgap [eV] | Ref. |
|---|---|---|
| Ag doped $TiO_2$ | 2.312 | [88] |
| Au doped $TiO_2$ | 0.996 | [88] |
| Pt doped $TiO_2$ | 0.754 | [88] |
| Pd doped $TiO_2$ | 0.363 | [88] |
| Ru doped $TiO_2$ | 0.176 | [88] |
| Wet $TiO_2$ (001) | 1.8571 | [89] |
| Pt doped Wet $TiO_2$ (001) | 1.4546 | [89] |
| Ru doped Wet $TiO_2$ (001) | 0.1636 | [89] |
| Co doped Wet $TiO_2$ (001) | 0.0539 | [89] |
| Ru clusters on $TiO_2$ | NA | [90] |
| Anatase $TiO_2$ | 3.05 | [91] |
| Pt adsorbed on $TiO_2$ | 3.06 | [91] |
| Pd adsorbed on $TiO_2$ | 3.05 | [91] |
| Rh adsorbed on $TiO_2$ | 2.80 | [91] |
| Ru adsorbed on $TiO_2$ | 3.10 | [91] |
| Anatase $TiO_2$ | 2.98 | [92] |
| Rutile $TiO_2$ | 2.78 | [92] |
| a$TiO_2$ | NA | [93] |
| Cu + N co-doped $TiO_2$ | NA | [94] |
| Cu doped anatase $TiO_2$ (101) | NA | [95] |
| Cu doped anatase $TiO_2$ (101) | NA | [15] |
| Co-doped $SrTiO_3$ | 3.07 | [96] |
| N-doped a$TiO_2$ | 2.25 | [97] |

**Table 1.** *Cont.*

| Nanomaterial | Bandgap [eV] | Ref. |
|---|---|---|
| S-doped anatase $TiO_2$ | 2.33 | [98] |
| Nb-doped anatase $TiO_2$ | 2.25 | [98] |
| (S, Nb)-doped anatase $TiO_2$ | 2.15 | [98] |
| $TiO_2$ hollow spheres doped with Mg | NA ($H_2$ production rate: 850 µmol/h/g. $O_2$ production rate: 425 µmol/h/g) | [99] |
| $TiO_2$ doped by lanthanides | NA | [100] |
| C@O-doped $TiO_2$ | 3.019 | [102] |
| C@gap-doped $TiO_2$ | 3.021 | [102] |
| Nd@Ti-doped $TiO_2$ | 3.032 | [102] |
| Nd@gap-doped $TiO_2$ | 2.353 | [102] |
| C@O&Nd@Ti-doped $TiO_2$ | 2.372 | [102] |
| C&Nd@gap-doped $TiO_2$ | 2.850 | [102] |
| $TiO_{2\text{-}X}$ | 2.6 ($H_2$ production rate: 46.9 µmol/h/g) | [103] |
| g-CS@$TiO_{2\text{-}X}$ | 2.5 ($H_2$ production rate: 255.2 µmol/h/g) | [103] |
| g-CS+$TiO_{2\text{-}X}$ | 2.3 ($H_2$ production rate: 68.3 µmol/h/g) | [103] |
| Se(IV) ion doped $TiO_2$ | 2.85 | [104] |
| N-doped $TiO_2$ | 3.06 | [105] |
| Co-doped $TiO_2$ | 2.92 | [105] |
| Co-1N-doped $TiO_2$ | 2.91 | [105] |
| Co-2N-doped $TiO_2$ | 2.90 | [105] |
| Co-3N-doped $TiO_2$ | 2.92 | [105] |
| Mesoporous carbonate-doped phase-junction $TiO_2$ nanotubes | 2.69-2.92 ($H_2$ production rate: 6108 µmol/h/g) | [106] |
| B-doped $TiO_2$ | 2.40 | [108] |
| S-doped $TiO_2$ | 2.23 | [108] |
| C-doped $TiO_2$ | 2.53 | [108] |
| P-doped $TiO_2$ | 2.30 | [108] |
| N-doped $TiO_2$ | 2.51 | [108] |
| F-doped $TiO_2$ | 2.61 | [108] |
| Cl-doped $TiO_2$ | 2.34 | [108] |
| N-$TiO_2$ | 2.94 | [109] |
| Cu-$TiO_2$ | 3.22 | [109] |
| (Cu, N)-$TiO_2$ | 2.96 | [109] |
| $TiO_2$/g-$C_3N_4$ | 2.34 | [109] |
| N-$TiO_2$/g-$C_3N_4$ | 2.31 | [109] |
| Cu-$TiO_2$/g-$C_3N_4$ | 2.23 | [109] |
| (Cu, N)-$TiO_2$/g-$C_3N_4$ | 2.26 | [109] |
| g-$C_3N_4$/$TiO_2$ | 2.21 | [110] |
| (C, N)-doped rutile $TiO_2$ | 2.59 | [111] |
| Rh, Nb co-doped $TiO_2$ | NA | [112] |

**Table 1.** *Cont.*

| Nanomaterial | Bandgap [eV] | Ref. |
|---|---|---|
| S, N, or S+N doped $TiO_2$ anatase (101) nanotubes | 2.78–4.32 | [113] |
| S-doped $TiO_2$ | 2.72 | [114] |
| Sc-doped three-layer fluorite structured $TiO_2$ | 4.00 | [115] |
| V-doped three-layer fluorite structured $TiO_2$ | 3.95 | [115] |
| Cr-doped three-layer fluorite structured $TiO_2$ | 3.98 | [115] |
| Mn-doped three-layer fluorite structured $TiO_2$ | 3.66 | [115] |
| Fe-doped three-layer fluorite structured $TiO_2$ | 3.39 | [115] |
| Co-doped three-layer fluorite structured $TiO_2$ | 4.01 | [115] |
| Ni-doped three-layer fluorite structured $TiO_2$ | 4.20 | [115] |
| Cu-doped three-layer fluorite structured $TiO_2$ | 4.20 | [115] |
| Zn-doped three-layer fluorite structured $TiO_2$ | 3.60 | [115] |
| 4d metals doped $TiO_2$ nanotubes | 2–4 | [116] |
| Three-layer $TiO_2$ (101) nanotubes | 3.83 | [117] |
| Six-layer $TiO_2$ (101) nanotubes | 4.17 | [117] |
| Nine-layer $TiO_2$ (001) nanotubes | 3.95 | [117] |
| Six-layer $TiO_2$ (001) nanotubes | 4.15 | [117] |
| Facer dependency of $TiO_2$ | NA | [118] |
| $TiO_2$ | NA | [119] |
| Phase stability in $TiO_2$ | NA | [120] |
| Rutile $TiO_2$ | NA | [121] |
| a$TiO_2$ | 2.70–2.85 | [14] |

As Table 1 clearly illustrates, the major focus for theoretical studies had been on bandgap calculations and alterations, but these numerical results had deviations from the results from experimental research. The majority of dopants introduced intermediate bandgaps to the structure, thus reducing the needed phonon energy for excitation. We find that by choosing the correct dopant, the effective bandgap can be lowered to 2.15 eV by co-doping $TiO_2$ with sulfur and niobium [98]. Other promising candidates are N-doped a$TiO_2$ (2.25 eV) [97] and the more complex g-$C_3N_4/TiO_2$ (2.21 eV) [110]. A general problem with the computational studies we have reviewed is the lack of a successful descriptor of the hydrogen evolution reaction (HER) activity, however, the hydrogen adsorption free energy, $\Delta G_H$, has shown promises [122].

## 4. Experimental Research

Recent advances in fabrication techniques have made it possible to deposit ultra-thin films, various-sized nanoparticles, and to create nanowires, nanorods, nanobelts, etc. This has made it possible to utilize interesting properties of nanostructure and improve $TiO_2$ photocatalysts.

### *4.1. Metal Dopants*

An interesting phenomenon that could be exploited to increase the solar absorption is the surface plasmon resonance (SPR) effect and localized surface plasmon resonance (LSPR) effect, where metal nanoparticles absorb incoming light outside the bandgap of the catalyst. The generated electrons will then be transferred to the surface of the photocatalyst and take part in the oxidation and reduction of the water molecules. To achieve this, one must add metal nanoparticles to the surface of the photocatalyst and let them absorb incoming radiation. Several attempts utilizing metal dopants on $TiO_2$ photocatalysts have revealed an increase in light absorption due to SPR/LSPR.

Zhao Li et al. worked on aluminum-doped $TiO_2$, and they report an increased PEC efficiency due to the LSPR effect [123]. Interestingly enough, they also found that an ultrathin (0.8–2.5 nm) layer of $Al_2O_3$ is formed naturally, which works as a protective layer against Al NPs corrosion and in reducing the surface charge recombination [123].

A similar increase in light absorption due to SPR and LSPR can be found using Co, Ni, titanium nitride (TiN), Au, Cu, or Ag dopants [124–129]. Nickel was also found to improve the separation of electron–hole pairs [125], while TiN assisted with charge generation, separation transportation, and injection efficiency [126]. Another advantage of the Ag nanoparticles is that they lower the charge carrier recombination rate [129]. In their research on Au dopants, Jinse Park et al. used ZnO–$TiO_2$ nanowires and found that the nanowires themselves excel in charge separation and transportation [127]. Shuai Zhang et al. used a Cu doped $TiO_2$ nanowire film, which showcased clear improvement in photocurrent density due to the unique architecture [128].

In a similar experiment, Jie Liu et al. used $Co_3O_4$ quantum dots on $TiO_2$ nanobelts and achieved $H_2$ and $O_2$ production rates of 41.8 and 22.0 µmol/hg [130]. The QDs favored transfer and accommodation of photo-generated electrons, in addition, to inhibit the recombination of charge carriers [130].

Doping could also induce a Schottky junction in the photocatalyst, which could help increase the charge transfer and help separate the photogenerated electrons and holes. He et al. showed this, using $TiO_2$ nanowire decorated with Pd NPs and achieving a photocurrent density of 1.4 $mA/cm^2$ [131]. The use of platinum within $TiO_2$ based photocatalysts is well known, and Lichao Wang et al. showed that by creating a $Pt/TiO_2$ photocatalyst, an $H_2$ production rate of 7410 µmol/gh is achievable [132].

Complex dopants have also been used on $TiO_2$, in addition to nanostructures. This makes it possible to combine the properties of the various dopants on $TiO_2$. In an attempt to increase the hydrogen production of $TiO_2$, Ejaz Hussain et al. doped $TiO_2$ with Pd–BaO NPs [133]. They achieved an $H_2$ production of 29.6 mmol/hg in a solution of 5% ethanol and 95% water [133]. Hussain et al. took advantage of the inherent high catalytic activity of the Pd nanoparticles, and the fact that barium oxide (BaO) enhances the electron transfer from the semiconductor band to the Pd centers [133]. In a similar approach, cadmium sulfide (CdS) was incorporated into a $TiO_2$ photoanode [134]. This utilized the suppression of electron-hole recombination and efficient charge separation/diffusion due to the nanorod structure, in addition to the SPR effect from the dopants [134]. Instead of doping $TiO_2$ only with CdS, it could be combined with tin (IV) oxide ($SnO_2$) nanosheets. The reason for this is that $TiO_2$ reduces the charge recombination between Cds and $SnO_2$ [135]. Thus, the number of electrons and holes reaching the surface and participating in the reduction or oxidation process increases.

It is also possible to dope $TiO_2$ with $Ti^{3+}$ and Ni to improve the overall efficiency; in fact, $Ti^{3+}$/Ni co-doped $TiO_2$ nanotubes have a bandgap of 2.84 eV [136]. This is roughly 12% narrower than that of pure $TiO_2$ and could be explained by the SPR effect.

Lately, there has been some research devoted to black titanium dioxide. Mengqiao Hu et al. used $Ti^{3+}$ self-doped mesoporous black $TiO_2/SiO_2/g–C_3N_4$ sheets [137]. The system has a bandgap of ~2.25 eV and photocatalytic hydrogen evolution of 572.6 µmol/gh. This is all due to the unique mesoporous framework enhancing the adsorption of pollutants and favoring the mass transfer, $Ti^{3+}$ self-doping reducing the bandgap, and extending the photoresponse to the visible light region [137].

Through modifying the $TiO_2$ NPs with 2D molybdenum disulfide ($MoSe_2$), Lulu Wu et al. achieved a hydrogen production rate of 5.13 µmol/h for samples with 0.1 wt.% MoSe2 [138]. They created $MoSe_2$ nanosheets, which were then combined with $TiO_2$ nanoparticles to create an efficient photocatalyst (Figure 8), by taking advantage of the wide light response and rapid charge migration ability of 2D nanosheets $MoSe_2$. A slightly different approach would be to wrap rutile $TiO_2$ nanorods with amorphous $Ta_2O_xN_y$ to achieve an optical bandgap of 2.86 eV with band edge positions suitable for water splitting [139].

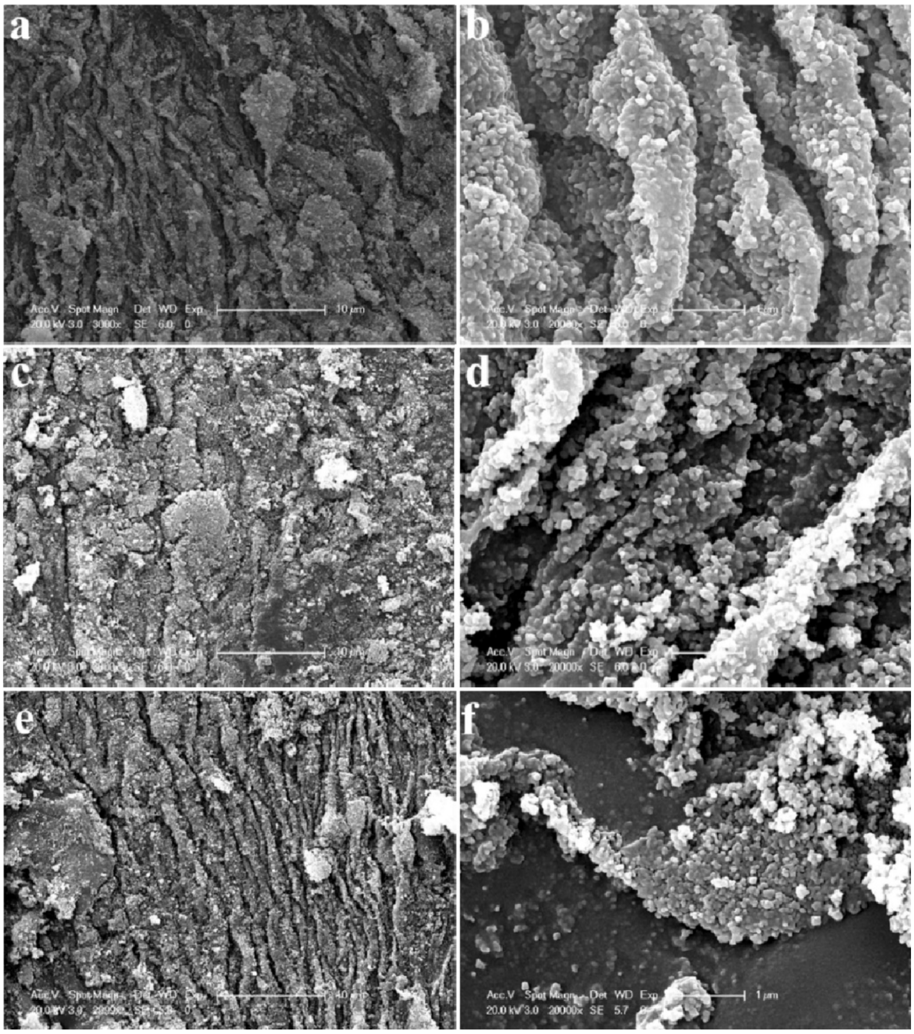

**Figure 8.** SEM images of $MoSe_2$ with $TiO_2$ nanoparticles synthesised using a simple hydrothermal method; (**a**,**b**) 0.025%, (**c**,**d**) 0,05%, and (**e**,**f**) 0.1% mass ratio of $MoSe_2$:$TiO_2$. Reprinted with permission from [138]. Copyright 2019, with permission from Elsevier.

Bismuth vanadate ($BiVO_4$), iron (III) oxide/hematite ($Fe_2O_3$), and bismuth ferrite ($BiFeO_3$) are materials with interesting properties for solar-driven water splitting. They all have low bandgaps, which could help with visible light absorption, and are both simple and inexpensive materials [140–142]

Xin Wu et al. utilized $BiFeO_3$ (BFO) on top of $TiO_2$ and found a photocurrent density as high as 11.25 mA/$cm^2$, 20 times higher than that of bare $TiO_2$ [143]. The improvement is mainly due to the heterostructure of BFO/$TiO_2$ and the ferroelectric polarization due to the introduction of BFO, which could lead to upward bending at the interface and thus effectively drive the separation and transportation of photogenerated carriers [143].

Bismuth vanadate is most often used together with a dopant. For example, Jia et al. used W to dope $TiO_2$/$BiVO_4$ nanorods and obtained a bandgap of 2.4 eV [144]. In addition, Wengfeng Zhou et al. synthesized an ultrathin Ti/$TiO_2$/$BiVO_4$ nanosheet heterojunction [145]. It had an enhanced photocatalytic effect due to the formation of a built-in electric field in the heterojunction between $TiO_2$ and $BiVO_4$ [145]. Using Co, Pi Quan Liu et al. modified a $TiO_2$/$BiVO_4$ composite photoanode, which shows improved visible light absorption and a more efficient charge transfer relay [146]. By combining FeOOH/$TiO_2$/$BiVO_4$, Xiang Yin et al. created a photoanode that led to a hydrogen production rate of 2.36 µmol/$cm^2$ after testing for 2.5 h [147].

However, it is possible to use $BiVO_4$ without a dopant BiV because $O_4$ and $TiO_2$ naturally complement each other. It allows for the exploitation of the excellent absorption properties of $BiVO_4$ to produce highly reductive electrons through $TiO_2$ sensitization under visible light [148]. Another example of this is how Ahmad Radzi et al. deposited $BiVO_4$ on $TiO_2$ to increase PEC efficiency [149].

Hematite is usually combined with more complex structures, for example, 3d ordered urchin-like $TiO_2$@$Fe_2O_3$ arrays [150]. Using these arrays Chai et al. reported a photocurrent density of 1.58 mA/$cm^2$ at 1.23 V vs. reversible hydrogen electrode (RHE) [150]. This is a clear improvement compared to pristine $TiO_2$.

A different approach is to use amorphous $Fe_2O_3$ with $TiO_2$ and silicon (Si). With this method, Zhang et al. achieved a photocurrent density of 3.5 mA/$cm^2$ at 1.23 V vs. RHE [151]. It is also possible to use $TiO_2$ as the dopant on hematite. Fan Feng et al. decorated a hematite PEC with $TiO_2$ at the grain boundaries [152] that increased the charge carrier density and improved the charge separation efficiency, resulting in a photocurrent density of 2.90 mA/$cm^2$ at 1.23 V vs. RHE [152].

However, one could also use a simple $TiO_2$/$Fe_2O_3$ heterojunction, which Deng et al. found improved the photocurrent density due to improved separation and transfer of photogenerated carriers [153].

A few studies are also reported on on metal-organic frameworks (MOFs) in cooperation with $TiO_2$.

Yoon et al. coated $TiO_2$ nanorods (NRs) with $NH_2$–MIL-125(Ti) and achieved a photocurrent density of 1.62 mA/$cm^2$ [154]. The high photocurrent can be explained by several factors: the large surface area and crystallinity of $TiO_2$ NRs, which leads to effective light absorption and charge transport. Or the moderate bandgap of MIL(125)–$NH_2$, the uniform and conformal coating of the MIL layer, and the efficient charge carrier separation and transportation through the type (II) band alignment of $TiO_2$ and MIL(125)–$NH_2$.

### *4.2. Non-Metal Dopants*

Metal dopants could act as recombination centers for electrons and holes and thus lowering the overall efficiency of the photocatalyst [155]. Thus, a large number of research studies have been going on toward doping $TiO_2$ with non-metal dopants, for example, Si, S, C, F, and N.

Yang Lu et al. doped $TiO_2$ nanowires with earth-abundant Si and achieved an 18.2 times increase in the charge carrier density, which was better than in N and Ti (III) doped $TiO_2$ [156]. The increase in visible light photocatalytic activity is due to the enhanced electron transport, because of higher charge-carrier density, longer electron lifetime, and larger diffusion coefficient in Si-doped $TiO_2$ NWs [156]. High-quality graphene could be of use in water splitting as quantum dots on rutile $TiO_2$ nanoflowers because they are highly luminescent and can absorb UV and visible light up to wavelengths of 700 nm [157]. Bellamkonda et al. found that multiwalled carbon nanotubes–graphene–$TiO_2$ (CNT–GR–$TiO_2$) could achieve a hydrogen production rate of 29 mmol/hg (19 mmol/hg for anatase $TiO_2$) [158]. They also had an estimated solar energy conversion efficiency of 14.6% and a bandgap of 2.79 eV, which was due to the generation of $Ti^{3+}$ and oxygen vacancies within the composite [158]. $TiO_2$ absorbs UV light due to its inherent large bandgap, Qiongzhi Gao et al. [159] utilized this and doped $TiO_2$ with hydrogenated F. The hydrogen-treated F atoms increased both UV and visible light absorption. When $TiO_2$ is doped with sulfur, an abundant element, a bandgap of 2.15 eV can be expected [160]. N and lanthanum (La) co-doping of $TiO_2$ does not reduce the bandgap, but the photocatalytic effect is seen to be enhanced due to an increase in surface nitrogen and oxygen vacancies [161].

### *4.3. Improved Production Methods*

As discussed, although there are several options in order to dope $TiO_2$ with metals and non-metals, the research community has devoted much energy to improving the characteristics of $TiO_2$ photocatalysts through appropriate synthesis conditions. It is possible to achieve improved mechanical strength, enhanced composite stability, surface area, roughness, and fill factor for $TiO_2$ by using branched multiphase $TiO_2$ [162].

Treating $TiO_2$ with $Ar/NH_3$ during the fabrication process, which could improve the density of the charge carrier and broaden the photon absorption both in the UV and visible light regions [163]. An increase in density of states at the surface and a 2.5-fold increase in photocurrent density at 1.23 vs. RHE could be achieved by anodizing and annealing $TiO_2$ during the fabrication process [164]. Ning Wei et al. showed that by controlling $TiO_2$ core shells, it was possible to achieve a bandgap of 2.81 eV, and had an $H_2$ evolution rate of 49.2 µmol/(h cm) [165].

Huali Huang et al. looked into the effect of annealing the atmosphere on the performance of $TiO_2$ NR [46]. Oxygen, air, nitrogen, and argon were used as the different atmospheres. The same rutile phase was observed, but it resulted in different $H_2$ activities. Samples annealed in argon showed the highest photocurrent density of 0.978 $mA/cm^2$ at 1.23 V vs. RHE [46], an increase of 124.8% compared to the oxygen annealed samples. It was found that the density of oxygen vacancies in the samples increased with the decrease in oxygen in the annealing atmosphere [46]. The increase in oxygen vacancies enhances visible light absorption and increases the electron conductivity (inhibits recombination of the charge carriers) [46].

Aleksander et al. examined what would happen if the substrate, which $TiO_2$ was fabricated on was changed [166]. The authors lowered the optical reflection by using black silicon, which in turn increased the light collection [166]. They also found that the addition of noble metals could induce SPR in the visible light region [166].

By combining improved production methods and doping/co-doping with metals/non-metals, $TiO_2$ could be realized as an efficient photocatalyst. Fu et. al. showed that by controlling the HCl concentration during the synthesis process, it was possible to synthesize well-crystallized rutile $TiO_2$ nanorods with special aspect ratios [167]. They proposed a process, as shown in Figure 9, for synthesizing rutile $TiO_2$ with different aspect ratios. Rutile $TiO_2$ nanorods with small aspect ratios were formed by placing titanium tetrachloride ($TiCl_4$) in liquid hydrochloric acid (HCl) before undertaking hydrothermal treatment. The key factors were the presence of $Cl^-$ and $H^+$ at high temperature and pressure. For the synthesis of nanorods with medium/large aspect ratios titanium butoxide (TBOT) was added dropwise to HCL (aq.)/NaCl (aq.) This created rutile/anatase crystal seeds, which were placed in HCl (aq.) for the final growth process. They concluded that with decreasing aspect ratios, the photocatalytic water splitting activity would increase for $TiO_2$ nanorods [167].

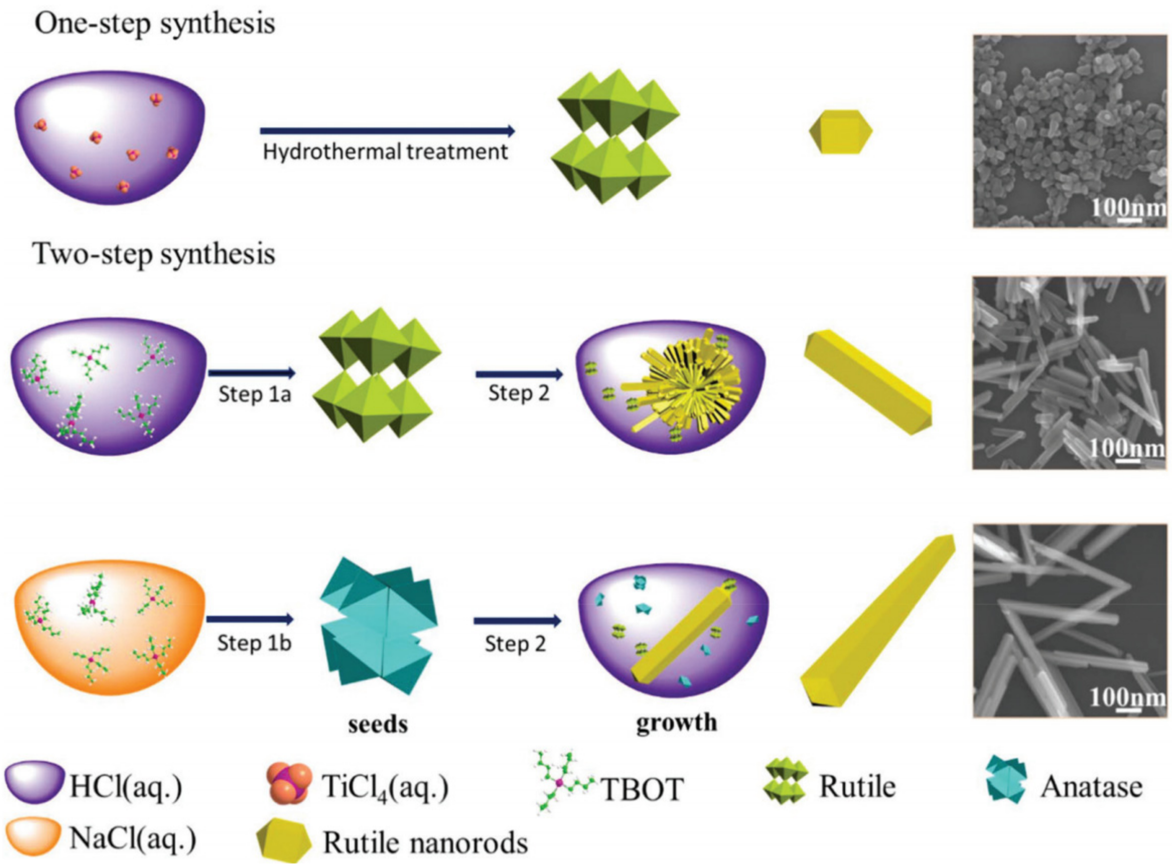

**Figure 9.** Schematic illustration of the synthesis of rutile $TiO_2$ with specific (small, medium, and large) aspect ratios. Reprinted with permission from [167]. Copyright 2018, with permission from RSC.

### *4.4. Collected Data*

We present in Table 2 the obtained bandgap, photocurrent density, $H_2$, and $O_2$ production rate values from experimental studies that are reviewed here.

We see from the data presented in Table 2 that it is possible to adjust the properties of $TiO_2$ photocatalysts by doping or through structural changes. For example, Elbakkay et al. achieved a bandgap of 2.15 eV using an S–$TiO_2$/S-reduced graphene oxide catalyst [160]. Both theoretical and experimental studies point at sulfur as a possible dopant for $TiO_2$ that could drastically reduce the effective bandgap of the photocatalyst. In general, theoretical studies tend to focus on simpler structures and doping of $TiO_2$, while experimental research has moved on toward more complex structures of $TiO_2$ that consist of several layers, materials, and nanostructures.

It is clear from Table 2 that the various solutions and potentials are used for measuring HER, and presenting photocurrent density in different ways is an issue that makes the direct comparison difficult. This hampers the evaluation of the most promising $TiO_2$ structure for photocatalytic activity. Likewise, the theoretical studies use different models and approximations that make it difficult to compare the numerical results for different $TiO_2$ structures. Combined theoretical and experimental study along with the establishment of standards, for example, for measuring $H_2$ production, would help the path to develop $TiO_2$ photocatalysts towards commercial realization.

**Table 2.** This table displays the bandgap, photocurrent density, and $H_2$ production rate experimentally achieved for doped/modified $TiO_2$ structures in articles reviewed in this study.

| **Nanomaterial** | **Bandgap [eV]** | **Photocurrent Density at 1.23 V vs. RHE [mA/cm$^2$]** | **$H_2$ Production Rate 1.5G Sunlight Bias at 1.23 vs. RHE** | **$O_2$ Production Rate 1.5G Sunlight Bias at 1.23 vs. RHE** | **Ref.** |
|---|---|---|---|---|---|
| $TiO_2$@$Fe_2O_3$/$TiO_2$ | 2.2 | 1.58, and 3.6 at 1.6 V vs. RHE | NA | NA | [150] |
| α-$Ta_2O_xN_y$ enwrapped $TiO_2$ rutile nanorods | 2.86 | 1.32 | 244.2 mmol/m$^2$h | 112.7 mmol/m$^2$h | [139] |
| Ag-$TiO_2$-NR05 | 2.64 | 0.08 and 0.10 mA/cm$^2$ at 1.2 and 1.6 V vs. RHE | NA | NA | [129] |
| W-$TiO_2$/$BiVO_4$ nanorods | 2.4 | 2.5 | 41 μmol/h | NA | [144] |
| Branched multiphase $TiO_2$ | 3.04 | 0.95 | NA | NA | [162] |
| $Co_3O_4$ quantum dots on $TiO_2$ | 3.07 | 0.0005 | 41.8 μmol/h/g | 22.0 μmol/h/g | [130] |
| Co-Pi modified 3D $TiO_2$/$BiVO_4$ | NA | 4.96 at 0.63 V vs. Ag/AgCl | NA | NA | [146] |
| Co doped $TiO_2$ nanotubes | 2.88 | 1.0 | NA | NA | [124] |
| Controllable $TiO_2$ core shells | 2.81 | 3.88 | 49.2 μmol/cm$^2$h | 25.2 μmol/cm$^2$h | [165] |
| A-$Fe_2O_3$/$TiO_2$/Si | NA | 3.5 | NA | NA | [151] |
| Al@$TiO_2$ | NA | NA | NA | NA | [123] |
| Si-doped $TiO_2$ nanowires | NA | NA | NA | NA | [156] |
| Three-layer ($SiO_2$, $Al_2O_3$, and $TiO_2$) structure with Au particles for LSPR | NA | NA | NA | NA | [168] |
| $BiFeO_3$/$TiO_2$ | NA | 11.25 | NA | NA | [143] |
| Graphene QDs decorated rutile $TiO_2$ nanoflowers | NA | ~0.32 at 0.5 V vs. Ag/AgCl | NA | NA | [157] |
| Hierarchical $TiO_2$/$Fe_2O_3$ | NA | 1.79 | NA | NA | [153] |
| CNT-GR-$TiO_2$ | 2.79 | NA | 29 mmol/h/g | NA | [158] |
| $SnO_2$ nanosheets with $TiO_2$ and CdS QD | NA | 4.7 at 0V vs. Ag/AgCl | NA | NA | [135] |
| $TiO_2$ nanotubes treated with Ar/$NH_{3+}$ | NA | 1 at 1.18 V vs. RHE | NA | NA | [163] |
| $TiO_2$ nanowire decorated with Pd | NA | 1.4 | NA | NA | [131] |
| $NH_2$-MIL-125(Yi) on $TiO_2$ nanorods | NA | 1.62 | NA | NA | [154] |
| Ni-doped $TiO_2$ nanotubes | NA | 0.93 at 0 V vs. Ag/AgCl | NA | NA | [125] |
| N doped La/$TiO_2$ | 2.96–2.99 | NA | 8.25 μmol/h/g | NA | [161] |

**Table 2.** *Cont.*

| Nanomaterial | Bandgap [eV] | Photocurrent Density at 1.23 V vs. RHE [mA/cm$^2$] | $H_2$ Production Rate 1.5G Sunlight Bias at 1.23 vs. RHE | $O_2$ Production Rate 1.5G Sunlight Bias at 1.23 vs. RHE | Ref. |
|---|---|---|---|---|---|
| TiN boosted N doped $TiO_2$ | NA | 3.12 | NA | NA | [126] |
| CuO@$TiO_2$ nanowires | NA | 0.56 | NA | NA | [128] |
| Pd-BaO NPs on $TiO_2$ | NA | NA | 29.6 mmol/h/g | NA | [133] |
| S-$TiO_2$/S-RGO | 2.15 | 3.36 at 1 V vs. Ag/AgCl | NA | NA | [160] |
| Anodized and $H_2$ annealed $TiO_2$ | NA | 2.5 fold $TiO_2$ | NA | NA | [164] |
| $TiO_2$ NPs modified with 2D $MoSe_2$ | NA | NA | 5.12 μmol/h | NA | [138] |
| Ultrathin Ti/$TiO_2$/$BiVO_4$ | NA | 5.8 μa/cm$^2$ at 0.5 V vs. Ag/AgCl | NA | NA | [145] |
| $TiO_2$ on black Si | NA | NA | NA | NA | [166] |
| ZnO-$TiO_2$ core-shell nanowires decorated with Au NPs | NA | 1.63 | NA | NA | [127] |
| $TiO_2$/CdS system | 2.25 | 30 mA/cm$^2$ (at 1 V vs. Ag/AgCl) under 1.5 AM | 1.3 mmol/cm$^2$h | NA | [134] |
| FeOOH/$TiO_2$/$BiVO_4$ | NA | 3.21 | 2.36 μmol/cm$^2$ | 1.09 μmol/cm$^2$h | [147] |
| hematite PEC decorated with $TiO_2$ at the grain boundaries | NA | 2.90 | NA | NA | [152] |
| the effect of annealing atmosphere on the performance of $TiO_2$ NR | NA | 0.978 | NA | NA | [46] |
| $Ti^{3+}$/Ni co-doped $TiO_2$ nanotubes | 2.84 | 0.87 | NA | NA | [136] |
| Hydrogenated F-doped $TiO_2$ | 3.0 | NA | 3.76 mmol/h/g | NA | [159] |
| $BiVO_4$ deposited on $TiO_2$ | NA | 35 μ under 100 mW/cm$^2$ in 0.5M $Na_2SO_4$ | NA | NA | [149] |
| $BiVO_4$ used together with $TiO_2$ | NA | ~0.3 at 1.0 V vs. RHE | NA | NA | [148] |
| Pt/$TiO_2$(anatase) photocatalyst | NA | NA | 7410 μmol/h/g | 5096 μmol/h/g | [132] |
| $Ti^{3+}$ self-doped mesoporous black $TiO_2$/$SiO_2$/g-$C_3N_4$ sheets | ~2.25 | NA | NA | NA | [137] |
| Rutile $TiO_2$ nanorods with small aspect ratio | NA | NA | 1229 μmol/h/g | 549 μmol/h/g | [167] |
| Rutile $TiO_2$ nanorods with medium aspect ratio | NA | NA | 783 μmol/h/g | 369 μmol/h/g | [167] |
| Rutile $TiO_2$ nanorods with large aspect ratio | NA | NA | 549 μmol/h/g | 252 μmol/h/g | [167] |

As we can observe from the results presented so far, great steps have been taken to make $TiO_2$ photocatalysts for water splitting a viable technology for green hydrogen production. However, even though the progress has been rapid over the past decade there are still obstacles in the way to large-scale production facilities.

Coordinated theoretical and experimental study of $TiO_2$ structures for enhancing the electronic, optical, and physical properties will help achieve the goal of efficient low-cost photocatalysts for water splitting.

In general, during the synthesis of the photocatalysts, there is uncertainty in the exact composition and structure of the compound [169,170]. This is especially prevalent for doping and the location of the dopants in the compound. For example, if the dopants are too deep or too shallow (on the surface), they will behave as recombination centers and thus reduce the overall solar to hydrogen efficiency [171]. The selection of deposition techniques for $TiO_2$ structures will have an effect on the performance as these techniques have advantages and disadvantages. For example, chemical vapor deposition (CVD) and physical vapor deposition (PVD) produce homogenous and flexible microstructure and super hard materials, but the drawbacks are challenges with deposition rate, maintenance cost, and the size of the component. Thermal spraying has the advantage of fast deposition rates, large components, and ease of exploitation, but does not produce coatings of the same quality as CVD, electrodeposition, or PVD [172]. In other words, there is always the dilemma of choosing the correct deposition method and figuring out how it could affect the performance of the material. The research community employs a variety of techniques to characterize the material, infrared spectroscopy, Raman spectroscopy, scanning electron microscopy (SEM), X-ray spectroscopy, etc. Because the reviewed studies employ different characterization methods to verify, for example, the bandgap of $TiO_2$ structures, a comparison of results in different studies becomes challenging. Another challenge is that experiments are not carried out under standardized conditions (e.g., with constant irradiance and homogeneous light distribution), the assessment of the real progress achieved with modified $TiO_2$ is often difficult. Furthermore, comparisons between pristine $TiO_2$ and enhanced photocatalysts are frequently biased because samples selected as reference materials present a relatively low photoactivity [173].

Computational modeling and simulations can help relieve some of these issues, although it comes with its own limitations. One advantage of theoretical simulations is that it is possible to create the exact structure you want to work on. Thus, we can investigate specific attributes and properties by fine-tuning the structure and composition of the compound. Moreover, the calculation of the $H_2$ and $O_2$ production is not based on measurement conditions, which makes results easier to compare.

### *4.5. Production Facilities*

The aforementioned challenges are not the only ones that the research community faces in using $TiO_2$ as the photocatalytic material for water splitting. Unfortunately, there is still a lack of scalable systems that could produce hydrogen in an economically feasible manner, even with an efficient catalyst [174]. Pinaud et. al. proposed and discussed the economic feasibility of four different designs of photocatalytic water splitting plants and the schematics are shown in Figure 10 [175].

Type 1 is a single bed particle suspension reactor and it is the simplest of the four. It consists of a low-lying horizontal plastic bag containing a slurry of photoactive particles in an electrolyte. The plastic bag is designed to allow light to penetrate, while it retains the electrolyte, photoactive particles, and evolved gases.

The Type 2 reactor is a dual bed with particle suspension, and it is similar to that of the Type 1 reactor. However, the biggest difference is that separate beds are used for $H_2$ and $O_2$ production.

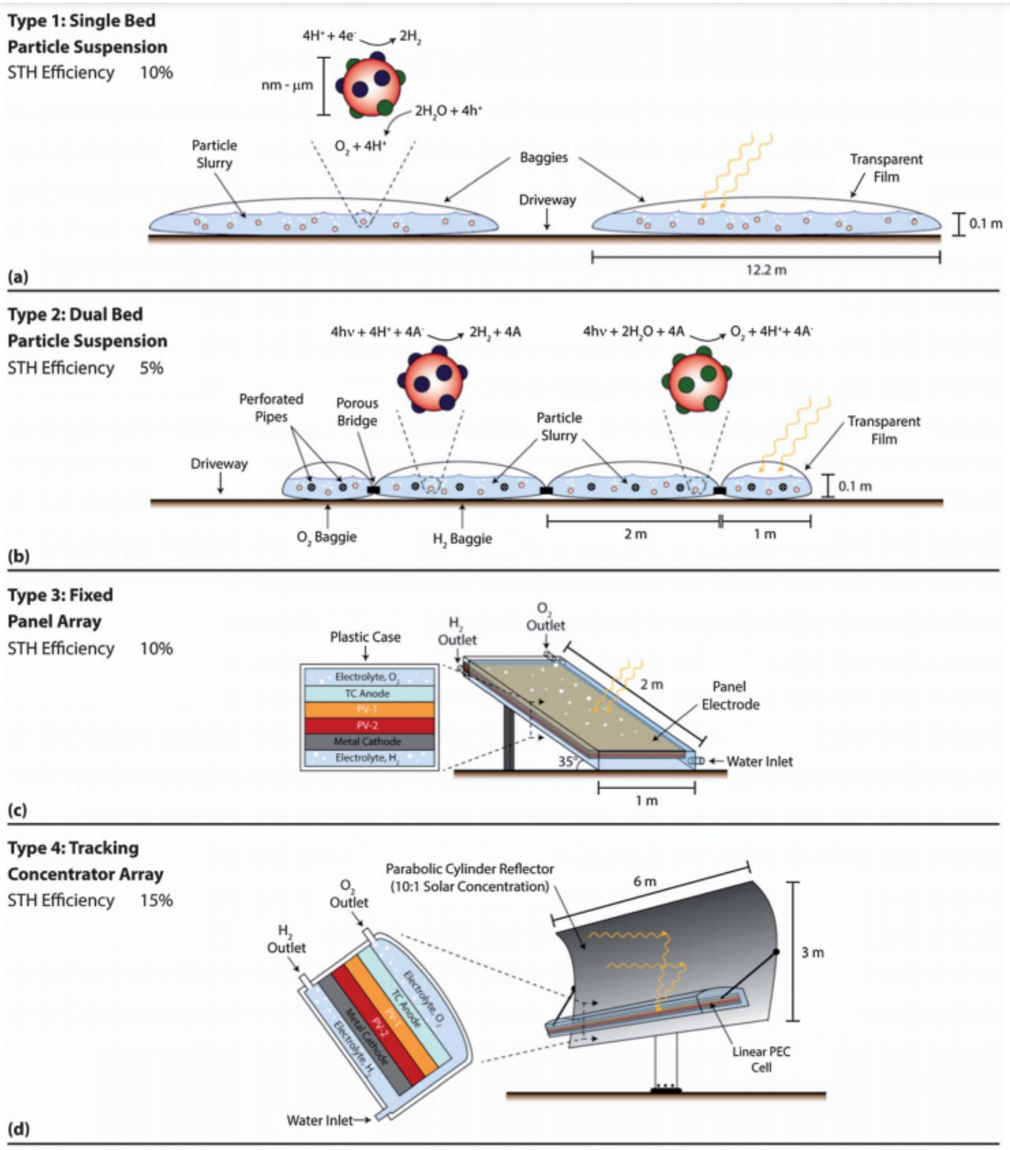

**Figure 10.** Schematic of the four different reactors. (**a**) Cross section of the Type 1 reactor showing the particle slurry contained by the baggies and separated by the driveway, (**b**) Type 2 reactor cross section with separate oxygen and hydrogen baggies connected by a porous bridge, (**c**) Type 3 reactor utilizing a photoelectrochemical (PEC) cell instead of photocatalytic water splitting (PWS) being directed toward the sun and (**d**) Type 4 reactor design that combines the PEC cell with an offset parabolic solar concentrator. Drawing not to scale. Reused with permission from [175]. Copyright 2013, with permission from Royal Society of Chemistry.

The third option, named Type 3 reactor, is a fixed panel array, which consists of an integral planar electrode with multiple photoactive layers sandwiched between two electrodes. The entire system is within a transparent plastic electrolyte reservoir. The final alternative is the Type 4 reactor, which is a tracking concentrator array that uses an offset parabolic cylinder array to focus sunlight on a linear PEC cell receiver and has two-axis steering to track the daily movement of the sun [175].

In general, it was found that the key component for realizing these designs was to improve the solar to hydrogen efficiencies [175]. However, there are also other limitations, such as safety issues with the $H_2$ and $O_2$ gas mixture, how to split and collect the $H_2$ and $O_2$ gasses, a lack of general understanding of how the photocatalyst particle works, the mechanical integrity of the plastic bags, etc. [175].

## 5. Conclusions and Long-Term Outlook

Even though considerable progress has been made in the development of solar-driven water splitting with $TiO_2$ as the photocatalyst, we believe there are four major challenges the research community must tackle before it becomes a viable technology.

The first challenge is the lack of a standard way to express the hydrogen production rates with varying photocatalytic materials. Research groups have been presenting these generations' rates in different ways that make the comparison challenging. As seen in the literature presented here, the measured hydrogen evolution rates depend on specific details of the experimental setup, such as the spectrum of the light source, the light intensity at the sample, co-catalyst selection, size of the potential, and type and selection of the solution. Suggestions and solutions for standard experimental setups are also needed. However, reporting the apparent quantum yield (AQY) instead of only the gas evolution could be a part of the solution [176,177]. This will help bridge the gap between experimental and theoretical results. Computational modeling has some of the same challenges as the model, assumptions, approximations, and software used will affect the numerical results that make the comparison of results demanding. The missing piece here is calculations of the hydrogen and oxygen evolution rates, and an alternative can be studying the Volmer reaction, the Tafel reaction or the Herovsky reaction, and the Gibbs free energy [178,179].

The second challenge is the material $TiO_2$ and its wide bandgap of 3.2 eV, which is in the ultraviolet section of the visible light spectrum. This means that 97% of the energy coming from the sun is not usable for $TiO_2$ photocatalysts. There have been several attempts to lower the bandgap of $TiO_2$, both experimentally and theoretically, which have been successful. However, the most successful experimental works are based on complex nanostructures or layered structures that are difficult and expensive to create at a larger scale. Computational modeling has in general focused more on various dopants and doping percentages. Unfortunately, the best results are seen when using noble metals or expensive metals. However, sulfur doping could be a solution to this problem. Combined $TiO_2$ with other earth-abundant materials as $MoS_2$ or $WS_2$ could be better photocatalysts in the future [180,181].

The third challenge is the lack of research combining experimental research with theoretical simulations to optimize the characteristics of $TiO_2$ structures for photocatalytic applications. This is a weakness in the current research as theoretical modeling and simulation could work as a great screening tool for the experimentalists, reducing their workload. Theoretical research could also help with the fundamental understanding of the process involved in solar-driven water splitting. By combining the two methods, it is easier to see the inner workings of the photocatalyst and to determine where improvement is needed. Moreover, computational work requires experimental verification and for validating the numerical results.

The final challenge is the lack of scalable systems that could produce hydrogen in an economically feasible manner, even with an efficient catalyst [174]. There is currently a lack of scalable and functional production facilities. The ones that do exist have a solar-to-hydrogen efficiency of 1.8% [182], indicating that further research is needed before photocatalytic water splitting is competitive with other hydrogen production methods. The main factor for the low efficiencies reported for photocatalytic hydrogen production is the low solar-to-hydrogen rates of the photocatalyst itself. An interesting idea is to look into combining $TiO_2$ with perovskites due to the latter's excellent optoelectronic properties. Naturally, water-insoluble perovskites combined with $TiO_2$ could be the missing link that solar-driven water splitting needs.

**Author Contributions:** Conceptualization, H.E. and D.V.; methodology, H.E.; writing—original draft preparation, H.E.; writing—review and editing, H.E., S.B., P.V., S.Y. and D.V.; supervision, D.V. All authors have read and agreed to the published version of the manuscript.

**Funding:** This research received no external funding.

**Institutional Review Board Statement:** Not Applicable.

**Informed Consent Statement:** Not Applicable.

**Data Availability Statement:** No new data were created or analyzed in this study. Data sharing is not applicable to this article.

**Acknowledgments:** The computations/simulations/[SIMILAR] were performed on resources provided by UNINETT Sigma2—the National Infrastructure for High Performance Computing and Data Storage in Norway (project: NN2867K).

**Conflicts of Interest:** The authors declare no conflict of interest.

## References

1. OECD/IEA. World Energy Outlook. 2016. Available online: http://www.iea.org/t&c (accessed on 14 May 2018).
2. Dincer, I.; Zamfirescu, C. *Sustainable Energy Systems and Applications*, 1st ed.; Springer: Berlin/Heidelberg, Germany, 2012; p. XVII. [CrossRef]
3. Tong, Y.; Liang, J.; Liu, H.K.; Dou, S.X. Energy storage in Oceania. *Energy Storage Mater.* **2019**, *20*, 176–187. [CrossRef]
4. Jafari, T.; Moharreri, E.; Amin, A.S.; Miao, R.; Song, W.; Suib, S.L. Photocatalytic water splitting-the untamed dream: A Review of recent advances. *Molecules* **2016**, *21*, 900. [CrossRef]
5. Sharma, P.; Kolhe, M.L. Review of sustainable solar hydrogen production using photon fuel on artificial leaf. *Int. J. Hydrog. Energy* **2017**, *42*, 22704–22712. [CrossRef]
6. Pulido Melián, E.; González Díaz, O.; Ortega Méndez, A.; López, C.R.; Nereida Suárez, M.; Doña Rodríguez, J.M.; Navío, J.A.; Fernández Hevia, D.; Pérez Peña, J. Efficient and affordable hydrogen production by water photo-splitting using $TiO_2$-based photocatalysts. *Int. J. Hydrog. Energy* **2013**, *38*, 2144–2155. [CrossRef]
7. Bicer, Y.; Dincer, I. Clean fuel options with hydrogen for sea transportation: A life cycle approach. *Int. J. Hydrog. Energy* **2018**, *43*, 1179–1193. [CrossRef]
8. van Biert, L.; Godjevac, M.; Visser, K.; Aravind, P.V. A review of fuel cell systems for maritime applications. *J. Power Sources* **2016**, *327*, 345–364. [CrossRef]
9. International Maritime Organization. Third IMO Greenhouse Gas Study 2014. Available online: http://www.imo.org/en/OurWork/Environment/PollutionPrevention/AirPollution/Pages/Greenhouse-Gas-Studies-2014.aspx (accessed on 14 May 2018).
10. Fujishima, A.; Honda, K. Electrochemical photolysis of water at a semiconductor electrode. *Nature* **1972**, *238*, 37. [CrossRef] [PubMed]
11. Wang, B.; Shen, S.; Mao, S.S. Black $TiO_2$ for solar hydrogen conversion. *J. Mater.* **2017**, *3*, 96–111. [CrossRef]
12. Chen, X.; Mao, S.S. Titanium dioxide nanomaterials: Synthesis, properties, modifications, and applications. *Chem. Rev.* **2007**, *107*, 2891–2959. [CrossRef]
13. Haggerty, J.E.S.; Schelhas, L.T.; Kitchaev, D.A.; Mangum, J.S.; Garten, L.M.; Sun, W.; Stone, K.H.; Perkins, J.D.; Toney, M.F.; Ceder, G.; et al. High-fraction brookite films from amorphous precursors. *Sci. Rep.-Uk* **2017**, *7*, 15232. [CrossRef] [PubMed]
14. Kaur, K.; Singh, C.V. Amorphous $TiO_2$ as a photocatalyst for hydrogen production: A DFT study of structural and electronic properties. *Energy Proc.* **2012**, *29*, 291–299. [CrossRef]
15. Zhang, W.; Yin, J.-R.; Tang, X.-Q.; Zhang, P.; Ding, Y.-H. Density functional theory studies on the structural and physical properties of Cu-doped anatase $TiO_2$ (101) surface. *Phys. E* **2017**, *85*, 259–263. [CrossRef]
16. Morgade, C.I.N.; Cabeza, G.F. First-principles study of codoping $TiO_2$ systems capable of improving the specific surface area and the dissociation of $H_2O$ to generate $H_2$ and $O_2$. *Comput. Mater. Sci.* **2017**, *127*, 204–210. [CrossRef]
17. Press, R.J.; Santhanam, K.S.V.; Miri, M.J.; Bailey, A.V.; Takacs, G.A. Introduction to hydrogen technology. *ChemSusChem* **2009**, *3*, 432.
18. Hoang, D.L.; Chan, S.H.; Ding, O.L. Kinetic and modelling study of methane steam reforming over sulfide nickel catalyst on a gamma alumina support. *Chem. Eng. J.* **2005**, *112*, 1–11. [CrossRef]
19. Ozcan, H.; Dincer, I. Thermodynamic analysis of a combined chemical looping-based trigeneration system. *Energy Convers. Manag.* **2014**, *85*, 477–487. [CrossRef]
20. Steinfeld, A. Solar hydrogen production via a two-step water-splitting thermochemical cycle based on Zn/ZnO redox reactions. *Int. J. Hydrog. Energy* **2002**, *27*, 611–619. [CrossRef]
21. Akkerman, I.; Janssen, M.; Rocha, J.; Wijffels, R.H. Photobiological hydrogen production: Photochemical efficiency and bioreactor design. *Int. J. Hydrog. Energy* **2002**, *27*, 1195–1208. [CrossRef]
22. Liao, C.-H.; Huang, C.-W.; Wu, J.C.S. Hydrogen production from semiconductor-based photocatalysis via water splitting. *Catalysts* **2012**, *2*, 490. [CrossRef]
23. Kudo, A. Photocatalysis and solar hydrogen production. *Pure Appl. Chem.* **2007**, *79*, 1917. [CrossRef]
24. Jang, J.S.; Kim, H.G.; Lee, J.S. Heterojunction semiconductors: A strategy to develop efficient photocatalytic materials for visible light water splitting. *Catal. Today* **2012**, *185*, 270–277. [CrossRef]
25. Moriya, Y.; Takata, T.; Domen, K. Recent progress in the development of (oxy)nitride photocatalysts for water splitting under visible-light irradiation. *Coordin. Chem. Rev.* **2013**, *257*, 1957–1969. [CrossRef]

26. Takata, T.; Jiang, J.; Sakata, Y.; Nakabayashi, M.; Shibata, N.; Nandal, V.; Seki, K.; Hisatomi, T.; Domen, K. Photocatalytic water splitting with a quantum efficiency of almost unity. *Nature* **2020**, *581*, 411–414. [CrossRef]
27. Cho, S.; Jang, J.-W.; Lee, K.-H.; Lee, J.S. Research Update: Strategies for efficient photoelectrochemical water splitting using metal oxide photoanodes. *APL Mater.* **2014**, *2*. [CrossRef]
28. Naik, V.M.; Haddad, D.; Naik, R.; Benci, J.; Auner, G.W. Optical properties of anatase, rutile and amorphous phases of $TiO_2$ thin films grown at room temperature by RF magnetron sputtering. *Mrs Proc.* **2002**, *755*, DD11.12. [CrossRef]
29. Liu, H.; Hsu, Y.; Su, H.; Huang, R.; Hou, F.; Tu, G.; Liu, W. A Comparative study of amorphous, anatase, rutile, and mixed phase $TiO_2$ films by mist chemical vapor deposition and ultraviolet photodetectors applications. *IEEE Sens. J.* **2018**, *18*, 4022–4029. [CrossRef]
30. Furube, A.; Asahi, T.; Masuhara, H.; Yamashita, H.; Anpo, M. Charge carrier dynamics of standard $TiO_2$ catalysts revealed by femtosecond diffuse reflectance spectroscopy. *J. Phys. Chem. B* **1999**, *103*, 3120–3127. [CrossRef]
31. Ohtani, B.; Ogawa, Y.; Nishimoto, S.-I. Photocatalytic activity of amorphous−anatase mixture of Titanium(IV) oxide particles suspended in aqueous solutions. *J. Phys. Chem. B* **1997**, *101*, 3746–3752. [CrossRef]
32. Stone, V.F.; Davis, R.J. Synthesis, Characterization, and Photocatalytic Activity of Titania and Niobia Mesoporous Molecular Sieves. *Chem. Mater.* **1998**, *10*, 1468–1474. [CrossRef]
33. Tanaka, K.; Capule, M.F.V.; Hisanaga, T. Effect of crystallinity of $TiO_2$ on its photocatalytic action. *Chem. Phys. Lett.* **1991**, *187*, 73–76. [CrossRef]
34. Liu, N.; Albu, S.P.; Lee, K.; So, S.; Schmuki, P. Water annealing and other low temperature treatments of anodic $TiO_2$ nanotubes: A comparison of properties and efficiencies in dye sensitized solar cells and for water splitting. *Electrochim. Acta* **2012**, *82*, 98–102. [CrossRef]
35. Gong, J.; Lai, Y.; Lin, C. Electrochemically multi-anodized $TiO_2$ nanotube arrays for enhancing hydrogen generation by photoelectrocatalytic water splitting. *Electrochim. Acta* **2010**, *55*, 4776–4782. [CrossRef]
36. Tiwari, J.N.; Tiwari, R.N.; Kim, K.S. Zero-dimensional, one-dimensional, two-dimensional and three-dimensional nanostructured materials for advanced electrochemical energy devices. *Prog. Mater. Sci.* **2012**, *57*, 724–803. [CrossRef]
37. Joy, J.; Mathew, J.; George, S.C. Nanomaterials for photoelectrochemical water splitting—Review. *Int. J. Hydrog. Energy* **2018**, *43*, 4804–4817. [CrossRef]
38. Kumar, P.; Devi, P.; Jain, R.; Shivaprasad, S.M.; Sinha, R.K.; Zhou, G.; Nötzel, R. Quantum dot activated indium gallium nitride on silicon as photoanode for solar hydrogen generation. *Commun. Chem.* **2019**, *2*, 4. [CrossRef]
39. Basu, K.; Zhang, H.; Zhao, H.; Bhattacharya, S.; Navarro-Pardo, F.; Datta, P.K.; Jin, L.; Sun, S.; Vetrone, F.; Rosei, F. Highly stable photoelectrochemical cells for hydrogen production using a $SnO_2$–$TiO_2$/quantum dot heterostructured photoanode. *Nanoscale* **2018**, *10*, 15273–15284. [CrossRef] [PubMed]
40. Liu, Z.; Wu, J.; Zhang, J. Quantum dots and plasmonic Ag decorated WO3 nanorod photoanodes with enhanced photoelectrochemical performances. *Int. J. Hydrog. Energy* **2016**, *41*, 20529–20535. [CrossRef]
41. Beermann, N.; Vayssieres, L.; Lindquist, S.E.; Hagfeldt, A. Photoelectrochemical studies of oriented nanorod thin films of hematite. *J. Electrochem. Soc.* **2000**, *147*, 2456–2461. [CrossRef]
42. Khan, S.U.M.; Sultana, T. Photoresponse of n-$TiO_2$ thin film and nanowire electrodes. *Sol. Energy Mat. Sol. Cells* **2003**, *76*, 211–221. [CrossRef]
43. Fitch, A.; Strandwitz, N.C.; Brunschwig, B.S.; Lewis, N.S. A comparison of the behavior of single crystalline and nanowire array ZnO photoanodes. *J. Phys. Chem. C* **2013**, *117*, 2008–2015. [CrossRef]
44. Zhang, J.Z. Metal oxide nanomaterials for solar hydrogen generation from photoelectrochemical water splitting. *Mrs Bull.* **2011**, *36*, 48–55. [CrossRef]
45. Varghese, O.K.; Grimes, C.A. Appropriate strategies for determining the photoconversion efficiency of water photoelectrolysis cells: A review with examples using titania nanotube array photoanodes. *Sol. Energy Mat. Sol. Cells* **2008**, *92*, 374–384. [CrossRef]
46. Huang, H.; Hou, X.; Xiao, J.; Zhao, L.; Huang, Q.; Chen, H.; Li, Y. Effect of annealing atmosphere on the performance of $TiO_2$ nanorod arrays in photoelectrochemical water splitting. *Catal. Today* **2019**, *330*, 189–194. [CrossRef]
47. Nie, Q.; Yang, L.; Cao, C.; Zeng, Y.; Wang, G.; Wang, C.; Lin, S. Interface optimization of ZnO nanorod/CdS quantum dots heterostructure by a facile two-step low-temperature thermal treatment for improved photoelectrochemical water splitting. *Chem. Eng. J.* **2017**, *325*, 151–159. [CrossRef]
48. Pokrant, S.; Dilger, S.; Landsmann, S.; Trottmann, M. Size effects of cocatalysts in photoelectrochemical and photocatalytic water splitting. *Mater. Today Energy* **2017**, *5*, 158–163. [CrossRef]
49. Kudo, A.; Miseki, Y. Heterogeneous photocatalyst materials for water splitting. *Chem. Soc. Rev.* **2009**, *38*, 253–278. [CrossRef] [PubMed]
50. Liu, X.; Gu, S.; Zhao, Y.; Zhou, G.; Li, W. BiVO4, $Bi_2WO_6$ and $Bi_2MoO_6$ photocatalysis: A brief review. *J. Mater. Sci. Technol.* **2020**, *56*, 45–68. [CrossRef]
51. Vishwakarma, A.K.; Tripathi, P.; Srivastava, A.; Sinha, A.S.K.; Srivastava, O.N. Band gap engineering of Gd and Co doped $BiFeO_3$ and their application in hydrogen production through photoelectrochemical route. *Int. J. Hydrog. Energy* **2017**, *42*, 22677–22686. [CrossRef]
52. Yin, W.-J.; Tang, H.; Wei, S.-H.; Al-Jassim, M.M.; Turner, J.; Yan, Y. Band structure engineering of semiconductors for enhanced photoelectrochemical water splitting: The case of $TiO_2$. *Phys. Rev. B* **2010**, *82*, 045106. [CrossRef]

53. Wang, J.; Sun, H.; Huang, J.; Li, Q.; Yang, J. Band Structure Tuning of $TiO_2$ for Enhanced Photoelectrochemical Water Splitting. *J. Phys. Chem. C* **2014**, *118*, 7451–7457. [CrossRef]
54. Zhang, G.; Zhang, W.; Minakata, D.; Chen, Y.C.; Crittenden, J.; Wang, P. The pH effects on $H_2$ evolution kinetics for visible light water splitting over the Ru/(CuAg)0.15In0.3Zn1.4S2 photocatalyst. *Int. J. Hydrog. Energy* **2013**, *38*, 11727–11736. [CrossRef]
55. Fekete, M.; Riedel, W.; Patti, A.F.; Spiccia, L. Photoelectrochemical water oxidation by screen printed ZnO nanoparticle films: Effect of pH on catalytic activity and stability. *Nanoscale* **2014**, *6*, 7585–7593. [CrossRef]
56. Momeni, M.M.; Ghayeb, Y. Visible light-driven photoelectrochemical water splitting on ZnO–$TiO_2$ heterogeneous nanotube photoanodes. *J. Appl. Electrochem.* **2015**, *45*, 557–566. [CrossRef]
57. Varadhan, P.; Fu, H.-C.; Priante, D.; Retamal, J.R.D.; Zhao, C.; Ebaid, M.; Ng, T.K.; Ajia, I.; Mitra, S.; Roqan, I.S.; et al. Surface Passivation of GaN Nanowires for Enhanced Photoelectrochemical Water-Splitting. *Nano Lett.* **2017**, *17*, 1520–1528. [CrossRef] [PubMed]
58. Ismail, A.A.; Bahnemann, D.W. Photochemical splitting of water for hydrogen production by photocatalysis: A review. *Sol. Energy Mat. Sol. Cells* **2014**, *128*, 85–101. [CrossRef]
59. Kresse, G.; Furthmüller, J. Efficient iterative schemes for ab initio total-energy calculations using a plane-wave basis set. *Phys. Rev. B* **1996**, *54*, 11169–11186. [CrossRef]
60. Kresse, G.; Furthmüller, J. Efficiency of ab-initio total energy calculations for metals and semiconductors using a plane-wave basis set. *Comp. Mater. Sci.* **1996**, *6*, 15–50. [CrossRef]
61. Kresse, G.; Hafner, J. Ab initio molecular dynamics for liquid metals. *Phys. Rev. B* **1993**, *47*, 558–561. [CrossRef]
62. Kresse, G.; Hafner, J. Ab initio molecular-dynamics simulation of the liquid-metal-amorphous-semiconductor transition in germanium. *Phys. Rev. B* **1994**, *49*, 14251–14269. [CrossRef] [PubMed]
63. Kresse, G.; Hafner, J. Norm-conserving and ultrasoft pseudopotentials for first-row and transition elements. *J. Phys.-Condens Mat.* **1994**, *6*, 8245–8257. [CrossRef]
64. Kresse, G.; Joubert, D. From ultrasoft pseudopotentials to the projector augmented-wave method. *Phys. Rev. B* **1999**, *59*, 1758–1775. [CrossRef]
65. Clark, S.J.; Segall, M.D.; Pickard, C.J.; Hasnip, P.J.; Probert, M.I.J.; Refson, K.; Payne, M.C. First principles methods using CASTEP. *Z. Krist.-Cryst. Mater.* **2005**, *220*, 567–570. [CrossRef]
66. Dovesi, R.; Erba, A.; Orlando, R.; Zicovich-Wilson, C.M.; Civalleri, B.; Maschio, L.; Rérat, M.; Casassa, S.; Baima, J.; Salustro, S.; et al. Quantum-mechanical condensed matter simulations with CRYSTAL. *Wires Comput. Mol. Sci.* **2018**, *8*, e1360. [CrossRef]
67. Dovesi, R.; Pascale, F.; Civalleri, B.; Doll, K.; Harrison, N.M.; Bush, I.; D'Arco, P.; Noël, Y.; Rérat, M.; Carbonnière, P.; et al. The CRYSTAL code, 1976–2020 and beyond, a long story. *J. Chem. Phys.* **2020**, *152*, 204111. [CrossRef]
68. Mortensen, J.J.; Hansen, L.B.; Jacobsen, K.W. Real-space grid implementation of the projector augmented wave method. *Phys. Rev. B* **2005**, *71*, 035109. [CrossRef]
69. Kan, M.; Wang, J.Y.; Li, X.W.; Zhang, S.H.; Li, Y.W.; Kawazoe, Y.; Sun, Q.; Jena, P. Structures and Phase Transition of a MoS2 Monolayer. *J. Phys. Chem. C* **2014**, *118*, 1515–1522. [CrossRef]
70. Xia, Z.; Tao, Y.; Pan, Z.; Shen, X. Enhanced photocatalytic performance and stability of 1T MoS2 transformed from 2H MoS2 via Li intercalation. *Results Phys.* **2019**, *12*, 2218–2224. [CrossRef]
71. Liu, P.; Kaltak, M.; Klimeš, J.; Kresse, G. Cubic scaling GW: Towards fast quasiparticle calculations. *Phys. Rev. B* **2016**, *94*, 165109. [CrossRef]
72. Ramberger, B.; Sukurma, Z.; Schäfer, T.; Kresse, G. RPA natural orbitals and their application to post-Hartree-Fock electronic structure methods. *J. Chem. Phys.* **2019**, *151*, 214106. [CrossRef]
73. Heyd, J.; Scuseria, G.E. Efficient hybrid density functional calculations in solids: Assessment of the Heyd-Scuseria-Ernzerhof screened Coulomb hybrid functional. *J. Chem. Phys.* **2004**, *121*, 1187–1192. [CrossRef]
74. Heyd, J.; Scuseria, G.E.; Ernzerhof, M. Hybrid functionals based on a screened Coulomb potential. *J. Chem. Phys.* **2003**, *118*, 8207–8215. [CrossRef]
75. Perdew, J.P.; Burke, K.; Ernzerhof, M. Generalized Gradient Approximation Made Simple. *Phys. Rev. Lett.* **1996**, *77*, 3865–3868. [CrossRef] [PubMed]
76. Wang, V.; Xu, N.; Liu, J.C.; Tang, G.; Geng, W.-T. VASPKIT: A User-friendly Interface Facilitating High-throughput Computing and Analysis Using VASP Code. *arXiv* **2019**, arXiv:1908.08269.
77. Togo, A.; Tanaka, I. First principles phonon calculations in materials science. *Scr. Mater.* **2015**, *108*, 1–5. [CrossRef]
78. Kumar, A. Different methods used for the synthesis of $TiO_2$ based nanomaterials: A review. *Am. J. Nano Res. Appl.* **2018**, *6*, 1. [CrossRef]
79. Nagaraju, G.; Tharamani, C.; Chandrappa, G.; Livage, J. Hydrothermal synthesis of amorphous MoS2nanofiber bundles via acidification of ammonium heptamolybdate tetrahydrate. *Nanoscale Res. Lett.* **2007**, *2*, 461–468. [CrossRef]
80. Bai, J.; Meng, T.; Guo, D.; Wang, S.; Mao, B.; Cao, M. Co9S8@MoS2 Core–Shell Heterostructures as Trifunctional Electrocatalysts for Overall Water Splitting and Zn–Air Batteries. *ACS Appl. Mater. Interfaces* **2018**, *10*, 1678–1689. [CrossRef]
81. Lee, J.-H.; Choi, H.-S.; Lee, J.-H.; Kim, Y.-J.; Suh, S.-J.; Chi, C.-S.; Oh, H.-J. Fabrication of titania nanotubular film with metal nanoparticles. *J. Cryst. Growth* **2009**, *311*, 638–641. [CrossRef]
82. Patil, U.M.; Kulkarni, S.B.; Deshmukh, P.R.; Salunkhe, R.R.; Lokhande, C.D. Photosensitive nanostructured $TiO_2$ grown at room temperature by novel "bottom-up" approached CBD method. *J. Alloy. Compd.* **2011**, *509*, 6196–6199. [CrossRef]

83. Wu, J.-M.; Hayakawa, S.; Tsuru, K.; Osaka, A. Nanocrystalline Titania Made from Interactions of Ti with Hydrogen Peroxide Solutions Containing Tantalum Chloride. *Cryst. Growth Des.* **2002**, *2*, 147–149. [CrossRef]
84. AlHammad, M.S. Nanostructure hydroxyapatite based ceramics by sol gel method. *J. Alloy. Compd.* **2016**, *661*, 251–256. [CrossRef]
85. Kluson, P.; Luskova, H.; Cajthaml, T.; Šolcová, O. Non thermal preparation of photoactive titanium (IV) oxide thin layers. *Thin Solid Film.* **2006**, *495*, 18–23. [CrossRef]
86. Arami, H.; Mazloumi, M.; Khalifehzadeh, R.; Sadrnezhaad, S.K. Sonochemical preparation of $TiO_2$ nanoparticles. *Mater. Lett.* **2007**, *61*, 4559–4561. [CrossRef]
87. Amaresh, S.; Karthikeyan, K.; Jang, I.C.; Lee, Y.S. Single-step microwave mediated synthesis of the CoS2 anode material for high rate hybrid supercapacitors. *J. Mater. Chem. A* **2014**, *2*, 11099–11106. [CrossRef]
88. Pan, Y.; Wen, M. Noble metals enhanced catalytic activity of anatase $TiO_2$ for hydrogen evolution reaction. *Int. J. Hydrog. Energy* **2018**, *43*, 22055–22063. [CrossRef]
89. Zhang, Y.; Kilin, D.S. Computational modeling of wet TiO2(001) anatase surfaces functionalized by transition metal doping. *Int. J. Quantum Chem.* **2012**, *112*, 3867–3873. [CrossRef]
90. Zhang, S.-T.; Li, C.-M.; Yan, H.; Wei, M.; Evans, D.G.; Duan, X. Density Functional Theory Study on the Metal–Support Interaction between Ru Cluster and Anatase $TiO_2$(101) Surface. *J. Phys. Chem. C* **2014**, *118*, 3514–3522. [CrossRef]
91. Jin, C.; Dai, Y.; Wei, W.; Ma, X.; Li, M.; Huang, B. Effects of single metal atom (Pt, Pd, Rh and Ru) adsorption on the photocatalytic properties of anatase $TiO_2$. *Appl. Surf. Sci.* **2017**, *426*, 639–646. [CrossRef]
92. Lin, Y.; Jiang, Z.; Zhu, C.; Zhang, R.; Hu, X.; Zhang, X.; Zhu, H.; Lin, S.H. The electronic structure, optical absorption and photocatalytic water splitting of (Fe + Ni)-codoped $TiO_2$: A DFT + U study. *Int. J. Hydrog. Energy* **2017**, *42*, 4966–4976. [CrossRef]
93. Ghuman, K.K. Mechanistic insights into water adsorption and dissociation on amorphous -based catalysts. *Sci. Technol. Adv. Mater.* **2018**, *19*, 44–52. [CrossRef]
94. Koteski, V.; Belošević-Čavor, J.; Umićević, A.; Ivanovski, V.; Toprek, D. Improving the photocatalytic properties of anatase $TiO_2$(101) surface by co-doping with Cu and N: Ab initio study. *Appl. Surf. Sci.* **2017**, *425*, 1095–1100. [CrossRef]
95. Assadi, M.H.N.; Hanaor, D.A.H. The effects of copper doping on photocatalytic activity at (101) planes of anatase $TiO_2$: A theoretical study. *Appl. Surf. Sci.* **2016**, *387*, 682–689. [CrossRef]
96. Sikam, P.; Moontragoon, P.; Sararat, C.; Karaphun, A.; Swatsitang, E.; Pinitsoontorn, S.; Thongbai, P. DFT calculation and experimental study on structural, optical and magnetic properties of Co-doped $SrTiO_3$. *Appl. Surf. Sci.* **2018**, *446*, 92–113. [CrossRef]
97. Ghuman, K.K.; Singh, C.V. Effect of doping on electronic structure and photocatalytic behavior of amorphous $TiO_2$. *J. Phys.-Condens Mat.* **2013**, *25*, 475501. [CrossRef]
98. Ren, D.; Li, H.; Cheng, X. Tailoring the electronic and optical properties of anatase $TiO_2$ by (S, Nb) co-doping from a DFT plus U calculation. *Solid State Commun.* **2015**, *223*, 54–59. [CrossRef]
99. Gao, L.; Li, Y.; Ren, J.; Wang, S.; Wang, R.; Fu, G.; Hu, Y. Passivation of defect states in anatase $TiO_2$ hollow spheres with Mg doping: Realizing efficient photocatalytic overall water splitting. *Appl. Catal. B-Environ.* **2017**, *202*, 127–133. [CrossRef]
100. Chen, W.; Yuan, P.; Zhang, S.; Sun, Q.; Liang, E.; Jia, Y. Electronic properties of anatase $TiO_2$ doped by lanthanides: A DFT+U study. *Phys. B* **2012**, *407*, 1038–1043. [CrossRef]
101. Li, H.; Li, W.; Liu, X.; Ren, C.; Miao, X.; Li, X. Engineering of Gd/Er/Lu-triple-doped Bi2MoO6 to synergistically boost the photocatalytic performance in three different aspects: Oxidizability, light absorption and charge separation. *Appl. Surf. Sci.* **2019**, *463*, 556–565. [CrossRef]
102. Shi, H.; Lin, Y.; Jiang, Z.; Su, Y.; Ding, X.; Zhang, X.; Zhu, H.; Zhang, R. Enhanced optical absorption and photocatalytic activity of anatase $TiO_2$ through C Nd-codoped: A DFT+ U calculations. *J. Phys. Chem. Solids* **2017**, *109*, 70–77. [CrossRef]
103. Jiang, Z.; Wan, W.; Wei, W.; Chen, K.; Li, H.; Wong, P.K.; Xie, J. Gentle way to build reduced titanium dioxide nanodots integrated with graphite-like carbon spheres: From DFT calculation to experimental measurement. *Appl. Catal. B-Environ.* **2017**, *204*, 283–295. [CrossRef]
104. Gurkan, Y.Y.; Kasapbasi, E.; Cinar, Z. Enhanced solar photocatalytic activity of $TiO_2$ by selenium(IV) ion-doping: Characterization and DFT modeling of the surface. *Chem. Eng. J.* **2013**, *214*, 34–44. [CrossRef]
105. Zhao, Y.; Wang, W.; He, L. The effects of Co/N dopants on the electronic, redox potential, optical, and photocatalytic water-splitting properties of $TiO_2$: First principles calculations. *Chem. Phys. Lett.* **2017**, *685*, 108–113. [CrossRef]
106. Wang, P.; Zhou, Q.; Xia, Y.; Zhan, S.; Li, Y. Understanding the charge separation and transfer in mesoporous carbonate-doped phase-junction $TiO_2$ nanotubes for photocatalytic hydrogen production. *Appl. Catal. B-Environ.* **2018**, *225*, 433–444. [CrossRef]
107. Wu, X.; Yin, S.; Dong, Q.; Guo, C.; Kimura, T.; Matsushita, J.-I.; Sato, T. Photocatalytic properties of Nd and C Codoped $TiO_2$ with the whole range of visible light absorption. *J. Phys. Chem. C* **2013**, *117*, 8345–8352. [CrossRef]
108. Zongyan, Z.; Xiang, Z.; Juan, Y.; Qingju, L. Effects of nonmetal doping on electronic structures and optical property of anatase $TiO_2$ from first-principles calculations. *Rare Met. Mat. Eng.* **2015**, *44*, 1568–1574. [CrossRef]
109. Zhao, Y.; Lin, Y.; Wang, G.; Jiang, Z.; Zhang, R.; Zhu, C. Electronic and optical performances of (Cu, N) codoped $TiO_2$/g-C3N4 heterostructure photocatalyst: A spin-polarized DFT + U study. *Sol. Energy* **2018**, *162*, 306–316. [CrossRef]
110. Lin, Y.; Shi, H.; Jiang, Z.; Wang, G.; Zhang, X.; Zhu, H.; Zhang, R.; Zhu, C. Enhanced optical absorption and photocatalytic $H_2$ production activity of g-C3N4/$TiO_2$ heterostructure by interfacial coupling: A DFT+ U study. *Int. J. Hydrog. Energy* **2017**, *42*, 9903–9913. [CrossRef]

111. Atanelov, J.; Gruber, C.; Mohn, P. The electronic and magnetic structure of p -element (C,N) doped rutile-$TiO_2$: A hybrid DFT study. *Comput. Mater. Sci.* **2015**, *98*, 42–50. [CrossRef]
112. Ghuman, K.K.; Singh, C.V. A DFT + U study of (Rh, Nb)-codoped rutile $TiO_2$. *J. Phys.-Condens Mat.* **2013**, *25*, 085501. [CrossRef]
113. Lisovski, O.; Chesnokov, A.; Piskunov, S.; Bocharov, D.; Zhukovskii, Y.F.; Wessel, M.; Spohr, E. Ab initio calculations of doped $TiO_2$ anatase (101) nanotubes for photocatalytical water splitting applications. *Mat. Sci. Semicon. Proc* **2016**, *42*, 138–141. [CrossRef]
114. Lisovski, O.; Piskunov, S.; Zhukovskii, Y.F.; Ozolins, J. Ab initiomodeling of sulphur doped $TiO_2$ nanotubular photocatalyst for water-splitting hydrogen generation. *Iop Conf. Ser.-Mat. Sci.* **2012**, *38*. [CrossRef]
115. Bocharov, D.; Piskunov, S.; Zhukovskii, Y.F.; Spohr, E.; D'Yachkov, P.N. First principles modeling of 3 d -metal doped three-layer fluorite-structured $TiO_2$(4,4) nanotube to be used for photocatalytic hydrogen production. *Vacuum* **2017**, *146*, 562–569. [CrossRef]
116. D'yachkov, E.P.; Bochkov, I.A.; Zaluev, V.A.; D'yachkova, P.N. Electronic properties of titanium dioxide nanotubes doped with 4d metals. *Russ. J. Inorg. Chem.* **2017**, *62*, 1048–1050. [CrossRef]
117. Lisovski, O.; Piskunov, S.; Zhukovskii, Y.F.; Bocharov, D. Quantum chemical simulations of titanium dioxide nanotubes used for photocatalytic water splitting. *J. Surf. Investig.* **2017**, *11*, 78–86. [CrossRef]
118. Ma, S.; Song, W.; Liu, B.; Zhong, W.; Deng, J.; Zheng, H.; Liu, J.; Gong, X.-Q.; Zhao, Z. Facet-dependent photocatalytic performance of $TiO_2$: A DFT study. *Appl. Catal. B-Environ.* **2016**, *198*, 1–8. [CrossRef]
119. Deák, P.; Kullgren, J.; Aradi, B.; Frauenheim, T.; Kavan, L. Water splitting and the band edge positions of $TiO_2$. *Electrochim. Acta* **2016**, *199*, 27–34. [CrossRef]
120. Hanaor, D.A.H.; Assadi, M.H.N.; Li, S.; Yu, A.; Sorrel, C.C. Ab Initio Study of Phase Stability in Doped $TiO_2$. *Comput. Mech.* **2012**, *50*, 185–194. [CrossRef]
121. Alghamdi, H.; Idriss, H. Study of the modes of adsorption and electronic structure of hydrogen peroxide and ethanol over $TiO_2$ rutile (110) surface within the context of water splitting. *Surf. Sci.* **2017**. [CrossRef]
122. Tsai, C.; Chan, K.; Nørskov, J.K.; Abild-Pedersen, F. Theoretical insights into the hydrogen evolution activity of layered transition metal dichalcogenides. *Surf. Sci.* **2015**, *640*, 133–140. [CrossRef]
123. Li, Z.; Shi, L.; Franklin, D.; Koul, S.; Kushima, A.; Yang, Y. Drastic enhancement of photoelectrochemical water splitting performance over plasmonic Al@TiO2 heterostructured nanocavity arrays. *Nano Energy* **2018**, *51*, 400–407. [CrossRef]
124. Venturini, J.; Bonatto, F.; Guaglianoni, W.C.; Lemes, T.; Arcaro, S.; Alves, A.K.; Bergmann, C.P. Cobalt-doped titanium oxide nanotubes grown via one-step anodization for water splitting applications. *Appl. Surf. Sci.* **2019**, *464*, 351–359. [CrossRef]
125. Dong, Z.; Ding, D.; Li, T.; Ning, C. Ni-doped $TiO_2$ nanotubes photoanode for enhanced photoelectrochemical water splitting. *Appl. Surf. Sci.* **2018**, *443*, 321–328. [CrossRef]
126. Li, Y.; Wang, J.-G.; Fan, Y.; Sun, H.; Hua, W.; Liu, H.; Wei, B. Plasmonic TiN boosting nitrogen-doped $TiO_2$ for ultrahigh efficient photoelectrochemical oxygen evolution. *Appl. Catal. B-Environ.* **2019**, *246*, 21–29. [CrossRef]
127. Park, J.; Desmukh, P.R.; Sohn, y.; Shin, W.G. ZnO-$TiO_2$ core-shell nanowires decorated with Au nanoparticles for plasmon-enhanced photoelectrochemical water splitting. *J. Alloy. Compd.* **2019**, *787*, 1310–1319. [CrossRef]
128. Zhang, S.; Cao, X.-b.; Wu, J.; Zhu, L.-w.; Gu, L. Preparation of hierarchical CuO@$TiO_2$ nanowire film and its application in photoelectrochemical water splitting. *T. Nonferr. Metal. Soc.* **2016**, *26*, 2094–2101. [CrossRef]
129. Sawant, S.Y.; Sayed, M.S.; Han, T.H.; Karim, M.R.; Shim, J.J.; Cho, M.H. Bio-synthesis of finely distributed Ag nanoparticle-decorated $TiO_2$ nanorods for sunlight-induced photoelectrochemical water splitting. *J. Ind. Eng. Chem.* **2019**, *69*, 48–56. [CrossRef]
130. Liu, J.; Ke, J.; Li, Y.; Liu, B.J.; Wang, L.D.; Xiao, H.N.; Wang, S.B. Co3O4 quantum dots/$TiO_2$ nanobelt hybrids for highly efficient photocatalytic overall water splitting. *Appl. Catal. B-Environ.* **2018**, *236*, 396–403. [CrossRef]
131. He, J.; Wang, M.; Wu, X.; Sun, Y.; Huang, K.; Chen, H.; Gao, L.; Feng, S. Influence of controlled Pd nanoparticles decorated $TiO_2$ nanowire arrays for efficient photoelectrochemical water splitting. *J. Alloy. Compd.* **2019**, *785*, 391–397. [CrossRef]
132. Wang, L.; Cao, S.; Guo, K.; Wu, Z.; Ma, Z.; Piao, L. Simultaneous hydrogen and peroxide production by photocatalytic water splitting. *Chin. J. Catal.* **2019**, *40*, 470–475. [CrossRef]
133. Hussain, E.; Majeed, I.; Nadeem, M.A.; Iqbal, A.; Chen, Y.; Choucair, M.; Jin, R.; Nadeem, M.A. Remarkable effect of BaO on photocatalytic $H_2$ evolution from water splitting via $TiO_2$ (P25) supported palladium nanoparticles. *J. Environ. Chem. Eng.* **2019**, *7*, 102729. [CrossRef]
134. Yoo, I.-H.; Kalanur, S.S.; Seo, H. A nanoscale p–n junction photoelectrode consisting of an NiOx layer on a $TiO_2$/CdS nanorod core-shell structure for highly efficient solar water splitting. *Appl. Catal. B-Environ.* **2019**, *250*, 200–212. [CrossRef]
135. Wang, Z.W.; Li, X.L.; Tan, C.K.; Qian, C.; Grimsdale, A.C.; Tok, A.I.Y. Highly porous $SnO_2$ nanosheet arrays sandwiched within $TiO_2$ and CdS quantum dots for efficient photoelectrochemical water splitting. *Appl. Surf. Sci.* **2019**, *470*, 800–806. [CrossRef]
136. Dong, Z.; Ding, D.; Li, T.; Ning, C. Facile preparation of $Ti^{3+}$/Ni co-doped $TiO_2$ nanotubes photoanode for efficient photoelectrochemical water splitting. *Appl. Surf. Sci.* **2019**, *480*, 219–228. [CrossRef]
137. Hu, M.; Xing, Z.; Cao, Y.; Li, Z.; Yan, X.; Xiu, Z.; Zhao, T.; Yang, S.; Zhou, W. Ti3+ self-doped mesoporous black $TiO_2$/$SiO_2$/g-C3N4 sheets heterojunctions as remarkable visible-lightdriven photocatalysts. *Appl. Catal. B-Environ.* **2018**, *226*, 499–508. [CrossRef]
138. Wu, L.L.; Shi, S.; Li, Q.D.; Zhang, X.Y.; Cui, X.L. $TiO_2$ nanoparticles modified with 2D MoSe2 for enhanced photocatalytic activity on hydrogen evolution. *Int. J. Hydrog. Energy* **2019**, *44*, 720–728. [CrossRef]
139. Zhang, H.W.; Ma, L.; Ming, J.T.; Liu, B.Q.; Zhao, Y.B.; Hou, Y.D.; Ding, Z.X.; Xu, C.; Zhang, Z.Z.; Long, J.L. Amorphous Ta2OxNy-enwrapped $TiO_2$ rutile nanorods for enhanced solar photoelectrochemical water splitting. *Appl. Catal. B-Environ.* **2019**, *243*, 481–489. [CrossRef]

140. Kaur, G.; Pandey, O.P.; Singh, K. Optical, structural, and mechanical properties of different valence-cation-doped bismuth vanadate oxides. *Phys. Status Solidi A* **2012**, *209*, 1231–1238. [CrossRef]
141. Yang, S.Y.; Seidel, J.; Byrnes, S.J.; Shafer, P.; Yang, C.H.; Rossell, M.D.; Yu, P.; Chu, Y.H.; Scott, J.F.; Ager Iii, J.W.; et al. Above-bandgap voltages from ferroelectric photovoltaic devices. *Nat. Nanotechnol.* **2010**, *5*, 143. [CrossRef]
142. Kay, A.; Cesar, I.; Grätzel, M. New Benchmark for Water Photooxidation by Nanostructured α-$Fe_2O_3$ Films. *J. Am. Chem. Soc.* **2006**, *128*, 15714–15721. [CrossRef] [PubMed]
143. Wu, X.; Li, H.; Wang, X.; Jiang, L.; Xi, J.; Du, G.; Ji, Z. Ferroelectric enhanced photoelectrochemical water splitting in $BiFeO_3/TiO_2$ composite photoanode. *J. Alloy. Compd.* **2019**, *783*, 643–651. [CrossRef]
144. Jia, Y.L.; Wang, Z.H.; Ma, Y.; Liu, J.L.; Shi, W.B.; Lin, Y.H.; Hu, X.; Zhang, K. Boosting interfacial charge migration of $TiO_2/BiVO_4$ photoanode by W doping for photoelectrochemical water splitting. *Electrochim. Acta.* **2019**, *300*, 138–144. [CrossRef]
145. Zhou, W.F.; Jiang, T.F.; Zhao, Y.; Xu, C.; Pei, C.G.; Xue, H.G. Ultrathin $Ti/TiO_2/BiVO_4$ nanosheet heterojunction arrays for photoelectrochemical water oxidation. *J. Alloy. Compd.* **2019**, *777*, 1152–1158. [CrossRef]
146. Liu, Q.; Mo, R.; Li, X.L.; Yang, S.; Zhong, J.X.; Li, H.X. Cobalt phosphate modified 3D $TiO_2/BiVO_4$ composite inverse opals photoanode for enhanced photoelectrochemical water splitting. *Appl. Surf. Sci.* **2019**, *464*, 544–551. [CrossRef]
147. Yin, X.; Liu, Q.; Yang, Y.H.; Liu, Y.; Wang, K.K.; Li, Y.M.; Li, D.W.; Qiu, X.Q.; Li, W.Z.; Li, J. An efficient tandem photoelectrochemical cell composed of $FeOOH/TiO_2/BiVO_4$ and $Cu_2O$ for self-driven solar water splitting. *Int. J. Hydrog. Energy* **2019**, *44*, 594–604. [CrossRef]
148. Polo, A.; Grigioni, I.; Dozzi, M.V.; Selli, E. Sensitizing effects of BiVO4 and visible light induced production of highly reductive electrons in the $TiO_2/BiVO_4$ heterojunction. *Catal. Today* **2018**. [CrossRef]
149. Radzi, A.A.S.M.; Safaei, J.; Teridi, M.A.M. Photoelectrochemical enhancement from deposition of BiVO4 photosensitizer on different thickness layer $TiO_2$ photoanode for water splitting application. *Nano-Struct. Nano-Objects* **2019**, *18*. [CrossRef]
150. Chai, X.B.; Zhang, H.F.; Pan, Q.; Bian, J.L.; Chen, Z.F.; Cheng, C.W. 3D ordered urchin-like $TiO_2$@$Fe_2O_3$ arrays photoanode for efficient photoelectrochemical water splitting. *Appl. Surf. Sci.* **2019**, *470*, 668–676. [CrossRef]
151. Zhang, W.; Chen, H.; Zhang, L.; Zhang, P.; Dong, E.; Ma, J.; Wang, G. Design and fabrication of an α-$Fe_2O_3$ $TiO_2$ Si 3D hierarchical photoanode for improved photoelectrochemical water splitting. *J. Alloy. Compd.* **2019**, *773*, 597–604. [CrossRef]
152. Feng, F.; Li, C.; Jian, J.; Qiao, X.; Wang, H.; Jia, L. Boosting hematite photoelectrochemical water splitting by decoration of TiO2 at the grain boundaries. *Chem. Eng. J.* **2019**, *368*, 959–967. [CrossRef]
153. Deng, J.; Zhuo, Q.; Lv, X. Hierarchical TiO2 Fe2O3 heterojunction photoanode for improved photoelectrochemical water oxidation. *J. Electroanal. Chem.* **2019**, *835*, 287–292. [CrossRef]
154. Yoon, J.W.; Kim, D.H.; Kim, J.H.; Jang, H.W.; Lee, J.H. NH2-MIL-125(Ti)/$TiO_2$ nanorod heterojunction photoanodes for efficient photoelectrochemical water splitting. *Appl. Catal. B-Environ.* **2019**, *244*, 511–518. [CrossRef]
155. Yalçın, Y.; Kılıç, M.; Çınar, Z. The Role of Non-Metal Doping in $TiO_2$ Photocatalysis. *J. Adv. Oxid. Technol.* **2010**, *13*, 281. [CrossRef]
156. Lu, Y.; Wei, Z.; Salke, N.P.; Yu, L.; Yan, H. Enhanced electron transport in rutile $TiO_2$ nanowires via H2S-assisted incorporation of dissolved silicon for solar-driven water splitting. *Appl. Catal. B-Environ.* **2019**, *244*, 767–772. [CrossRef]
157. Bayat, A.; Saievar-Iranizad, E. Graphene quantum dots decorated rutile $TiO_2$ nanoflowers for water splitting application. *J. Energy Chem.* **2018**, *27*, 306–310. [CrossRef]
158. Bellamkonda, S.; Thangavel, N.; Hafeez, H.Y.; Neppolian, B.; Rao, G.R. Highly active and stable multi-walled carbon nanotubes-graphene-$TiO_2$ nanohybrid: An efficient non-noble metal photocatalyst for water splitting. *Catal. Today* **2019**, *321*, 120–127. [CrossRef]
159. Gao, Q.; Si, F.; Zhang, S.; Fang, Y.; Chen, X.; Yang, S. Hydrogenated F-doped $TiO_2$ for photocatalytic hydrogen evolution and pollutant degradation. *Int. J. Hydrog. Energy* **2019**, *44*, 8011–8019. [CrossRef]
160. Elbakkay, M.H.; El Rouby, W.M.A.; El-Dek, S.I.; Farghali, A.A. S-$TiO_2$/S-reduced graphene oxide for enhanced photoelectrochemical water splitting. *Appl. Surf. Sci.* **2018**, *439*, 1088–1102. [CrossRef]
161. Dubnova, L.; Zvolska, M.; Edelmannova, M.; Matejova, L.; Reli, M.; Drobna, H.; Kustrowski, P.; Koci, K.; Capek, L. Photocatalytic decomposition of methanol-water solution over N-La/$TiO_2$ photocatalysts. *Appl. Surf. Sci.* **2019**, *469*, 879–886. [CrossRef]
162. Liu, X.; Cao, X.E.; Liu, Y.; Li, X.; Wang, M.; Li, M. Branched multiphase TiO2 with enhanced photoelectrochemical water splitting activity. *Int. J. Hydrog. Energy* **2018**, *43*, 21365–21373. [CrossRef]
163. Xu, Y.; Ahemd, R.; Klein, D.; Cap, S.; Freedy, K.; McDonnel, S.; Zangari, G. Improving photo-oxidation activity of water by introducing Ti3+ in self-ordered $TiO_2$ nanotube arrays treated with Ar NH3. *J. Power Sour.* **2019**, *414*, 242–249. [CrossRef]
164. Xu, Y.; Lin, Q.Y.; Ahmed, R.; Hoglund, E.R.; Zangari, G. Synthesis of $TiO_2$-based nanocomposites by anodizing and hydrogen annealing for efficient photoelectrochemical water oxidation. *J. Power Sour.* **2019**, *410*, 59–68. [CrossRef]
165. Wei, N.; Liu, Y.; Feng, M.; Li, Z.X.; Chen, S.G.; Zheng, Y.B.; Wang, D.A. Controllable $TiO_2$ core-shell phase heterojunction for efficient photoelectrochemical water splitting under solar light. *Appl. Catal. B-Environ.* **2019**, *244*, 519–528. [CrossRef]
166. Alexander, F.; AlMheiri, M.; Dahal, P.; Abed, J.; Rajput, N.S.; Aubry, C.; Viegas, J.; Jouiad, M. Water splitting $TiO_2$ composite material based on black silicon as an efficient photocatalyst. *Sol. Energy Mat. Sol. Cells* **2018**, *180*, 236–242. [CrossRef]
167. Fu, B.; Wu, Z.; Cao, S.; Guo, K.; Piao, L. Effect of aspect ratios of rutile TiO2 nanorods on overall photocatalytic water splitting performance. *Nanoscale* **2020**, *12*, 4895–4902. [CrossRef] [PubMed]
168. Abed, J.; AlMheiri, M.; Alexander, F.; Rajput, N.S.; Viegas, J.; Jouiad, M. Enhanced solar absorption of gold plasmon assisted TiO2-based water splitting composite. *Sol. Energy Mat. Sol. Cells* **2018**, *180*, 228–235. [CrossRef]

169. Pérez-Larios, A.; Lopez, R.; Hernández-Gordillo, A.; Tzompantzi, F.; Gómez, R.; Torres-Guerra, L.M. Improved hydrogen production from water splitting using $TiO_2$–ZnO mixed oxides photocatalysts. *Fuel* **2012**, *100*, 139–143. [CrossRef]
170. Wang, Q.; Huang, J.; Sun, H.; Zhang, K.-Q.; Lai, Y. Uniform carbon dots@TiO2 nanotube arrays with full spectrum wavelength light activation for efficient dye degradation and overall water splitting. *Nanoscale* **2017**, *9*, 16046–16058. [CrossRef] [PubMed]
171. Leung, D.Y.; Fu, X.; Wang, C.; Ni, M.; Leung, M.K.; Wang, X.; Fu, X. Hydrogen production over titania-based photocatalysts. *ChemSusChem* **2010**, *3*, 681–694. [CrossRef]
172. Makhlouf, A.S.H.; Tiginyanu, I. *Nanocoatings and Ultra-Thin Films*; Woodhead Publishing: Cambridge, UK, 2011; p. 448.
173. Hernández-Alonso, M.; Fresno, F.; Suárez, S.; Coronado, J. Development of alternative photocatalysts to $TiO_2$: Challenges and opportunities. *Energy Environ. Sci.* **2009**, *2*, 1231–1257. [CrossRef]
174. Goto, Y.; Hisatomi, T.; Wang, Q.; Higashi, T.; Ishikiriyama, K.; Maeda, T.; Sakata, Y.; Okunaka, S.; Tokudome, H.; Katayama, M.; et al. A Particulate Photocatalyst Water-Splitting Panel for Large-Scale Solar Hydrogen Generation. *Joule* **2018**, *2*, 509–520. [CrossRef]
175. Pinaud, B.A.; Benck, J.D.; Seitz, L.C.; Forman, A.J.; Chen, Z.; Deutsch, T.G.; James, B.D.; Baum, K.N.; Baum, G.N.; Ardo, S.; et al. Technical and economic feasibility of centralized facilities for solar hydrogen production via photocatalysis and photoelectrochemistry. *Energy Environ. Sci.* **2013**, *6*, 1983–2002. [CrossRef]
176. Han, L.; Lin, M.; Haussener, S. Reliable Performance Characterization of Mediated Photocatalytic Water-Splitting Half Reactions. *ChemSusChem* **2017**, *10*, 2158–2166. [CrossRef]
177. Kisch, H.; Bahnemann, D. Best Practice in Photocatalysis: Comparing Rates or Apparent Quantum Yields? *J. Phys. Chem. Lett.* **2015**, *6*, 1907–1910. [CrossRef] [PubMed]
178. Liang, Z.; Zhong, X.; Li, T.; Chen, M.; Feng, G. DFT Study on the Hydrogen Evolution Reaction for Different Facets of Co2P. *ChemElectroChem* **2019**, *6*, 260–267. [CrossRef]
179. Skúlason, E.; Karlberg, G.S.; Rossmeisl, J.; Bligaard, T.; Greeley, J.; Jónsson, H.; Nørskov, J.K. Density functional theory calculations for the hydrogen evolution reaction in an electrochemical double layer on the Pt(111) electrode. *Phys. Chem. Chem. Phys.* **2007**, *9*, 3241–3250. [CrossRef] [PubMed]
180. Parzinger, E.; Miller, B.; Blaschke, B.; Garrido, J.A.; Ager, J.W.; Holleitner, A.; Wurstbauer, U. Photocatalytic Stability of Single- and Few-Layer MoS2. *ACS Nano* **2015**, *9*, 11302–11309. [CrossRef]
181. Li, Z.; Meng, X.; Zhang, Z. Recent development on MoS2-based photocatalysis: A review. *J. Photoch. Photobio. C* **2018**, *35*, 39–55. [CrossRef]
182. Zhao, Y.; Ding, C.; Zhu, J.; Qin, W.; Tao, X.; Fan, F.; Li, R.; Li, C. A Hydrogen Farm Strategy for Scalable Solar Hydrogen Production with Particulate Photocatalysts. *Angew. Chem. Int. Edit.* **2020**, *59*, 9653–9658. [CrossRef] [PubMed]

PAPER B

# BANDGAP ENGINEERING IN $CsSn_{X}Pb_{1\text{-}X}I_{3}$ AND THEIR INFLUENCE ON LIGHT ABSORPTION

H. Eidsvåg, M. Rasukkannu, P. Vajeeston, and D. Velauthapillai

*In Materials Letters*, volume 218, pages 253-256, 2018

Materials Letters 218 (2018) 253–256

Contents lists available at ScienceDirect

Materials Letters

journal homepage: www.elsevier.com/locate/mlblue

Featured Letter

# Bandgap engineering in $CsSn_xPb_{(1-x)}I_3$ and their influence on light absorption

Håkon Eidsvåg [a], Murugesan Rasukkannu [a], Ponniah Vajeeston [b,*], Dhayalan Velauthapillai [a]

[a] Western Norway University of Applied Sciences, Department of Computing, Mathematics and Physics, Inndalsveien 28, Box 5063, Bergen, Norway
[b] Center for Materials Science and Nanotechnology, Department of Chemistry, University of Oslo, Box 1033 Blindern N-0315, Oslo, Norway

ARTICLE INFO

*Article history:*
Received 17 January 2018
Accepted 5 February 2018
Available online 6 February 2018

*Keywords:*
$CsPbI_3$
$CsSnI_3$
$CsSn_{0.5}Pb_{0.5}I_3$
Bandgap engineered solar cells
Simulation and modelling
Solar energy materials

ABSTRACT

We present first-principle computational modelling of the perovskite $CsSn_xPb_{(1-x)}I_3$ (x = 0, 0.5 and 1), aimed at increasing the efficiency of perovskite photovoltaics. Using density functional theory calculations with a hybrid functional, we predict that both $CsPbI_3$ and $CsSnI_3$ are stable structures with direct bandgaps, suitable for photovoltaic application. On the other hand, the stable structure of $CsSn_{0.5}Pb_{0.5}I_3$ exhibits an indirect bandgap, which could work as a direct bandgap due to the short electron-hole distance. The results of this study demonstrates that through bandgap engineering, we can obtain larger photon absorption ranges and higher efficiencies for perovskite based photovoltaics.

## 1. Introduction

In the last few years perovskite-based photovoltaics has emerged as a possible solution to the world's energy problem, having now reached efficiencies as high as 22.1% [1]. The current research is focused on methylammonium lead trihalide perovskites ($MAPbX_3$; MA = $CH_3NH_3^+$, X = Cl, Br, I) and metal halide perovskites ($ABX_3$; A = Cs, Rb, B = Sn, Pb, Ge, X = Cl, Br, I), with the aim of increasing the efficiency and solve the instability issue of perovskites [2,3]. Especially $CsPbI_3$ and the lead free $CsSnI_3$ have shown great potential. One of the main solutions for increasing efficiency is the doping of the perovskites, as this can have a major effect on many electronic properties. However, bandgap engineering in combination with theoretical simulations of perovskites seems to gather little attention from the research community.

With this in mind, this article proposes a new perovskite configuration, which combines $CsPbI_3$ and $CsSnI_3$ to improve the bandgap and the absorption range. The idea is to utilise simultaneously the two different absorption ranges, 675–750 nm and 875–1050 nm for $CsPbI_3$ and $CsSnI_3$ respectively, to achieve a higher absorption efficiency. We show through density functional theory (DFT) simulations that bandgap engineering of $CsSn_xPb_{(1-x)}I_3$ is possible in a solid solution. Furthermore, we investigate and compare the structural stability of $CsPbI_3$, $CsSnI_3$ and $CsSn_{0.5}Pb_{0.5}I_3$.

## 2. Methods and approaches

The total energies have been calculated by the projected augmented plane-wave (PAW) implementation of the Vienna ab initio simulation package (VASP) [4]. For the exchange-correlation functional part, we used the Perde-Burke-Ernzerhof (PBE) version of the generalized gradient approximation (GGA) [5]. The ionic coordinates are fully optimised using an energy converged threshold of a $10^{-6}$ eV per atom. We used the hybrid nonlocal exchange-correlation functional of Heyd-Scuseria-Ernzerhof (HSE06) to calculate the electronic structure and optical properties. In the HSE06 method, the screened parameter is set to 0.2 $Å^{-1}$ and 30% of the screened Hartree-Fock (HF) exchange is mixed with the PBE exchange functional [6]. The cut-off energy for the plane-wave basis set is set to 600 eV, and we use a 10 × 10 × 10 Γ-centred Monkhorst-pack **k**-point mesh for sampling the Brillouin zone. These settings are used in both PBE and HSE06 calculations for α-$CsSnI_3$. We used a similar density of **k**-points and energy cut-off to estimate total energy as a function of volume for all the structures considered in the present study.

## 3. Results and discussion

### 3.1. Structural description and relative stability

$CsSnI_3$ is a unique phase-change material that exhibits four polymorphs [7]. Two polymorphs are stable at room temperature: one has a one-dimensional double-chain structure and is yellow in

---

* Corresponding author.
*E-mail address:* ponniahv@kjemi.uio.no (P. Vajeeston).

https://doi.org/10.1016/j.matlet.2018.02.021
0167-577X/© 2018 Elsevier B.V. All rights reserved.

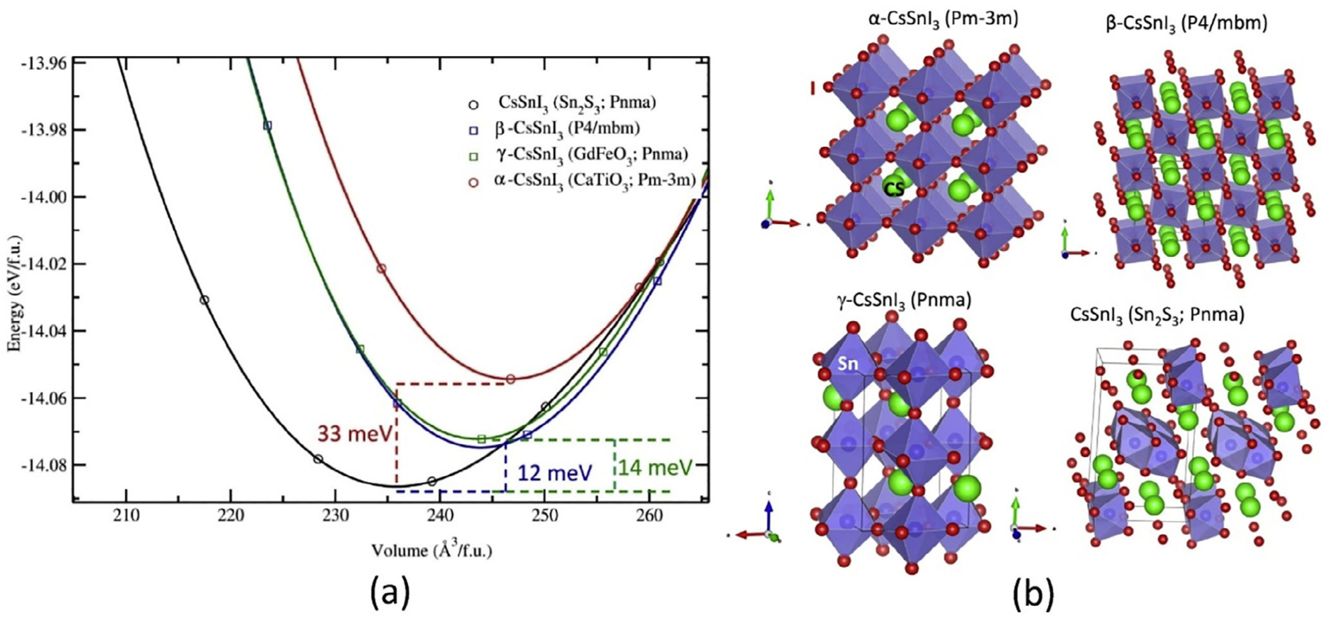

**Fig. 1.** (a) Calculated total energy (per formula unit; f.u.) as a function of the volume of the unit cell for the different polymorphs of $CsSnI_3$. The involved energy differences between the different polymorphs are indicated. (b) Crystal structure of $CsSnI_3$ polymorphs. The illustration contains legends for the different atoms.

color (Y-$CsSnI_3$; $Sn_2S_3$-type), and another has a three-dimensional perovskite structure (see Fig. 1b) and is black in color (γ-$CsSnI_3$). When heated above 425 K, the Y phase transforms to a black cubic perovskite phase (α-$CsSnI_3$), which, on subsequent cooling, converts to a black tetragonal phase (β-$CsSnI_3$) at 426 K (instead of Y) and a black orthorhombic phase (γ-$CsSnI_3$) at 351 K. In order to understand the relative stability of these four phases we have calculated the total energy as a function of unit-cell volume, which are displayed in Fig. 1a. Among the considered structures, the $Sn_2S_3$-type atomic arrangement is found to have the lowest total energy. The calculated ionic positions and lattice parameters for the four phases are found to be in good agreement with experimental findings [3]. It is interesting to note that the energy difference between α-, β-, γ- and Y-$CsSnI_3$ is very small, and hence, one can easily modify one polymorph into another by application of moderate temperature or pressure. This is in agreement with the work of Chung et al. [3] who found that $CsSnI_3$ stabilize in four different structures depending upon the synthesis method/condition and temperature. Similarly, for the $CsPbI_3$ and $CsSn_{0.5}Pb_{0.5}I_3$ phases, our theoretical energy-volume curves shows that both of them stabilize in orthorhombic structures with the Pnma space group (α-phase; $Sn_2S_3$-type). At ambient conditions $CsPbI_3$ crystallize in an orthorhombic structure, which at high temperature is transformed into a cubic ($CaTiO_3$-type) structure [8]. The energy difference between the two phases of $CsPbI_3$ is 0.15 eV and the calculated structural parameters are in good agreement with the experimental findings [8]. The crystal structure of $CsSn_{0.5}Pb_{0.5}I_3$ is currently unknown and the present study predict that at ambient conditions $CsSn_{0.5}Pb_{0.5}I_3$ crystallizes in an orthorhombic $Sn_2S_3$-derived structure.

### *3.2. Nature of electronic structure and related properties*

The calculated band structures for the low-energy structures are shown in Fig. 2, highlighting the relevant points in reciprocal space. $CsSnI_3$ is found to have three polymorphs with direct bandgaps (Y-, α- and β-$CsSnI_3$) and one with an indirect bandgap (γ-$CsSnI_3$). The polymorphs with direct bandgaps are suitable for photovoltaic application due to the efficient electron-hole transport. For $CsPbI_3$ we observe a direct bandgap at the Γ point, indicating the reason why it is a successful perovskite solar cell material. For $CsSn_{0.5}Pb_{0.5}I_3$ an indirect bandgap is observed, due the valence band maximum (VBM) being found between Y-H and Γ-X while the conduction band minima (CBM) is between Z-D. However, we found that the electron/hole jump distance is minimum at Z-D. Furthermore, the energy difference between the

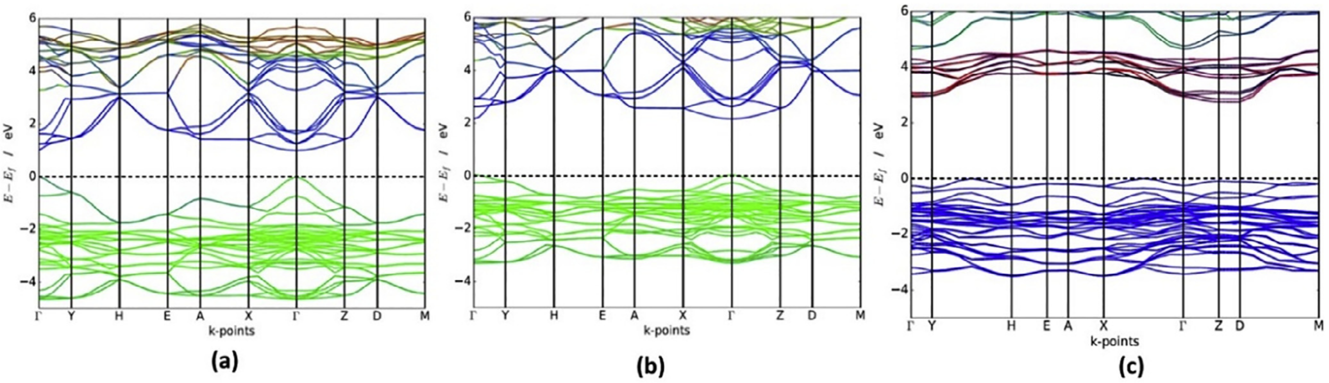

**Fig. 2.** Calculated band structures at the HSE06 level of the stable orthorhombic structures of (a) $CsSnI_3$, (b) $CsPbI_3$ and (c) $CsSn_{0.5}Pb_{0.5}I_3$.

VBM and the band energy in the Z-D is ca 0.001 eV. This makes it possible for this compound to function as a direct bandgap material. This bandgap properties require further research to understand how it works in the real condition. Table 1 summarizes the band parameters obtained from the calculated band structures of studied compounds.

### 3.3. Optical properties

Fig. 3 shows the absorption coefficients and the imaginary part of the dielectric function for the three perovskites and their stable polymorphs. The peak for Y- $CsPbI_3$ seen at 3.5 eV is in agreement with experimental literature. When lead is substituted with Sn, we get the expected red shift in absorption coefficient [9]. For $CsSn_{0.5}Pb_{0.5}I_3$ we anticipated an absorbance coefficient with a maximum in between the other two. However, we found the maximum peak to be blue shifted compared to that of both $CsSnI_3$ and $CsPbI_3$. In addition, we found the maximum peak value for $CsSn_{0.5}Pb_{0.5}I_3$ to be higher than that of the other two perovskites.

Moving on to the imaginary part of the dielectric function, we see once again that by combining $CsSnI_3$ and $CsPbI_3$ into $CsSn_{0.5}Pb_{0.5}I_3$ the maximum peak position is shifted towards higher energies (blue shifted) instead of being found in between the maximum peaks of $CsSnI_3$ and $CsPbI_3$ respectively. The

**Table 1**
Calculated bandgap values, space groups, Mulliken population and BOP for the perovskites based on the two different approximations.

| Phase | Space group | Bandgap (eV) | | Type of bandgap | Mulliken population charges | BOP |
|---|---|---|---|---|---|---|
| | | GGA | HSE06 | | | |
| α-$CsSnI_3$ | *Pm-3m* | 0.500 | 0.870 | Direct | Cs: 0.61, Sn: 0.08,<br>I: −0.23 | 0.47 (Sn-I) |
| Y-$CsSnI_3$ | *Pnma* | 0.650 | 1.017 | Direct | Cs: 0.66, Sn: 0.26,<br>I1: −0.39, I2: −0.17, I3: −0.17 | −0.56 (Sn-I)<br>0.33 (Sn-i)<br>−1.69 (Cs-I) |
| β-$CsSnI_3$ | *P4/mbm* | 0.671 | 1.060 | Direct | Cs: 0.66, Sn: 0.19,<br>I1: −0.23, I2: −0.31 | 0.16 (Sn-I) |
| γ-$CsSnI_3$ | *Pnma* | 2.030 | 2.670 | Indirect | Cs: 0.58, Sn: 0.25,<br>I1: −0.35, I2: −0.24 | −0.10 (Sn-I)<br>−0.30 (Cs-I) |
| $CsPbI_3$ | *Pnma* | 1.500 | 2.170 | Direct | Cs: 0.69, Pb: 0.47,<br>I1: −0.25, I2: −0.42, I3: −0.49 | −0.64 (Pb-I)<br>−0.62 (Cs-I) |
| $CsPbI_3$ | *Pm-3m* | 1.503 | 2.0934 | Direct | Cs: 0.67, Pb: 0.48,<br>I: −0.34 | −0.58 (Pb-I)<br>−0.81 (Cs-I) |
| $CsSn_{0.5}Pb_{0.5}I_3$ | *Pnma* | 2.05 | 2.713 | Indirect/direct | Cs: 0.68 to 0.71,<br>Sn: 0.25, Pb: 0.47,<br>I: −0.26 to −0.48 | 0.25 (Sn-I)<br>0.08 (Sn-I)<br>−0.73 (Pb-I)<br>−1.37 (Cs-I)<br>−1.05 (Cs-Pb) |

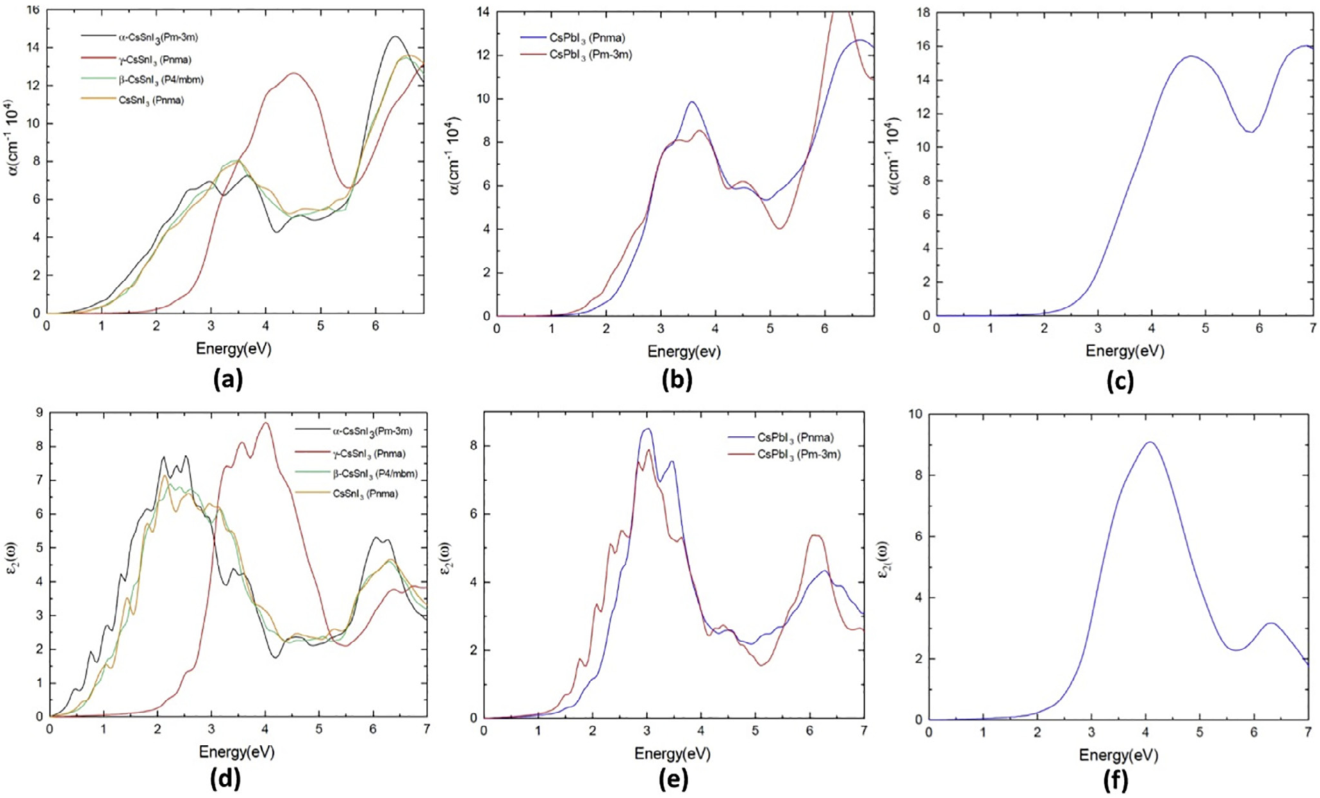

**Fig. 3.** Calculated absorption coefficients for (a) different polymorphs of $CsSnI_3$, (b) $CsPbI_3$ and (c) $CsSn_{0.5}Pb_{0.5}I_3$, and imaginary part of the complex dielectric function for (d) different polymorphs of $CsSnI_3$, (e) $CsPbI_3$ and (f) $CsSn_{0.5}Pb_{0.5}I_3$. We used HSE06 for these calculations.

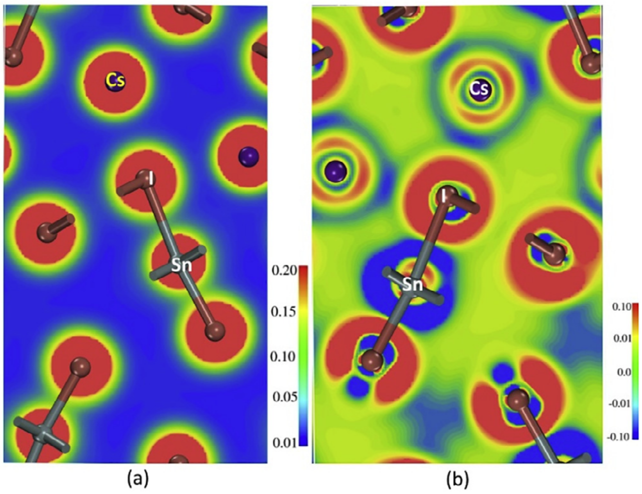

**Fig. 4.** Calculated valence-electron-density map (a), and (b) charge transfer plot for Y-$CsSnI_3$.

maximum value rises from 7.6 ω and 8.5 ω for $CsSnI_3$ and $CsPbI_3$ respectively to 9.2 ω for $CsSn_{0.5}Pb_{0.5}I_3$. This indicates that electromagnetic radiation will travel further into the material before being absorbed.

### 3.4. Chemical bonding

Based on the charge distribution plots for $CsSnI_3$ reported in Fig. 4, it is clear that the electrons resides around the individual atoms. Furthermore, the spherically-shaped charge distribution indicates that the bonding between Sn – I, Sn – Cs and Cs – I is primarily ionic. The charge transfer map reveals a polar character to the compound with depletion of charge around the Cs and Sn atoms. Although Mulliken analysis is more qualitative than quantitative it has proven useful in the analysis of chemical bonds [10]. Our bond overlap population (BOP) values are low, which supports our findings of ionic binding. $CSPbI_3$ displays the same ionic trend, with an even stronger charge depletion around the Cs and Pb atoms. The BOP analysis confirms the ionic bonding with its low values. However, for $CsSn_{0.5}Pb_{0.5}I_3$ we have the charge primarily distributed around the Sn and I atoms with little charge around Cs and Pb. Once again, we get low BOP values indicating an ionic nature of the bonds. The charge transfer plot indicates towards a slight polar character as charge gathers around the I atoms, however in general the atoms share the charge.

The Mullikan population charges for the Cs site is around +0.65e for all three compounds, confirming what is seen in the charge distribution plot that Cs does not fully donate its one valence electron to I, Pb or Sn in any of the configurations. For I the charges varies from −0.17e to −0.49e depending on the configuration, while Pb and Sn is consistent over the various configurations with charges of around 0.47e and 0.25e respectively. In other words, Cs, Pb and Sn all donate parts of their valence electrons to the I atoms.

## 4. Conclusion

In conclusion, we demonstrated that $CsSnI_3$ could be stabilized in four different polymorphs, three of which contain a direct bandgap ideal for photovoltaic applications. By adding Pb to the perovskite to create $CsSn_{0.5}Pb_{0.5}I_3$, we found that although this the new perovskite has an indirect bandgap, it could work as a direct bandgap material due to the lower electron-hole distance in the Z-D region. In general, we found that by combining $CsSnI_3$ and $CsPbI_3$ we got a new compound with different electronic and optical structure in addition to different chemical bonding. Based on this it could be viable to combine various compounds in an attempt to end up with an optimal compound for photovoltaic applications.

## Acknowledgements

The authors gratefully acknowledge the Western Norway University of Applied Sciences for financially support, and the Research Council of Norway for providing the computer time at the Norwegian supercomputer facilities (under the project numbers NN2867K and NN2875k). The authors also acknowledge F. Bianchini for fruitful discussions.

## References

[1] X. Qiu, B. Cao, S. Yuan, X. Chen, Z. Qiu, Y. Jiang, Q. Ye, H. Wang, H. Zeng, J. Liu, M. G. Kanatzidis, From unstable $CsSnI_3$ to air-stable $Cs_2SnI_6$: a lead-free perovskite solar cell light absorber with bandgap of 1.48 eV and high absorption coefficient, Sol. Energy Mater. Sol. Cells 159 (2016) 227–234.

[2] M. Ahmad, G. Rehman, L. Ali, M. Shafiq, R. Iqbal, R. Ahmad, T. Khan, S. Jalali-Asadabadi, M. Maqbool, I. Ahmad, Structural, electronic and optical properties of $CsPbX_3$ (X = Cl, Br, I) for energy storage and hybrid solar cell applications, J. Alloy. Compd. 705 (2017) 828–839.

[3] I. Chung, J.H. Song, J. Im, J. Androulakis, C.D. Malliakas, H. Li, A.J. Freeman, J.T. Kenney, M.G. Kanatzidis, $CsSnI_3$: semiconductor or metal? High electrical conductivity and strong near-infrared photoluminescence from a single material. High hole mobility and phase-transitions, J. Am. Chem. Soc. 134 (20) (2012) 8579–8587.

[4] G. Kresse, J. Furthmüller, Efficient iterative schemes for ab initio total-energy calculations using a plane-wave basis set, Phys. Rev. B 54 (16) (1996) 11169–11186.

[5] J.P. Perdew, K. Burke, M. Ernzerhof, Generalised gradient approximation made simple, Phys. Rev. Lett. 77 (18) (1996) 3865.

[6] J. Heyd, G.E. Scuseria, Efficient hybrid density functional calculations in solids: assessment of the Heyd-Scuseria-Ernzerhof screened Coulomb hybrid functional, J. Chem. Phys. 121 (3) (2004) 1187–1192.

[7] K. Yamada, S. Funabiki, H. Horimoto, T. Matsui, T. Okuda, S. Ichiba, Structural phase transitions of the polymorphs of $CsSnI_3$ by means of rietveld analysis of the X-ray diffraction, Chem. Lett. 20 (5) (1991) 801–804.

[8] D.M. Trots, S.V. Myagkota, High-temperature structural evolution of caesium and rubidium triiodoplumbates, J. Phys. Chem. Solids 69 (10) (2008) 2520–2526.

[9] T.C. Jellicoe, J.M. Richter, H.F. Glass, M. Tabachnyk, R. Brady, S.E. Dutton, A. Rao, R.H. Friend, D. Credgington, N.C. Greenham, M.L. Bohm, Synthesis and optical properties of lead-free cesium tin halide perovskite nanocrystals, J. Am. Chem. Soc. 138 (9) (2016) 2941–2944.

[10] R.S. Mulliken, Electronic population analysis on LCAO–MO molecular wave functions, J. Chem. Phys. 23 (10) (1955) 1833–1840.

# $Cs_2AgBiBr_6$ AS A MIXED ANION PEROVSKITES FOR PHOTOVOLTAIC APPLICATIONS: A FIRST-PRINCIPLE STUDY

---

C. P. Wanniarachchi, H. Eidsvåg, T. Arunasalam, P. Ravirajan, D. Velauthapillai, and P. Vajeeston

*In materialstoday: PROCEEDINGS*, volume 64, Part 5, pages 1783-1788, 2022

Materials Today: Proceedings 64 (2022) 1783–1788

Contents lists available at ScienceDirect

Materials Today: Proceedings

journal homepage: www.elsevier.com/locate/matpr

# $Cs_2AgBiBr_6$ as a mixed anion perovskites for photovoltaic applications: A first-principle study

W.A. Chapa Pamodani Wanniarachchi [a,b], Håkon Eidsvåg [b], Thevakaran Arunasalam [a], Punniamoorthy Ravirajan [a], Dhayalan Velauthapillai [b], Ponniah Vajeeston [c,*]

[a] Clean Energy Research Laboratory (CERL), Department of Physics, University of Jaffna, Jaffna 40000, Sri Lanka
[b] Faculty of Engineering, Western Norway University of Applied Sciences, 5020 Bergen, Norway
[c] Department of Chemistry, Center for Materials Science and Nanotechnology, University of Oslo Box 1033, Blindern, N-0315 Oslo, Norway

## ARTICLE INFO

*Article history:*
Available online 8 July 2022

*Keywords:*
$Cs_2AgBiBr_6$
Optoelectronic properties
Bandgap
Cubic
Tetragonal

## ABSTRACT

*Ab initio* calculations were performed for cubic Fm-3 m (225) and tetragonal (I4/m) phases for $Cs_2AgBiBr_6$(CaB2). We used the Vienna Ab Initio Simulation Package (VASP) to calculate the ground state properties using two different exchange-correlation functionals, namely the Generalized gradient approximation method (GGA) and the screened hybrid functional as proposed by Heyd, Scuseria, and Ernzerhof (HSE06) method. Tetragonal $Cs_2AgBiBr_6$ phase was stabilized in the tetragonal phase. The bandgap ($E_g$) was calculated using HSE06 for the polymorphs optimized at the PBE level and it is found that they belong to the indirect bandgap. The calculated bandgap for cubic and tetragonal phases in HSE06 for $Cs_2AgBiBr_6$ were 1.97 eV, and 2.4 eV, respectively. The character of chemical bonding in $CaB_2$ is discussed based on electronic structures, charge density, charge transfer, and bond overlap population analyses.

Selection and peer-review under responsibility of the scientific committee of the Functional Materials for Energy, Environment and Biomedical Applications.

## 1. Introduction

Crystalline silicon is the most used material for photovoltaic applications. However, over the last decade, perovskite solar cells made from metal halide perovskite materials are cheaper and potentially more efficient than other thin-film solar cells [1]. Perovskite is one of the common crystal structures that can be found on Earth[2]. Due to its optimal structural and electronic properties, perovskites have received much attention in a variety of thematic areas and applications such as ferroelectricity, piezoelectricity, high-Tc superconductivity, ferromagnetism, giant magnetoresistance, photocatalysis, and photovoltaics [3]. The Pb-based hybrid perovskites ($APbI_3$) have been in focus in solar cell applications as they offer high power conversion efficiencies (PCE) comparable to the well-established Si-based solar cells where *A* could be an organic cation of $CH_3NH_3$ (Methylammonium) [4] or $(H_2N)_2CH^+$ (Formamidinium) [5]. Recent studies show that ($FAPbI_3$) formamidinium lead triiodide gives a high efficiency of 25.6% which is stable for 450 h [6]. $Pb^{2+}$ is responsible for unique optoelectronic properties of $APbI_3$ perovskites because of its 6 $s^2$, $p^0$ configuration, which results in lone 6 $s^2$ pairs and inactive $6p^0$ states [7] and also the high symmetry nature of lead halide perovskite. Nevertheless, the toxicity of lead and the long-term device stability issues are the major barriers to limiting its commercialization. Lead toxicity can be eliminated by replacing Pb with the other group cations. Apart from $Pb^{2+}$, $Tl^{3+}$, and $Bi^{3+}$ also have the electronic configuration of 6 $s^2$ $6p^0$.

During the annealing process of $MAPbI_3$ ($M = CH_3$; $A = NH_3$), degradation is noted to occur at 85 °C in an inert atmosphere [9]. Experimentally, it is shown that mixing $MAPbI_3$ with a small quantity of inorganic cations such as $Cs^+$ with methylammonium ($CH_3NH_3^+$)/formamidinium ($CH_3(NH_2)_2^+$) results in a photostable material [10]. Cs metal halides are thus of interest and these were first synthesized already in 1893, and $CsPbI_3$ and $CsPbBr_3$ are shown to have thermal stability up to the melting point of 460 °C [11]. This makes Cs based metal halides interesting, and Pb(II) ion could also be replaced with the combination of monovalent cation $Ag^+$ and trivalent cation $Bi^{3+}$. Most of the theoretical and experimental studies have been carried out with the inorganic

---

* Corresponding author.
*E-mail addresses:* ponniahv@kjemi.uio.no, vajeeston.ponniah@smn.uio.no (P. Vajeeston).

https://doi.org/10.1016/j.matpr.2022.06.063
2214-7853/
Selection and peer-review under responsibility of the scientific committee of the Functional Materials for Energy, Environment and Biomedical Applications.

double perovskite of $Cs_2AgBiCl_6$ and $Cs_2AgBiBr_6$ [12]. All these studies are setup for optoelectronic applications which crystallize in cubic structure space group of Fm-3 m with an indirect bandgap. $Cs_2AgBiBr_6$ is shown to have good thermal and ambient stability without encapsulation[13]. A recent study reported that $Cs_2AgBiBr_6$ had high-hole mobility of 0.29 $cm^2s^{-1}V^{-1}$ in Field-Effect Transistor Applications [14]. However, there is limited discussion on the crystallography of $Cs_2AgBiBr_6$ and its impact on optoelectronic applications. In addition, the pressure[15] and the temperature[16] could influence the material to change its crystal structure and the electronic configuration. For example, at 122 K there is a phase transition between the room temperature cubic structure (Fm-3 m) and the low-temperature tetragonal phase(I4/m). This phase transition could affect the optical and electronic properties in terms of bandgap energies and the charge carrier lifetime[16]. At 4.5 GPa, cubic $Cs_2AgBiBr_6$ transfers to the tetragonal phase(I4/m) and they showed that beyond the 6.5Gpa the bandgap of the tetragonal phase narrows from 2.3 eV to 1.7 eV[15]. This leaves an interesting question regarding what structural changes we will see and how the optoelectronic properties would change in these phases.

## 2. Computational modelling

In this study, we focus on Cs2AgBiBr6, and the total energies of $Cs_2AgBiBr_6$ have been computed using the Vienna ab initio simulation package (VASP)[17]. The core states are described with potential generated through the projected augmented plane wave (PAW) method [18]. The exchange and correlation functions are treated within the GGA approach, using the approximation proposed by Perdew, Burke, and Ernzerhof (PBE)[19]. We optimized the atomic positions as well as the cell size and volume, minimizing both the stress tensor and the Hellman–Feynman forces with an overall force tolerance of $10^{-3}$ eV Å$^{-1}$. The HSE06 functional was used for computing the electronic structure. Our parameterization included a screened parameter of 0.2 Å$^{-1}$ and 30% mixing of the screened Hartree-Fock (HF) exchange with the PBE functional [20]. Fully converged results were obtained with a kinetic cut-off energy of 600 eV, and a $6 \times 6 \times 6$ $\Gamma$-centered Monkhorst-Pack grids for integration over the Brillouin zone. This setting was used in both PBE and HSE06 calculations. The vibrational properties were computed with the frozen phonon approach, using suitably large supercell of the optimized structures. The Phonopy software was used to calculate the phonon dispersion curve and the associated density of states [21]. An atomic displacement of 0.0075 Å was used, and displacements in opposite directions were considered to improve the overall accuracy of the calculation of the force constants.

### 2.1. Structural stability

To understand the relative stability between cubic and tetragonal phases, we perform the geometry optimization by using the Murnaghan equation of fitting, in which the total energy of the unit cell is minimized concerning the cell volume within the DFT framework [22].

$$E = E_0 + \frac{B_0}{B_0'}(V - V_0) - \frac{B_0 V_0}{B_0'(1 - B_0')}\left[\left(\frac{V}{V_0}\right)^{1-B_0'} - 1\right] \tag{1}$$

Where V is the primitive-cell volume, B is the bulk modulus, which provides the behavior of the crystal volume under hydrostatic pressure[23], and B' is its first pressure derivative. The zero indexes are the values at zero pressure[24].

The structural stability of the cubic and tetragonal phases has been studied with the GGA-PBE method.

The calculated energy volume curve clearly indicates that the tetragonal phase has a lower ground state energy than the cubic phase, see Fig. 1. This means the tetragonal phase of $Cs_2AgBiBr_6$ is more structurally stable than the cubic phase. The computed lattice parameters are given in below Table1.

#### 2.1.1. Dynamical stability

To understand the dynamical stability of the studied polymorphs of $Cs_2AgBiBr_6$, we carried out phonon calculations and these are the first such results reported. In addition to the total phonon density of states (PDOS), we also calculated the phonon dispersion curves, at the equilibrium volume. Along the high symmetry direction of the Brillouin zone for cubic and tetragonal variations are presented in Fig. 2 with their corresponding PDOS. From our study, we found that for the tetragonal structure all phonon modes are positive and this structure is dynamically stable. On the other hand, the cubic structure has several negative modes especially G-X, K-G-L, and U-X, and the cubic phase is dynamically unstable.

#### 2.1.2. Mechanical stability

Material's mechanical behavior could be explained by the elastic modulus. The relationship between the stress and strain can be described by Constitutive law within the elastic region and it can be simplified in Voigt notation [29].

$$\boldsymbol{\sigma_i} = \sum_{j=1}^{6} \boldsymbol{c_{ij}\varepsilon_{ij}} \tag{2}$$

The elastic constants describe the response to an applied force, as either applied strain or the required stress to maintain a certain deformation. Both stress and strain have three tensile and three shear components. Due to this, the elastic constants of a crystal can be described using a $6 \times 6$ symmetric matrix, having 27 components where 21 of which are independent [30]. Naturally, we can reduce the number of components by utilizing any existing symmetry in the material. A cubic crystal has only three independent

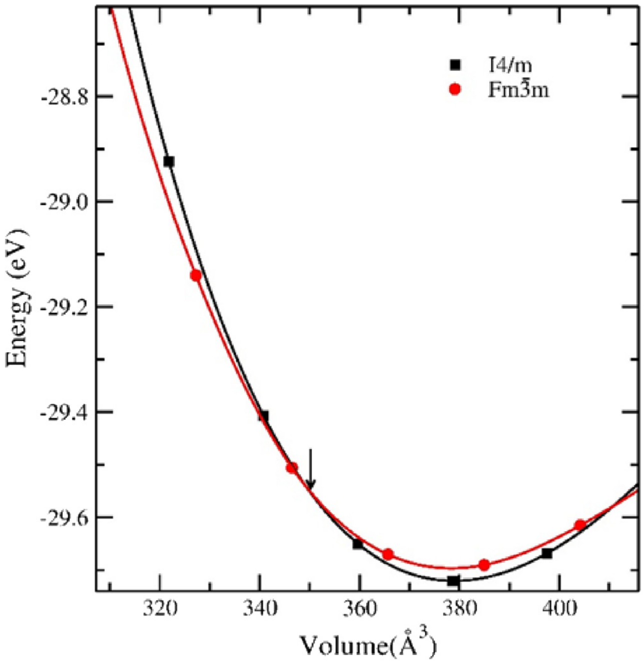

**Fig. 1.** The total energy as a function of the volume of $Cs_2AgBiBr_6$ halide double perovskite in cubic and tetragonal phases.

**Table 1**
Obtained equilibrium lattice parameters (in Å), using GGA.

| | $Cs_2AgBiBr_6$(Fm-3 m) | $Cs_2AgBiBr_6$(I4/m) |
|---|---|---|
| a | 11.4836,11.462[25], 11.25[26],11.53 [27],11.271[28] | 8.0428,7.844[25],7.879 [16] |
| c | | 11.6667,11.425 [25],11.323[16] |
| Volume/ $Å^3$ | 378 | 385 |

**Table 2**
The calculated single-crystal elastic constants Cij (in GPa), bulk modulus B (in GPa), shear modulus G (in GPa), Poisson's ratio (v), Young's modulus E (in GPa), Pugh's indicator B/G and Debye temperature ($T_D$, in K) for $Cs_2AgBiBr_6$ phases. Subscript V indicates the Voigt bound, R indicates the Reuss bound, and H indicates the Hill average.

| Phase | $Cs_2AgBiBr_6$ | |
|---|---|---|
| | Cubic | Tetragonal |
| $C_{ij}$ | $C_{11}$ = 25.409, 59.02[32],44.05[33],47.94[25], 38.74[34]<br>$C_{12}$ = 14.483, 13.37[32], 16.36[33], 10.75 [25],7.58[34]<br>$C_{44}$ = 6.301,8.15[32],6.56[33],5.13[25],7.46 [34] | $C_{11}$ = 23.826, 44.76 [25]<br>$C_{12}$ = 13.449, 32.02 [25]<br>$C_{13}$ = 13.802, 16.85 [25]<br>$C_{33}$ = 24.311, 62.75 [25]<br>$C_{44}$ = 4.237, 8.81 [25]<br>$C_{66}$ = 3.139, 11.62 [25] |
| $B_v$ | 18.13 | 17.12 |
| $B_R$ | 18.125 | 17.039 |
| $B_H$ | 18.125, 25.59[33] | 17.079 |
| $G_v$ | 5.97 | 4.38 |
| $G_R$ | 5.937 | 3.680 |
| $G_H$ | 5.951,8.89[33] | 4.032 |
| $E_V$ | 16.13 | 12.12 |
| $E_R$ | 16.057 | 10.298 |
| $E_H$ | 16.092 | 11.213 |
| $v_v$ | 0.35 | 0.38 |
| $v_R$ | 0.352 | 0.399 |
| $v_H$ | 0.352 | 0.391 |
| (B/G) | 3.04 | 4.24 |
| $T_D$ | 112.7,136[33],137.08[25] | 93.2,138.456[25], 114[35] |

elastic constants (C11, C12, and C44), each of which is representative of three deformations ($C_{12} = C_{13}$, $C_{11} = C_{33} = C_{31}$, $C_{44} = C_{66}$) [31]. The mechanical stability criteria is given as [25].

$$C_{44} > 0;\ C_{11} > C_{12};\ C_{11} + 2\,C_{12} > 0 \tag{3}$$

Cubic structure of $Cs_2AgBiBr_6$ fulfills mechanical stability criteria.

Tetragonal phase ($C_{11}$, $C_{33}$, $C_{44}$, $C_{66}$, $C_{12}$, and $C_{13}$)and its mechanical stability criteria [25] are discussed below and tetragonal structure of $Cs_2AgBiBr_6$ too satisfies the criteria.

$$C_{11} > 0,\ C_{33} > 0,\ C_{44} > 0,\ C_{66} > 0, C_{11} - C_{12} > 0,\ C_{11} + C_{33} - 2C_{13} > 0, 2(C_{11} + C_{12}) + C_{33} + 4C_{13} > 0 \tag{4}$$

Similar to the elastic constant tensor, the bulk (Bv, $B_R$) and the shear moduli (Gv, $G_R$) provide information regarding the material hardness under deformation. These parameters are computed for the considered phases of $Cs_2AgBiBr_6$ and listed in Table2. These properties can be directly computed from the elastic constants tensors. Using Pugh's criterion which is based on the value B/G ratio, we could determine whether the material is ductile or brittle. When B/G > 1.75, it shows the character of ductility and when it is less than 1.75, the material shows brittle character. Our calculations show that $Cs_2AgBiBr_6$ is ductile in both phases[25].

### 2.2. Electronic properties

The bandstructure of $Cs_2AgBiBr_6$ was calculated, to investigate whether it is an insulator, a conductor, or a semiconductor. Electronic calculations were done using GGA and HSE06 methods. The band structures E(k) were computed on a discrete k mesh along with the high-symmetry directions in the Brillouin zone (BZ). In Fig. 3, we can clearly see that both $Cs_2AgBiBr_6$ phases are semiconductors with an indirect bandgap. The lowest of the conduction band (CBM) lies at the L-point whereas the valence band maxima (VBM) lies at X point in cubic phase materials. For the tetragonal phase, CBM lies at X and VBM lies at L high symmetric points in the first BZ. As expected the band gap values obtained with GGA are underestimations, thus we perform more accurate calculations with HSE06 [36]. When the symmetry of the material decreases from cubic to tetragonal phase, the bandgap value increases, which proven by our computed electronic bandgaps in Table 3 of both the cubic and tetragonal phases of $Cs_2AgBiBr_6$. This

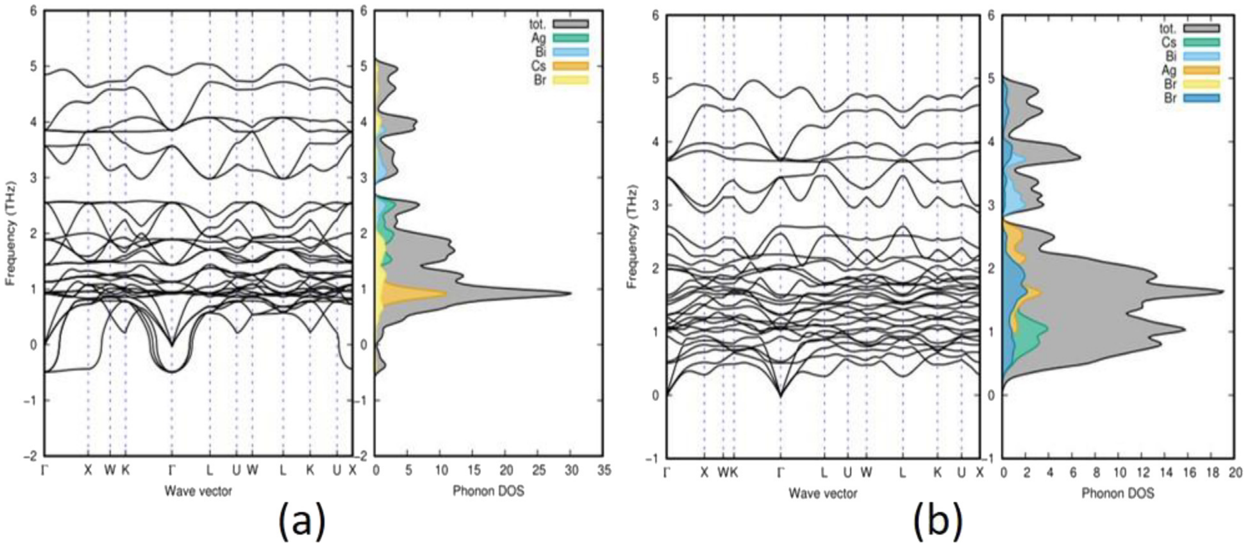

**Fig. 2.** Phonon dispersion curves of $Cs_2AgBiBr_6$ halide double perovskite for **a** cubic and **b** tetragonal phases.

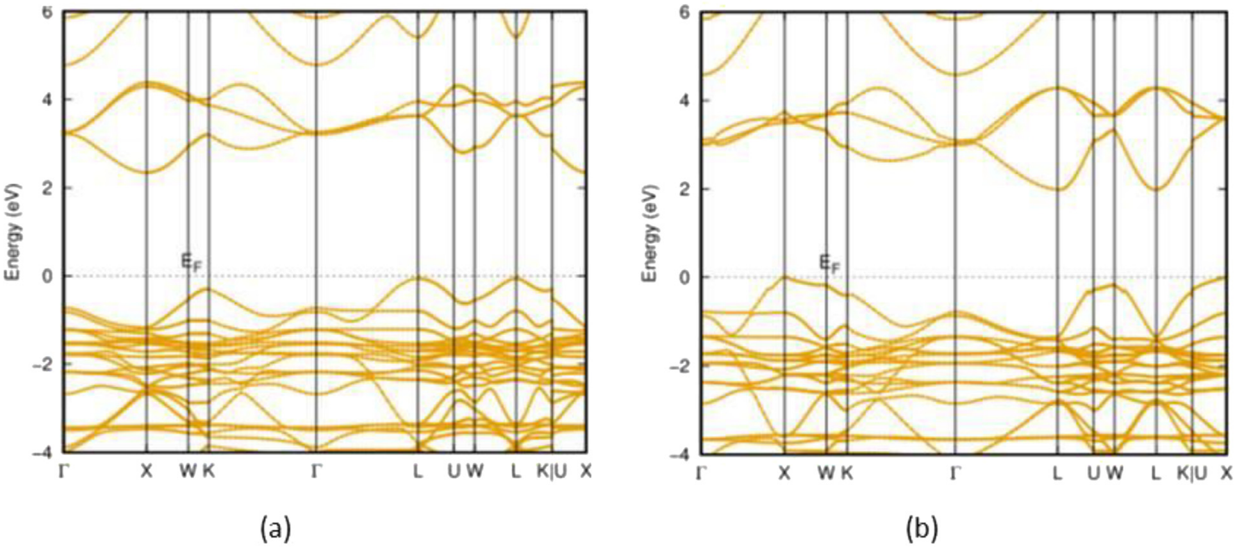

**Fig. 3.** Band diagrams of $Cs_2AgBiBr_6$ halide double perovskite for **a** cubic and **b** tetragonal phases.

**Table 3**
Calculated bandgaps (eV) of $Cs_2AgBiBr_6$ halide double perovskite (cubic and tetragonal phases) using GGA and HSE06.

| | $Cs_2AgBiBr_6$(Fm-3 m) | $Cs_2AgBiBr_6$(I4/m) |
|---|---|---|
| **GGA** | **1.35,** 1.42[22], 1.26[25] | **1.49**, 2.06[25] |
| **HSE06** | **1.97,** 2.06[38], 1.79[39]<br>2.59, 1.34, 2.4[40]<br>1.98[41] | **2.4,** 2.3[15] |

indicates that structural distortion and symmetry deterioration lead to bandwidth narrowing and energetic stability[37] (See Table 4.).

The electrons' motion can be described with the definite position and momentum under the assumption of all moving charge carriers that are close to the band edge in terms of a semi-classical approach. We could explain the mobility of moving charge carriers using effective mass (m*) as it is a quantity that is used to simplify band structures by modeling the behavior of a free particle with that mass. This formula was derived by using approximations in Taylor's series expansion at the band edge in the region of parabolic fitting[42].

$$m^* = \hbar^2 \left(\frac{d^2E}{dK^2}\right)^{-1} \tag{5}$$

m* is the effective mass of the charge carrier, k is the wave vector, ħ is the reduced Planck constant and E is the energy of an electron at wave vector k in that band. The parabolic nature (second derivate) of the bandstructure plot, reveals which one of the structures that will have the highest electron mobility as the second derivative and the effective mass are inversely proportional. In Fig. 3, the bandstructures of HSE06 show a high dispersive (large second derivative) of the CBM compared to the VBM. This indicates a lower effective mass of electrons compared to the effective mass of the holes. Using the transfer rate of charge carriers (v), we can discover the nature of the mobility or conductivity based on the following equation.

$$v = \frac{\hbar k}{m^*} \tag{6}$$

As the equation illustrates, electron mass increases when the mobility is reduced, and vice versa. Our calculations show that both $Cs_2AgBiBr_6$ structures have higher electron mobility ($m_e$) compared to hole mobility ($m_h$). Effective mass calculations for both cubic and tetragonal structures are presented in different directions in the BZ.

**Table 4**
Effective masses ($m_e$, $m_h$) calculated for cubic and tetragonal $Cs_2AgBiBr_6$ double perovskite using GGA approximation.

| Direction | $Cs_2AgBiBr_6$(Fm-3 m) | | $Cs_2AgBiBr_6$(I4/m) | |
|---|---|---|---|---|
| | $m_e^*/m_o$ | $m_h^*/m_o$ | $m_e^*/m_o$ | $m_h^*/m_o$ |
| (G → K) | 0.376 | 0.447 | 1.020 | 0.293 |
| (G → L) | 0.310 | 0.366 | 1.027 | 0.364 |
| (G → X) | 0.328 | 0.678 | 1.566 | 0.421 |

### 2.3. Chemical bonding

To gain a better understanding of bonding interactions, the calculated valence-charge-density distribution was used. Both cubic and tetragonal polymorphs are having almost a similar feature as shown in Fig. 4. According to the charge-density distribution at the Cs, Ag, Bi, and Br sites, it is evident that the highest charge density resides in the immediate vicinity of the nuclei. As also evidenced from the almost spherical charge distribution, the bonding between Cs and Br is virtually pure ionic and between Cs-Br is predominantly ionic. The type of charge distribution seen in Fig. 4 (b–d) appears to be typical for ionic compounds. On the other hand, the charge distribution at the Ag, Br, and Bi sites are of non-spherical nature and the considerable charges are shared between the Ag-Br, and Bi-Br atoms (see Fig. 4 a and c), which implies that there must be a significant amount of covalent character in the Bi-Br, Ag-Br bonds. Fig. 4 (e–h) depicts the charge transfer (i.e., the electron distribution in the compound minus the electron density of the corresponding overlapping free atoms) in $Cs_2AgBiBr_6$. This illustration further reconfirms that the charge has been depleted from the Cs and Ag sites and are transferred to the Br sites. The overall message is that $Cs_2AgBiBr_6$ is to be regarded as a mixed bonding substance.

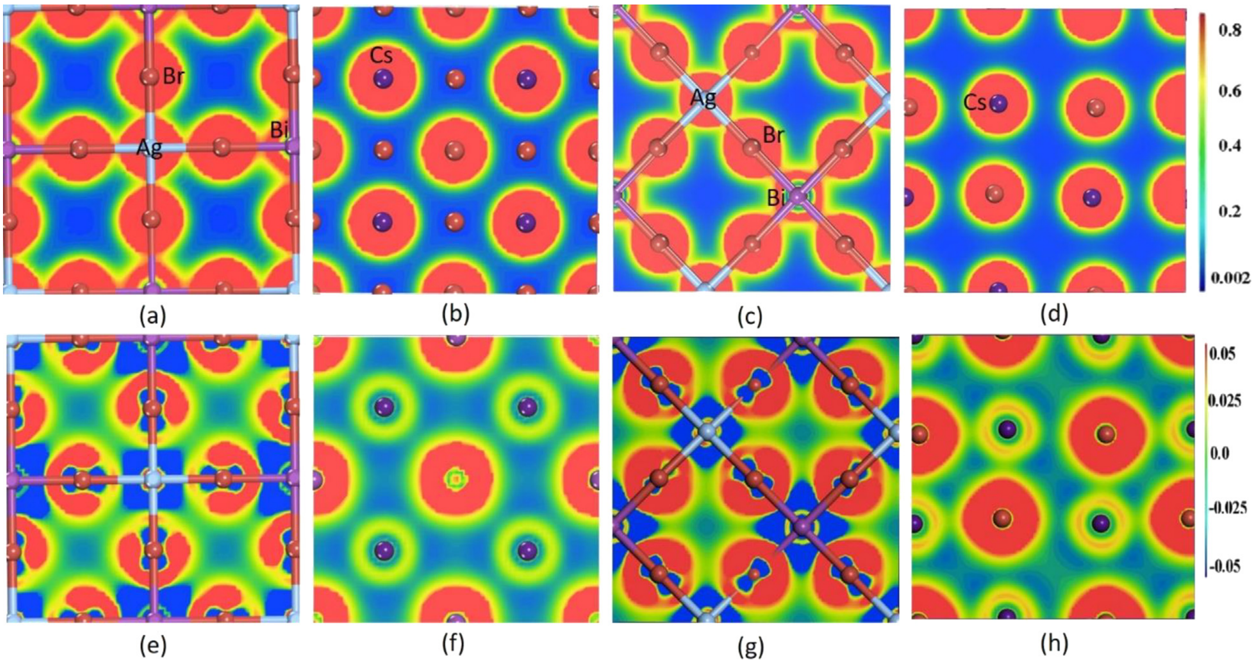

(a) (b) (c) (d)

(e) (f) (g) (h)

**Fig. 4.** Calculated charge density (a–d), and charge transfer (e–h), plots along (1 0 0) for $Cs_2AgBiBr_6$ in the cubic (charge density a, b; charge transfer e, f) and tetragonal (charge density c, d; charge transfer g, h) structure.

## 3. Conclusion

Structural stability, electronic structure, and chemical bonding of the cubic and tetragonal phase of $Cs_2AgBiBr_6$ were investigated using the PAW potential method by adopting the first principle calculations.

The main results obtained are as follows:

- Tetragonal phase of $Cs_2AgBiBr_6$ is found to be more stable than its cubic blende phase.
- The phonon calculations reveal that the tetragonal structure of $Cs_2AgBiBr_6$ is found to be dynamically stable while the cubic structure shows the negative frequency making it dynamically unstable.
- The single crystal elastic tensor calculations show that both phases are mechanically stable and both are ductile.
- Our band structure calculations show that the $Cs_2AgBiBr_6$ polymorphs are semiconductors with indirect bandgaps.
- Our calculations show cubic and tetragonal phases of $Cs_2AgBiBr_6$ that have the potential to be used in flexible optoelectronic applications

## CRediT authorship contribution statement

**W.A. Chapa Pamodani Wanniarachchi:** Conceptualization, Software, Investigation, Writing – original draft. **Håkon Eidsvåg:** Writing – review & editing. **Thevakaran Arunasalam:** Conceptualization, Supervision. **Punniamoorthy Ravirajan:** Conceptualization, Writing – review & editing, Supervision, Project administration, Funding acquisition. **Dhayalan Velauthapillai:** Funding acquisition, Supervision, Conceptualization, Writing – review & editing, Project administration. **Ponniah Vajeeston:** Supervision, Conceptualization, Methodology, Software, Investigation, Writing – review & editing.

## Declaration of Competing Interest

The authors declare that they have no known competing financial interests or personal relationships that could have appeared to influence the work reported in this paper.

## Acknowledgments

This research was funded by the the Capacity Building and Establishment of Research Consortium (CBERC), grant number LKA-3182-HRNCET, and Higher Education and Research collaboration onNanomaterials for Clean Energy Technologies (HRNCET) project, Grant Number NORPART/2016/10237.

The authors gratefully acknowledge the Research Council of Norway for providing the computer time (project number NN2867k) at the Norwegian supercomputer facility.

## References:

[1] T. Leijtens, G.E. Eperon, N.K. Noel, S.N. Habisreutinger, A. Petrozza, H.J. Snaith, Stability of metal halide perovskite solar cells, Adv. Energy Mater. 5 (20) (2015) Oct, https://doi.org/10.1002/AENM.201500963.

[2] R. M. Hazen, S. S. American, and N. June, "Perovskites gives rise to materials that have a wide array of electrical properties," *Sci. Am.*, vol. 258, no. 6, pp. 74–81, 1988, [Online]. Available: http://www.jstor.org/stable/24989124

[3] G. Volonakis, M.R. Filip, A.A. Haghighirad, N. Sakai, B. Wenger, H.J. Snaith, F. Giustino, Lead-free halide double perovskites via heterovalent substitution of noble metals, J. Phys. Chem. Lett. 7 (7) (2016) 1254–1259, https://doi.org/10.1021/acs.jpclett.6b00376.

[4] A. Kojima, K. Teshima, Y. Shirai, T. Miyasaka, Organometal halide perovskites as visible-light sensitizers for photovoltaic cells, J. Am. Chem. Soc. 131 (17) (2009) 6050–6051, https://doi.org/10.1021/ja809598r.

[5] A.M. Peir?, P. Ravirajan, K. Govender, D.S. Boyle, P. O'Brien, D.D.C. Bradley, J. Nelson, J.R. Durrant, Hybrid polymer/metal oxide solar cells based on ZnO columnar structures, J. Mater. Chem. 16 (21) (2006) 2088.

[6] J. Werner, "Perovskite/Silicon Tandem Solar Cells: Toward Affordable Ultra-High Efficiency Photovoltaics ?," vol. 8659, pp. 1–161, 2018

[7] E. S.-P. review and undefined 1926, "An undulatory theory of the mechanics of atoms and molecules," *APS*, Accessed: Apr. 17, 2020. [Online]. Available: https://journals.aps.org/pr/abstract/10.1103/PhysRev.28.1049.

[9] B. Conings *et al.*, "Intrinsic Thermal Instability of Methylammonium Lead Trihalide Perovskite," 2015, doi: 10.1002/aenm.201500477

[10] D.P. McMeekin, G. Sadoughi, W. Rehman, G.E. Eperon, M. Saliba, M.T. Hörantner, A. Haghighirad, N. Sakai, L. Korte, B. Rech, M.B. Johnston, L.M. Herz, H.J. Snaith, A mixed-cation lead mixed-halide perovskite absorber for tandem solar cells, Science 351 (6269) (2016) 151–155.

[11] R.J. Sutton, G.E. Eperon, L. Miranda, E.S. Parrott, B.A. Kamino, J.B. Patel, M.T. Hörantner, M.B. Johnston, A.A. Haghighirad, D.T. Moore, H.J. Snaith, Bandgap-tunable cesium lead halide perovskites with high thermal stability for efficient solar cells, Adv. Energy Mater. 6 (8) (2016) 1502458.

[12] M. R. Filip, S. Hillman, A. Haghighirad, H. J. Snaith, and F. Giustino, "Band Gaps of the Lead-Free Halide Double Perovskites Cs 2 BiAgCl 6 and Cs 2 BiAgBr 6," 2016, doi: 10.1021/acs.jpclett.6b01041.

[13] C. Wu *et al.*, "CommuniCation The Dawn of Lead-Free Perovskite Solar Cell: Highly Stable Double Perovskite Cs 2 AgBiBr 6 Film," 2017, doi: 10.1002/advs.201700759

[14] G. Abiram, F. Heidari Gourji, S. Pitchaiya, P. Ravirajan, T. Murugathas, and D. Velauthapillai, "Air processed Cs 2 AgBiBr 6 lead-free double perovskite high-mobility thin-film field-effect transistors," 123AD, doi: 10.1038/s41598-022-06319-z

[15] Q. Li, Y. Wang, W. Pan, W. Yang, B.o. Zou, J. Tang, Z. Quan, High-pressure band-gap engineering in lead-free Cs 2 AgBiBr 6 double perovskite, Angew. Chem. 129 (50) (2017) 16185–16189, https://doi.org/10.1002/ange.201708684.

[16] L. Schade *et al.*, "Structural and Optical Properties of Cs 2 AgBiBr 6 Double Perovskite," vol. 2, p. 14, 2022, doi: 10.1021/acsenergylett.8b02090

[17] G. Kresse, D. Joubert, From ultrasoft pseudopotentials to the projector augmented-wave method, Phys. Rev. B - Condens. Matter Mater. Phys. 59 (3) (1999) 1758–1775, https://doi.org/10.1103/PhysRevB.59.1758.

[18] Q. Xu *et al.*, "SPARC: Simulation Package for Ab-initio Real-space Calculations," *SoftwareX*, vol. 15, p. 100709, 2021, doi: 10.1016/j.softx.2021.100709.

[19] J.P. Perdew, K. Burke, M. Ernzerhof, Generalized gradient approximation made simple, Phys. Rev. Lett. 77 (18) (1996) 3865–3868, https://doi.org/10.1103/PhysRevLett.77.3865.

[20] J. Heyd, G.E. Scuseria, Efficient hybrid density functional calculations in solids: assessment of the Heyd-Scuseria-Ernzerhof screened Coulomb hybrid functional ARTICLES YOU MAY BE INTERESTED IN, J. Chem. Phys. 121 (3) (2004) 1187–1192, https://doi.org/10.1063/1.1760074.

[21] A. Togo, I. Tanaka, First principles phonon calculations in materials science, Scripta Mater. 108 (2015) 1–5, https://doi.org/10.1016/j.scriptamat.2015.07.021.

[22] N. Rajeev Kumar, R. Radhakrishnan, Electronic, optical and mechanical properties of lead-free halide double perovskites using first-principles density functional theory, Mater. Lett. 227 (2018) 289–291, https://doi.org/10.1016/j.matlet.2018.05.082.

[23] S. Wu, S.S. Naghavi, G.H. Fecher, C. Felser, A critical study of the elastic properties and stability of heusler compounds: phase change and tetragonal <i>X<sub>2</sub>YZ</i> compounds, J. Mod. Phys. 09 (04) (2018) 775–805, https://doi.org/10.4236/jmp.2018.94050.

[24] C. M. You, "Periodic Hartree-Fock linear combination of crystalline orbitals calculation of the structure , equation of state and elastic properties of titanium diboride Periodic Hartree – Fock linear combination of crystalline orbitals calculation of the structure ," 2000.

[25] T. Bellakhdar, Z. Nabi, B. Bouabdallah, B. Benichou, H. Saci, Ab initio study of structural, electronic, mechanical and optical properties of the tetragonal Cs2AgBiBr6 halide double perovskite, Appl. Phys. A 128 (2) (2022), https://doi.org/10.1007/s00339-022-05276-8.

[26] A.H. Slavney, T. Hu, A.M. Lindenberg, H.I. Karunadasa, A bismuth-halide double perovskite with long carrier recombination lifetime for photovoltaic applications, J. Am. Chem. Soc. 138 (7) (2016) 2138–2141, https://doi.org/10.1021/jacs.5b13294.

[27] N.R. Kumar, R. Radhakrishnan, Electronic, optical and mechanical properties of lead-free halide double perovskites using first-principles density functional theory, Mater. Lett. 227 (2018) 289–291, https://doi.org/10.1016/j.matlet.2018.05.082.

[28] E.T. McClure, M.R. Ball, W. Windl, P.M. Woodward, Cs2AgBiX6 (X = Br, Cl): new visible light absorbing, lead-free halide perovskite semiconductors, Chem. Mater. 28 (5) (Mar. 2016) 1348–1354, https://doi.org/10.1021/acs.chemmater.5b04231.

[29] N. Xu, "VASPKIT : A User-friendly Interface Facilitating High-throughput Computing and Analysis Using VASP Code," no. August 2019, 2021.

[30] P. Vajeeston, H. Fjellvåg, First-principles study of structural stability, dynamical and mechanical properties of Li 2 FeSiO 4 polymorphs, RSC Adv. 7 (27) (2017) 16843–16853.

[31] M. Rasukkannu, D. Velauthapillai, and P. Vajeeston, "Hybrid Density Functional Study of Au 2 Cs 2 I 6 ," no. December, 2018, doi: 10.3390/en11123457.

[32] L. Dong, S. Sun, Z. Deng, W. Li, F. Wei, Y. Qi, Y. Li, X. Li, P. Lu, U. Ramamurty, Elastic properties and thermal expansion of lead-free halide double perovskite Cs2AgBiBr 6, Comput. Mater. Sci. 141 (2018) 49–58, https://doi.org/10.1016/J.COMMATSCI.2017.09.014.

[33] N. Guechi, A. Bouhemadou, S. Bin-omran, A. Bourzami, L. Louail, and F. Abbas Setif, "Elastic, Optoelectronic and Thermoelectric Properties of the Lead-Free Halide Semiconductors Cs2AgBiX 6 (X = Cl, Br): Ab Initio Investigation," *J. Electron. Mater.*, vol. 47, 1900, doi: 10.1007/s11664-017-5962-2.

[34] M.N. Islam, J. Podder, T. Saha, P. Rani, Semiconductor to metallic transition under induced pressure in Cs 2 AgBiBr 6 double halide perovskite: a theoretical DFT study for photovoltaic and optoelectronic applications, RSC Adv. 11 (39) (2021) 24001–24012, https://doi.org/10.1039/d1ra03161a.

[35] L. S. J. Zelewski, y, z J. M. Urban, y A. Surrente, y D. K. Maude, y A. Kuc, x P. Schade, x R. D. Johnson, x M. Dollmann, x P. K. Nayak, x H. J. Snaith, y and M. Radaelli, x R. Kudrawiec, z R. J. Nicholas, x P. Plochocka, and Baranowski, "Revealing the nature of photoluminescence emission in the metal-halide double perovskite Cs2AgBiBr6," *Mater. Chem. C*, vol. 7, pp. 8350–8356, 2019.

[36] P. Borlido, T. Aull, A.W. Huran, F. Tran, M.A.L. Marques, S. Botti, Large-Scale benchmark of exchange–correlation functionals for the determination of electronic band gaps of solids, J. Chem. Theory Comput. 15 (9) (2019) 5069–5079, https://doi.org/10.1021/acs.jctc.9b00322.

[37] T. Umebayashi, K. Asai, T. Kondo, A. Nakao, Electronic structures of lead iodide based low-dimensional crystals, Phys. Rev. B - Condens. Matter Mater. Phys. 67 (15) (2003), https://doi.org/10.1103/PhysRevB.67.155405.

[38] E.T. McClure, M.R. Ball, W. Windl, P.M. Woodward, Cs2AgBiX6 (X = Br, Cl): new visible light absorbing, lead-free halide perovskite semiconductors, Chem. Mater. 28 (5) (2016) 1348–1354, https://doi.org/10.1021/acs.chemmater.5b04231.

[39] C.N. Savory, A. Walsh, D.O. Scanlon, Can Pb-free halide double perovskites support high-efficiency solar cells?, ACS Energy Lett 1 (5) (2016) 949–955, https://doi.org/10.1021/acsenergylett.6b00471.

[40] M.A. Ghebouli, T. Chihi, B. Ghebouli, M. Fatmi, Study of the structural, elastic, electronic and optical properties of lead free halide double perovskites Cs2AgBiX6(X = Br, Cl), Chinese J. Phys. 56 (1) (2018) 323–330, https://doi.org/10.1016/j.cjph.2018.01.004.

[41] G. Liu *et al.*, "Extending Absorption of Cs 2 AgBiBr 6 to Near-Infrared Region (≈1350 nm) with Intermediate Band," 2021, doi: 10.1002/adfm.202109891

[42] D. Akinwande, Y. Nishi, H.-S.-P. Wong, An analytical derivation of the density of states, effective mass, and carrier density for achiral carbon nanotubes, IEEE Trans. Electron Devices 55 (1) (2008) 289, https://doi.org/10.1109/TED.2007.911078.

## *Further reading*

[8] R. Mohan, "Green bismuth," 2010. doi: 10.1038/nchem.609.

PAPER D

# IN-DEPTH FIRST-PRINCIPLE STUDY ON NOVEL $MoS_2$

---

H. Eidsvåg, M. Rasukkannu, D. Velauthapillai, and P. Vajeeston

*In RSC Advances*, volume 11, pages 3759-3769, 2021

RSC Advances

PAPER

Cite this: *RSC Adv.*, 2021, **11**, 3759

# In-depth first-principle study on novel $MoS_2$ polymorphs†

Håkon Eidsvåg, *[a] Murugesan Rasukkannu,[a] Dhayalan Velauthapillai[a] and Ponniah Vajeeston[b]

Received 11th December 2020
Accepted 8th January 2021

DOI: 10.1039/d0ra10443d

rsc.li/rsc-advances

Molybdenum disulphide ($MoS_2$) is a rising star among transition-metal dichalcogenides in photovoltaics, diodes, electronic circuits, transistors and as a photocatalyst for hydrogen evolution. A wide range of $MoS_2$ polymorphs with varying electrical, optical and catalytic properties is of interest. However, in-depth studies on the structural stability of the various $MoS_2$ polymorphs are still lacking. For the very first time, 14 different $MoS_2$ polymorphs are proposed in this study and in-depth analysis of these polymorphs are carried out by employing first-principle calculations based on density functional theory (DFT). In order to investigate the feasibility of these polymorphs for practical applications, we employ wide range of analytical methods including band structure, phonon and elastic constant calculations. Three of the polymorphs were shown to be unstable based on the energy volume calculations. Among the remaining eleven polymorphs ($1T_1$, $1T_2$, 1H, 2T, 2H, $2R_1$, $2R_2$, $3H_a$, $3H_b$, 3R and 4T), we confirm that the $1T_1$, $1T_2$, $2R_2$ and 3R polymorphs are not dynamically stable based on phonon calculations. Recent research suggests that stabilising dopants (*e.g.* Li) are needed if 1T polymorphs to be synthesised. Our study further shows that the remaining seven polymorphs are both dynamically and mechanically stable, which make them interesting candidates for optoelectronics applications. Due to high electron mobility and a bandgap of 1.95 eV, one of the $MoS_2$ polymorphs ($3H_b$-$MoS_2$) is proposed to be the most promising candidate for these applications.

## Introduction

Recent research has established transition-metal dichalcogenides (TMDs) as a promising material within several fields.[1] This is due to their unique optical, electronic and structural properties, which are dependent on the layered structure of the TMDs.[2–4] Molybdenum disulphide ($MoS_2$) is perhaps the most well-known TMD with an indirect electronic bandgap of 1.2 eV (experimental value for bulk $MoS_2$),[5] which is surprising as it has a graphene-like polymorph. This is mainly because the electronic properties for TMDs are based on filling the d orbitals, in contrast to graphene and silicon where it is the hybridization of s and p orbitals that lays the foundation for the electronic properties.[6] In addition to the low bandgap, $MoS_2$ is a low-cost material; it has a high surface-to-volume ratio and an abundance of active sites making it attractive in several fields.[7] Currently, $MoS_2$ is known for its properties as a lubricant[8] and lately in photovoltaic (PV) cells,[9] as a photocatalyst for hydrogen evolution,[10] as gas or biosensors[11,12] and as a transistor that can operate at room temperature.[4] Especially within photocatalytic water splitting $MoS_2$ is seen as the potential successor to $TiO_2$ photocatalysts due to the tuneable bandgaps, its high charge carrier mobility, high transparency and excellent chemical stability.[7]

The $MoS_2$ polymorphs consists of a layer of Mo (transition metal) sandwiched between two layers of S (chalcogens) and strong covalent bonds are present within the sandwich, while the interlayer bonds between two layers are van der Waals bonds.[13] Depending on the coordinate configuration $MoS_2$ can exist in different phases including 2H, 3R, 1T, 1T′, 1T″, *etc.*[14,15] Amongst these, two phases stand out in terms of favourable structural properties: 2H $MoS_2$ is a thermodynamically stable phase with A–B–A sandwich layers that occurs at ambient pressure conditions, this is also the most commonly used phase. 1T is a metastable phase, A–B–C layers, and has not been strictly determined due to a lack of a strict structural refinement. Another important distinction between the two phases is that 1T is metallic while 2H is a semiconductor/insulator.[11]

An alternative to adding dopants to transform materials from insulators to metals is utilising high pressure during the synthesis. It is well known that bilayer sheets of $MoS_2$ go through a semiconductor–metal transition upon vertical compressive pressure. Early research suggests that bulk $MoS_2$ could metallize under pressure as they found that the bandgap

---

[a] *Department of Computing, Mathematics and Physics, Western Norway University of Applied Sciences, Inndalsveien 28, Box 5063, Bergen, Norway. E-mail: heid@hvl.no*

[b] *Center for Materials Science and Nanotechnology, Department of Chemistry, University of Oslo, Box 1033 Blindern N-0315, Oslo, Norway*

† Electronic supplementary information (ESI) available. See DOI: 10.1039/d0ra10443d

shrinks due to a negative pressure coefficient of resistivity, $dE_G/dP < 0$.[16] Unfortunately, the structural transition is unknown, and it requires further research.

Most of the work done on $MoS_2$ by the research community so far is experimental with focus on synthesis, characterization and application of the material as a photocatalyst.[7,11,12,17–20] However, over the last years, we have seen a rise in computational work,[21] including a pioneering work by Byskov *et al.*[22] As the $MoS_2$ structure can easily be modified by changing the stacking sequence and/or the layer distance, a variety of $MoS_2$ polymorphs could be synthesised. However, a fundamental understanding of how these modifications will affect the structural stability of the material is still lacking. This knowledge is of utmost importance as different configurations have different properties, making them viable for a diverse range of applications. So far, the challenges have been to synthesise $MoS_2$ polymorphs and to identify the stacking sequences. In this study, we propose as many as 14 different $MoS_2$ polymorphs and carry out in-depth theoretical analysis on their properties based on DFT calculations. We verify analytically how the different layers and coordinate configuration of $MoS_2$ affect the stability and electronic properties of the bulk material. For the very first-time, direct comparison between calculated Raman and IR spectra for pure 1T-$MoS_2$ and 2H-$MoS_2$. The main objective of this study is to explore the possible metastable phases of $MoS_2$ and their relative stability.

## Method of calculations

All the calculations were performed within the periodic density functional theory framework, as it is implemented in the VASP code.[23–27] The interaction between the core (Mo: [Kr] $4d^5$ $5s^1$, and S: [Ne] $3s^2$ $3p^4$) and the valence electrons were described using the projector-augmented wave (PAW) method.[26,28] In order to speed up our structural optimisation process, the initial structures were optimised with the Perdew–Burke–Ernzerhof (PBE) exchange–correlation functional.[27] The obtained PBE level optimised structures were further optimised with the DFT/vdW-DF2 method and based on this, the energy volume curves were generated.[29–31] Our previous calculations suggested[32] that structural parameters in oxides could be reliably predicted only by using large energy-cut off to guarantee basis-set completeness. Hence, we have used a cut-off of 600 eV. The atoms were deemed to be relaxed when all atomic forces were less than 0.02 eV $\text{Å}^{-1}$ and the geometries were assumed to get optimized when the total energy converged to less than 1 meV between two consecutive geometric optimization steps. The electronic properties were computed by using the screened hybrid functional as proposed by Heyd, Scuseria and Ernzerhof (HSE06) for the polymorphs optimized at the PBE level.[33] If not specified differently, we used a Monkhorst–Pack $9 \times 9 \times 9$ *k*-mesh for the structural optimization and the electronic polymorph studies. Band polymorphs were computed by solving the periodic Kohn–Sham equation on ten *k*-points along each direction of high symmetry of the irreducible part of the first Brillouin zone.

The supercell method is used for phonon calculations.[34] The VASP code is used to calculate the real space force constants of supercells, and the PHONOPY[35] code is used to calculate the phonon frequencies from the force constants on a supercell consisting of at least 32 atoms in all systems. In order to get the force-constant matrices for each binary system, every atom is displaced by a finite displacement of 0.01 Å in *x*-, *y*- and *z*-direction. Strict energy convergence criteria of ($10^{-8}$ eV) and $4 \times 4 \times 4$ *k*-points were used for the force constant calculations. After getting the force-constant matrices, the dynamical matrix is built for different **q** vectors in the Brillouin zone. The eigenvalues of phonon frequencies and eigenvectors of phonon modes are found by solving the dynamical matrix. The thermodynamic properties require summations over the phonon eigenvectors which is implemented in the PHONOPY code. We have checked the dynamical stability of all systems, and no imaginary modes are observed in the polymorphs. The thermal properties, including heat capacity, free energy and entropy, were obtained from the calculated PhDOS. The phonon band polymorphs figures for all the studied systems have also been added to the ESI under SI3 and SI4.† Our study is then completed by evaluating the mechanical stability by computing the single-crystal elastic constants. A set of strains ($-0.015$ $-0.010$ $-0.005$ 0.000 0.005 0.010 0.015) is applied to the crystal cell, and the stress tensor is calculated. The elastic constants are then evaluated by linear fitting of the stress–strain curve using VASPKIT.[36]

## Results and discussion

### Structural stability and optimization

Structurally, $MoS_2$ can be regarded as strongly bonded two-dimensional S–Mo–S layers or sandwiches which are loosely coupled to one another by relatively weak van der Waals-type forces. Within a single S–Mo–S sandwich, the Mo and S atoms create two-dimensional hexagonal arrays. Depending on the relative alignment of the two S-atom sheets within a single S–Mo–S sandwich, two distinct two-dimensional crystal polymorphs are obtained. In one, the metal atoms are octahedrally coordinated by six neighbouring S atoms, whereas in the other, the coordination of the metal atoms is trigonal prismatic. Variations in the stacking sequence and registry of successive S–Mo–S sandwiches along the hexagonal *c* axis lead to a large number of crystal polymorphs or polytypes in three dimensions. These are referred to as the 1T, 2H, 3R, $4H_a$, $4H_b$ and 6R phases. In this abbreviated notation, the integer indicates the number of S–Mo–S sandwiches per unit cell along the hexagonal *c* axis and T, H, and R denote trigonal, hexagonal, and rhombohedral symmetries, respectively. Variations in the stacking sequence like A, A′, B, B′, C, C″, *etc.* (for more details see Fig. 3) and variation in the layer–layer distances means we can tune these compounds into several modifications. In order to understand the relative stability of these modifications, we have considered the following 14 polymorphs and they have been used as starting inputs in the structural optimization calculations (number of formula units; and Materials Project ID are given in parenthesis; low energy polymorph identified this work is

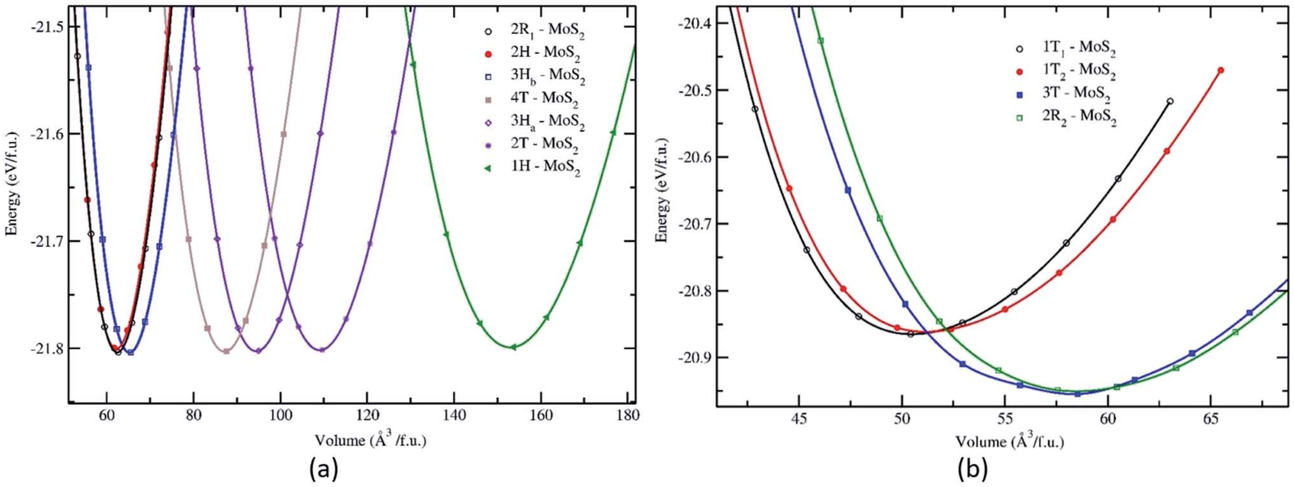

Fig. 1 Calculated total energy as a function of the volume of the unit cell for the different phases and polymorphs of $MoS_2$. The total energy *vs.* volume curve for the group A (a) and group B (b). All the energy volumes are normalized to one formula unit (f.u.).

highlighted as bold letters): $R3m$ (1, 1434, $\mathbf{2R_1}$), $P\bar{3}m1$ (4, 1027525, **4T**), $P6_3/mmc$ (2, 2815, **2H**); $P\bar{6}m2$ (3, 1025874, $\mathbf{3H_a}$), $P\bar{3}m1$ (3, 1023939, **2T**), $P6_3/mmc$ (6, 1018809, $\mathbf{3H_b}$), $P\bar{6}m2$ (1, 1023924, **1H**), $Pmmn$ (18, 990083), $F\bar{4}3m$ (4, 11780), $R\bar{3}m$ (1, 558544, **3T**), $P\bar{3}m1$ (1, 1238797, $\mathbf{2R_2}$), $I\bar{4}2d$ (2, 1042086), $P\bar{3}$ (1, $\mathbf{1T_2}$) and $P\bar{3}m1$ (1, $\mathbf{1T_1}$). However, the following polymorphs $Pmmn$ (18, 990083), $F\bar{4}3m$ (4, 11780) and $I\bar{4}2d$ (2, 1042086) are omitted from the rest of the analysis. This is because their energy-volume data are far away from the others as presented in Fig. 1, they are also unstable compared to the other polymorphs.

The structural stability of the several different phases of $MoS_2$ has been studied to find the most stable phase and polymorph for further investigation and research. Our first step was to perform a total energy calculation as a function of volume for all the phases. Based on this calculation we divided the phases into two different groups (according to the energetics), group A and group B. The polymorphs in group A, shown in Fig. 1a, are (space group and space group number are given in the parenthesis): 2R$_1$-$MoS_2$ ($P3m1$; 156), 2H-$MoS_2$ ($P6_3/mmc$; 194), 3H$_b$-$MoS_2$ ($P6_3/mmc$; 194), 4T-$MoS_2$ ($P\bar{3}m1$; 164), 3H$_a$-$MoS_2$ ($P\bar{6}m2$; 187), 2T-$MoS_2$ ($P\bar{3}m1$; 164), and 1H-$MoS_2$ ($P\bar{6}m2$; 187). In group B, as shown in Fig. 1b, we have placed the following polymorph models: 1T$_1$-$MoS_2$ ($P\bar{3}$; 164), 1T$_2$-$MoS_2$ ($P\bar{3}m1$; 164), 3T-$MoS_2$ ($R\bar{3}m$; 166) and 2R$_2$-$MoS_2$ ($P\bar{3}m1$; 164). It should be noted that the 2H and 3R variants the Mo–S coordination is trigonal prismatic and the layers stacking sequence are significantly different (see Fig. 2).[37] On the other hand, the 1T variants consist of $MoS_2$ layers with almost perfectly ordered $MoS_6$ octahedra.[37]

As shown in Fig. 1, the total energy curves clearly show that group A is energetically favoured over group B with an energy difference of 0.8 eV. In general, we see that our first principle calculations coincide well with experimental results.[38–41] Interestingly, we observe in Fig. 1a that the various polymorphs in group A seem to have the same minimum energy, although with a varying range of volume. Which indicates that $MoS_2$ can easily be found in any of these variants. The calculated positional and lattice constants of different polymorphs are presented in Table 1. From the space group numbers and names, we see that all group B polymorphs and three of the group A polymorphs are trigonal, while the last four group A polymorphs are hexagonal. From Fig. 1 it is clear that the hexagonal polymorphs have a wider spread in volume than the trigonal polymorphs. However, the involved energy difference in group A is small, and it is hard to conclude whether trigonal or hexagonal polymorphs are more energetically favourable. Regarding the group

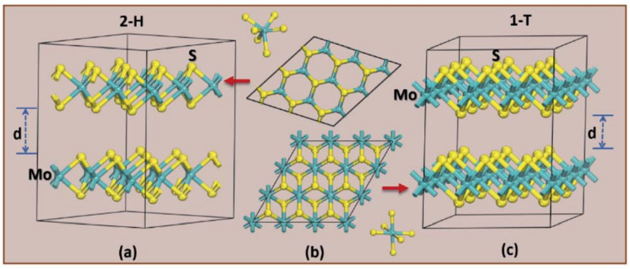

Fig. 2 The difference in crystal structure for 2H (a) and 1T (c) $MoS_2$ polymorphs. (b) Shows a top-down look on the hexagonal polymorph of 2H (top) and 1T (bottom).

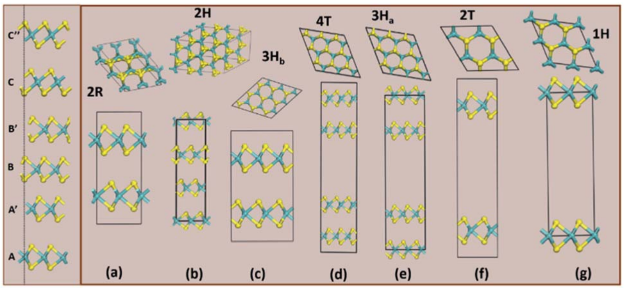

Fig. 3 The column on the left shows the various stacking sequences (A, A′, B, B′, C, C″) for $MoS_2$. On the right side, we see how the group A polymorphs are stacked.

B polymorphs, three of them are trigonal crystal systems and of them 3T-$MoS_2$ has the lowest energy. Another point of interest is how the volume affects the energy of the unit cell. For group A there is little difference between the energies and all the polymorphs could be synthesised (based on Fig. 1). However, for group B it appears that the two larger polymorphs (with regards to volume) are more energy favourable compared to the smaller ones.

Nonetheless, Fig. 1 only gives an indication of which polymorphs $MoS_2$ prefers to be in, which is why we calculated the elasticity constants and phonon densities.

### Band structure

In order to verify which of these polymorphs are viable for *e.g.* photocatalytic processes, photovoltaic cells or in transistors we carry out in depth electronic calculations. Materials with semiconducting properties could be used to absorb visible light, while metals could be used as conductors. Our HSE06 bandgap calculations, presented in Fig. 4, clearly states that the group B polymorphs are metallic, which is in line with previous findings.[42] However, the polymorphs in group A are semiconductors with indirect bandgaps as the valence band is at the $\Gamma$ point, while the conduction band minimum is although accurate in its band polymorph description, underestimates the bandgap value. GGA calculations are less accurate than HSE06 (ref. 43 and [44]) but they are cheaper in computing time, making them excellent for first-time investigations and gives an idea about the bandgap configuration. This is confirmed when the GGA results are compared to the HSE06 calculations, which are also presented in Table 2. Our HSE06 results coincide well with the experimentally found bandgaps for $MoS_2$ which are within the range of 1.2–1.9 eV.[7] The valence bands and conduction bands for the polymorphs in both groups are derived from Mo-d and S-p states.[21] This shows that the group A $MoS_2$ is well suited for photovoltaic solar cell and photocatalytic water splitting applications.

The electron effective mass is an indication of the mass of the structure/particle when it responds to forces. It can be used

Table 1 Polymorph and lattice parameters for the investigated polymorphs

| Polymorph | Cell constants (Å) | Coordinates |
|---|---|---|
| 2R$_1$-$MoS_2$ ($P3m1$; 156) | $a = 3.1887$, $b = 3.1887$, $c = 21.3444$ | Mo$_1$ (1$a$): 0, 0, 0<br>Mo$_2$ (1$a$): 2/3, 1/3, 1/3<br>Mo$_3$ (1$a$): 1/3, 2/3, 2/3<br>S1 (1$a$): 0, 0, 0.5928<br>S2 (1$a$): 2/3, 1/3, 0.9271<br>S3 (1$a$): 1/3, 2/3, 0.2604<br>S4 (1$a$): 0, 0, 0.7400<br>S5 (1$a$): 2/3, 1/3, 0.0733<br>S6 (1$a$): 1/3, 2/3, 0.4067 |
| 2T-$MoS_2$ ($P\bar{3}m1$; 164) | $a = 3.1891$, $b = 3.1891$, $c = 24.8987$ | Mo (2$d$): 1/3, 2/3, 0.8505<br>S1 (2$d$): 1/3, 2/3, 0.2122<br>S2 (2$d$): 1/3, 2/3, 0.0868 |
| 4T-$MoS_2$ ($P\bar{3}m1$; 164) | $a = 3.1889$, $b = 3.1889$, $c = 39.7944$ | Mo$_1$ (2$d$): 1/3, 2/3, 0.0936<br>Mo$_2$ (2$d$): 1/3, 2/3, 0.7193<br>S1 (2$d$): 1/3, 2/3, 0.3199<br>S2 (2$d$): 1/3, 2/3, 0.9457<br>S3 (2$d$): 1/3, 2/3, 0.2414<br>S4 (2$d$): 1/3, 2/3, 0.8672 |
| 1H-$MoS_2$ ($P\bar{6}m2$; 187) | $a = 3.1881$, $b = 3.1881$, $c = 17.4639$ | Mo (1$a$): 0, 0, 0<br>S (2$h$): 1/3, 2/3, 0.0894 |
| 3H$_a$-$MoS_2$ ($P\bar{6}m2$; 187) | $a = 3.1890$, $b = 3.1890$, $c = 32.3461$ | Mo$_1$ (2$h$): 1/3, 2/3, 0.7698<br>Mo$_2$ (1$e$): 2/3, 1/3, 0<br>S1 (2$h$): 1/3, 2/3, 0.0483<br>S2 (2$i$): 2/3, 1/3, 0.2785<br>S3 (2$i$): 2/3, 1/3, 0.8181 |
| 3H$_b$-$MoS_2$ ($P6_3/mmc$; 194) | $a = 3.1890$, $b = 3.1890$, $c = 14.8916$ | Mo (2$d$): 2/3, 1/3, 1/4<br>S (4$f$): 2/3, 1/3, 0.8549 |
| 2H-$MoS_2$ ($P6_3/mmc$; 194) | $a = 3.1779$, $b = 3.1779$, $c = 14.1156$ | Mo (2$b$): 0, 0, 1/4<br>S (4$f$): 2/3, 1/3, 0.3608 |
| 2R$_2$-$MoS_2$ ($P\bar{3}m1$; 164) | $a = 3.1798$, $b = 3.1798$, $c = 6.5738$ | Mo (1$b$): 0, 0, 1/2<br>S (2$d$): 2/3, 1/3, 0.2575 |
| 3T-$MoS_2$ ($R\bar{3}m$; 166) | $a = 3.2060$, $b = 3.2060$, $c = 19.7232$ | Mo (3$a$): 1/3, 2/3, 2/3<br>S (6$c$): 0, 0, 0.2534 |
| 1T$_1$-$MoS_2$ ($P\bar{3}$; 164) | $a = 3.1900$, $b = 3.1900$, $c = 5.9450$ | Mo (1$a$): 0, 0, 0<br>S (2$d$): 1/3, 2/3, 0.2488 |
| 1T$_2$-$MoS_2$ ($P\bar{3}m1$; 164) | $a = 3.1900$, $b = 3.1900$, $c = 5.9450$ | Mo (1$a$): 0, 0, 0<br>S (2$d$): 1/3, 2/3, 0.2488 |

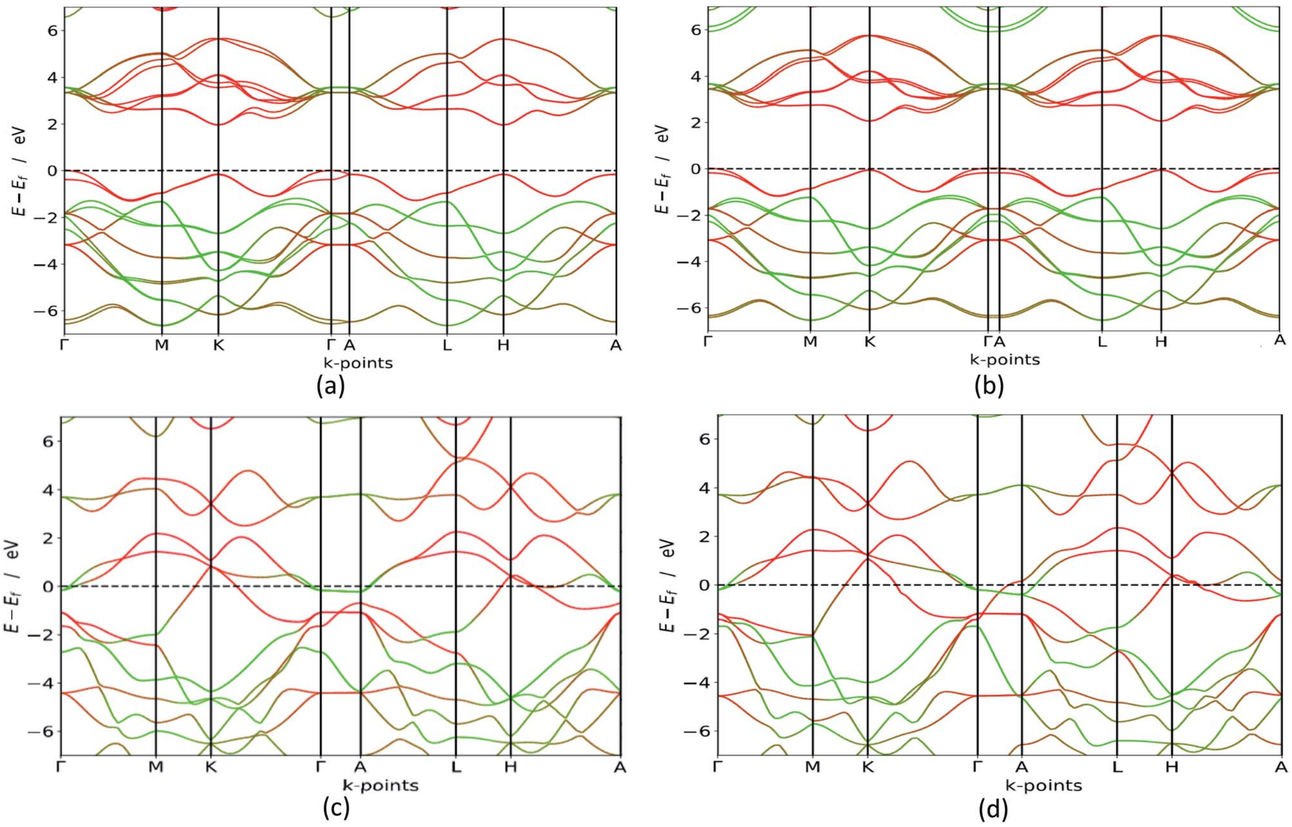

Fig. 4 HSE06 band structure (colour code: green line – S, red line – Mo) for $3H_b$ in (a), 1H in (b), $2R_2$ in (c) and $1T_1$ in (d). We see that the group A polymorphs are semiconductors with a bandgap between 1.8 and 2.1 eV, while the group B polymorphs are metallic. The other polymorphs are seen in the ESI.†

to calculate electron mobility and diffusion constants. We used Fonari and Sutton's effective mass calculator for our calculations.[45] The higher curvature of the conduction band minimum compared to the valence band minimum indicates a higher hole effective mass than the electron effective mass. This indicates that $MoS_2$ has higher electron mobility, compared to the hole mobility, due to the lower electron effective mass.

We calculated the effective masses for the semiconductor (group A) polymorphs to confirm the findings in the band structures. In general, the effective masses of electrons and holes are relevant for the mobility, electrical resistivity, quantum confinement,[46,47] and free-carrier optical response in semiconductor materials. For the first time, effective masses are presented for seven different polymorphs of $MoS_2$ and are shown in Table 2. We have compared them to a $2H$-$MoS_2$ polymorph from Rasmussen *et al.* to get an indication of how our polymorphs measure up against previously studied polymorphs, and we see that our values are lower for electrons.[48] This is due to the different approximations ($G_0W_0$) used in the calculations.

Table 2 Calculated GGA and HSE06 total bandgaps ($E_g$; in eV), type of bandgap, the effective mass of electrons and effective mass of holes. The effective masses are calculated along the $K$–$\Gamma$ $K$-path

| Name | GGA band gap (eV) | HSE06 band gap (eV) | The effective mass of electrons $m_e^*(m_e)$ in $K$–$\Gamma$ directions | Effective mass of holes $m_h^*(m_e)$ in $K$–$\Gamma$ direction | Effective mass of hole $m_h^*(m_e)$ in $\Gamma$–$A$ and $\Gamma$–$M$ directions | Type of bandgap |
|---|---|---|---|---|---|---|
| $2R_1$-$MoS_2$ | 1.41 | 1.87 | 0.50 | 0.57 | 0.92 ($\Gamma$–$A$) | Indirect |
| $2H$-$MoS_2$ | 1.42 | 1.94 | 0.51 | 0.55 | 0.86 ($\Gamma$–$A$) | Indirect |
| $3H_b$-$MoS_2$ | 1.45 | 1.95 | 0.22 | 0.03 | 1.01 ($\Gamma$–$A$) | Indirect |
| $4T$-$MoS_2$ | 1.48 | 1.96 | 0.48 | 0.56 | 1.82 ($\Gamma$–$M$) | Indirect |
| $3H_a$-$MoS_2$ | 1.50 | 1.98 | 0.47 | 0.56 | 1.89 ($\Gamma$–M) | Indirect |
| $2T$-$MoS_2$ | 1.54 | 2.04 | 0.47 | 0.56 | 2.32 ($\Gamma$–$M$) | Indirect |
| $1H$-$MoS_2$ | 1.64 | 2.12 | 0.47 | 0.56 | 2.96 ($\Gamma$–$M$) | Indirect |
| $MoS_2$ (ref. 48) | 1.58 (LDA) | 2.48 ($G_0W_0$) | 0.55 | 0.53 | NA | NA |

For photocatalytic processes, the transfer of carriers to the reactive sites is easier with smaller effective masses.[49] Compared to 2H-$TiO_2$ ($1.4m_e$ and $5m_h$)[48] and 1T-$TiO_2$ ($8.2m_e$ and $1.1m_h$)[48] the electron mobility in $MoS_2$ is better than that of $TiO_2$. This combined with a much lower bandgap (3.2 eV for $TiO_2$ (ref. 50)) clearly show that $MoS_2$ is a better photocatalyst than $TiO_2$.

Further research on carrier transport characteristics is needed as the presence of valleys and defects in the polymorph, charge carrier scattering, reduced mean free path and elastic scattering time all influence the carrier mobility in the crystal.

### Phonon calculations

In order to understand the dynamical stability of the studied polymorphs we carried out phonon calculations. In addition to the total phonon density of states (PDOS), we calculated the phonon dispersion curves, at the equilibrium volume, along the high symmetry direction of the Brillouin zone for all the polymorphs and these variations are presented in Fig. 5 with their corresponding PDOS. None of the group A polymorphs displays any soft/negative modes, which means that they should be dynamically stable. Whereas the group B polymorphs show the presence of negative modes, making them dynamically unstable. This shows that going from 2H polymorphs to 1T polymorphs creates a less stable polymorph, which is supported by experimental findings.[51]

The total phonon density of states is calculated at the equilibrium volumes for the different polymorphs of $MoS_2$. From Fig. 5 we observe that the two group B polymorphs (all four can be found in SI 4a–d†) contains unstable (imaginary) phonon modes while for the two group A (SI 3a–g† for the remaining polymorphs) polymorphs we only have stable (real) modes. These findings indicate that the group A polymorphs are dynamically stable, while the group B polymorphs are dynamically unstable. All group A polymorphs have a similar PDOS, this combined with the low energy difference between phases indicates that one can easily modify one polymorph into another using temperature or pressure. This explains why depending on different synthesis routes it is possible to stabilise different $MoS_2$ polymorphs.[7] Not surprisingly we find that $1T_2$-$MoS_2$ and $1T_1$-$MoS_2$ have very similar wave vectors, PDOS and partial PDOS, as they are both trigonal and share the same lattice parameters (see Table 1) although they are in different space groups. Comparing 3T-$MoS_2$ to $2R_2$-$MoS_2$ there is a slight difference

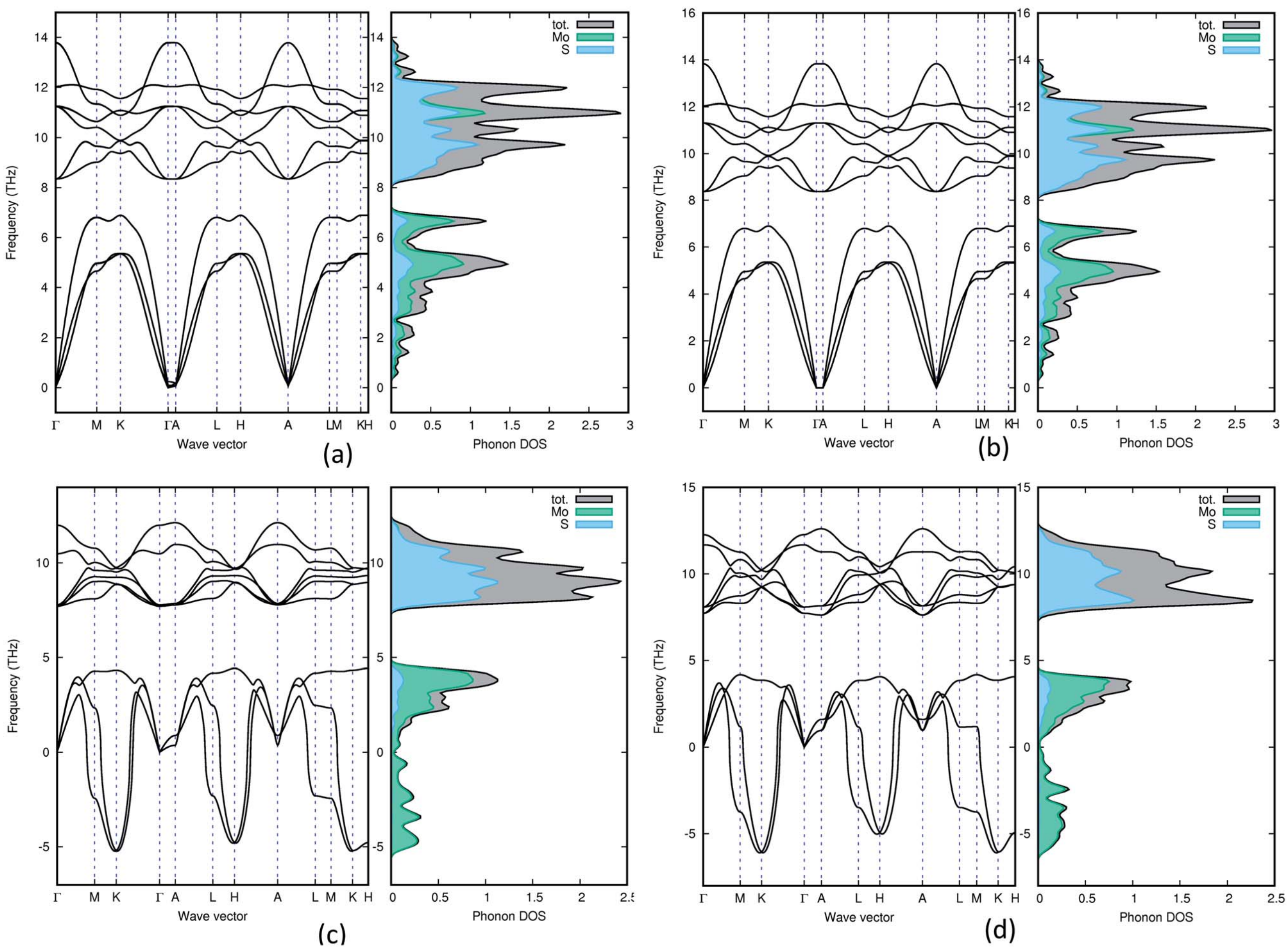

Fig. 5 Phonon density of states for $3H_b$ (a), 1H (b), $2R_2$ (c) and $1T_1$ (d). Both group B polymorphs ($2R_2$ and $1T_1$) contains negative frequencies, which means that they are dynamically unstable.

in where the maximum peaks are, this could be explained by the difference in the volume of the unit cell. For group A, they all seem quite similar, except for 2H-$MoS_2$ which have a slightly different distribution in the higher frequency area compared to the others. Indicating that it has fewer occupied states in the 11 THz regions compared to the others.

The partial PDOS are included in Fig. 5 as well and it is clear that the smaller atom S dominates the higher frequencies (above 8 THz), while the heavier Mo atom dominates the lower frequencies. However, some S modes appear in the low-frequency region and for the 2H polymorphs, a few Mo modes appear above 10 THz.

## Mechanical stability

We have computed the single-crystal elastic constants to help us understand the mechanical stability of the investigated $MoS_2$ phases. The elastic constants of a material describe how the material responds to an applied force, as either applied strain or the required stress to maintain a certain deformation. Both stress and strain have three tensile and three shear components. Due to this, the elastic constants of a crystal can be described using a 6 × 6 symmetric matrix, having 27 components where 21 of those are independent. Naturally, we can reduce the number of components by utilising any existing symmetry in the polymorph. The 6 × 6 matrix is known as $C_{ij}$, the stiffness matrix, and it can be used to calculate properties as the bulk modulus, Poisson coefficient and Lame constants. Previous studies show that the accuracy of the DFT elastic constant is within 10% of the experimental values.[63] Hence, we can safely use our results to predict the elastic constant for our $MoS_2$ polymorphs.

For trigonal polymorphs the mechanical stability criteria of the elastic constants are:[64]

$$B_{T1} = C_{11} - C_{12} > 0$$

$$B_{T2} = (C_{11} + C_{12})C_{33} > 2C_{13}^2$$

$$B_{T3} = (C_{11} - C_{12})C_{44} > 2C_{14}^2$$

$$B_{T4} = C_{44} > 0$$

For the hexagonal polymorphs the stability criteria are:[64]

$$B_{H1} = C_{11} > |C_{12}|$$

$$B_{H2} = (C_{11} + C_{12})C_{33} > 2C_{13}^2$$

$$B_{H3} = C_{44} > 0$$

$$B_{H4} = C_{66} > 0$$

As seen in Table 3, only 1$T_2$-$MoS_2$ is found to be mechanically unstable since it does not fulfil the Born criteria. Even though group B polymorphs fulfil the Born criteria this does not imply that these could be synthesised as they were found to be dynamically unstable based on the phonon analysis. In general, if a compound is found to be dynamically stable, it indicates that it has either a stable phase or a possible metastable phase. All A group materials are both dynamically and mechanically stable, so these polymorphs can be synthesised experimentally. Since the B group materials are dynamically unstable, but mechanically stable (except 1$T_2$-$MoS_2$) we could conclude that these polymorphs have metastable phases. This explains why monovalent elements/nanoparticles/nanoobjects have been added to stabilise group B polymorphs.[29,65–67]

Table 3 The calculated single-crystal elastic constants $C_{ij}$ (in GPa), bulk modulus $B$ (in GPa), shear modulus $G$ (in GPa), Poisson's ratio $\nu$, Young's modulus $E$ (in GPa). Subscript V indicates the Voigt bound, R indicates the Reuss bound and H indicates the Hill bound

| Polymorph | 2$R_1$-$MoS_2$ | 2T-$MoS_2$ | 4T-$MoS_2$ | 1H-$MoS_2$ | 3$H_a$-$MoS_2$ | 3$H_b$-$MoS_2$ | 2H-$MoS_2$ | 2$R_2$-$MoS_2$ | 3T-$MoS_2$ | 1$T_1$-$MoS_2$ | 1$T_2$-$MoS_2$ |
|---|---|---|---|---|---|---|---|---|---|---|---|
| Crystal system | Trigonal | Trigonal | Trigonal | Hexagonal | Hexagonal | Hexagonal | Hexagonal | Trigonal | Trigonal | Trigonal | Trigonal |
| $C_{11}$ | | 105 | 132 | 75 | 123 | 176 | 190 | 140 | 177 | 187 | 195 |
| $C_{12}$ | | 27 | 34 | 19 | 31 | 45 | 48 | 8 | −4 | 37 | 44 |
| $C_{13}$ | | 0.1 | 0.40 | 0.1 | 0.5 | 0.6 | 2 | 10 | 14 | 30 | 58 |
| $C_{14}$ | | 0 | 0 | 0 | 0 | 0 | 0 | 0 | 0 | 0 | 0 |
| $C_{33}$ | | 0.3 | 1 | 0.3 | 1 | 2 | 7 | 14 | 29 | 10 | 12 |
| $C_{44}$ | | 39 | 49 | 28 | 0.4 | 66 | 71 | 66 | 90 | 75 | 75 |
| $C_{66}$ | | 0.2 | 0.42 | 0.1 | 46 | 0.3 | 0.21 | 4 | 6 | 31 | −82 |
| Born | | Yes | Yes | Yes | Yes | Yes | Yes | Yes | Yes | Yes | No |
| $B_V$ | | 29 | 37 | 21 | 35 | 50 | 55 | 39 | 48 | 64 | 80 |
| $B_R$ | | 0.3 | 1 | 0.3 | 1 | 2 | 7 | 14 | 26 | 4 | −125 |
| $B_H$ | | 15 | 19 | 11 | 18 | 26 | 31 | 26 | 37 | 34 | −23 |
| $G_V$ | | 20 | 72 | 14 | 24 | 34 | 37 | 32 | 44 | 104 | −2 |
| $G_R$ | | 0.4 | 1 | 0.2 | 1 | 0.8 | 1 | 4 | 12 | 5 | −41 |
| $G_H$ | | 10 | 36 | 7 | 12 | 17 | 19 | 18 | 28 | 55 | −21 |
| $\nu_V$ | | 0.22 | −0.09 | 0.22 | 0.22 | 0.22 | 0.23 | 0.18 | 0.15 | −0.03 | 0.51 |
| $\nu_R$ | | 0.08 | 0.19 | 0.25 | 0.23 | 0.35 | 0.46 | 0.36 | 0.30 | 0.01 | 0.35 |
| $\nu_H$ | | 0.22 | −0.08 | 0.22 | 0.22 | 0.23 | 0.25 | 0.22 | 0.20 | −0.02 | 0.14 |
| $E_V$ | | 49 | 131 | 35 | 58 | 83 | 90 | 76 | 102 | 203 | −5 |
| $E_R$ | | 0.9 | 2 | 0.5 | 2 | 2 | 2 | 11 | 31 | 10 | −110 |
| $E_H$ | | 25 | 66 | 18 | 30 | 43 | 47 | 45 | 68 | 106 | −48 |

To investigate how the polymorphs would react to applied mechanical forces, we calculated the Voigt (V), Reuss (R) and Hill (H) modulus through the elastic stiffness moduli, $C_{ij}$. These were then used to calculate the bulk modulus B, shear modulus $G$, Young's modulus $E$ and Poisson's ratio $\nu$. The calculated values are found in Table 3.

The Hill average young modulus for $1T_2$-$MoS_2$ (−48 GPa) is negative, which indicates that the atoms are stretched instead of being compressed. For 2T-$MoS_2$ (25 GPa), 4T-$MoS_2$ (66 GPa), 1H-$MoS_2$ (18 GPa), $3H_a$-$MoS_2$ (30 GPa), $3H_b$-$MoS_2$ (43 GPa), 2H-$MoS_2$ (47 GPa), $2R_2$-$MoS_2$ (45 GPa), 3T-$MoS_2$ (68 GPa) and $1T_1$-$MoS_2$ (106 GPa) the atoms are compressed due to the positive value. We see that there is spread in the stiffness of the polymorphs varying from 1H-$MoS_2$ with 18 GPa (like peptide nanotubes[68,69]) up to $1T_1$-$MoS_2$ at 106 GPa (like bronze, brass and some titanium alloys[70]).

Looking at the Poisson's ratio, we see that 4T-$MoS_2$ and $1T_1$-$MoS_2$ have negative values, −0.08 and −0.02, which makes them auxetic materials. This means that when the materials are subjected to a positive strain along a longitudinal axis, the transverse strain would increase the cross-sectional area. $MoS_2$ is known for being among crystalline materials that have polymorphs with negative Poisson's ratio,[71] and 1T polymorphs are the more common auxetic polymorphs.[72] Auxetic materials are expected to have mechanical properties such as high energy absorption and fracture resistance.

The other materials vary from a Poisson's ratio of 0.14 ($1T_2$-$MoS_2$) up to 0.25 (2H-$MoS_2$), which is a range from foam-like compressibility to cast iron. The average of our polymorphs seems to be 0.2, which is around cast iron. In addition to Youngs' modulus and Poisson's ratio, we can also calculate shear modulus over bulk modulus ($G/B$), a value that will determine if the material is ductile or brittle. The critical value for high (low) $G/B$ that separates ductile and brittle materials is 0.5.[73] Our calculated $G/B$ values are below 0.5, implying that all the polymorphs have brittle characteristics except $3H_a$-$MoS_2$ which has a $G/B$ value of 0.97. $3H_a$-$MoS_2$ is thus expected to be a ductile material.

### Raman and IR spectra

**IR spectrum.** The IR spectra of all the studied $MoS_2$ polymorphs are presented in Fig. 6, and the corresponding modes are presented in Table 4. From the calculated values, we clearly observe that the high frequency modes are caused by S–Mo–S rotation, whereas low frequency modes are caused by Mo–S vibrations. According to crystal symmetry, $A_{2u}$ and $E_{1u}$ IR modes refer to a bulk material, while $A''_2$ plus $E'$ correspond to single layer, and $A_{2u}$ and $E_u$ are active IR modes for double layer $MoS_2$.[52] Based on the calculated IR spectra for the group B polymorphs shown in Fig. 6b, we see that 3T-$MoS_2$ is a double-layer polymorph (due to comparatively larger intermediate distance between the layers), while $1T_1$-$MoS_2$ and $1T_2$-$MoS_2$ contain the $^2E_u$ from double-layer polymorphs in addition to much softer $^2A_u$ mode. Our results clearly show that the group B polymorphs are only metastable, and this may the reason for lack of other theoretical IR studies in the literature on these polymorphs. This makes it difficult to verify this result due to lack of literature data. Further theoretical and experimental studies are needed on this aspect.

Regarding the group A polymorphs, we clearly notice the presence of $^2E_{1u}$ and $^2A_{2u}$ active modes for $3H_b$-$MoS_2$ and 2H-$MoS_2$ indicating that they are $MoS_2$ bulk polymorphs. 4T-$MoS_2$ has $E_u$ and $A_{2u}$ as active modes, which is also an indication of a bulk polymorph. Due to the presences of the $E'$ and $^5A''_2$ modes (due to comparatively larger intermediate distance between the layers) we find $3H_a$-$MoS_2$ to be a single layer. The $E_u$ modes seen for 2T-$MoS_2$ confirms that this a double layer polymorph, while the $E'$ mode for 1H-$MoS_2$ makes it a single layer polymorph. $2R_1$-$MoS_2$ on the other hand shows E modes and $A_1$, neither of these modes have previously been reported as active IR modes for $MoS_2$. This could be an artefact from the calculation method, although the historical known accuracy speaks against this. However, it could also be a result of the interlayer distance and van der Waals forces making it harder to differentiate between the $MoS_2$ layers of the polymorph. Another possible explanation is that the polymorphs

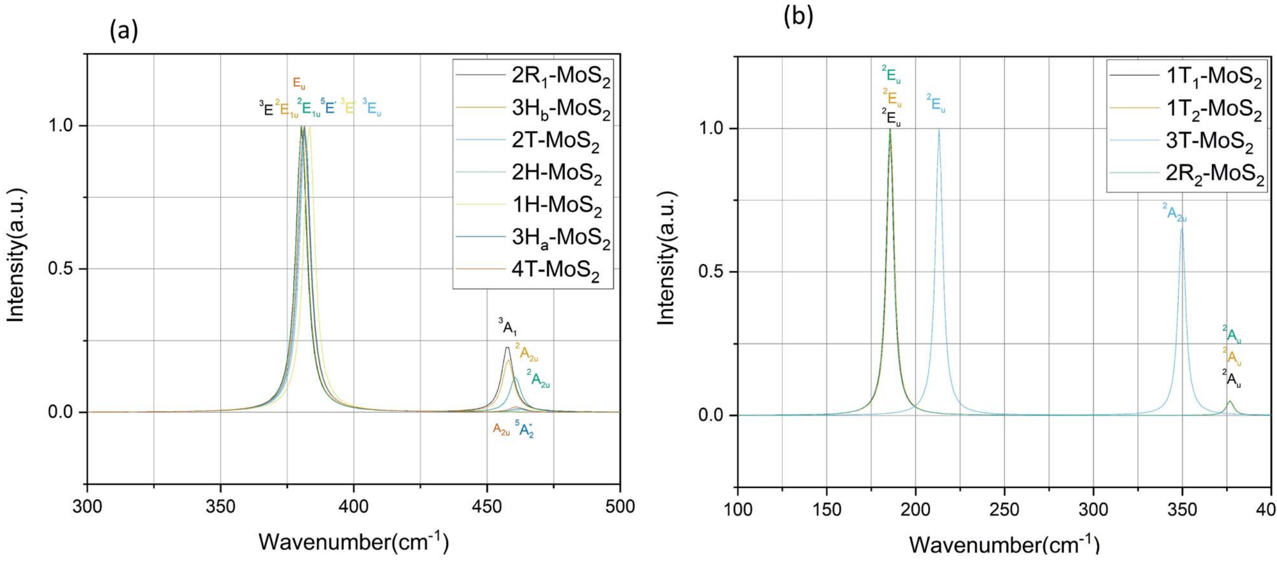

Fig. 6 IR spectra for the group A polymorphs (a) and the group B polymorphs (b).

Table 4 The calculated Raman and IR frequency (in $cm^{-1}$) for the modes at the $\Gamma$ point of the Brillouin zone for $MoS_2$ polymorphs

| Polymorph | Raman active modes | IR active modes |
|---|---|---|
| $2R_1$-$MoS_2$ | $^3E$: 286, 381. $^3A_1$: 405 | $^3E$: 380. $^3A_1$: 457 |
| 2H-$MoS_2$ | $^2E_{2g}$: 30, 382. $^1E_{1g}$: 283. $^1A_{1g}$: 404 | $^2E_{1u}$: 380. $^2A_{2u}$: 460 |
| $3H_b$-$MoS_2$ | $^2E_{2g}$: 36, 380. $^1E_{1g}$: 284. $^1A_{1g}$: 403 | $^2E_{1u}$: 380. $^2A_{2u}$: 458 |
| 4T-$MoS_2$ | $E_g$: 14, 33, 282, 283, 380. $A_{1g}$: 22, 53, 401, 403, 461, 463 | $E_u$: 26, 281, 283, 380. $A_{2u}$: 43, 399, 402, 463 |
| $3H_a$-$MoS_2$ | $^4E''$: 19. $^5E'$: 283, 381. $^4A'_1$: 398, 461 | $^5E'$: 381. $^5A''_2$: 461 |
| 2T-$MoS_2$ | $^3A_{1g}$: 40, 400. $^3E_g$: 284, 382 | $^3E_u$: 382 |
| 1H-$MoS_2$ | $^1E''$: 284. $^2E'$: 383 | $^3E'$: 384 |
| $1T_1$-$MoS_2$ | $^1E_g$: 274. $^1A_{1g}$: 386 | $^2E_u$: 186. $^2A_u$: 377 |
| $1T_2$-$MoS_2$ | $^1E_g$: 275. $^1A_{1g}$: 386 | $^2E_u$: 186. $^2A_u$: 377 |
| 3T-$MoS_2$ | $^1E_g$: 258. $^1A_{1g}$: 398 | $^2E_u$: 213. $^2A_{2u}$: 350 |
| $2R_2$-$MoS_2$ | $^1E_g$: 274. $^1A_{1g}$: 386 | $^2E_u$: 185. $^2A_u$: 376 |
| Bulk 2H-$MoS_2$ | $E^1_{2g}$: $384^a$, $382^b$, $384^c$. $A_{1g}$: $408^a$, $408^b$, $408^c$ | $E_{1u}$: $382^e$, $384^f$, $384^g$. $A_{2u}$: $468^f$, $470^g$ |
| Mono 2H-$MoS_2$ | $E'$: $384^d$, $385^c$. $A'_1$: $403^d$, $404^c$ | |

[a] From ref. 58. [b] From ref. 59. [c] From ref. 60. [d] From ref. 49. [e] From ref. 61. [f] From ref. 62. [g] From ref. 54.

are tilted slightly, and therefore exist in a state between 2H and 1T. This would change the crystal symmetry enough to introduce previously unseen modes.

**Raman spectra.** All of our polymorphs exhibit the signature Raman active modes $E^1_g$ and $A_{1g}$,[53] as shown in Fig. 7 and Table 4. In group B polymorphs, out-of-plane $^1A_{1g}$ mode is dominant, which indicates single degenerate wave functions, except for 3T-$MoS_2$ which is dominated by the in-plane $^1E_g$ mode. Compared to the modes of 3T-$MoS_2$ we see that the modes of the other polymorphs are redshifted. The observed redshift could be attributed to the larger interlayer distances (a factor of almost 4, see Table 1). This could lead to an increase in the dielectric screening of the long-range Coulomb forces and thus reduce the overall restoring force on the atoms. From Fig. 7, we observe that the group A polymorphs have a widespread in dominating modes compared to group B. The $E^1_g$, $E^2_{2g}$ and $A_{1g}$ modes around 280 $cm^{-1}$, 380 $cm^{-1}$ and 410 $cm^{-1}$ are in agreement with experimental studies.[54,55] The modes seen at the lower end of Fig. 7 (<100 $cm^{-1}$) arise from the vibration of an S–Mo–S layer against adjacent layers, while $E^1_{2g}$ stems from opposite vibration of two S atoms with respect to the Mo atom. In general, the $A_{1g}$ mode is associated with the out-of-plane vibrations of only S atoms in opposite directions. The additional $^4A'_1$ mode (~460 $cm^{-1}$) for $3H_a$-$MoS_2$ are due to strong electron–phonon couplings and could come from a second-order process involving the longitudinal acoustic phonons at $M$ point (LA($M$)).[56] We also note that the $E^1_g$ and $A_{1g}$ are redshifted compared to the Raman modes of group B polymorphs. Raman spectra can be used to verify the crystallinity of a material. The Raman spectra for crystalline materials contain sharper peaks or long-range correlations, while amorphous materials only have short-range ordering.[57] Raman spectra indicates clearly

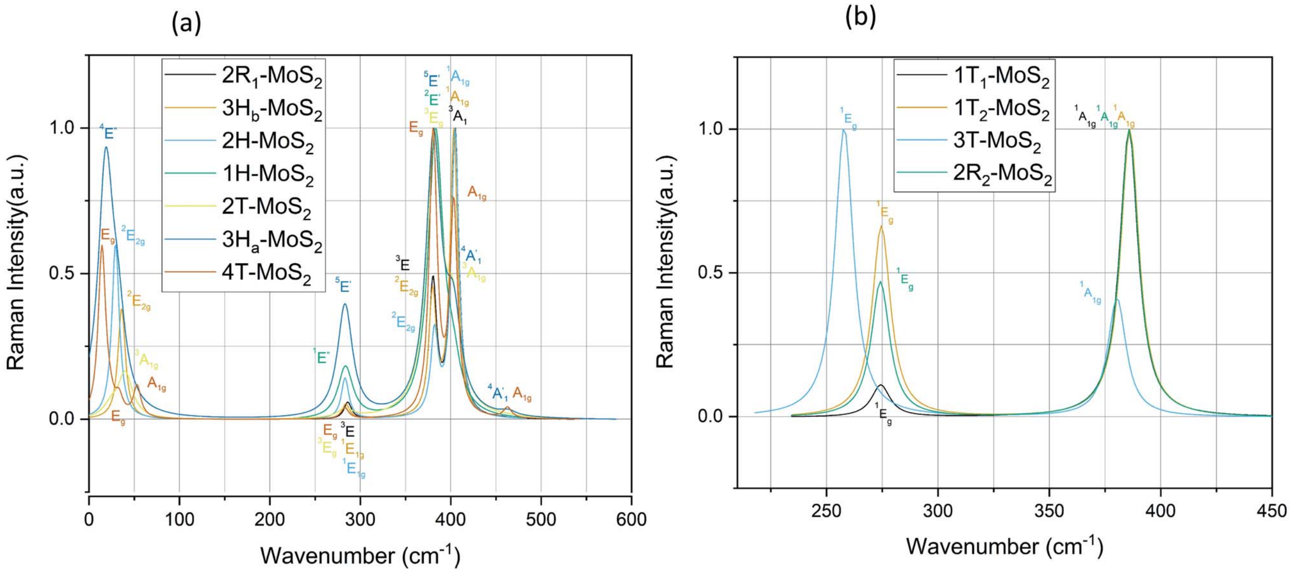

Fig. 7 Raman spectra for the group A polymorphs (a) and the group B polymorphs (b).

that the $MoS_2$ polymorphs considered in this study are shown to have crystalline characteristics.

For the sake of checking the validity of our approach, we have tabulated experimental as well as other theoretical findings on 2H-$MoS_2$ polymorph. Based on our knowledge, there are still no studies reported on 1T polymorphs due to the synthesis and stability challenges of these polymorphs. We see that in general, we have the same major peaks around 380 $cm^{-1}$ and 405 $cm^{-1}$ for group A polymorphs as reported in the literature. The same is observed with the IR modes, which are in good agreement with reported literature data.

## Conclusion

For the very first time 14 different $MoS_2$ polymorphs are proposed and studied using DFT total-energy calculations, band structure analysis, phonon density of states and elastic constants calculations. The in-depth study shows.

- Three of the polymorphs were omitted from the study because their energy-volume data were far away from the data for other polymorphs, which indicates that these polymorphs are unstable.
- Polymorphs in group B (1$T_1$-$MoS_2$, 1$T_2$-$MoS_2$, 3T-$MoS_2$ and 2$R_2$-$MoS_2$) are all metallic and lacked dynamical stability. 1$T_2$-$MoS_2$ is neither dynamical stable nor mechanical stable.
- Group A (2$R_1$-$MoS_2$, 3$H_b$-$MoS_2$, 2H-$MoS_2$, 1H-$MoS_2$, 2T-$MoS_2$, 3$H_a$-$MoS_2$ and 4T-$MoS_2$) polymorphs are semiconductors with an indirect bandgap, the range for the seven polymorphs is 1.87 eV to 2.12 eV. They are all dynamically and mechanically stable.
- 2$R_1$-$MoS_2$ has the lowest bandgap of 1.87 eV.
- 4T-$MoS_2$ stands out due to being auxetic, which means it has a high level of fracture resistance.
- 3$H_b$-$MoS_2$ has the lowest effective electron mass ($0.22m_e$ *vs.* for example $1.4m_e$ for 2H-$TiO_2$, which is widely used in PV and photocatalytic applications).

Our theoretical analysis show that the candidates in group A can be readily synthesised. Here further experimental verification is needed. The bandgap range of 1.87 eV to 2.12 eV makes the group A polymorphs viable for photovoltaic and photocatalytic applications. Out of the seven polymorphs in group A, 3$H_b$-$MoS_2$, with its high electron mobility and with the bandgap of 1.95 eV, is the most promising candidate for photovoltaic and photocatalytic applications. $MoS_2$ has recently shown promise as electron and/or hole-transport layer in perovskite solar cells, and the high carrier mobility of 3$H_b$-$MoS_2$ makes it a promising candidate for this use.

The group B polymorphs were only found to be metastable phases (except 1$T_2$-$MoS_2$) and cannot be synthesised. Due to the transitions of metastable phases in 1T polymorphs, more research on these polymorphs is needed such that the synthesis of a pure 1T-$MoS_2$ single-layer polymorph is viable.

## Conflicts of interest

There are no conflicts of interest to declare.

## Acknowledgements

The authors acknowledge the Research Council of Norway for providing the computer time (under the project number NN2875k and NN2867k) at the Norwegian supercomputer clusters.

## References

1 D. Voiry, A. Goswami, R. Kappera, C. d. C. C. e. Silva, D. Kaplan, T. Fujita, M. Chen, T. Asefa and M. Chhowalla, *Nat. Chem.*, 2014, **7**, 45.
2 Z. Yin, H. Li, H. Li, L. Jiang, Y. Shi, Y. Sun, G. Lu, Q. Zhang, X. Chen and H. Zhang, *ACS Nano*, 2012, **6**, 74–80.
3 M. Xu, T. Liang, M. Shi and H. Chen, *Chem. Rev.*, 2013, **113**, 3766–3798.
4 B. Radisavljevic, A. Radenovic, J. Brivio, V. Giacometti and A. Kis, *Nat. Nanotechnol.*, 2011, **6**, 147–150.
5 K. K. Kam and B. A. Parkinson, *J. Phys. Chem.*, 1982, **86**, 463–467.
6 D. Voiry, A. Mohite and M. Chhowalla, *Chem. Soc. Rev.*, 2015, **44**, 2702–2712.
7 C. Wu, J. Zhang, X. Tong, P. Yu, J. Y. Xu, J. Wu, Z. M. Wang, J. Lou and Y. L. Chueh, *Small*, 2019, **15**, e1900578.
8 M. Dallavalle, N. Sändig and F. Zerbetto, *Langmuir*, 2012, **28**, 7393–7400.
9 M.-L. Tsai, S.-H. Su, J.-K. Chang, D.-S. Tsai, C.-H. Chen, C.-I. Wu, L.-J. Li, L.-J. Chen and J.-H. He, *ACS Nano*, 2014, **8**, 8317–8322.
10 Z. Li, X. Meng and Z. Zhang, *J. Photochem. Photobiol., C*, 2018, **35**, 39–55.
11 M. Donarelli and L. Ottaviano, *Sensors*, 2018, **18**(11), 3638.
12 S. Barua, H. S. Dutta, S. Gogoi, R. Devi and R. Khan, *ACS Appl. Nano Mater.*, 2017, **1**, 2–25.
13 N. Bandaru, R. S. Kumar, D. Sneed, O. Tschauner, J. Baker, D. Antonio, S.-N. Luo, T. Hartmann, Y. Zhao and R. Venkat, *J. Phys. Chem. C*, 2014, **118**, 3230–3235.
14 Y.-C. Lin, D. Dumcenco, Y.-s. Huang and K. Suenaga, *Nat. Nanotechnol.*, 2014, **9**, 391–396.
15 A. Enyashin, L. Yadgarov, L. Houben, I. Popov, M. Weidenbach, R. Tenne, M. Bar-Sadan and G. Seifert, *J. Phys. Chem. C*, 2011, **115**, 24586.
16 L. Hromadová, R. Martoňák and E. Tosatti, *Phys. Rev. B: Condens. Matter Mater. Phys.*, 2013, **87**, 144105.
17 S. Ahmad and S. Mukherjee, *Graphene*, 2014, **3**, 52–59.
18 B. Han and Y. H. Hu, *Energy Sci. Eng.*, 2016, **4**, 285–304.
19 J. Sun, X. Li, W. Guo, M. Zhao, X. Fan, Y. Dong, C. Xu, J. Deng and Y. Fu, *Crystals*, 2017, **7**, 198.
20 M. R. Vazirisereshk, A. Martini, D. A. Strubbe and M. Z. Baykara, *Lubricants*, 2019, **7**, 57.
21 O. V. Yazyev and A. Kis, *Mater. Today*, 2015, **18**, 20–30.
22 L. S. Byskov, J. K. Nørskov, B. S. Clausen and H. Topsøe, *J. Catal.*, 1999, **187**, 109–122.
23 P. Hohenberg and W. Kohn, *Phys. Rev.*, 1964, **136**, B864–B871.
24 W. Kohn and L. J. Sham, *Phys. Rev.*, 1965, **140**, A1133–A1138.

25 G. Kresse and J. Furthmüller, *Phys. Rev. B: Condens. Matter Mater. Phys.*, 1996, **54**, 11169–11186.

26 G. Kresse and D. Joubert, *Phys. Rev. B: Condens. Matter Mater. Phys.*, 1999, **59**, 1758–1775.

27 J. P. Perdew, K. Burke and M. Ernzerhof, *Phys. Rev. Lett.*, 1996, **77**, 3865–3868.

28 P. E. Blöchl, *Phys. Rev. B: Condens. Matter Mater. Phys.*, 1994, **50**, 17953–17979.

29 L. Andrinopoulos, N. D. M. Hine and A. A. Mostofi, *J. Chem. Phys.*, 2011, **135**, 154105.

30 P. L. Silvestrelli, *Phys. Rev. Lett.*, 2008, **100**, 053002.

31 P. L. Silvestrelli, *J. Phys. Chem. A*, 2009, **113**, 5224–5234.

32 P. Ravindran, R. Vidya, A. Kjekshus, H. Fjellvåg and O. Eriksson, *Phys. Rev. B: Condens. Matter Mater. Phys.*, 2006, **74**, 224412.

33 J. Heyd, G. E. Scuseria and M. Ernzerhof, *J. Chem. Phys.*, 2003, **118**, 8207–8215.

34 A. van de Walle and G. Ceder, *Rev. Mod. Phys.*, 2002, **74**, 11–45.

35 A. Togo and I. Tanaka, *Scr. Mater.*, 2015, **108**, 1–5.

36 V. Wang, N. Xu, J. C. Liu, G. Tang and W.-T. Geng, 2019, arXiv:1908.08269.

37 W. Zhao, J. Pan, Y. Fang, X. Che, D. Wang, K. Bu and F. Huang, *Chem.–Eur. J.*, 2018, **24**, 15942–15954.

38 Z. Xia, Y. Tao, Z. Pan and X. Shen, *Results Phys.*, 2019, **12**, 2218–2224.

39 C. Lane, D. Cao, H. Li, Y. Jiao, B. Barbiellini, A. Bansil and H. Zhu, *Condens. Matter*, 2019, **4**, 53.

40 M. Kan, J. Y. Wang, X. W. Li, S. H. Zhang, Y. W. Li, Y. Kawazoe, Q. Sun and P. Jena, *J. Phys. Chem. C*, 2014, **118**, 1515–1522.

41 A. N. Enyashin, L. Yadgarov, L. Houben, I. Popov, M. Weidenbach, R. Tenne, M. Bar-Sadan and G. Seifert, *J. Phys. Chem. C*, 2011, **115**, 24586–24591.

42 H. Huang, Y. Cui, Q. Li, C. Dun, W. Zhou, W. Huang, L. Chen, C. A. Hewitt and D. L. Carroll, *Nano Energy*, 2016, **26**, 172–179.

43 P. Borlido, T. Aull, A. W. Huran, F. Tran, M. A. L. Marques and S. Botti, *J. Chem. Theory Comput.*, 2019, **15**, 5069–5079.

44 J. Heyd, J. E. Peralta, G. E. Scuseria and R. L. Martin, *J. Chem. Phys.*, 2005, **123**, 174101.

45 A. Fonari and C. Sutton, *Effective Mass Calculator*, 2012.

46 L. A. Cipriano, G. Di Liberto, S. Tosoni and G. Pacchioni, *Nanoscale*, 2020, **12**, 17494–17501.

47 C. Liang, X. Sui, A. Wang, J. Chang, W. Wang, Z. Chen, W. Jiang, Y. Ma, J. Zhang, X. Liu and Y. Zhang, *Adv. Mater. Interfaces*, 2020, **7**, 2001130.

48 F. A. Rasmussen and K. S. Thygesen, *J. Phys. Chem. C*, 2015, **119**, 13169–13183.

49 X. Li, Y. Dai, M. Li, W. Wei and B. Huang, *J. Mater. Chem. A*, 2015, **3**, 24055–24063.

50 C. Dette, M. A. Pérez-Osorio, C. S. Kley, P. Punke, C. E. Patrick, P. Jacobson, F. Giustino, S. J. Jung and K. Kern, *Nano Lett.*, 2014, **14**, 6533–6538.

51 S. Jayabal, J. Wu, J. Chen, D. Geng and X. Meng, *Mater. Today Energy*, 2018, **10**, 264–279.

52 X. Zhang, X.-F. Qiao, W. Shi, J.-B. Wu, D.-S. Jiang and P.-H. Tan, *Chem. Soc. Rev.*, 2015, **44**, 2757–2785.

53 L. Liang and V. Meunier, *Nanoscale*, 2014, **6**, 5394–5401.

54 T. J. Wieting and J. L. Verble, *Phys. Rev. B: Condens. Matter Mater. Phys.*, 1971, **3**, 4286–4292.

55 J. M. Chen and C. S. Wang, *Solid State Commun.*, 1974, **14**, 857–860.

56 H. Li, Q. Zhang, C. C. R. Yap, B. K. Tay, T. H. T. Edwin, A. Olivier and D. Baillargeat, *Adv. Funct. Mater.*, 2012, **22**, 1385–1390.

57 A. Z. Samuel, *Spectrochim. Acta, Part A*, 2020, **224**, 117431.

58 C. Lee, H. Yan, L. E. Brus, T. F. Heinz, J. Hone and S. Ryu, *ACS Nano*, 2010, **4**, 2695–2700.

59 B. P. Majee, S. Mishra, R. K. Pandey, R. Prakash and A. K. Mishra, *J. Phys. Chem. C*, 2019, **123**, 18071–18078.

60 K. Gołasa, M. Grzeszczyk, K. P. Korona, R. Bożek, J. Binder, J. Szczytko, A. Wysmołek and A. Babiński, *Acta Phys. Pol., A*, 2013, **124**, 849–851.

61 X. Guo, H. Chen, X. Wen and J. Zheng, *J. Chem. Phys.*, 2015, **142**, 212447.

62 Q. C. Sun, X. S. Xu, L. I. Vergara, R. Rosentsveig and J. L. Musfeldt, *Phys. Rev. B: Condens. Matter Mater. Phys.*, 2009, **79**, 205405.

63 P. Ravindran, L. Fast, P. A. Korzhavyi, B. Johansson, J. Wills and O. Eriksson, *J. Appl. Phys.*, 1998, **84**, 4891–4904.

64 F. Mouhat and F.-X. Coudert, *Phys. Rev. B: Condens. Matter Mater. Phys.*, 2014, **90**, 224104.

65 Z. Lei, J. Zhan, L. Tang, Y. Zhang and Y. Wang, *Adv. Energy Mater.*, 2018, **8**, 1703482.

66 Q. Liu, Q. Fang, W. Chu, Y. Wan, X. Li, W. Xu, M. Habib, S. Tao, Y. Zhou, D. Liu, T. Xiang, A. Khalil, X. Wu, M. Chhowalla, P. M. Ajayan and L. Song, *Chem. Mater.*, 2017, **29**, 4738–4744.

67 P. Luo, F. Zhuge, Q. Zhang, Y. Chen, L. Lv, Y. Huang, H. Li and T. Zhai, *Nanoscale Horiz.*, 2019, **4**, 26–51.

68 N. Kol, L. Adler-Abramovich, D. Barlam, R. Z. Shneck, E. Gazit and I. Rousso, *Nano Lett.*, 2005, **5**, 1343–1346.

69 L. Niu, X. Chen, S. Allen and S. J. B. Tendler, *Langmuir*, 2007, **23**, 7443–7446.

70 E. Toolbox, *Young's Modulus - Tensile and Yield Strength for common Materials*, https://www.engineeringtoolbox.com/young-modulus-d_417.html, accessed 06.08.2020.

71 R. V. Goldstein, V. A. Gorodtsov and D. S. Lisovenko, *Dokl. Phys.*, 2011, **56**, 602–605.

72 L. Yu, Q. Yan and A. Ruzsinszky, *Nat. Commun.*, 2017, **8**, 15224.

73 S. F. Pugh, *London, Edinburgh Dublin Philos. Mag. J. Sci.*, 1954, **45**, 823–843.

# PAPER E

# DOPED $MoS_2$ POLYMORPH FOR IMPROVED HYDROGEN EVOLUTION REACTION

---

H. Eidsvåg, P. Vajeeston, and D. Velauthapillai

*Submitted to Journal of Computational Physics X, 2023*

# Doped $MoS_2$ polymorph for improved hydrogen evolution reaction

Håkon Eidsvåg*[a], Ponniah Vajeeston[b] and Dhayalan Velauthapillai[a]

a. Western Norway University of Applied Sciences, Department of Computing, Mathematics and Physics, Inndalsveien 28, Box 5063, Bergen, Norway

b. Center for Materials Science and Nanotechnology, Department of Chemistry, University of Oslo, Box 1033 Blindern N-0315, Oslo, Norway

## Abstract

Green hydrogen produced from solar energy could be one of the solutions to the growing energy shortage as non-renewable energy sources are phased out. However, the current catalyst materials used for photocatalytic water splitting (PWS) cannot compete with other renewable technologies when it comes to efficiency and production cost. Transition-metal dichalcogenides, such as molybdenum disulphides ($MoS_2$) have previously proven to have electronic and optical properties that could tackle these challenges. In this work optical properties, D-band centre and Gibbs free energy are calculated for seven $MoS_2$ polymorphs using first principal calculations and density functional theory (DFT) to show that they could be suitable as a photocatalysts for PWS. Out of the seven, the two polymorphs $3H_a$ and $2R_1$ were shown to have D-band centre values closest to the optimal value, while the Gibbs free energy for all seven polymorphs was within 5 % of each other. In a previous study, we found that $3H_b$ had the highest electron mobility among all seven polymorphs and an optimal bandgap for photocatalytic reactions. The $3H_b$ polymorphs was therefore selected for further study. In-depth analysis on enhancement of the electronic properties and the Gibbs free energy through substitutional doping with Al, Co, N, and Ni were carried out. For the very first time ever, substitutional doping of $MoS_2$ was attempted. We found that replacing one Mo atom with Al, Co, I, N and Ni lowered the Gibbs free energy with a factor of ten, which would increase the hydrogen evolution reaction of the catalyst. Our study further shows that $3H_b$ with one S atom replaced with Al, Co, I, Ni or Ni is dynamically and mechanically stable, while for $3H_b$ with one Mo atom replaced with Al and Ni makes the structure stable. Based on the low Gibbs free energy, stability, and electronic bandgap $3H_b$ $MoS_2$ doped with Al or Ni for one Mo atom emerges as a promising candidate for photocatalytic water splitting.

Keyword

$MoS_2$; hydrogen; Gibbs Free energy; absorption, doping

## 1. Introduction

Hydrogen produced from water and powered by solar energy is considered one of the most profitable and sustainable alternatives to fossil fuels due to the abundance of water and sun light. There are several technologies being developed to obtain hydrogen from water, such as electrolysis, photolysis, biological treatment techniques and thermolysis [1]. Of these, photocatalytic water splitting is seen as one of the most promising technologies due to its low production cost, good solar-to-hydrogen (STH) efficiency, ease of hydrogen and oxygen separation and the possibility of both large and small scale facilities [2–4]. However, the current achieved STH, lifetime and production costs are not good enough to warrant large scale production facilities [5,6].

Transition-metal dichalcogenides have been seen as a possible solution to tackle these challenges due to their intriguing electronic and optical properties [7]. Especially $MoS_2$, with its catalytic properties [8,9], could be a promising photocatalytic candidate. Atomically $MoS_2$ is a thin material, which means that the catalytic active sites are exposed to the reactants. This feature increases the efficiency of the chemical process. $MoS_2$ is also already used in industry as a catalyst, with established and optimised production methods making it a low cost material [10]. Recent work has looked into how $MoS_2$ can be used for photocatalytic degradation of dyes and found that it is very effective towards organic dyes and toxic pollutants [11,12]. This is due to the fact that $MoS_2$ photocatalyzes in the visible region, it has a high specific surface area, efficient charge separation and it exists in several different polymorphs [13]. Through small modifications of the compound composition, crystal structure or production method the performance of $MoS_2$ can be significantly altered [14–18]. The inclusion of dopants or change in crystal structure have a large impact on the catalytic activity by changing the electronic and optical structure of $MoS_2$. This makes it possible to alter the $MoS_2$ structure in such a way that the STH efficiency is increased. Over the past years research into $MoS_2$ as catalyst and cocatalyst for photocatalytic water splitting has increased [17,19,20]. In a previous article we investigated 14 different $MoS_2$ polymorphs using density functional theory calculations. Here we found that seven of these polymorphs were both dynamically and mechanically stable, and that they have bandgaps in the range of 1.87 eV to 2.12 eV [21]. This makes them interesting and viable candidates for photocatalytic water splitting.

In this article, we will therefore investigate these seven $MoS_2$ polymorphs further and look into properties influencing their photocatalytic water splitting potential. The D-band centre and Gibbs free energy are used as descriptors for the potential hydrogen production, and the obtained values are compared to existing literature. In addition, we explore if there are any temperature dependent phase transitions in the structures and we obtain their absorption spectra. This provides us with a clear overview of the different polymorph's potential as a catalyst for photocatalytic water splitting. Based on these results and the results from our previous paper [21], one of the polymorphs ($3H_b$-$MoS_2$) was selected for further experimentation as it was deemed to have the highest potential for PWS based on its absorption spectra, bandgap, and high electron mobility. It was decided to dope $3H_b$-$MoS_2$ with Al, Co, I, N and Ni to see how that would affect the Gibbs free energy and the bandstructure. We chose these elements based on existing work and as they represent at vide array of metals and non-metals. Al-doped $MoS_2$ has been proven to be a stable configuration with tuneable carrier density [22] and it has shown promise as a catalyst for CO oxidation [23]. In combination with g-$C_3N_4$ Co-doped $MoS_2$ shows promise as an effective photocatalyst due to the distortions in the $MoS_2$ the induced by Co atoms [24]. Co-doped $MoS_2$ has also shown to give good results as a HER catalyst for electrochemical water splitting [25]. N and Ni as dopants have improved the catalytic performance of $MoS_2$ for electrochemical water splitting [26]. It is reported that the catalytic current density of N-doped $MoS_2$ can reach 15 times that of pristine $MoS_2$ [27]. Ni on the other hand was found to add more electrochemical sites, improve the conductivity of the catalyst and increase the turnover frequency [28]. Although other halogens such as Cl and F have been used with success to activate both the basal plane sites [26] and the edge sites [29], no work has been done with I. Based on this did we decide to use I as a dopant here to investigate how it would affect $MoS_2$ and its photocatalytic properties. Through DFT calculations the effects of substitutional doping (both Mo and S were replaced with the dopants) on Gibbs free energy, bandgap, optical spectra, stability, and charge density were investigated. Showcasing that through doping it is possible to create $MoS_2$ catalysts that has the potential of a high STH efficiency.

## 2. Computational method

Every calculation was performed using the periodic density functional theory framework through the VASP code [30–34]. We used the projector-augmented wave (PAW) method to describe the interaction between the core (Mo:[Kr], and S:[Ne]) and the valence electrons [33,35]. The structures were optimised using the Perdew-Burke-Eruzerhof (PBE) exchange-correlation functional and further optimised with the DFT/vdW-DF2 method [36–38]. For the phonon calculations the supercell method was used. The real space force constants of the super cell were calculated with the VASP code, then the PHONOPY code was used to calculate the phonon frequencies from the force constants in the supercell consisting of at least 32 atoms in all systems. Every atom was displaced by a finite displacement of 0.01 Å in x-, y- and z-direction to get the force-constant matrices for each binary system. 4x4x4 **k**-points and strict energy convergence criteria ($10^{-8}$ eV) were used for the force constant calculations. We then built a dynamical matrix for the different **q** vector in the Brillouin zone. By solving this matrix, the phonon frequency eigenvalues and phonon mode eigenvector were found. The PHONOPY [39] code was then used to calculate the thermodynamic properties through a summation over the phonon eigenvectors. Based on this the energy versus temperature curves were generated. Our previous calculations suggested [40] that structural parameters in oxides could be reliably predicted only by using large energy-cut off to guarantee basis-set completeness. Hence, we have used a cut-off of 500 eV. The electronic properties were computed by using the screened hybrid functional as proposed by Heyd, Scuseria and Ernzerhof (HSE06) and generalised gradient approximation (GGA+U) for the polymorphs optimized at the PBE level [41]. If not specified differently, we used a Monkhorst–Pack 9 X 9 X 9 **k**-mesh for the structural optimization and the electronic polymorph studies. Band polymorphs were computed by solving the periodic Kohn–Sham equation on ten **k**-points along each direction of high symmetry of the irreducible part of the first Brillouin zone. Gibbs free energy and optical properties were calculated using a Gamma 8 x 8 x 1 **k**-mesh. VASPKIT [42] and SUMO[43] have been used for postprocessing and plot production. For the doped structures GGA+U was used for the bandgap calculations, see table 1 for the chosen U values.

*Table 1: U values chosen for the GGA+U calculations.*

| Atom | U |
|---|---|
| Mo | 3.28 [44] |
| S | 4.0 [44] |
| Al | 4.0 [45] |
| Co | 3.0 [46] |
| I | 8.0 [47] |
| N | 7.0 [48] |
| Ni | 6.0 [49] |

## 3. Catalytic properties of $MoS_2$ polymorphs

### 3.1. Energy vs volume and temperature dependency

$MoS_2$ can exist in several different crystal polymorphs or polytypes in three dimensions due to the large variation in stacking sequences and number of successive S-Mo-S sandwiches along the hexagonal c axis. The different variants are called 1T, 2H, 3R, $4H_a$ and 6R. Here the integer stands for the number of S-Mo-S sandwiches per unit cell along the hexagonal c axis, while the T, H and R indicate the type of symmetry. Tetragonal, hexagonal, and rhombohedral respectively. In our previous work, we studied 14 novel polymorphs to understand how the stacking sequence and layer-layer distance influences the properties of the compound [21]. Seven of these were found to be both mechanically and dynamically stable, making them interesting for further research [21]. To increase our understanding of the polymorphs properties we have now investigated how temperature would influence the relative stability of the polymorphs and if it would induce any phase transitions. Figure 1 shows energy versus temperature curves for the seven stable polymorphs. The starting point for these calculations was the preferred volume found in our previous work. As seen below increasing the temperature doesn't change the relative stability between the polymorphs. In fact, only between 400 K and 600 K we can see a small deviation and $3H_a$ transitions to be the most stable polymorph at 500 K. However, the change is only 0.9 eV as seen in Figure 1 and we believe that this phase transition is a numerical artefact caused by the calculation. This means that temperature is not a large factor for these polymorphs and one can choose the most appropriate one for a specific application without having to consider phase transitions.

*Figure 1: Energy vs temperature curve for the seven studied polymorphs. Zoomed in insert between 0 to 200 K is added to show the small difference between the structures.*

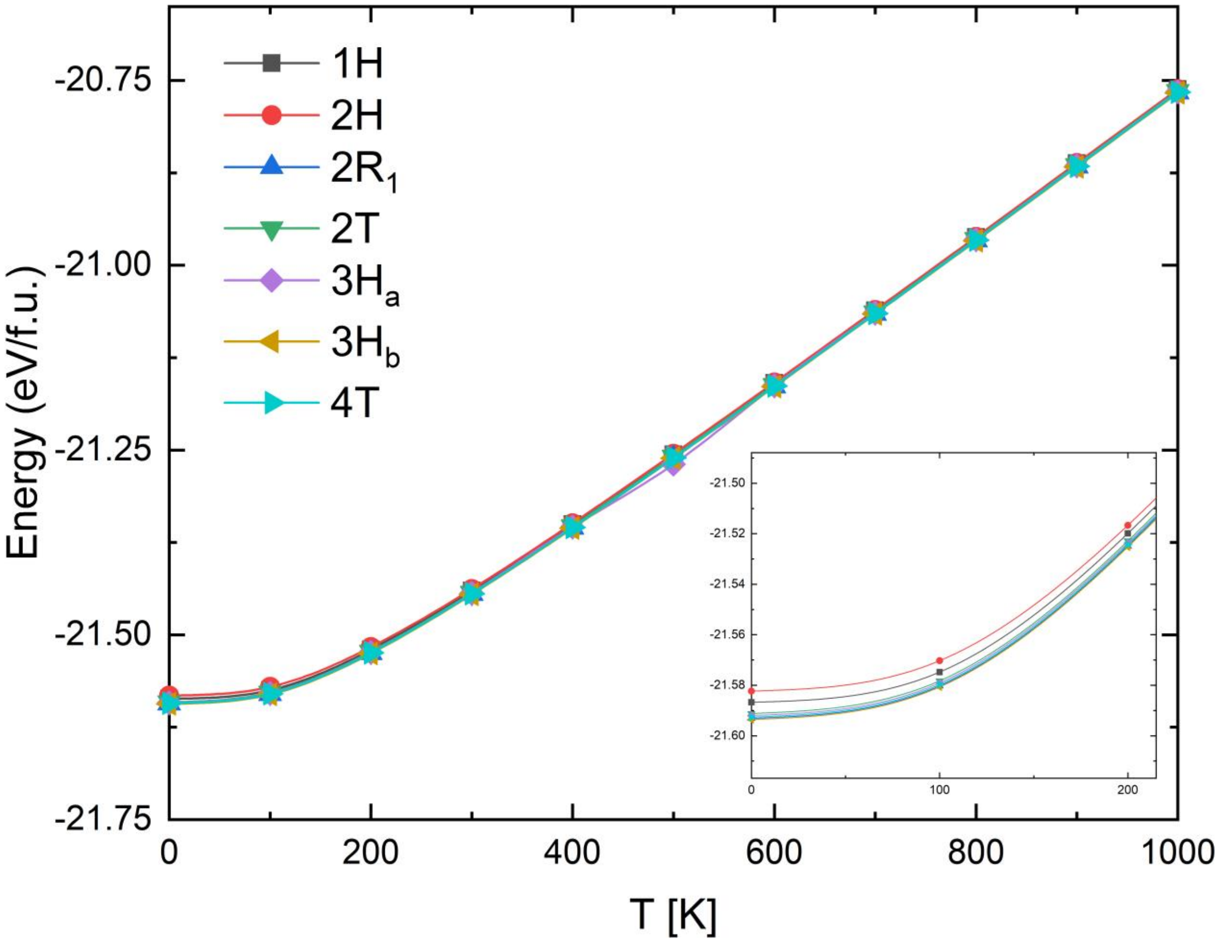

## 3.2. Optical properties

In 1996 Norskov and co-workers proposed the d-band centre theory, which correlates the energy of the d-band centre of gravity of a metal catalyst with the adsorption energy, activation energy, and dissociation energy of small molecules [50,51] . They state that the electron density of states (DOS) close to the Fermi level is correlated to the adsorbate substrate adsorption energy due to interactions between electrons occupying d-type orbitals of the metal (d-band) and those of the adsorbate [50,51]. In general, if the d-band centre is downshifted compared to the Fermi level it is an indication of good catalytic activity.

Although there have been significant efforts to verify the d-band theory, it has not been proven to be valid for all systems. In general, more complex systems have other factors, not included in the d-band centre theory, influencing the catalytic activity. However, our systems are deemed to be of a simple enough character that the d-band centre will provide an indication on the catalytic activity. Pt is considered to have an optimal position for the d-band centre for most favourable hydrogen binding energy, -1.929 eV with respect to the Fermi level [52]. Our results are presented in Table 1 below. 1H and 2T have positive shifted d-band centres compared to the Fermi-level, in addition they are far away from the optimal value of -1.929 eV. This means that they have higher energy in the antibonding states and the bond between the structure surface and adsorbed material will be higher [53,54]. Leading to a decrease in the chance for photocatalytic reactions. However, the closer the d-band centre is to the Fermi-level the better charge carrier transfer [55] . 2H, $2R_1$, $3H_a$, $3H_b$ and 4T have downshifted d-band centre indicating that they could be effective photocatalysts. Especially $2R_1$ and $3H_a$, -1.520 eV and – 1.541 eV respectively, which have d-band centre values not far from the optimal value of -1.929 eV. The binding strength of H will be less compared to that of the other structures, thus demanding less energy to be remove it from the surface and create $H_2$ atoms.

*Table 2: D-band centre for the stable polymorphs.*

| **Polymorph** | **D-band centre [eV]** | **Fermi level [eV]** |
|---|---|---|
| 1H | 0.334 | -2.552 |
| 2H | 0.276 | 3.511 |
| $2R_1$ | -1.520 | 3.285 |
| 2T | 0.328 | -0.882 |
| $3H_a$ | -1.541 | 0.003 |
| $3H_b$ | 0.369 | 2.865 |
| 4T | -0.544 | 0.555 |

An important parameter for a catalyst used for photocatalytic water splitting is the absorption coefficient as it determines how far into the material the light will travel before it is absorbed. For water splitting applications, the catalytic materials must have a high absorption coefficient in the visible region, to ensure that photons are absorbed. In addition to the absorption coefficient, we have also calculated the refractive index of the material to better understand the polymorphs optical properties.

All off the polymorphs showcase the same rise in absorption coefficient, see Figure 2a, at 2 eV (620 nm) that corresponds to orange light. Followed by a larger and wider upswing at 2.7 eV to 3.5 eV (460 nm to 355 nm), which is in the blue and violet range of visible light. This indicates that polymorphs can absorb photons at both ends of the visible light spectra, but there is still considerable number of photons not absorbed. This could be remedied by introducing dopants that would influence the optical properties of the polymorphs. Making the polymorphs tuned for the specific needs of photocatalytic water splitting.

Our calculations shows that $2R_1$ ($2.67\text{x}10^5$ $cm^{-1}$) has the highest absorption coefficient within the visible spectra. It is closely followed by 2H and $3H_b$ at $2.33\ \text{x}10^5$ $cm^{-1}$ and $2.28\ \text{x}10^5$ $cm^{-1}$, while 1H clearly has the lowest absorption coefficient ($1.62\text{x}10^5$ $cm^{-1}$) in the visible region. $2R_1$, 2H and $3H_b$ are, based on the absorption coefficient, the best candidates for photocatalytic water splitting.

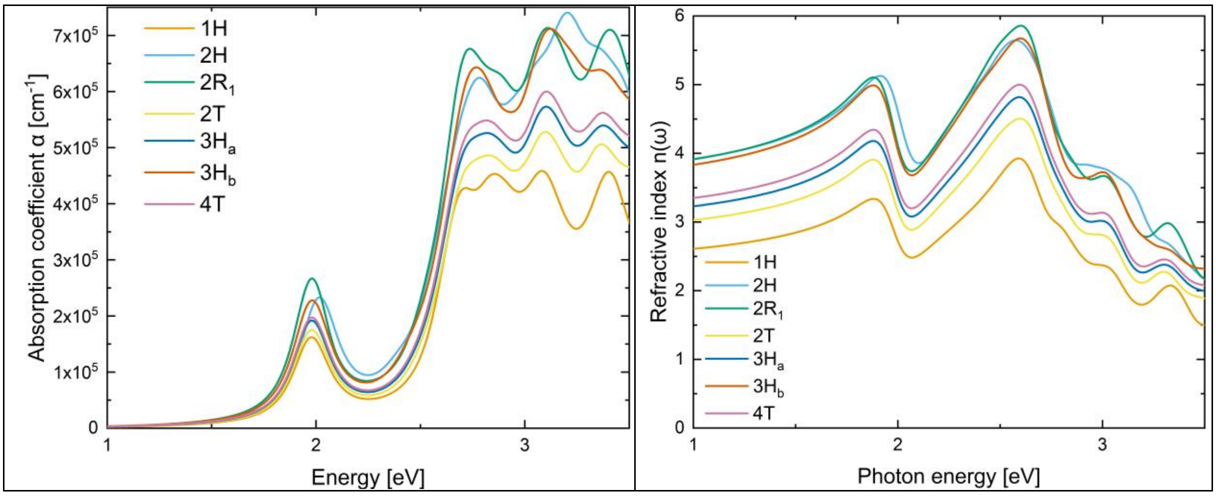

*Figure 2: Calculated absorption coefficient (a) and refractive index (b)*

The refractive index (Figure 2b), of the material determines how light propagates inside a material and the higher refractive index the slower light will travel through the material. This results in higher irradiance in the material, which enhances the photocatalytic activity of the material. We see that $2R_1$, 2H and $3H_b$ have the largest peaks around 5 in the visible region. This means that they are classified as high refractive index materials ($n>3.9$) [56] making them ideal candidates for photonic devices such as solar cells, photonic crystals and PWS. This is because they have a larger scattering cross section [57] and smaller mode volumes [58] than normal refractive index materials. Our results agree with those found by Islam et. al. [59] and we see that $MoS_2$ has a larger refractive index than $TiO_2$ (2.48 – 2.62) [60].

### 3.3. Gibbs free energy

Photocatalytic water splitting can be split into two half-reactions: hydrogen evolution reaction (HER) and oxygen evolution reaction (OER), with the overall HER being able to follow two different reaction mechanisms: Volmer-Tafel and Volmer-Heyrovsky. In the Volmer step protons are reduced to produce adsorbed hydrogen on the electrode surface (equation 1). After this step the reaction can either follow the Tafel route or the Heyrovsky route. The Volmer-Tafel reaction involves two adsorbed hydrogen atoms on the electrode surface adjacent to each other combining to a hydrogen molecule (equation 2). The Volmer-Heyrovsky reaction on the other hand utilises a proton from the surrounding water to react with an adsorbed hydrogen atom to produce a hydrogen molecule (equation 3) [61].

$$2H^{+} + 2e^{-} \rightarrow 2H_{ads}\ (Volmer)\ (1)$$

$$H_{ads} + H_{ads} \rightarrow H_{2(g)}\ (Tafel)\ (2)$$

$$H^{+} + H_{ads} + e^{-} \rightarrow H_{2(g)}\ (Heyrovsky)\ (3)$$

where $H^+$ is a proton and $H_{ads}$ is adsorbed hydrogen atoms.

What is clear from this is that regardless of the path taken by the HER, the adsorption energy of the hydrogen atom is crucial when looking at the catalytic activity of a material. The adsorption energy hydrogen is linked to the Gibbs free energy ($\Delta G_H$) of hydrogen on the compound surface and is widely accepted as an indicator of catalytic activity [62,63].

The Gibbs free energy can be calculated by the following equation:

$$\Delta G_H = E_{ads} + \Delta E_{ZPE} - T\Delta S_H\ (4).$$

Here $E_{ads}$ is the adsorption energy, $\Delta E_{ZPE}$ is the zero-point energy differences of $H_2$ in the adsorbed and gas phase state with its values ranging from 0.01 to 0.04 eV and $T\Delta S_H$ is entropy changes for finite variations at constant temperature T. For the materials we study here $\Delta E_{ZPE}$ is set to 0.04 eV based on calculations done by Nørskov et. al. [64]. The value for the term ($T\Delta S_H$) can be approximated to -0.2 eV at 298 K [65], which lets us rewrite the equation to $\Delta G_H = E_{ads} + 0.24\ eV$ [64,66,67].
In general, there are three possibilities for the hydrogen adsorption:

1) Exothermic hydrogen adsorption, when this happens the coverage of hydrogen atoms will be too high and the reaction will slow down [65]. This occurs for $\Delta G_H < 0$. However, the transformation can occur naturally [68]. A large and negative $\Delta G_H$ also means that $H_{ads}$ has a weak interaction with the electrode surface and this will slow down the Volmer step, which consequently slows down the overall reaction [63].
2) Endothermic hydrogen adsorption, here the energy barrier for proton ($H^+$) formation is too high [65]. $\Delta G_H > 0$. In addition, the natural direction of the reaction is opposite to what is desired (a nonspontaneous reaction) [68]. Here the $H_{ads}$ is bound strongly with electrode surface, which makes the initial Volmer step easy. However, the following Tafel or Heyrovsky steps difficult [63].
3) The system is at equilibrium and we have enough of all the reactants [65,68]. $\Delta G_H = 0$.

It is well known that an optimal photocatalytic material should have $\Delta G_H = 0$ and thus the adsorption energy $E_{ads}$ should be of the order of -0.24 eV [63,65].

We have calculated adsorption energies of H at three different locations as it is position dependent [69]. Our chosen locations are S top (Figure 3a), S interface (Figure 3b) and S bridge (Figure 3c). The adsorption energy was calculated as

$$E_H^{ads} = E_T[system + H] - E_T[system] - \frac{1}{2}E_{H_2}\ (5).$$

Where $E_T$[system + H] represents the total energy of $MoS_2$ with an adsorbed H atom, $E_T$[system] is the energy of $MoS_2$ without an adsorbed molecule and $E_{H_2}$ is the energy of a hydrogen molecule in gas phase. The Gibbs free energies are presented in Table 2. From the calculated values we see that there is not so much differences in potential catalytic activity among different polymorphs, with Gibbs values ranging from 1.746 eV to 1.852 eV. The positive values of $\Delta G_H$ indicates that the adsorbed hydrogens are bound strongly to the $MoS_2$ surface. This makes the initial Volmer step easy to undergo, while the following Tafel or Heyrovsky steps are more difficult [63] which reduces the overall STH efficiency.

It is generally believed that the basal plane of $MoS_2$ is close to inert and it is the edges that contribute to the catalytic activity [70]. If we compare our results for the basal plane with that of Seo et. al. [71] who got Gibbs energy values ranging from -0.36 eV to 0.66 eV for 1L, 2L and 3L monolayer $MoS_2$ structure using the edge as active sites, this assumption appears to be true.

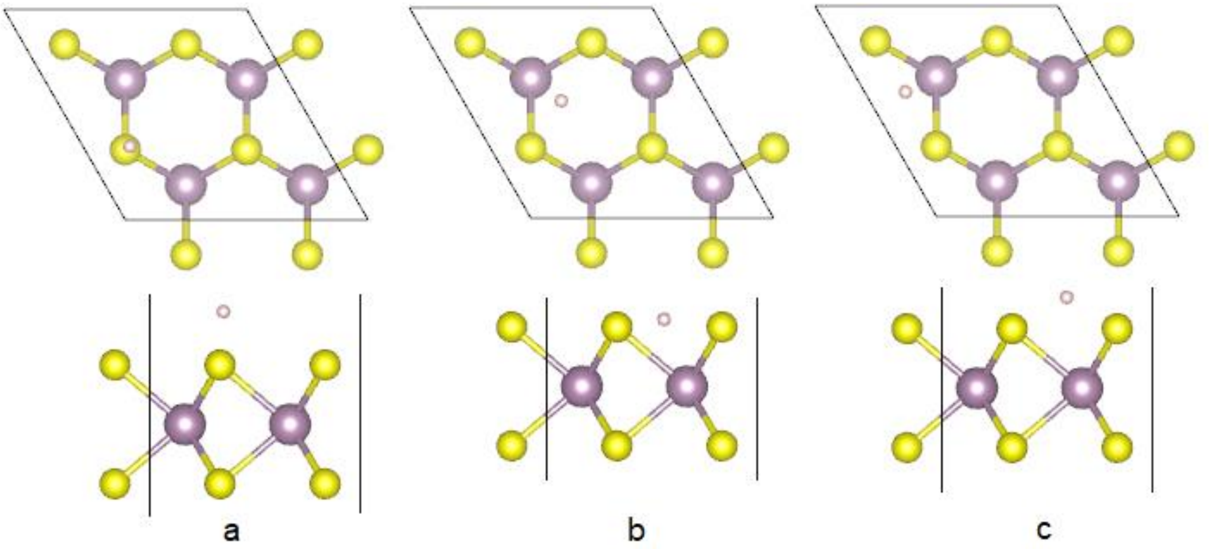

*Figure 3: Location of the adsorbed hydrogen atom. a) top, b) interface and c) bridge.*

*Table 3: Calculated Gibbs energy values, using Equation 4, for the seven stable polymorphs calculated at three different locations.*

| Polymorph | Bridge gibbs [eV] | Inter gibbs [eV] | Top gibbs [eV] |
|---|---|---|---|
| 1H | 1.77 | 1.77 | 1.77 |
| 2H | 1.75 | 1.75 | 1.85 |
| $2R_1$ | 1.75 | 1.75 | 1.75 |
| 2T | 1.77 | 1.77 | 1.77 |
| $3H_a$ | 1.77 | 1.77 | 1.76 |
| $3H_b$ | 1.75 | 1.75 | 1.75 |
| 4T | 1.76 | 1.76 | 1.75 |

## 4. Doped $3H_b$-$MoS_2$ polymorph

$3H_b$-$MoS_2$ was chosen over the other structures for its better electron mobility, suitable bandgap and absorption coefficient. We performed substitutional doping of both Mo atoms and S atoms. For S substitution a doping percentage of 6.250% was chosen, while for Mo 12.5%. That is, we replaced one S atom and one Mo atom respectively.

### 4.1. Gibbs free energy for doped polymorph

Gibbs free energy calculated for Al, Co, I, N or Ni doped $3H_b$-$MoS_2$ are shown in Table 3 and 4. We found that by replacing one S atom with either Al, Co, I, N or Ni decreased the Gibbs free energy, however the values are much further away from the optimal value (zero). In general, negative values indicate that the adsorption process is exothermic and that the surface will be flooded with hydrogen atoms, hindering the other reactants needed for a complete reaction. The large negative values also means that the $H_{ads}$ has a weak interaction with the material surface, which results in a slower Volmer step and a reduced overall turnover rate [63]. Due to the size of the super cell a smaller doping percentage was not possible, and a larger percentage was not attempted. Nonetheless, the addition of a dopant clearly influenced the $3H_b$-$MoS_2$ structures Gibbs free energy and electronic structure, showcasing the influence of dopants as a powerful tool in developing new photocatalysts.

When the Mo atom is substituted with a dopant atom we see a clear improvement in the Gibbs free energy as all dopants brings it closer to zero. There is also a greater disparity between the different adsorption sites, where the best results are seen for hydrogen adsorbed at the interface (Figure 3b). This is especially significant for Co that sports a rather high Gibbs free energy for the bridge and top location (> 1 eV), while for the interface site the Gibbs free energy is -0.02 eV, making it an incredible photocatalyst when the hydrogens are adsorbed at this location. Unfortunately, it is not possible to force hydrogen to be adsorbed at specific locations. However, the hydrogen production rate must be tested experimentally before a final verdict can be cast on this compound. N doped $MoS_2$ has on average the lowest values and they are comparable with that of the edge sites [71], which proves that through doping the basal layer of $MoS_2$ can be a valid photocatalyst.

*Table 4: Gibbs energy values for substitutional doped $3H_b$. One Mo is replaced with either one Al, Co, I, N or one Ni atom.*

| Mo Replaced on 3Hb | Bridge Gibbs [eV] | Inter Gibbs [eV] | Top Gibbs [eV] |
|---|---|---|---|
| Al | 0.77 | -0.17 | 0.77 |
| Co | 1.17 | -0.02 | 1.18 |
| I | 0.73 | 0.29 | 0.73 |
| N | -0.28 | 0.27 | -0.28 |
| Ni | 0.96 | -0.20 | 0.90 |

*Table 5: Gibbs energy values for substitutional doped 3Hb. One S atom is replaced with either one Al, Co, I, N or one Ni atom.*

| S Replaced on 3Hb | Bridge Gibbs [eV] | Inter Gibbs [eV] | Top Gibbs [eV] |
|---|---|---|---|
| Al | -6.99 | -6.45 | -5.55 |
| Co | -6.38 | -4.83 | -5.06 |
| I | -11.18 | -11.16 | -11.16 |
| N | -12.44 | -12.44 | -12.44 |
| Ni | -7.46 | -6.13 | -6.42 |

Through doping the electronic structure of the investigated polymorphs are changed, leading to changes in the band structures and bandgaps. Thus, GGA bandstructure calculations were performed to investigate how the different dopants influence the bandgap. It is also important to investigate the structures stability, bandstructure and optical spectra before one can conclude whether a doped structure can perform as a photocatalyst.

## 4.2. GGA bandgaps

The electronic structure is one of the key properties when determining if a material is suitable for photocatalytic processes or photovoltaic cells as it determines the amount absorbed sun light.

Our GGA bandgap calculations for Mo substituted with Al or I and S substituted with Co or Ni are presented in Figure 4, while the rest are seen in the supplementary information (Figure S1 and S2). Our calculations show that only four out of the ten doped structures are semiconductors, those are Mo substituted with Al or I and S substituted with Co or Ni. Of these four, Mo substituted with Al appears to have an intermediate bandgap.

Mo substituted with Co, N and Ni and S substituted with Al are metals, while S substituted with N is a semi/anisotropic metal. This means that the material becomes a metal or semiconductor depending on the direction taken through the Brillouin zone, which makes them non-appropriate for photocatalytic applications. When S is substituted with I the material becomes an insulator making it unsuitable as a catalyst.

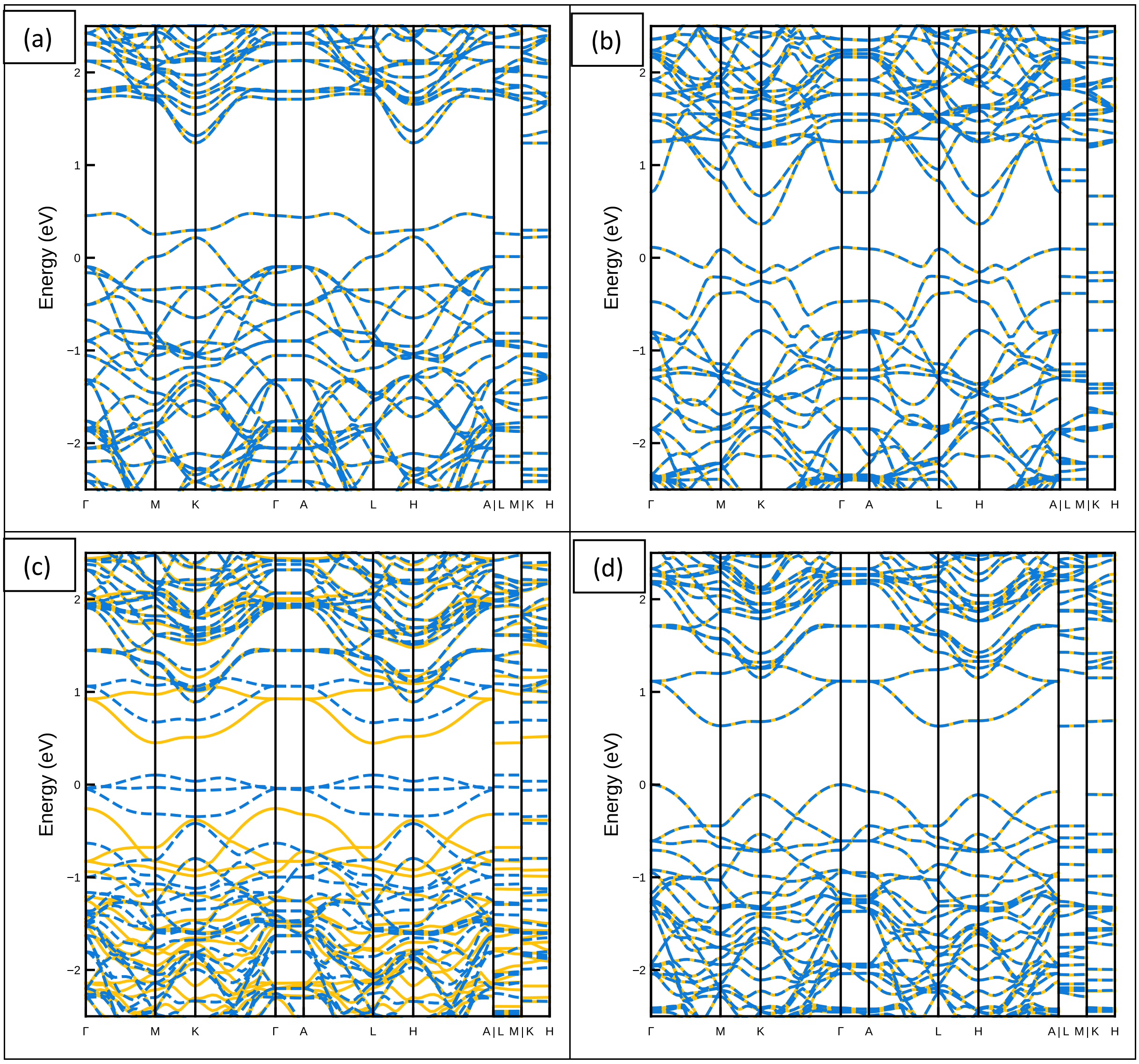

*Figure 4: GGA band structures for doped $3H_b$. Here Mo is substituted with Al (a), Mo substituted with I (b), S substituted with Co, and S substituted with Ni (d).*

## 4.3. Formation Energy

We calculated the formation energy to compare the stability of the doped structures with each other. This was done with the following expression [72]:

$$\Delta H = E_{doped} - [E_{structure} + E_{dopant} - E_{atom}]$$

Where $E_{doped}$ and $E_{structure}$ are the total energies of the supercell with and without dopants respectively, $E_{dopant}$ is the total energy of the dopant and $E_{atom}$ is the total energy of the replaced atom. The results are shown below in Table 5. From these calculations it is clear that replacing Mo with Al, Co, I, N or Ni results in a more thermodynamical stable compared to replacing one S atom in $3H_b$-$MoS_2$. Mo substituted with Al appears to be the most stable of the doped structures, closely followed by Mo substituted with Co and then N. The calculated formation energies for all doped materials results are positive, which means that these compounds will not be created spontaneously and external factors (e.g., pressure, temperature, or energy) are needed to create them as the reactants are more stable than the product.

*Table 5: Calculated formation energy for the doped $3H_b$-$MoS_2$ structure.*

| Structure | Formation Energy (ΔH) |
|---|---|
| $Mo_7S_{16}Al$ | 3.19 |
| $Mo_7S_{16}Co$ | 3.51 |
| $Mo_7S_{16}I$ | 7.68 |
| $Mo_7S_{16}N$ | 3.85 |
| $Mo_7S_{16}Ni$ | 4.27 |
| $Mo_8S_{15}Al$ | 11.13 |
| $Mo_8S_{15}Co$ | 11.37 |
| $Mo_8S_{15}I$ | 15.62 |
| $Mo_8S_{15}N$ | 11.79 |
| $Mo_8S_{15}Ni$ | 12.22 |

### 4.4. Mechanical Stability

In addition, to influencing the electronic structure the dopants will also affect the mechanical and dynamical stability of the polymorph. The elastic constants of a material can be used as a descriptor for how the material will react to an applied force, as either applied strain or stress. Thus, it is possible to use them to understand the mechanical stability of a material.

The stress and strain have three shear and three tensile components. Therefore, it is possible to describe the elastic constants of a crystal using a 6x6 symmetric matrix with 27 components. 21 of those 27 are independent of the others and in addition we can use any existing symmetry in the crystal to reduce the number of components. The stiffness matrix, $C_{ij}$, which the 6x6 matrix also is known as, can be used to calculate the bulk modulus, Poisson coefficient and Lame constants. In general, it has been found that the DFT elastic constants are within 10% of experimental values [73].

For hexagonal polymorphs the stability criteria are [74]

$$B_{H1} = C_{11} > |C_{12}|$$

$$B_{H2} = C_{11} > 0$$

and for oblique polymorphs the stability criteria are [74]

$$B_{O1} = C_{11} > 0$$

$$B_{O2} = C_{11}C_{22} > C_{12}C_{12}$$

$$B_{=3} = |C_{ij}| > 0$$

Table 6: The calculated single-crystal elastic constants *Cij* (in GPa), bulk modulus B (in GPa), shear modulus G (in GPa), Poisson's ratio ν, Young's modulus E (in GPa). Subscript V indicates the Voigt bound, R indicates the Reuss bound and H indicates the Hill bound.

| Polymorph | $3H_B$[21] | Al for Mo | Co for Mo | I for Mo | N for Mo | Ni for Mo | Al for S | Co for S | I for S | N for S | Ni for S |
|---|---|---|---|---|---|---|---|---|---|---|---|
| Crystal system | Hexagonal | Hexagonal | Hexagonal | Hexagonal | Oblique | Hexagonal | Hexagonal | Hexagonal | Hexagonal | Hexagonal | Hexagonal |
| $C_{11}$ | 176 | 223 | 161 | 212 | 254 | 196 | 301 | 300 | 296 | 326 | 302 |
| $C_{12}$ | 45 | 68 | 72 | 56 | -10 | 90 | 99 | 103 | 93 | 107 | 100 |
| $C_{13}$ | 0.6 | 0 | 0 | 0 | - | 0 | 0 | 0 | 0 | 0 | 0 |
| $C_{16}$ | - | - | - | - | 23 | - | - | - | - | - | - |
| $C_{26}$ | - | - | - | - | -53 | - | - | - | - | - | - |
| $C_{66}$ | 46 | 77 | 44 | 78 | 116 | 53 | 101 | 98 | 101 | 109 | 101 |
| Born | Yes | Yes | Yes | Yes | Yes | Yes | Yes | Yes | Yes | Yes | Yes |
| $B_V$ | 50 | 146 | 116 | 134 | 119 | 143 | 200 | 202 | 195 | 216 | 201 |
| $B_R$ | 2 | 146 | 116 | 134 | 117 | 143 | 200 | 202 | 195 | 216 | 201 |
| $B_H$ | 26 | 146 | 116 | 134 | 118 | 143 | 200 | 202 | 195 | 216 | 201 |
| $G_V$ | 34 | 77 | 44 | 78 | 123 | 53 | 101 | 98 | 101 | 109 | 101 |
| $G_R$ | 0.8 | 77 | 44 | 78 | 109 | 53 | 101 | 98 | 101 | 109 | 101 |
| $G_H$ | 17 | 77 | 44 | 78 | 116 | 53 | 101 | 98 | 101 | 109 | 101 |
| E | 43 | 202 | 128 | 197 | 171-292 (232) | 154 | 268 | 264 | 267 | 291 | 269 |
| G | 17 | 77 | 44 | 78 | 103-116 (110) | 53 | 101 | 98 | 101 | 109 | 101 |
| ν | 0.23 | 0.306 | 0.450 | 0.263 | -0.167-0.197 (0.015) | 0.462 | 0.329 | 0.345 | 0.315 | 0.328 | 0.330 |
| $G_H/B_H$ | 0.653 | 0.527 | 0.379 | 0.582 | 0.932 | 0.370 | 0.505 | 0.485 | 0.518 | 0.505 | 0.502 |

The $3H_B$ structure was found to be mechanically stable with all five dopants and for both Mo and S substitutional doping as they all fulfil the Born criteria. This means that the doped structure can keep its pore size and structure under a mechanical load. To further investigate how the doped structure would react to applied mechanical forces, we used the stiffness matrix to calculate the Voigt (V), Reuss (R) and Hill (H) modulus. With these we calculated the bulk modulus B, shear modulus G, Young's modulus E and Poisson's ratio ν for all doped $3H_b$-$MoS_2$ structures. The values are shown in Table 5.

Young's modulus characterises how a structure reacts to a force applied lengthwise, both under compression and extension. All of our doped structures have positive Young's modulus ranging from 128 GPa (higher than for bronze, titanium and annealed copper [75]) up to 291 GPa (beryllium [75]), indicating that they are quite stiff materials and would react slowly to applied pressure. In order to determine whether the doped structures are ductile or brittle we calculated the shear bulk modulus ratio, 0.5 is the cut-off below which materials are categorized as ductile [48]. Our results show that seven of the doped structures are brittle, although three of them are just above the threshold. As they are so close to the threshold values, experimental tests would be needed to determine if $MoS_2$ structues with one S atom substituted for one Al, N or Ni atom are in fact brittle. Our simulations show that only when Co and Ni are substituted for Mo or Co substituted for S in $3H_b$-$MoS_2$ the doped materials become ductile.

Poisson's ratio is a measure of the Poisson effect, a materials deformation perpendicular to the direction of the applied force. A value close to zero indicates that the material's structure (e.g. foam) would collapse in the compression, while materials with a much larger bulk modulus than shear modulus (rubber) will have a Poisson ratio around 0.5 [78]. Co and Ni substitution for Mo have quite high values (0.450 and 0.462) putting them in the upper region together with gold and saturated clay. I substitution for Mo on the other hand is in the mid-range where similar materials would be magnesium and variants of cast iron. The rest are in the range of 0.306 to 0.345 which is similar to the Poisson ratio of stainless steel, aluminium alloy and copper. Compared to the values obtained for $3H_b$ in our previous paper we see that the shear modulus has increased for the doped structures indicating that they will withstand higher values of shear stress. Adding dopants has also made the structures ductile in the case of Co and Ni substitution for Mo and Co substitution for S. This showcases the power of doping when it comes to altering and improving mechanical properties of materials.

### 4.5. Dynamical stability

It is not enough for a material to be mechanically stable; it must also be dynamically stable. In order to verify this, we performed phonon and phonon density of states calculations. In addition, we have calculated the phonon dispersion curves, at the equilibrium volume, along the high symmetry direction of the Brillouin zone and these results are seen in figure 5 and 6. The $3H_b$ structures where one Mo atom was replaced with one Co, I or one N atom have clear and distinctive negative frequencies, as seen in Figure 5b, 5c and 5d respectively, which makes the dynamically unstable structures.

In general, if a material is mechanically stable and dynamically unstable it could have a metastable phase and by using dopants, nanoparticles and nanoobjects the structures can be stabilised.

For Mo replaced with either one Al or one Ni atom small and similar negative modes are seen for both structures between A-L, M-Γ, Γ-K and H-A.

The imaginary modes seen in Figure 5a and 5e are believed to be caused by lattice distortions stemming from the creation of the super cell. The effect of these distortions can potentially be dealt with by changing the supercell size. Phonon calculations also require extremely ($10^{-8}$) accurate forces [79], while the volume relaxation calculations were performed using $10^{-6}$ as the accuracy limit. This difference in accuracy could have caused these small imaginary modes we see for Al or Ni. Another possible explanation is slightly wrong magnetic moment in the input files for the phonon calculations. Wolloch et. al. found that quite small differences in the magnetic moment can help stabilise a structure [79]. Based on this we conclude that these two structures are in fact dynamically stable.

For the S substituted structures presented in Figure 5, we see the same type of negative modes appear as seen in 5a and 5e. Especially for S replaced with either Co, I and N, Figure 5b, 5c and 5d respectively, the negative frequency is near zero and definitely an artefact from the calculations. Thus, we can conclude that all the S substituted structures are dynamically stable.

*Figure 5: Phonon density of states for $3H_b$ doped with Al (a), Co (b), I (c), N (d) and Ni (e) for Mo.*

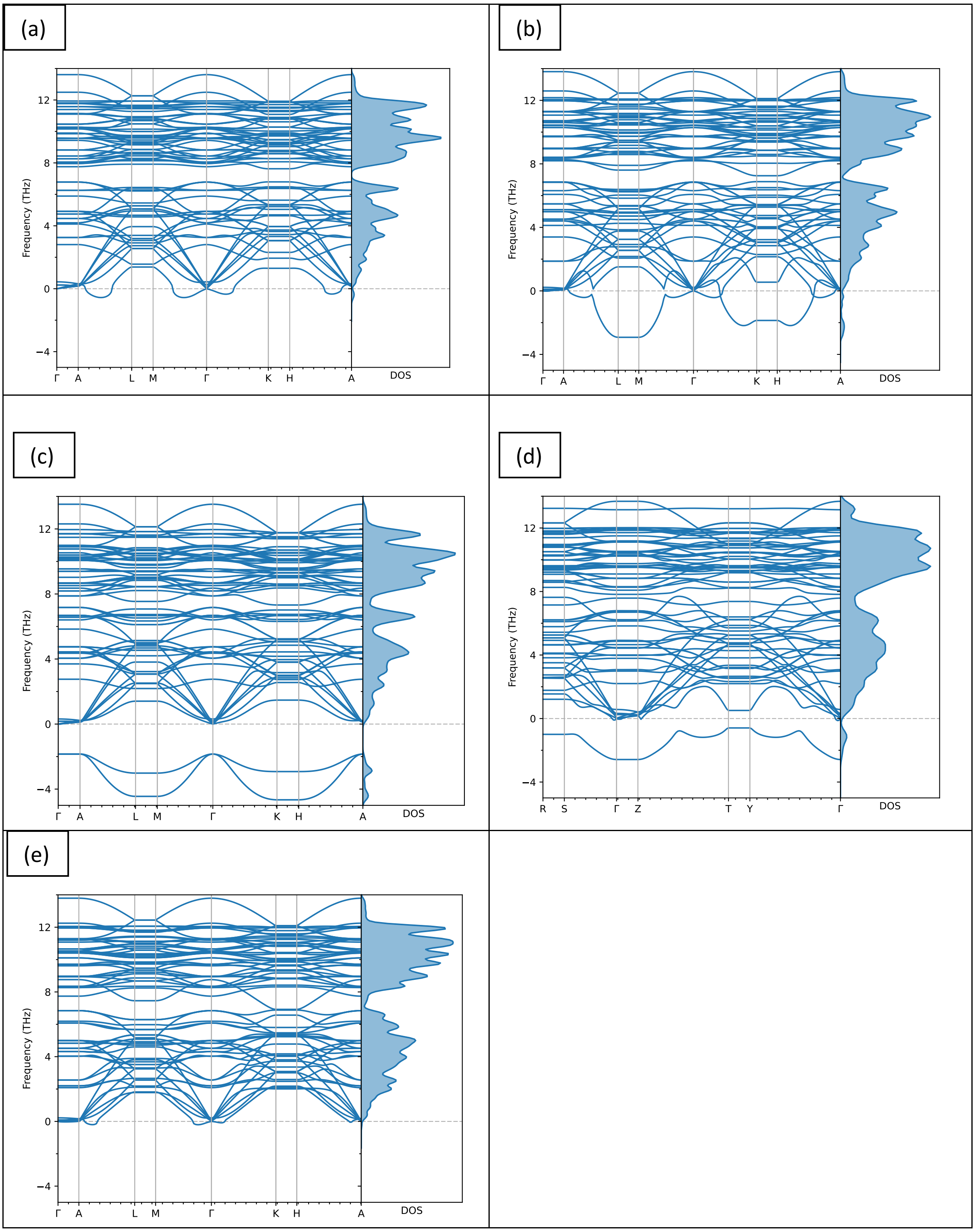

*Figure 6: Phonon density of states for $3H_b$ with S substituted for Al (a), Co (b), I (c), N (d) and Ni (e)*

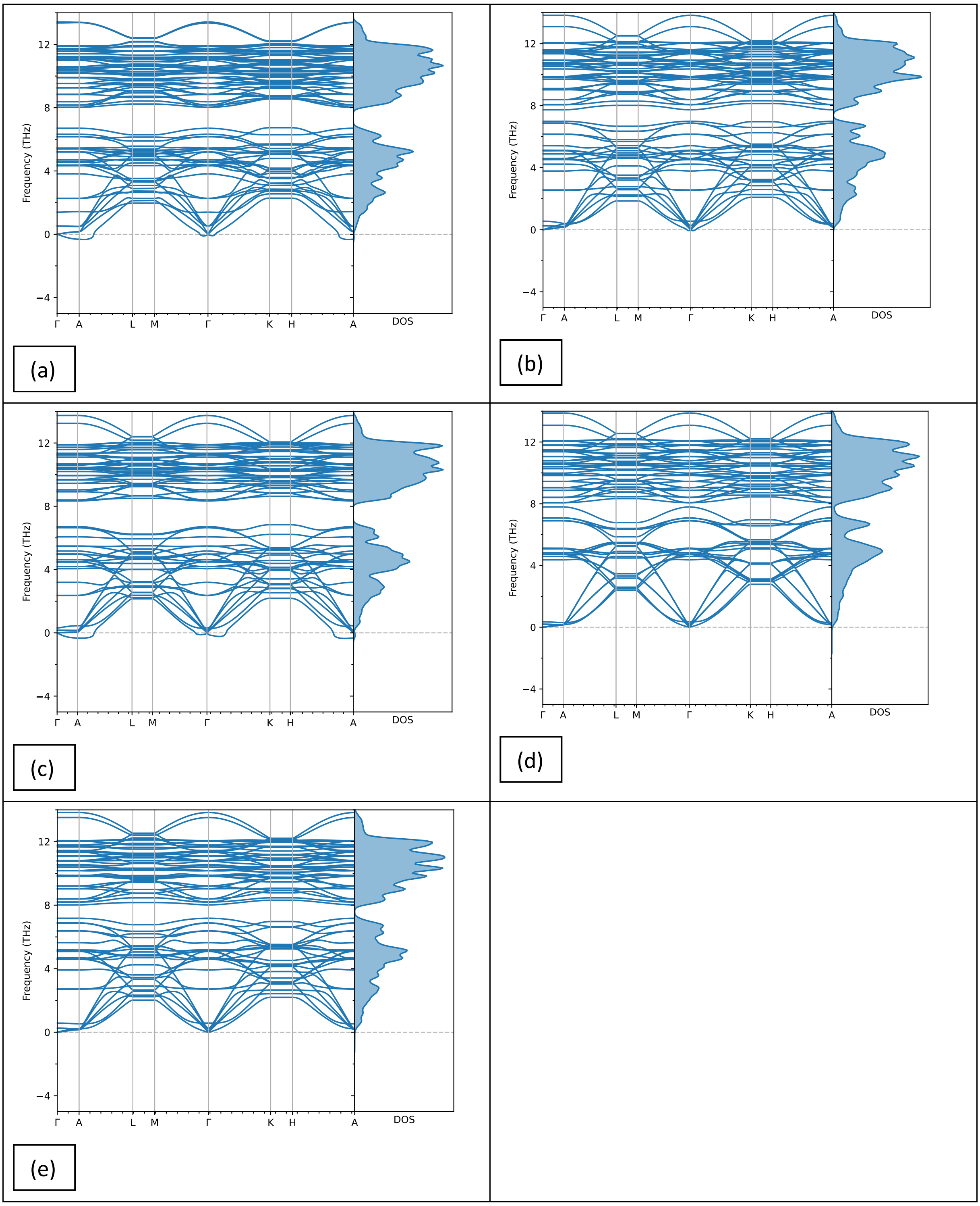

### 4.6. Charge density calculations

The charge density map showed in Figure 7a for $3H_b$-$MoS_2$ clearly shows that the electrons reside around the individual atoms. In addition, the spherically-shaped charge distribution indicates that the bonding between Mo – S and S – S is primarily ionic. The charge transfer plots in Figure 7b reveals a depletion of charge around the Mo atoms, while we get a charge accumulation around the S atoms and between the Mo and S atoms. As the charge transfer plot shows the charge gathers around the S atoms and indicates a slight polar character for the compound-. The electron localization function (ELF), Figure 7c, is a measure of the spatial localization of electrons and that helps to map electron pair probability in multielectron systems. Our ELF findings are consistent with that of the charge transfer plot, and we can thus expect the electron to be found outside of the S atoms.

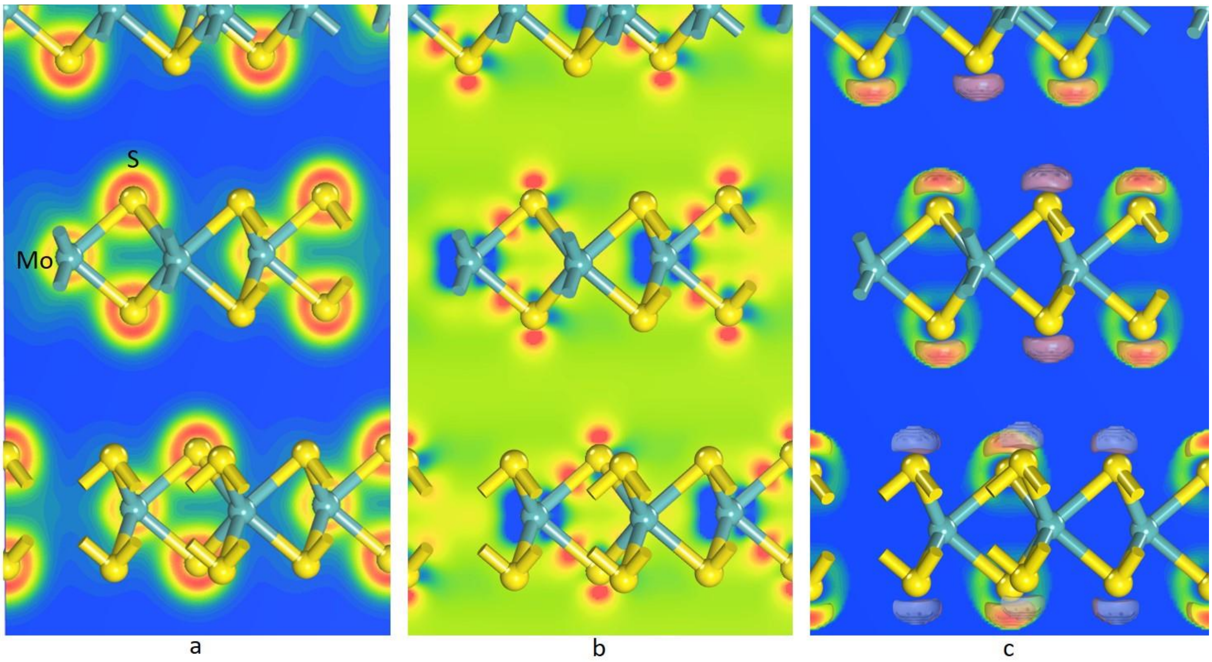

*Figure 7: Calculated charge density map (a), charge transfer plot (b) and electron localization function (c) for 3H$_b$-MoS$_2$.*

## 5. Conclusion

Seven MoS$_2$ polymorphs were studied with regards to phase transition and their photocatalytic capabilities were analysed using catalytic indicators as D-band centre, Gibbs free energy and absorption coefficient. The most promising candidate, 3H$_b$-MoS$_{2,}$ was chosen for further enquiries and was substitutional doped with Al, Co, I, N and Ni atoms at two different locations. This study shows the following

- No phase transitions caused by temperature changes were found for 1H, 2H, 2R$_1$, 2T, 3H$_a$, 3H$_b$ and 4T polymorphs.
- All seven polymorphs have their absorption peak at 620nm in the visible spectra,
    - 2R$_1$ has the highest maximum (2.67x10$^5$ cm$^{-1}$) followed by 2H and 3H$_b$ at 2.33 x10$^5$ cm$^{-1}$ and 2.28 x10$^5$ cm$^{-1}$ respectively.
- 2R$_1$, 2H, 3H$_b$, 4T and 3H$_a$ are high refractive index materials (n>3.9).
- Different dopants of 3H$_b$-MoS$_2$ resulted in varying bandgaps.
    - Only four were seen to be semiconductors: Mo substituted with Al and I, and S substituted with Co and Ni.
    - S substituted with I is an insulator.
    - The remaining five structures, Mo substituted with Co, N or Ni and S substituted with Al or N, are metallic.
- Mo substitutional doped MoS$_2$ with Al, Co, I, N and Ni reduces the Gibbs free energy with a factor of ten.

    - $3H_b$-$MoS_2$ doped with N for Mo (-0.28 – 0.27 eV) has a lower Gibbs free energy than the edge sites of $MoS_2$.
- Only Co, I and N for Mo doped $3H_b$-$MoS_2$ are dynamically unstable.
    - The other seven structures are both mechanically and dynamically stable.
    - Structures with Mo replaced are more thermodynamical stable than structures with S substituted.

Our calculations show that $3H_b$-$MoS_2$ doped with Al and Ni for one Mo atom and $3H_b$-MoS2 doped with Al, Co, I, N and Ni for one S atom are dynamically and mechanically stable. This makes it possible to synthesise and perform experimental tests on these structures. Through doping, we lowered the Gibbs free energy of $3H_b$-$MoS_2$ and made the basal plane competitive with the edge sites, especially for N for Mo. Our study indicates that $3H_b$-$MoS_2$ substitutional doped with Al for Mo atoms are promising candidates for photocatalytic water splitting. However, the best doping percentage and optimal dopant needs to be found through further theoretical and experimental studies.

### Author Contributions

**Håkon Eidsvåg:** Conceptualization, Methodology, Software, Formal analysis, Writing – Original Draft, Writing – Review & Editing, Visualization; **Dhayalan Velauthapillai:** Supervision, Resources, Validation, Writing – Review & Editing; **Ponniah Vajeeston:** Validation, Supervision, Writing – Review & Editing

### Conflicts of interest

There are no conflicts of interest to declare.

### Acknowledgements

The authors acknowledge the Research Council of Norway for providing the computer time (under the project number NN2875k and NN2867k) at the Norwegian supercomputer clusters.

### References

1. Chen, W.-H. *et al.* A review on the visible light active modified photocatalysts for water splitting for hydrogen production. *International Journal of Energy Research* **46**, 5467–5477 (2022).

2. Jafari, T. *et al.* Photocatalytic Water Splitting-The Untamed Dream: A Review of Recent Advances. *Molecules* vol. 21 (2016).

3. Steinfeld, A. Solar hydrogen production via a two-step water-splitting thermochemical cycle based on Zn/ZnO redox reactions. *International Journal of Hydrogen Energy* **27**, 611–619 (2002).

4. Kudo, A. Photocatalysis and solar hydrogen production. *Pure and Applied Chemistry* **79**, 1917–1927 (2007).

5. Fajrina, N. & Tahir, M. A critical review in strategies to improve photocatalytic water splitting towards hydrogen production. *International Journal of Hydrogen Energy* **44**, 540–577 (2019).

6. Wang, Q. & Domen, K. Particulate Photocatalysts for Light-Driven Water Splitting: Mechanisms, Challenges, and Design Strategies. *Chem. Rev.* **120**, 919–985 (2020).

7. Gupta, U. & Rao, C. N. R. Hydrogen generation by water splitting using MoS2 and other transition metal dichalcogenides. *Nano Energy* **41**, 49–65 (2017).

8. Li, S. *et al.* Edge-Enriched 2D MoS2 Thin Films Grown by Chemical Vapor Deposition for Enhanced Catalytic Performance. *ACS Catal.* **7**, 877–886 (2017).

9. Ji, X. *et al.* Graphene/MoS2/FeCoNi(OH)x and Graphene/MoS2/FeCoNiPx multilayer-stacked vertical nanosheets on carbon fibers for highly efficient overall water splitting. *Nat Commun* **12**, 1380 (2021).

10. Chen, T.-Y. *et al.* Comparative study on MoS2 and WS2 for electrocatalytic water splitting. *International Journal of Hydrogen Energy* **38**, 12302–12309 (2013).

11. Jaleel UC, J. R., R, M., Devi K R, S., Pinheiro, D. & Mohan, M. K. Structural, Morphological and Optical Properties of MoS2-Based Materials for Photocatalytic Degradation of Organic Dye. *Photochem* **2**, 628–650 (2022).

12. Gawari, D., Pandit, V., Jawale, N. & Kamble, P. Layered MoS2 for photocatalytic dye degradation. *Materials Today: Proceedings* **53**, 10–14 (2022).

13. Sivaranjani, P. R., Janani, B., Thomas, A. M., Raju, L. L. & Khan, S. S. Recent development in MoS2-based nano-photocatalyst for the degradation of pharmaceutically active compounds. *Journal of Cleaner Production* **352**, 131506 (2022).

14. Voiry, D. *et al.* Conducting MoS2 Nanosheets as Catalysts for Hydrogen Evolution Reaction. *Nano Lett.* **13**, 6222–6227 (2013).

15. Lukowski, M. A. *et al.* Enhanced Hydrogen Evolution Catalysis from Chemically Exfoliated Metallic MoS2 Nanosheets. *J. Am. Chem. Soc.* **135**, 10274–10277 (2013).

16. Wang, H. *et al.* Electrochemical tuning of vertically aligned MoS2 nanofilms and its application in improving hydrogen evolution reaction. *Proceedings of the National Academy of Sciences* **110**, 19701–19706 (2013).

17. Lv, Y. *et al.* Dimensionality-dependent MoS2 toward efficient photocatalytic hydrogen evolution: from synthesis to modifications in doping, surface and heterojunction engineering. *Materials Today Nano* **18**, 100191 (2022).

18. Shi, X. *et al.* Nickel nanoparticle-activated MoS 2 for efficient visible light photocatalytic hydrogen evolution. *Nanoscale* **14**, 8601–8610 (2022).

19. Zhao, H. *et al.* Transition-Metal-Based Cocatalysts for Photocatalytic Water Splitting. *Small Structures* **3**, 2100229 (2022).

20. Khan, M. M. & Rahman, A. Chalcogenides and Chalcogenide-Based Heterostructures as Photocatalysts for Water Splitting. *Catalysts* **12**, 1338 (2022).

21. Eidsvåg, H., Rasukkannu, M., Velauthapillai, D. & Vajeeston, P. In-depth first-principle study on novel MoS2 polymorphs. *RSC Advances* vol. 11 3759–3769 (2021).

22. Vandalon, V., Verheijen, M. A., Kessels, W. M. M. & Bol, A. A. Atomic Layer Deposition of Al-Doped MoS2: Synthesizing a p-type 2D Semiconductor with Tunable Carrier Density. *ACS Appl. Nano Mater.* **3**, 10200–10208 (2020).

23. Li, D., Li, W. & Zhang, J. Al doped MoS2 monolayer: A promising low-cost single atom catalyst for CO oxidation. *Applied Surface Science* **484**, 1297–1303 (2019).

24. Liang, Z. *et al.* Co doped MoS2 as cocatalyst considerably improved photocatalytic hydrogen evolution of g-C3N4 in an alkalescent environment. *Chemical Engineering Journal* **421**, 130016 (2021).

25. Dai, X. *et al.* Co-Doped MoS2 Nanosheets with the Dominant CoMoS Phase Coated on Carbon as an Excellent Electrocatalyst for Hydrogen Evolution. *ACS Appl. Mater. Interfaces* **7**, 27242–27253 (2015).

26. Yang, Y.-Q., Zhao, C.-X., Bai, S.-Y., Wang, C.-P. & Niu, C.-Y. Activating MoS2 basal planes for hydrogen evolution through the As doping and strain. *Physics Letters A* **383**, 2997–3000 (2019).

27. Yang, Q. *et al.* Activating MoS2 with Super-High Nitrogen-Doping Concentration as Efficient Catalyst for Hydrogen Evolution Reaction. *J. Phys. Chem. C* **123**, 10917–10925 (2019).

28. Wang, D., Zhang, X., Shen, Y. & Wu, Z. Ni-doped MoS2 nanoparticles as highly active hydrogen evolution electrocatalysts. *RSC Adv.* **6**, 16656–16661 (2016).

29. Zhang, R. *et al.* Creating Fluorine-Doped MoS2 Edge Electrodes with Enhanced Hydrogen Evolution Activity. *Small Methods* **5**, 2100612 (2021).

30. Hohenberg, P. & Kohn, W. Inhomogeneous Electron Gas. *Physical Review* vol. 136 B864–B871 (1964).

31. Kohn, W. & Sham, L. J. Self-Consistent Equations Including Exchange and Correlation Effects. *Physical Review* vol. 140 A1133–A1138 (1965).

32. Kresse, G. & Furthmüller, J. Efficient iterative schemes for ab initio total-energy calculations using a plane-wave basis set. *Physical Review B* vol. 54 11169–11186 (1996).

33. Kresse, G. & Joubert, D. From ultrasoft pseudopotentials to the projector augmented-wave method. *Physical Review B* vol. 59 1758–1775 (1999).

34. Perdew, J. P., Burke, K. & Ernzerhof, M. Generalized Gradient Approximation Made Simple. *Phys. Rev. Lett.* vol. 77 3865–3868 (1996).

35. Blöchl, P. E. Projector augmented-wave method. *Physical Review B* vol. 50 17953–17979 (1994).

36. Andrinopoulos, L., Hine, N. D. M. & Mostofi, A. A. Calculating dispersion interactions using maximally localized Wannier functions. *J. Chem. Phys.* vol. 135 154105 (2011).

37. Silvestrelli, P. L. Van der Waals Interactions in DFT Made Easy by Wannier Functions. *Phys. Rev. Lett.* vol. 100 053002 (2008).

38. Silvestrelli, P. L. van der Waals Interactions in Density Functional Theory Using Wannier Functions. *J. Phys. Chem. A* vol. 113 5224–5234 (2009).

39. Togo, A. & Tanaka, I. First principles phonon calculations in materials science. *Scripta Mater.* vol. 108 1–5 (2015).

40. Ravindran, P., Vidya, R., Kjekshus, A., Fjellvåg, H. & Eriksson, O. Theoretical investigation of magnetoelectric behavior in $\mathrmBi\mathrmFe\mathrmO_3$. *Physical Review B* vol. 74 224412 (2006).

41. Heyd, J., Scuseria, G. E. & Ernzerhof, M. Hybrid functionals based on a screened Coulomb potential. *J. Chem. Phys.* vol. 118 8207–8215 (2003).

42. Wang, V., Xu, N., Liu, J. C., Tang, G. & Geng, W.-T. VASPKIT: A User-friendly Interface Facilitating High-throughput Computing and Analysis Using VASP Code. *arXiv e-prints* arXiv:1908.08269 (2019).

43. Ganose, A. M., Jackson, A. J. & Scanlon, D. O. sumo: Command-line tools for plotting and analysis of periodic *ab initio* calculations. *Journal of Open Source Software* **3**, 717 (2018).

44. Kirchner-Hall, N. E., Zhao, W., Xiong, Y., Timrov, I. & Dabo, I. Extensive Benchmarking of DFT+U Calculations for Predicting Band Gaps. *Applied Sciences* **11**, 2395 (2021).

45. O'Rourke, C. & Bowler, D. R. Intrinsic Oxygen Vacancy and Extrinsic Aluminum Dopant Interplay: A Route to the Restoration of Defective TiO2. *J. Phys. Chem. C* **118**, 7261–7271 (2014).

46. Farkaš, B., Santos-Carballal, D., Cadi-Essadek, A. & de Leeuw, N. H. A DFT+U study of the oxidation of cobalt nanoparticles: Implications for biomedical applications. *Materialia* **7**, 100381 (2019).

47. Welch, E., Scolfaro, L. & Zakhidov, A. Density functional theory + U modeling of polarons in organohalide lead perovskites. *AIP Advances* **6**, 125037 (2016).

48. Parhizgar, S. S. & Beheshtian, J. Effect of nitrogen doping on electronic and optical properties of ZnO sheet: DFT+U study. *Computational Condensed Matter* **15**, 1–6 (2018).

49. Yu, M., Yang, S., Wu, C. & Marom, N. Machine learning the Hubbard U parameter in DFT+U using Bayesian optimization. *npj Comput Mater* **6**, 1–6 (2020).

50. Hammer, B. & Norskov, J. K. Why gold is the noblest of all the metals. *Nature* vol. 376 238–240 (1995).

51. Hammer, B. & Nørskov, J. K. Electronic factors determining the reactivity of metal surfaces. *Surface Science* vol. 343 211–220 (1995).

52. Zheng, J., Sheng, W., Zhuang, Z., Xu, B. & Yan, Y. Universal dependence of hydrogen oxidation and evolution reaction activity of platinum-group metals on pH and hydrogen binding energy. *Science Advances* **2**, e1501602 (2016).

53. Nørskov Jens, K., Abild-Pedersen, F., Studt, F. & Bligaard, T. Density functional theory in surface chemistry and catalysis. *Proceedings of the National Academy of Sciences* vol. 108 937–943 (2011).

54. Guo, Q. *et al.* Optimal d-band-induced Cu3N as a cocatalyst on metal sulfides for boosting photocatalytic hydrogen evolution. *Journal of Materials Chemistry A* vol. 8 22601–22606 (2020).

55. Zhou, Y., Qin, W., Sun, X., Zhu, Y. & Niu, J. Synergistic effects on d-band center via coordination sites of M-N3P1 (M = Co and Ni) in dual single atoms that enhances photocatalytic dechlorination from tetrachlorobispheonl A. *Journal of Hazardous Materials* vol. 430 128419 (2022).

56. Chen, C. T. *et al.* Very High Refractive Index Transition Metal Dichalcogenide Photonic Conformal Coatings by Conversion of ALD Metal Oxides. *Sci Rep* **9**, 2768 (2019).

57. Born, M. & Wolf, E. *Principles of optics: electromagnetic theory of propagation, interference and diffraction of light*. (Cambridge University Press, 2017).

58. Coccioli, R., Boroditsky, M., Kim, K. W., Rahmat-Samii, Y. & Yablonovitch, E. Smallest possible electromagnetic mode volume in a dielectric cavity. *IEE Proceedings - Optoelectronics* **145**, 391–397 (1998).

59. Islam, K. M. *et al.* In-Plane and Out-of-Plane Optical Properties of Monolayer, Few-Layer, and Thin-Film MoS2 from 190 to 1700 nm and Their Application in Photonic Device Design. *Advanced Photonics Research* vol. 2 2000180 (2021).

60. Möls, K. *et al.* Influence of phase composition on optical properties of TiO2: Dependence of refractive index and band gap on formation of TiO2-II phase in thin films. *Optical Materials* vol. 96 109335 (2019).

61. Kakaei, K., Esrafili, M. D. & Ehsani, A. Chapter 7 - Alcohol Oxidation and Hydrogen Evolution. in *Interface Science and Technology* (eds. Kakaei, K., Esrafili, M. D. & Ehsani, A.) vol. 27 253–301 (Elsevier, 2019).

62. Tang, Q. & Jiang, D. Mechanism of Hydrogen Evolution Reaction on 1T-MoS2 from First Principles. *ACS Catalysis* vol. 6 4953–4961 (2016).

63. Zou, X. & Zhang, Y. Noble metal-free hydrogen evolution catalysts for water splitting. *Chemical Society Reviews* vol. 44 5148–5180 (2015).

64. Nørskov, J. K. *et al.* Trends in the Exchange Current for Hydrogen Evolution. *J. Electrochem. Soc.* **152**, J23 (2005).

65. Greeley, J., Nørskov, J. K., Kibler, L. A., El-Aziz, A. M. & Kolb, D. M. Hydrogen Evolution Over Bimetallic Systems: Understanding the Trends. *ChemPhysChem* **7**, 1032–1035 (2006).

66. Tan, T. L., Wang, L.-L., Johnson, D. D. & Bai, K. A Comprehensive Search for Stable Pt–Pd Nanoalloy Configurations and Their Use as Tunable Catalysts. *Nano Lett.* **12**, 4875–4880 (2012).

67. Mir, S. H. *et al.* Two-dimensional boron: Lightest catalyst for hydrogen and oxygen evolution reaction. *Applied Physics Letters* vol. 109 053903 (2016).

68. Castellan, G. W. *Physical Chemistry*. (Addison-Wesley, 1983).

69. Pan, H., Feng, Y. P. & Lin, J. Hydrogen adsorption by tungsten carbide nanotube. *Applied Physics Letters* vol. 90 223104 (2007).

70. Zhu, J. *et al.* Boundary activated hydrogen evolution reaction on monolayer MoS2. *Nature Communications* vol. 10 1348 (2019).

71. Seo, B. *et al.* Monolayer-Precision Synthesis of Molybdenum Sulfide Nanoparticles and Their Nanoscale Size Effects in the Hydrogen Evolution Reaction. *ACS Nano* vol. 9 3728–3739 (2015).

72. Martínez, N. & Martínez, J. A. R. First-principles study on the formation energies of $Ga_{1-x}Cr_{x}As$. *J. Phys.: Conf. Ser.* **743**, 012007 (2016).

73. Ravindran, P. *et al.* Density functional theory for calculation of elastic properties of orthorhombic crystals: Application to TiSi2. *J. Appl. Phys* vol. 84 4891–4904 (1998).

74. Wang, V. *et al.* High-Throughput Computational Screening of 2D Semiconductors and Heterostructures for Photocatalytic Water Splitting. Preprint at https://doi.org/10.48550/arXiv.1806.04285 (2022).

75. Engineering ToolBox. Young's Modulus, Tensile Strength and Yield Strength Values for some Materials. *Engineering ToolBox* vol. 2020 (2003).

76. Goldstein, R. V., Gorodtsov, V. A. & Lisovenko, D. S. Variability of elastic properties of hexagonal auxetics. *Dokl. Phys.* vol. 56 602–605 (2011).

77. Pugh, S. F. XCII. Relations between the elastic moduli and the plastic properties of polycrystalline pure metals. *London, Edinburgh, Dublin Philos. Mag. J. Sci.* vol. 45 823–843 (1954).

78. Jastrzebski, Z. D. *The Nature of Properties of Engineering Materials*. (John Wiley and Sons Ltd, 1987).

79. Wolloch, M. *et al.* Impact of lattice dynamics on the phase stability of metamagnetic FeRh: Bulk and thin films. *Phys. Rev. B* **94**, 174435 (2016).

## Supplementary information

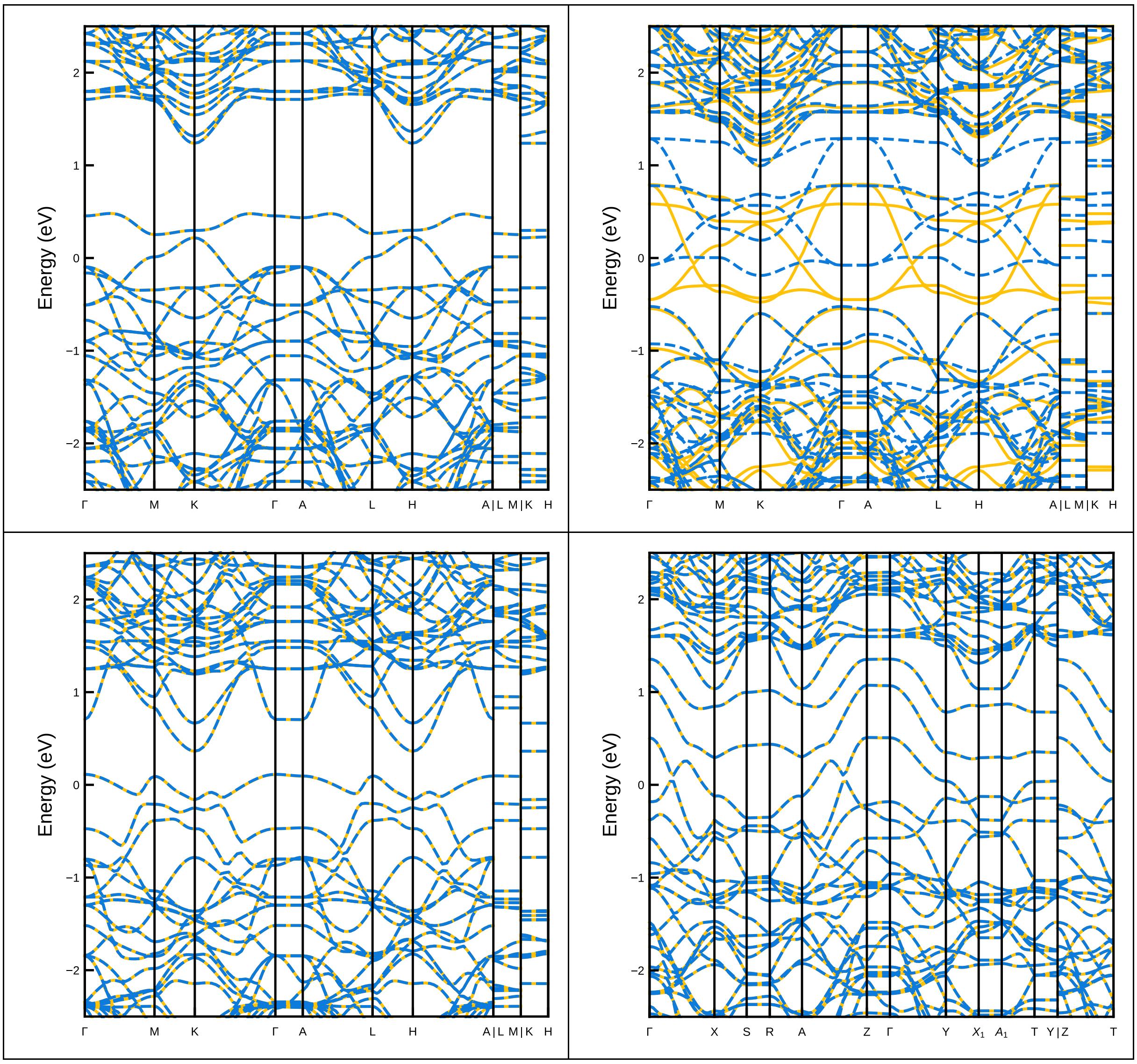

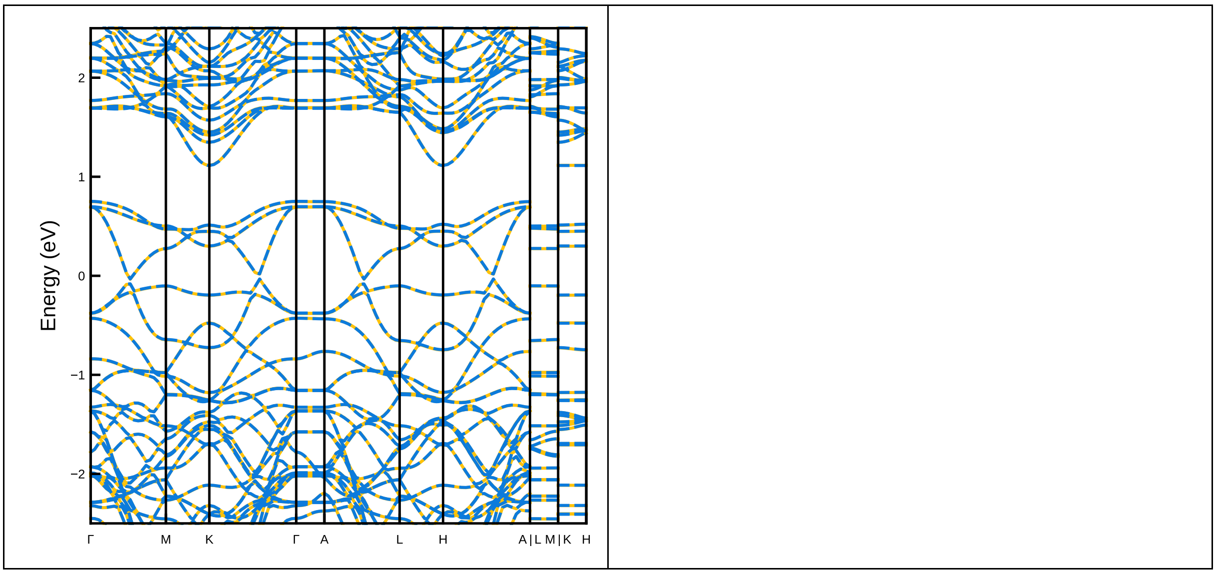

*Figure S1:* GGA band structures for doped 3H$_b$. Here one Mo is substituted with one Al (a), Co (b), I (c), N (d), Ni (e).

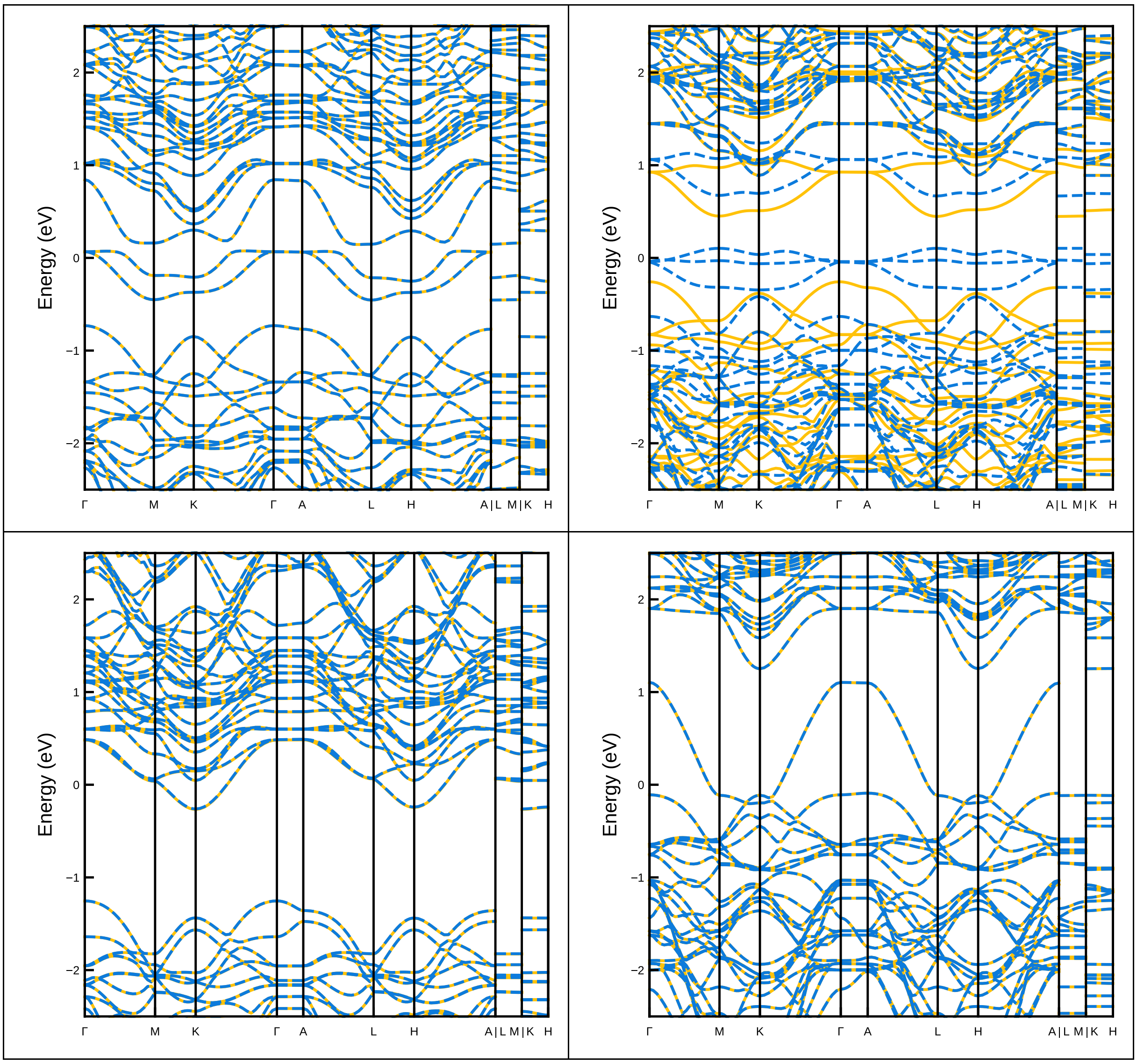

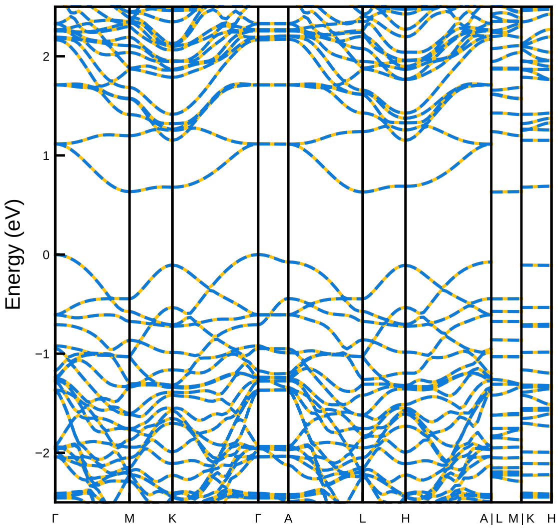

*Figure S2: GGA band structures for doped 3Hb. Here one S is substituted with one Al (a), Co (b), I (c), N (d), Ni (e).*